August 2014

Thesis for Master Degree

Nondestructive Evaluation of Thin Thickness Metal Plate by using the Sheet-Type Induced Current and Linearly Integrated Hall sensor Array

Graduate School of Chosun University

Department of Control and Instrumentation Engineering

Vu Hoang Hai

유도형면전류와선형홀센서배열을이용한박판금속의비파괴평가

Nondestructive Evaluation of Thin Thickness Metal Plate by using the Sheet-Type Induced Current and Linearly Integrated Hall Sensor Arrays

2014 년 8 월 25 일

조선대학교 대학원

제어계측공학과

부황하이

유도형면전류와선형홀센서배열을이용한박판금속의비파괴평가

지도교수 이 진 이

이 논문을 공학석사 학위신청 논문으로 제출함

2014 년 4 월

조선대학교 대학원

제어계측공학과

부황하이

부황하이의 석사학위 논문을 인준함

위원장   조선대학교   교수   고낙용   (인)

위 원   조선대학교   교수   조창현   (인)

위 원   조선대학교   교수   이진이   (인)

2014 년 5 월

조선대학교 대학원

Contents

List of Figures

List of Table

초 록

유도형면전류와 선형홀센서배열을 이용한 박판금속의 비파괴평가

부황하이

지도교수 : 이 진 이

조선대학교 일반대학원 제어계측공학과

본 논문에서는 교류형 자기카메라(AC-type magnetic camera)에 의한 와전류 검사(eddy current testing, ECT)에서의 균열의 정량적 평가를 소개한다. 교류형 자기카메라는 유도면전류(sheet-type induced current, STIC)를 발생시키는 여자기(exciter), 선형배열 홀센서(linearly integrated Hall sensor array, LIHaS), 신호 증폭기, 교류-직류 신호 변환기(root-mean-square (RMS)-to-DC converter), 아날로그-디지털 신호 변환기(analog-to-digital converter), 리니어 가이드 스캐너(linear guided scanner) 및 컴퓨터로 구성된다. 검사방법을 검증하기 위하여 티타늄, 백동, 인코넬 600, 스테인레스 스틸의 평판형 시험편을 사용하였다. 시험편의 부식을 모사하기 위하여 크기 및 깊이가 다른 인공 결함을 도입하였다. 교류전류가 인가된 여자기를 시편에 근접하면 시편의 표면에 와전류가 유도된다. 유도된 와전류는 부식 및 결함의 존재에 의하여 왜곡되며, 선형배열 홀센서를 이용하여 왜곡된 와전류의 분포를 측정할 수 있다. 실제 실험에서는 정밀 모터가 부착되어 있는 리니어 가이드 스캐너에 선형배열 홀센서를 장착하여 시험편 표면에 도입된 결함을 측정하였다. 또한, 여자기에 여러 종류의 주파수를 인가하여 주파수에 따른 결함 검출능의 차이를 확인하였다. 상술한 방법으로 각각의 시험편에 도입한 결함을 성공적으로 검출할 수 있었으며, 취득한 결함 데이터를 이용하여 결함의 위치 판별(표면 또는 이면) 및 결함의 크기 등을 추정할 수 있는 알고리즘을 개발하였다.

KEYWORDS: NDT, Crack, Eddy current testing, Discrimination, Eddy Current.

ABSTRACT

Nondestructive Testing Nondestructive Evaluation of Thin Thickness Metal Plate by using the Sheet-type Induced Current and Linearly Integrated Hall Sensor Arrays

Vu Hoang Hai

Advisor: Prof. Jinyi Lee, PhD

Dept. of Control and Instrumentation Eng.,

Graduate School of Chosun University.

This thesis introduces an AC-type magnetic camera in quantitative evaluation of crack in eddy current testing. The AC-type magnetic camera consists of a sheet-type induced current (STIC) source, a linearly integrated Hall sensor array (LIHaS), a linear guided scanner, amplifiers, root-mean-square (RMS) converter, analog-to-digital converter and a computer. Plate specimens made of different material such as titanium, copper-nickel, inconel600, stainless steel (STS304) was used. Cracks with different sizes and depths were introduced in the specimens to simulate the corrosion in the metal structures. When the STIC is excited with an alternating current and bring proximity to the test material, consequently eddy current will be induced in the test material. The presence of corrosion or crack distorts the eddy current and this distortion could be measured by linearly integrated Hall sensor arrays. During the experiment, the LIHaS is placed on the specimens and scanning was performed using linear guide scanner to inspect the cracks on the surface of the specimen (near/far-side crack). Different excited frequencies were used to study the effect of detectability of the defects in the test specimens. Subsequent to successful detection of all the kinds of cracks, several quantitative algorithms were developed to discriminate the location of crack (near/far-side) and estimate the crack volume in the thin-thickness metal plate.

KEYWORDS: NDT, Crack, Eddy current testing, Discrimination, Eddy Current.

Chapter 1 INTRODUCTION

1.1 Nondestructive testing

1.1.1 Introduction

NDT has its origins prior to the 1920's, but development of the majority of methods that are known nowadays did not appear until late in the 1930's [1]. The NDT is known variously as Nondestructive Evaluation (NDE), Nondestructive Inspection (NDI), and Nondestructive Characterization (NDC). Nondestructive testing is a wide group of analysis techniques used to evaluate the properties of a component or a system without causing damage to them [2]. By definition non-destructive testing is the testing of materials, for surface or internal flaws or metallurgical condition, without interfering in any way with the integrity of the material or its suitability for service. Non-destructive Testing is not just a method for rejecting substandard material; it is also an assurance that the supposedly good is good. The NDT technique uses a variety of principles; there is no single method around which a black box may be built to satisfy all requirements in all circumstances.

Standard classification of NDT methods was introduced for the field of flaw detection has a formal character and discrimination based the entire variety of NDT methods and means rather by the way of identification of the applied effect than by the type of physical fields, such as active and passive. In active techniques some form of physical energy is introduced in to a structure or specimen and then the change in the input energy can be observed if there is any flaw of crack present in the specimen. Upon classifying the active methods by the type of physical fields we obtain the following types:

- Electric.
- Magnetic.
- Electromagnetic.
- Thermal.
- Mechanical.

Collection @ chosun

In Passive techniques the crack is determined by using proper physical fields reflecting or reaction from the inspection material. The following NDT methods may be referred to passive ones:

- Visual analysis method.

- Liquid penetrates.

- Acoustic emission method.

- Thermal method (contact and non-invasive).

1.1.2 Different NDT methods

Non-destructive testing adopts measurement and instrumentation methods to measure the physical state of an object. The choice of method or methods is governed by the objects' physical size, material, location and expected flaw that would be detrimental to the object's function. An NDT method is classified according to its underlying physical principle. For example, the common methods are:

- Visual and optical testing (VT)
- Liquid penetrate testing (PT)
- Magnetic particle testing (MT)
- Acoustic emission testing (AE)
- Radiographic testing (RT)
- Ultrasonic testing (UT)
- Electromagnetic testing (ET)

The earliest forms of NDT are visual; dye penetrated, acoustic emission (sonic method) and radiographic testing methods [3]. These methods applied manually to test the object. The most common NDT is visual and optical testing. In many instances, a trained inspector armed with simple tools, such as a flashlight and magnifying glass, to inspect the difficult-to-see areas, a device known as a bore scope is often used. This method is not very suitable for all the ceases such as small surface cracks or subsurface cracks, the inspector should be patient and skillful. Another common technique is that of dye-penetrant or liquid penetrant inspection which is used for the detection of surface breaking discontinuities especially cracks. A film of penetrating liquid is coated onto the component and allowed to ingress into any cracks or indentations over time. The excess film is then removed and a developer applied to the surface. The developer

2

draws the penetrant out of any flaws causing local discolorations. The process parameters of penetrant and developer dwell time and cleaning are extremely important. The whole process is somewhat messy and can be unreliable if not carried out with care.
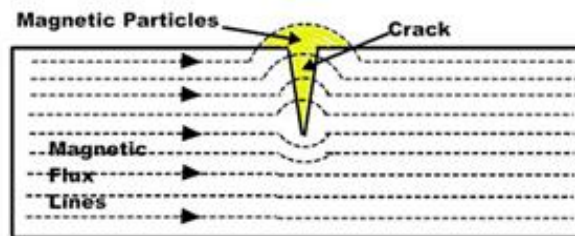
Figure 1-1 Magnetic particle testing **[4]**

Figure 1-1 shows the magnetic particle testing [4]. A crack in a ferrous material will deform a magnetic field, so by dispersing magnetic particles on the surface of a component and applying a magnet a crack can be highlighted by the distortion of the magnetic flux lines indicated by the particles. Magnetic particle inspection (MPI) [4] may be used on ferromagnetic materials. The component is first magnetized and then a fine iron-compound powder is dusted over the surface. Magnetic particle methods are based on the collection of loose magnetic particles at locations of MFL on an object. For these methods to be employed, the object under test must be electrically conductive and ferromagnetic. Magnetic particle techniques thus allow the detection of surface-breaking cracks in steel objects of complex geometry. The concepts underlying MPI are simple, but it is a non-quantitative technique, can be unreliable and requires a high level of operator skill.

Ultrasonic method is very strong and most common and offers the potential for a cost effective methodology which is used to detect wide verity of flaws which may be buried deep below the surface of the component under investigation. The term ultrasonic refers to sound waves of frequency above the limit of human hearing. Ultrasonic testing employs an extremely diverse set of methods based upon the generation and detection of mechanical vibrations or waves within test objects. The velocity of ultrasonic waves traveling through a material is a simple function of the material's modulus and density, and strongly reflected at boundaries where material properties change, and thus are often used for thickness measurements and crack detection [5]. There are, however, a number of disadvantages with ultrasonic inspection. Firstly, the transducer must, in general, be well coupled to the specimen or most of the incident

3

ultrasonic wave will be reflected straight back. Secondly, the technique is unsuitable for laminated or layered structures this is due to large reflections at the layer interfaces.
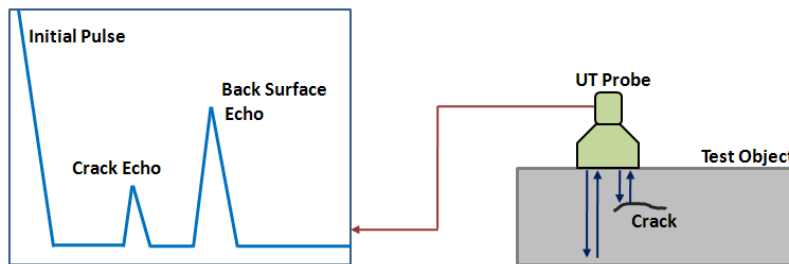
Figure 1-2 Ultrasonic Testing Principle [6]

Figure 1-2 shows ultrasonic testing principle [6]. Recently, a new ultrasonic technique that requires no couplant and no contacts have emerged. The technique, called Electromagnetic Acoustic Transducer (EMAT), uses the Lorenz force and the magnetostrictive effect to generate and receive acoustic signals for ultrasonic inspection. The non-contacting nature of EMAT offers advantages, such as capability of inspecting high temperature samples [6]. The drawback of the method is the relatively low transmitted energy into the sample and this requires more robust signal processing than that of conventional ultrasonic techniques.
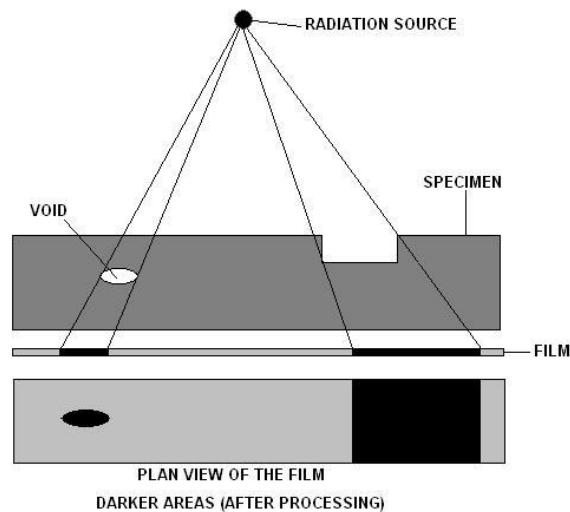
Figure 1-3 Radiography Testing Principle [7]

Figure 1-3 shows the radiography testing principle. It is the next most common NDT. Significant activity in the field occurred almost immediately after Roentgen discovery of X-

4

rays in 1895 [7]. Discontinuities such as pores or inclusions in metals are readily detected in many cases. Cracks may also be detected using radiographic techniques, However, X- and -y-rays are inherently dangerous and the equipment used is generally bulky. Energy levels must be chosen carefully in order that scattering effects, which would otherwise reduce image contrast, are minimized. In addition, access is required to both sides of a component, something which is often difficult with in-service inspection. Eddy current NDE is a prime method for detecting hidden corrosion in electrically conducting materials. The method is based on generating a localized alternating current field in the sample using a probe coil same probe coil or another detector then measures the material's response to the induced eddy currents. The detailed discussion is carried out in the next section.
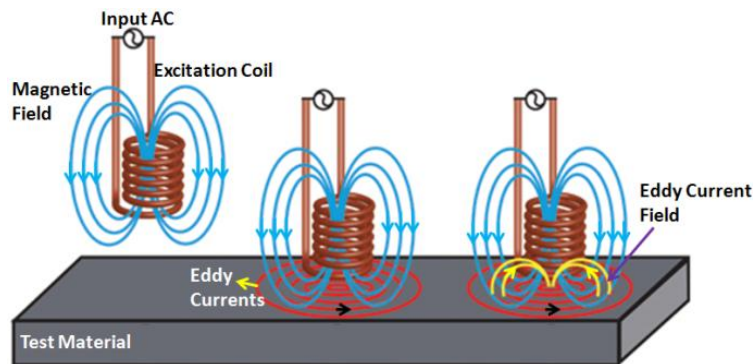
Figure 1-4 Eddy current Testing Principle [8]

Figure 1-4 shows the eddy current testing (ECT) principle [8]. It is one of the oldest NDT methods. ECT utilizes principle of electromagnetic induction to detect discontinuities in conductive materials. The use of eddy currents for nondestructive testing was originally carried out on a large scale by Forster in Germany in 1940's, after then it has developed rapidly. The method utilizes a coil carrying an alternating current at a given frequency, which is placed in the vicinity of a metal sample under test. The alternating magnetic flux generated in the sample induces eddy currents which produce a secondary magnetic flux in the coil which is generally out of phase with the primary flux. In this way the impedance of the coil is changed both in magnitude and phase by amounts dependent on the values of the electrical conductivity and the magnetic permeability of that part of the sample in which the eddy currents are induced [8]. With it, the sizes of surface and subsurface cracks in metals can be determined to within fractions of millimeters and values of electrical conductivities and magnetic permeability can

5

be measured with accuracies of better than one per cent. An important advantage of using eddy currents is that, unlike ultrasonic and magnetic particle methods, contact between the detector and the sample surface is not required, so that careful surface preparation other than the removal of metallic adherents in unnecessary. There are several limitations, among them: only conductive materials can be tested, the finish of the material may cause bad readings, the depth of penetration into the material is limited by the material's conductivity, and flaws that lie parallel to the probe may be undetectable.

1.1.3 Application of NDT

NDT is very important because often the cracks that we are looking for are not visible because paint or some other coating may cover them. There might also be cracks that are so small they cannot be seen with our eyes or any other visual method of inspection. NDT is used in many industries to monitor in service components for signs of fatigue or damage, as well as approving new items for use. Its purpose is to ensure the safety of the public, workforce, plant, environment and profit. Today, new products to a great extent consist of very complex and expensive materials and components. Quality tests with destructive testing methods will be replaced more and more by non-destructive testing methods. This helps to save money and time in the field of product development. Furthermore, these methods can be used for inline quality control, i.e. to test every single product and therefore, permanently guarantee high quality standards. Moreover, testing is always possible during product usage.

- Flaw Detection and Evaluation
- Leak Detection
- Location Determination
- Dimensional Measurements
- Structure and Microstructure Characterization
- Estimation of Mechanical and Physical Properties
- Stress (Strain) and Dynamic Response Measurements
- Material Sorting and Chemical Composition Determination

NDT applications at almost any stage in the production or life cycle of a component:

- To assist in product development
- To screen or sort incoming materials

6

- To monitor, improve or control manufacturing processes
- To verify proper processing such as heat treating
- To verify proper assembly
- To inspect for in-service damage

1.2 NDT in large industrial structures

1.2.1 Nuclear Power Industry
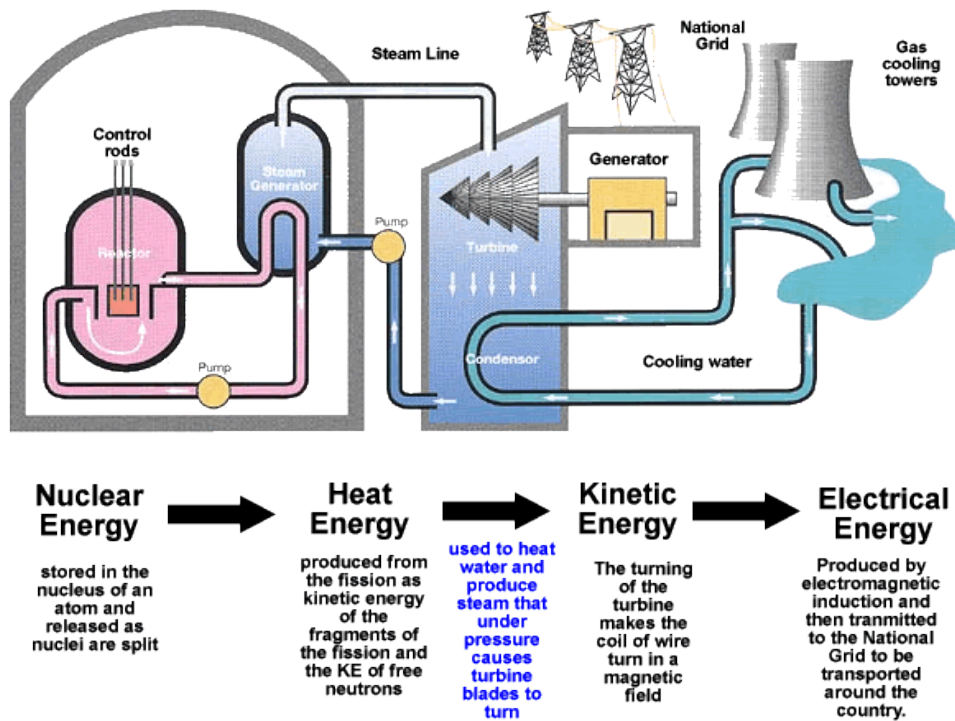
Figure 1-5 Principle of nuclear Power Plant [9]

Nowadays, because the demand of human on using an energy increase highly, thus we use different methods to convert physical energy into electrical energy, for example, thermal, wind, oil, etc.. Another most important energy form of energy generation are thermal power plant, hydroelectric power plant, etc., which are not enough so after 2nd world war the

technical advancements in science lead us to the building nuclear power plants. It affected to economic benefits and decrease Co^2 that caused the phenomenon of greenhouse effect.

Figure 1-5 shows the principle of nuclear power plant [9]. It has been in operation since the 1950s. Although today they have modern nuclear power plant however the basic workings of the nuclear power plant are the same, which is the nuclear fission. The fuel rod usually is used Uranium. The nuclear fission phenomenon of the atom of Uranium occurs inside a nuclear reactor. It generates the heat energy and this energy has used to generate a vapor of water. This vapor of water is transferred through tubing to the turbine, which will convert to mechanical energy into electrical energy by generator [9].

1.2.1.1 Kinds of Nuclear Power Plants

The nuclear plants can be discrimination based on the structure of nuclear reactor. There are two most common type of commercial reactors used to generate electricity are pressurized water reactors (PWR) and boiling water reactors (BWR).
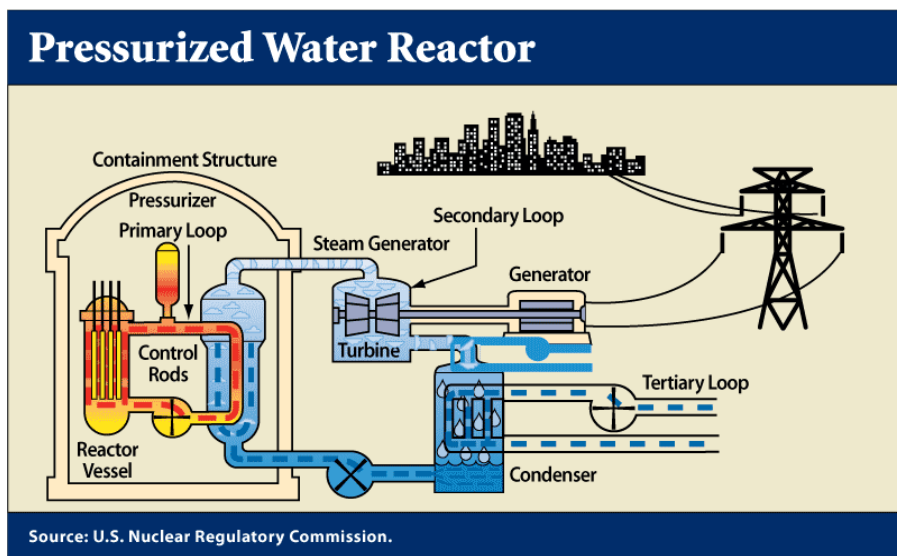
Figure 1-6 Principle of Pressurized water reactors (PWRs) [10]

Figure 1-6 shows the principle of pressurized water reactors (PWRs). They have three loops [10]. The primary loop, in which the water passes through reactor core and caries heat

8

energy generated to steam generator. Its heat is about 600^0F under high pressure and it does not boil. The secondary loop, in which the heat from primary loop is transferred to steam generator. At here, the pressure and temperate decrease is about 400-500^{0}F, and the water boil, will be convert into steam. This steam is transferred to turbine and it converts the mechanical energy of turbine into electricity energy. The third loop, the unused heat energy is rejected to atmosphere either passes through a cooling tower or into cooling pond or river.
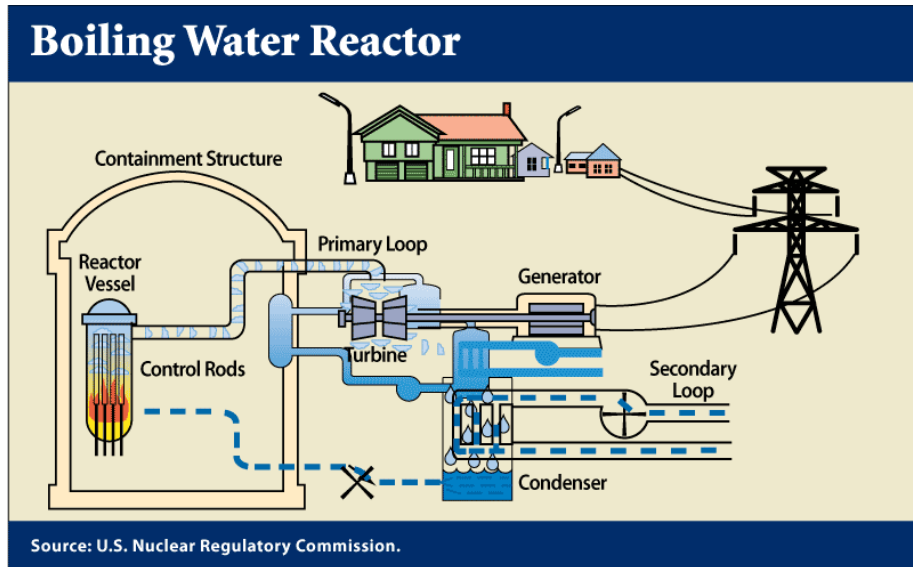
Figure 1-7 Principle of Boiling water reactors (BWRs) [10]

Figure 1-7 shows the principle of boiling water reactors (BWRs). It has two loops. The primary loop, the water passes through reactor core. At here it boils and creates steam. This steam is transferred directly to steam generator. It converts the mechanical energy of turbine into electricity energy. The steam passes through a condenser and it is turned into water. This water return to the reactor score and this process is repeated. The second loop, unused heat energy is rejected to atmosphere [10].

1.2.1.2 The small bore piping system and Damages

The small bore piping system is the heat exchanger tubing. Figure shows the heat exchanger tubing in NPPs. It is one of the very important structural components in NPPs.

9

External heat transfer effect, it like as barriers separate between radioactive component and non-radioactive. Generally the NPPS have 2 to 4 sets of steam generator tubing, each set consist of 3000 to 6000 tubes, each tube is about 20mm in diameter and 21m in length [11][12].

Initially, almost the heat exchanger tubing of the PWR steam generator placed in-serve in the west countries(except German) was made from Nickel based Alloy 600 (76% Ni, 15.5 Cr, 8% Fe, <0.15% C). The German steam generator designed by Siemens/KWU use Alloy 800M tubing. Now almost heat exchanger use Alloy 690 (61% Ni, 29.5% Cr, 9% Fe, < 0.025% C), some of use Alloy 800M tubing.

Figure 1-8 The heat exchanger tubing in NPPs [11]

There are some types of cracks appear in the heat exchanger, such as flow-accelerated corrosion (FAC), inter-granular attacks (IGA), inter-granular stress corrosion cracking (IGSCC)…

FAC is corrosion mechanical in which a normally protective oxide layer on a metal surface dissolves is fast flowing water and the rate of FAC depend on the flow of velocity. IGA and IGSCC appear on the outside surface of the tubing. IGSCC requires tensile stress, material susceptibility and corrosion environment (high temperate and aggressive chemicals). IGSCC cracks occur along the grain boundaries, oriented normal to the maximum principal stress. IGA is characterized by local, corrosion loss of material on the grain boundaries; it does not require large tensile stress.

1.2.2 Aerospace industry

Aviation technology opens a new era in passenger transportation. However, it is accompanied by great danger. So non-destructive testing is a reliable method as a guarantee of safety. Aerospace components are designed to be as light as possible while still performing their intended function; it is achieved by special design techniques [11]. They are carefully inspected before assembly and be checked periodically throughout the life cycle activities. Because the planes are assembled from many complex compositions, so choosing appropriate methods are needed. Here are some commonly used methods: 1) Liquid penetrant 2) Magnetic particle, 3) Eddy current 4) Ultrasonic 5) Radiography (x-ray/gamma ray) 6) Visual/Optical 7) Sonic/Resonance 8) Infrared Thermograph [13], [14].

1.3 Eddy current NDT

1.3.1 History and principle

1.3.1.1 History of eddy current testing

Michal Faraday was a chemist and physicist prominent British. He was born November 22, 1791 and lost August 25, 1867. During his career he was best known for the discovery of the phenomenon of electromagnetic induction, diamagnetism, electro-magnetic rotations and some other phenomena. Eddy current testing is rooted from the phenomenon of electromagnetic induction was discovered in 1831. However its applications are widely applied just after World War II. Today, eddy current testing has been widely used in many fields especially in aviation technology and nuclear power plants [15], [16].

1.3.1.2 Principle

Eddy currents are created through a process called electromagnetic induction. When alternating current is applied to the conductor, the magnetic field developed inside and around the conductor. If other electrical conductors are brought closer to the field, induced current will appear on second conductor. Eddy currents are induced current flow in the circle path.

We know that the eddy current can measure the thickness of the material. But this is also its limits if the object is too thick. This limit is known through the skin effect. That is the eddy current density will decrease exponentially with depth. The depth that eddy currents penetrate into a material is affected by the frequency of the excitation current and the electrical conductivity and magnetic permeability of the specimen (Figure 1-9). The depth at which eddy current density has decreased to 1/e, or about 37% of the surface density, is called the standard depth of penetration (δ), which is given by the following equation:

$$\delta = 1 \Big/ \sqrt{\pi f \mu \sigma} \qquad (1)$$

Where:

        δ: the standard depth of penetration (mm)

        f: the test frequency (Hz)

        μ: the permeability of the test object (H/mm)

        σ: the electrical conductivity of the test material.

The depth of penetration decreases with increasing frequency and increasing conductivity and magnetic permeability. When the eddy currents flowing in the test object produces magnetic fields which oppose the primary field, thus reducing net magnetic flux and causing a decrease in current flow as depth increases. Alternatively, eddy currents near the surface can be viewed as shielding the coil's magnetic field, thereby weakening the magnetic field at greater depths and reducing induced currents [17].
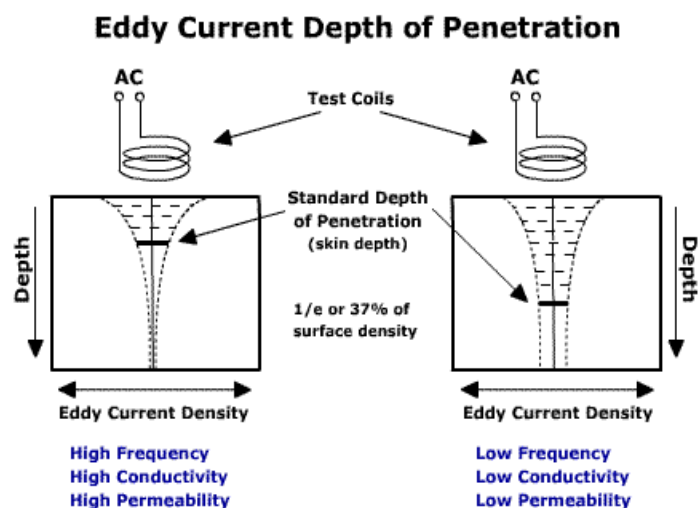
Figure 1-9 Eddy current depth of penetration [17]
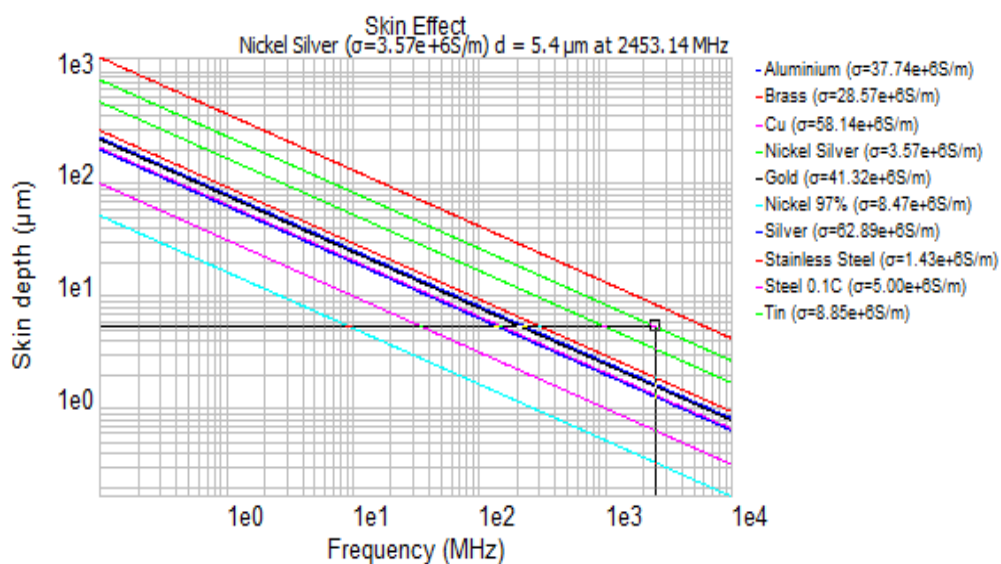
Figure 1-10 Relation between the skin depth and frequency of excitation for different materials
[17]

1.3.2 Eddy current probes

The probe in the major component eddy current testing, which is basically consists of an excitation coil and detection coil; the detection coil can be replaced by a solid state magnetic field sensors such as Hall-sensor or GMR sensor. The excitation coil is used to induce the eddy currents in to the test object by exciting it by an alternating current. The detection coil (or sensor) is used to detect the resultant magnetic field due to the induced eddy currents in the test object. Depending on the shape and structure of the examined or test material the ECT probe can be divided as:

- Surface probes (pancake probes)
- Encircling probes
- Inner diameter probes or bobbin coil probes

Figure 1-11 shows schematic and photographs of surface probe. Surface probes or pancake probes are coils whose axis is perpendicular to the surface of the test object. During the measurement the surface probes are placed on the surface of the specimen. These probes can be used for surface and sub-surface crack detection. High permeability materials such as ferrites can be used as the core of the excitation coil for high concentration of flux at the inspection area. These types of sensors are used in flat surface inspection, pancake-type probes can be used in either manual or automatic eddy current testing particularly suitable for the maintenance of aeronautic parts [18].
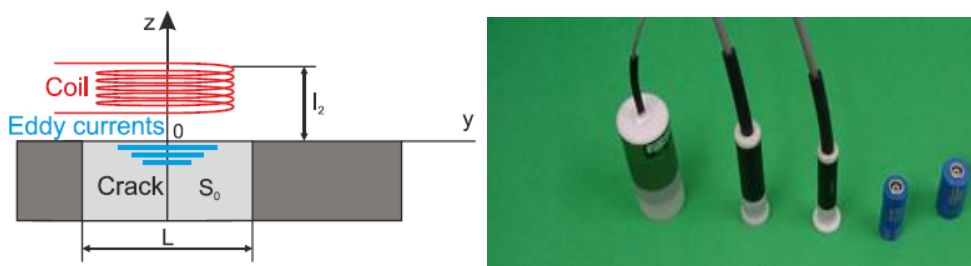
Figure 1-11 Schematic and photographs of surface probe [18].

Most commonly used ECT probes are encircling probes, encircling coils that normally used for in-line inspection of round products and tube products. The product to be tested is

14

inserted through a circular coil; either coil can be scanned on the surface of the tube specimen or the tube can be moved inside the coil as shown in the Figure 1-12. Encircling coils are sensitive to discontinuities or cracks which are parallel to the axis of the tube or bar as eddy currents distributed in radial circumferences in an opposing sense of currents around the excitation coil current [19].
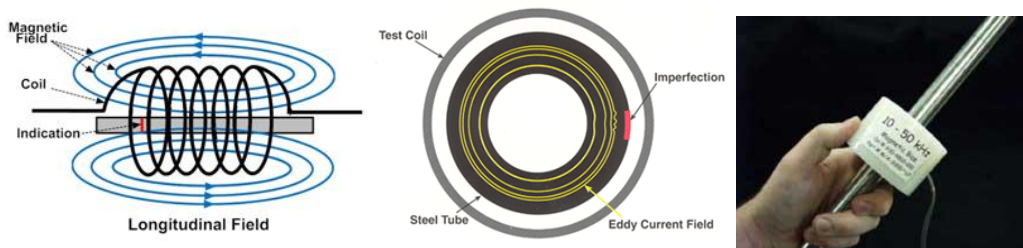
Figure 1-12 Configuration and photograph of encircling probe

Inner diameter (ID) probes which are also referred as bobbin probes or feed through probes are designed for tubular test specimen, the probe is inserted into the tube; these probes are also called the bobbin probes. The bobbin type probes are most commonly used for in-service inspection of heat exchangers. Normally, these probes are wound with the coil axis along the center of the tube so that the probe inspects an area around the entire circumference of the test object at one time as shown in the Figure 1-13.
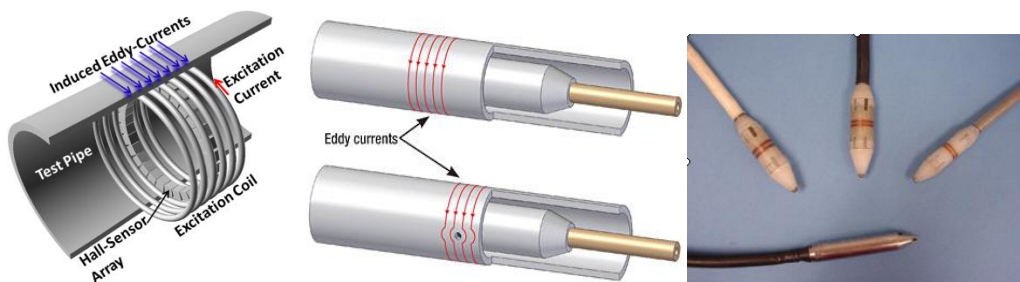
Figure 1-13 Schematic and photograph of bobbin type ECT coil [19].

There are two methods to detect the induced eddy currents, by using simple coil or solid-state magnetic field sensors. The selection of sensor depends on several factors such as operating frequency, magnetic field range and complexity of the structure which allows suitable size of the sensor for eddy current testing [20]. Several common magnetic sensors are:

15

Hall's effect sensor (Hall sensor), giant magneto-resistance sensor (GMR), and anisotropic magneto-resistance (AMR).

1.3.4 ECT for Small Bore-Piping System in NPP

1.3.4.1 Bobbin-type Eddy Current Testing

Bobbin probe is industry standard which is used to inspect flaws in steam generator and heat exchanger tube in NPPs. It really confidence and prove good method to detect flaws. Addition it is fast and can be performed as speed up to 6 ft/sec. Figure 1-14a shows typical bobbin probe for steam generation tubing.

However, one of limitation of bobbin coil is they cannot detect circumferential crack on tube because eddy current are parallel to the crack and are not interrupted by the crack, as shown in Figure 1-14b. One of another limitation of bobbin coil is resolution. Because there is only one bobbin coil, so the probe could not detect crack in circumferential direction of pipe [21]-[24].
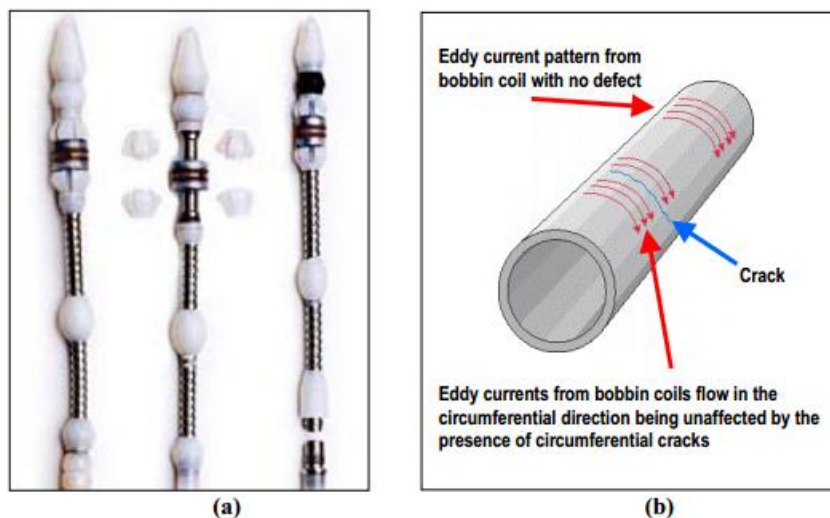
Figure 1-14 Bobbin probe (a) View of typical bobbin probes for steam generator tubing inspection. (b) The limitation of bobbin probe for detecting circumferential [21].

1.3.4.2 MPRC

A mention previous section, bobbin probe cannot detect circumferential crack so Motorized rotating pancakes coil (MPRC) probe is used to overcome this limitation. They contain a single pancake coil that is rotated as the probe is pulled slowly in the section area. They can detect both axial and circumferential crack and also provide information about flaw morphology. Figure 1-15a shows the distortion to the eddy current testing pattern generated by pancake coil in the presence of a circumferential crack. Figure 1-15b shows the configuration MPRC probe. However the limitation of MPRC is their speed. Their speed is about 80 to 120 times slower than the speed of bobbin coil [23] due to its scanning type. Also, the MPRC is complicated in configuration because of including rotating motor.
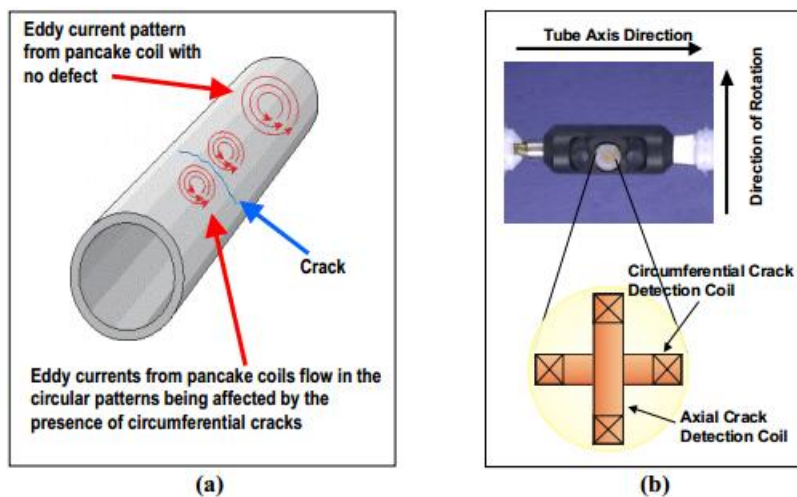
Figure 1-15 MPRC probe (a) the distortion to the eddy current testing pattern generated by pancake coil in the presence of a circumferential crack, (b) the configuration of MPRC probe [23].

1.3.4.3 X-probe

The main limitation of MPRC is their speed, so X-probe has been developed. An X-probe uses a number of arrayed sensing coils so that axial and circumferential cracks can be inspected at high speeds without the need of rotation motor. The number of sensing arrayed coils in each circumferential direction array is from 4 to 19 depending on the tube diameter.

17

Thus, the resolution is low and limitation in accuracy of quantitative evaluation of crack size. Figure 1-16 shows a sample of an X-probe which includes an bobbin probe and an arrayed sensing coil [21], [25]-[26].

Figure 1-16 X-probe [21], [25]-[26]

1.3.5 ECT for thin thick plates in Aerospace

One application where the eddy current technique is commonly used to measure material thickness is in the detection and characterization of corrosion damage on the skins of aircraft. Eddy current techniques can be used to do spot checks or scanners can be used to inspect small areas. Eddy current inspection has an advantage over ultrasound in this application because no mechanical coupling is required to get the energy into the structure. Therefore, in multi-layered areas of the structure like lap splices, eddy current can often determine if corrosion thinning is present in buried layers.

Eddy current inspection has an advantage over radiography for this application because only single sided access is required to perform the inspection. To get a piece of film on the back side of the aircraft skin might require removing interior furnishings, panels, and insulation which could be very costly. Advanced eddy current techniques have been being developed that can determine thickness changes down to about three percent of the skin thickness [27].

1.4 Purpose and object of the study

Several NDT methods have been in use for the life assessment of large industrial structures like NPPs, aerospace and petrochemical. Among all existing NDT methods electromagnetic NDT methods are more often applied for the metallic components. There is an interesting research has been doing by the researcher in order to meet the current requirements of industry, such as fast, low cost and one of the recent trends of NDE is to provide quantitative

18

as well as qualitative assessments of materials. This evaluation is known as quantitative non-destructive evaluation (QNDE) such as estimation of crack sizes, shape, and locations (surface or sub-surface). The presented ECT system has limitation in scanning speed or low resolution of sensor. Thus, the QNDE of crack is limited.

The main objective of this study is to develop fast, reliable and accurate QNDE system for cracks in metal objects specifically targeted for the thin thick plates in nuclear and aerospace industries. To overcome the limitation of the previous QNDE systems, arrayed Hall sensor which has high resolution is proposed in this study. The objectives of this study to fulfill our aim are: (a) introduce a magnetic camera NDT system based on eddy current testing method, (b) prepare thin thickness metal plate test specimens using different materials such as stainless steel, Inconel, copper, titanium of different sizes and introduce artificial cracks with different depths in order to simulate the real situation in the industrial structures, (c) obtain the images of the cracks by scanning the magnetic camera on the both sides of the test object (to visualize the near-side and far-side cracks), (d) apply different signal processing methods to clear visualization of cracks, (e) study different algorithms for discriminate crack position (near-side or far-side) and evaluate crack volume.

Chapter 2 PRINCIPLE

2.1 Construction of magnetic cameras
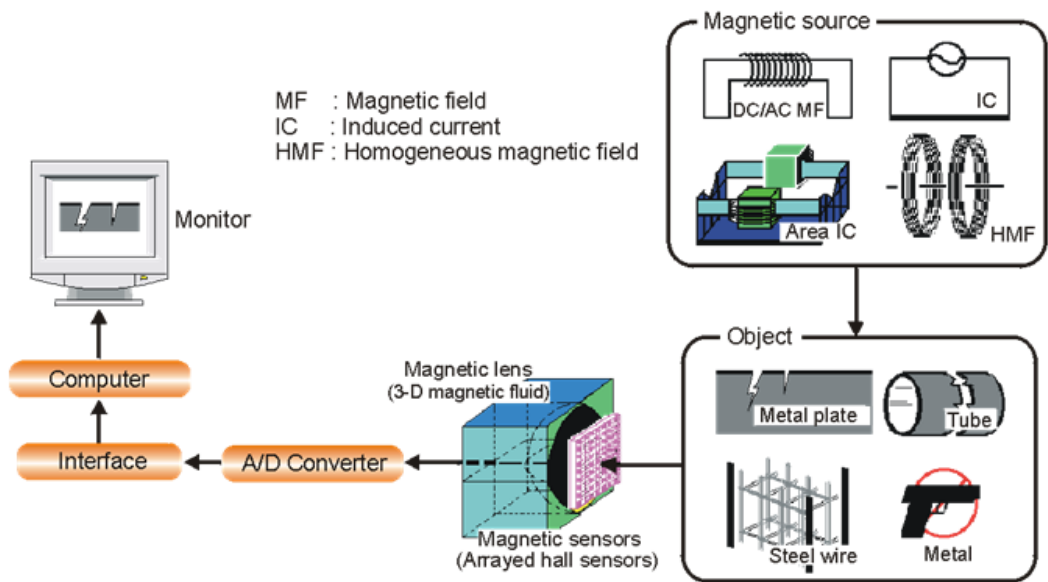
Figure 2-1 Construction of magnetic cameras

Figure 2-1shows the magnetic camera consists of a magnetic source, a magnetic sensor array, and circuitry including analog-to-digital (AD) converters, an interface, a computer and a display. The magnetic source, consisting of a direct magnetic field, an alternating magnetic field, an electrical field, an induced current, an area-type induced current or terrestrial magnetism are applied to the objects.. The magnetic field is distorted according to the existence of cracks. Because of this distortion, the distribution of the magnetic field in the air is changed. The distribution of the magnetic field can be translated into analog signals by using the magnetic sensor array. The digital signals, which are translated from the analog signals by using the AD converters, are inputted to the computer, stored, processed and displayed.

2.2 Sensor

Hall sensors can be used as the magnetic sensor to measure the distribution of a magnetic field. The Hall sensor is based on the Hall Effect. Hall sensors are used in the NDT field because of their full scale operational region (FSO) and sensitivity. Therefore, Hall sensors are used as the magnetic sensor in the magnetic camera system. According to the sensor array and scanning method, the magnetic camera is classified into four categories.

(1) Linearly integrated Hall sensors array (LIHaS): The linearly integrated Hall sensor array is used for measuring the distribution of a magnetic field. Hall sensors are arrayed on the same wafer in a matrix [28]- [29].

(2) Area-type integrated Hall sensors array (AIHaS). The sensors are arrayed on a wafer or a PCB in a matrix. Basically, we don't need to scan the sensors [30].

(3) Cylinder-type integrated Hall sensor array (CIHaS). The sensors are arrayed on a 32x32 matrix on wafer, which was bent to have a diameter of at least 15 mm. The sensor were then fixed onto a non-metallic fixture and electric wires connected by using ball bonder. It used to inspect the inner-diameter (ID) and outer-diameter (OD) stress corrosion cracks (SCCs) in small-bore piping system [31].

(4) Bobbin-type integrated Hall sensor array (BIHaS). It is same CIHaS however it only is one linearly integrated hall sensor array [32].

Figure 2-2 shows four types of sensor array: LIHaS, AIHaS, CIHaS and BIHaS. The sensor array has high spatial resolution due to the small size of Hall sensor element. For instance, the spatial resolutions of the LIHaS, AIHaS, CIHaS and BIHaS are 0.52 mm, 0.78 mm, 0.78 mm, 0.78 mm respectively, developed in our laboratory. In this research, the LIHaS is used.
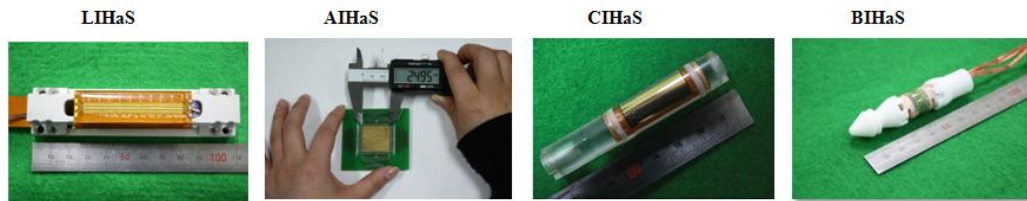
Figure 2-2 Different types of sensor array

2.3 Excitation Source

There are many kinds of magnetic sources for example the cross-type magnetic flux leakage (C-MFL) [33], the direct current magnetic flux leakage (DC-MFL) [34], the plate-type magnetic flux leakage (P-MFL) [35], the in-side solenoid magnetic flux leakage (IS-MFL) [35], the vertical-type magnetic flux leakage(V-MFL) [36], the sheet-type induced current (STIC) [37], the improved sheet-type induced current (i-STIC) [37], the combined induced current and magnetic flux leakage (CIC-MFL) [38], and the magnetic fluid penetration testing (MFPT) [39] methods. This research experimented with Copper-Nickel, Inconel, Stainless-steel, and Titanium. They are paramagnetic materials so AC magnetic sources were used to detect cracks on the thin thickness plate in the NPPs and aircrafts. The AC magnetic sources as the sheet-type induced current (STIC), the improved sheet-type induced current (i-STIC) are usually used with AIHaS, as shown in Figure 2-4. In this research, the STIC magnetic source is used.

22
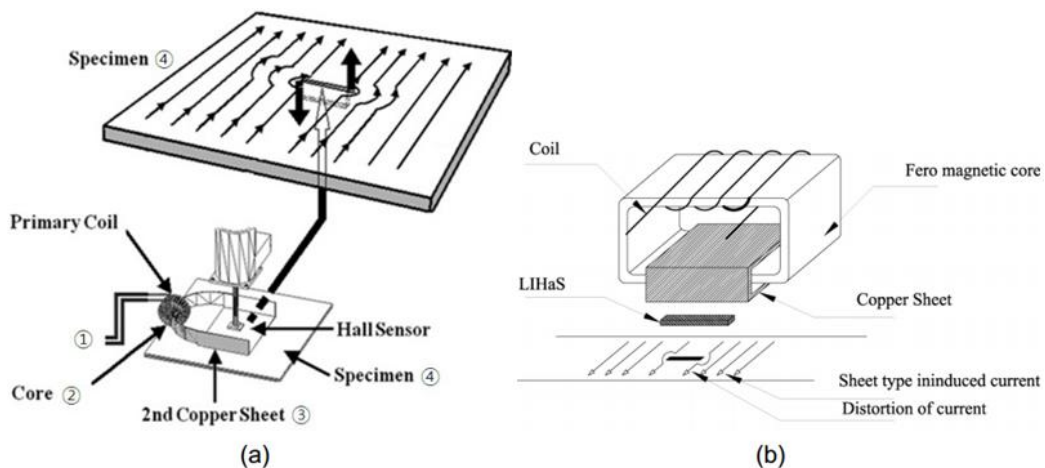
Figure 2-3 Principle of induced current: (a) Sheet-type induced current (STIC); (b) Improved sheet-type induced current (i-STIC) [37]

A sheet-type current can be induced in the specimen by using the STIC and i-STIC [37]. In Figure 2-3 (a), when alternating current is placed to the primary coil (1) then alternating magnetic field occurs in the core (2). This magnetic field generates alternating sheet-type induced current in the copper sheet (3). Then sheet-type current induces current in the specimen (4) under the copper sheet. The current on the specimen is distorted because of the existence of a crack so the distribution of magnetic field is changed. The i-STIC, as shown in Figure 2-3(b), can generate a larger induced current than the STIC. It is useful for the scan-type magnetic camera. The STIC is suitable for use by the area-type magnetic camera. The distorted magnetic field can be measured by using the Hall sensor array, and so reveal cracks on ferromagnetic, paramagnetic and combined materials. The crack detection ability is excellent in metals with a high conductivity. Fatigue cracks in aluminum alloys and the magnesium plates have been detected.

The combined induced current and magnetic flux leakage (CIC-MFL) is similar to the DC-MFL, as shown in Figure 2-4(a) [38]. The magnetic field occurs when alternating current is input to the coils, which are wound around the poles of the magnetizer, as shown in Figure 2-4(b).The current is induced in the vertical direction with the magnetic field, as shown in Figure 2-4(c). If the crack direction is vertical with the magnetization direction, the leakage magnetic flux is maximized in the ferromagnetic material. If the crack length direction is

23

parallel to the magnetization direction, the distortion of the induced current is also maximized. Correspondingly, we can detect cracks in any direction by using the CIC-MFL on ferromagnetic materials. The CIC-MFL is also useful for inspecting cracks on paramagnetic materials using induced current. The crack inspection ability is maximized when the length of the crack is vertical to the direction of the induced current.

(a)

(b)
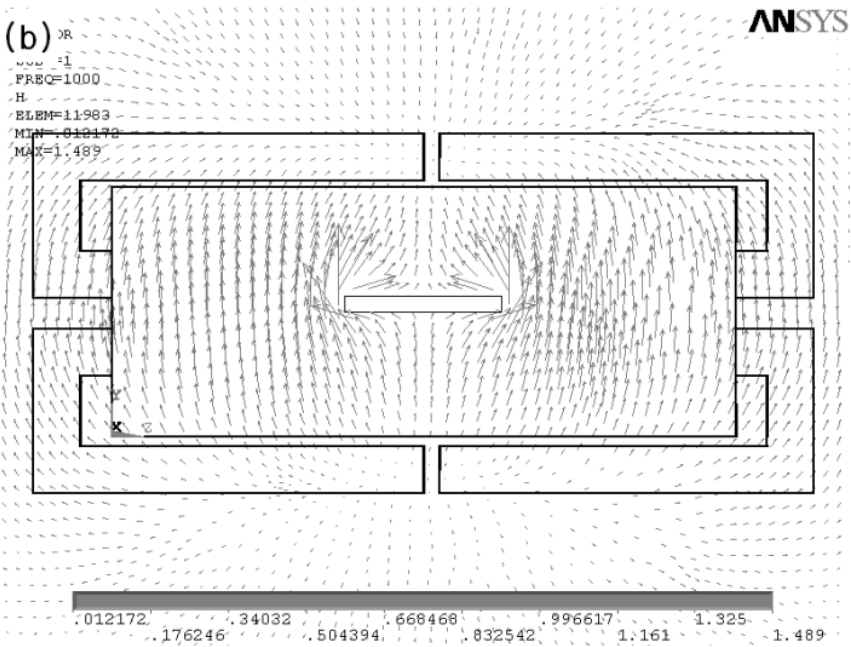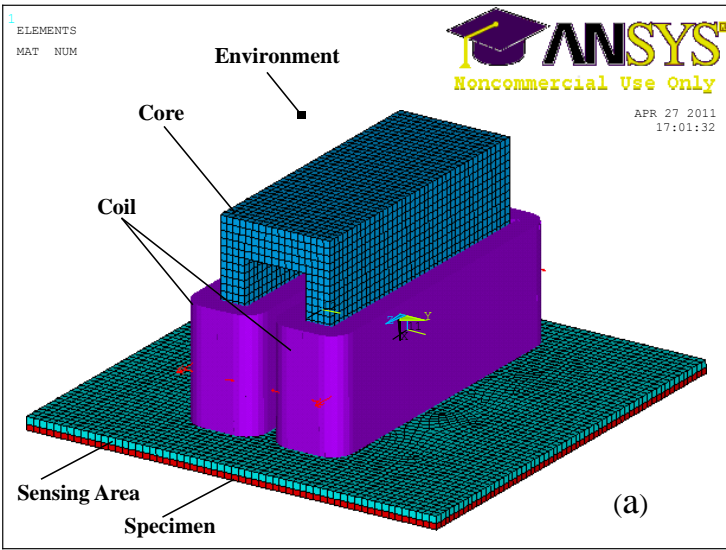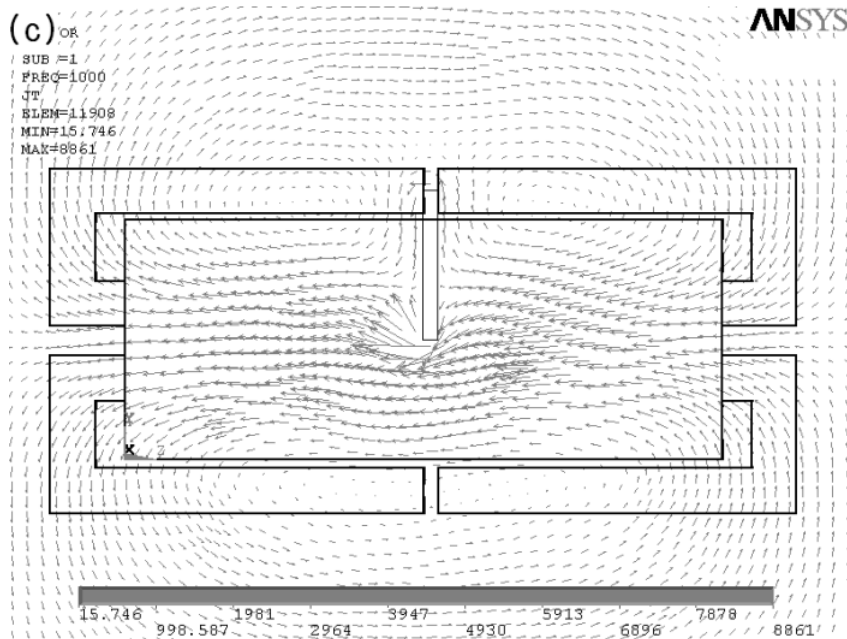
Figure 2-4 Principle of CIC-MFL; (a) Construction, (b) Simulated magnetic field generation, (c) Simulated electrical field generation [38]

2.4 Signal processing

The eddy current behaves according to the skin effect, and the skin depth is calculated using Eq. (1). The presence of the crack obstructs the eddy current flow, inducing an alternating magnetic field (AMF). The Hall sensors measure the Hall voltage, the radial component of the AMF that is perpendicular to the sensor's surface, which is expressed by Eq. (2). The output voltages from the Hall sensors are transferred to the amplifiers, after which the noise is filtered using high-pass filters (HPFs). Next, the signal is converted to a DC signal via root-mean-square (RMS) circuits, and then transferred to the computer through an ADC converter and interface. Correspondingly, the output signal is expressed by Eq. (3) that is RMS voltage.

$$\delta = \frac{1}{\sqrt{\pi f \mu \sigma}} \tag{1}$$

$$V_H(t) = K \cdot I \cdot B_Z(t) = K \cdot I \cdot B_0 \cdot Sin(2\pi f \cdot t + \varphi) \tag{2}$$

25

$$V_{RMS} = \sqrt{\frac{1}{T} \int_0^T [V_H(t)]^2 dt} = K \cdot I \cdot B_0 \sqrt{\frac{1}{T} \int_0^T Sin^2(2\pi f \cdot t + \varphi) dt} \qquad (3)$$

$$= \frac{K \cdot I \cdot B_0}{\sqrt{2}}$$

where f, μ, and σ are the excited frequency, absolute permeability, and electrical conductivity, respectively, of the specimen; K, I, t, B_0, T, and φ are the Hall constant, input current of the Hall sensor, and the time, amplitude, period and phase of the alternating magnetic field ($B_Z(t)$), respectively, which is perpendicular to the Hall sensor surface.

Chapter 3 EXPERIMENTAL RESULTS AND DISCUSSIONS

3.1 Experimental setup

Figure 3-1 shows the block diagram of the system including XY precision motorized stage, LIHaS, signal processing circuits, and computer. XY motorized stage is used to scan the LIHaS in the 2–dimensional XY. Figure 3-2 shows the real image of the signal processing circuit including 32 amplifiers; 32 high pass filters (HPFs), 32 root-mean-square (RMS) circuits. The number of amplifiers, HPFs and RMS circuits are same with the number of Hall sensors, which are 64. Thus, two circuit boards in Figure 3-2 are used. The output voltage of the LIHaS is gained 60 dB through the commercial amplifiers (AD8221) and filtered by HPFs at 300 Hz cut-off frequency. The voltage is then converted to DC by using commercial root-mean-square (RMS) circuits (AD8436). Thus, the phase signal is neglected and only the RMS voltage is measured [40], [44]. The RMS voltage is digitized by an ADC (NI PCI 6071E) before transferred to computer. The ADC has 64 channels, 12 bits resolution, ±10 V full-scale operation, and 1.25 MS/s maximum sampling rate. In the experiment, we used ±10 V operation respect to 4.882 mV resolution of the ADC. The start trigger of the ADC is controlled by a pulse from the XY motorized stage for matching the position of the probe with measuring signal.
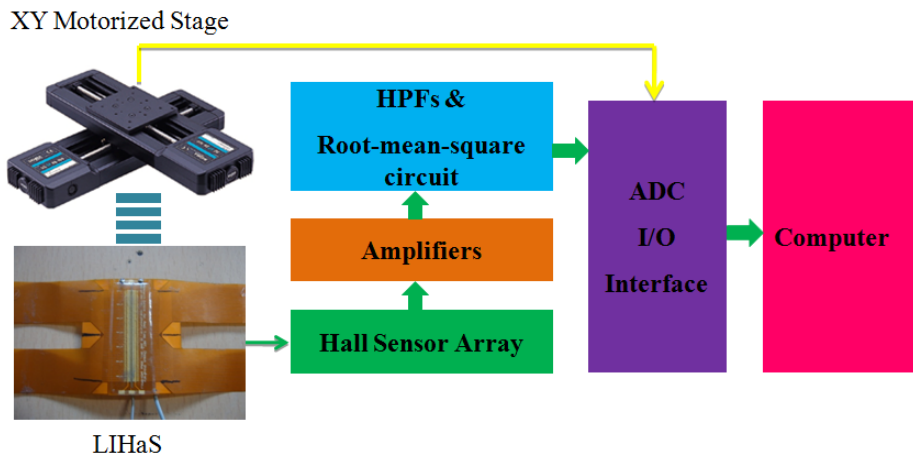
Figure 3-1 Block diagram of the magnetic camera
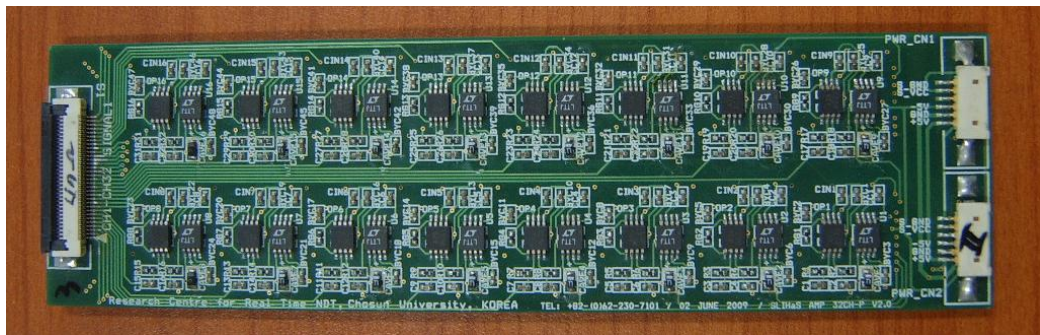
Figure 3-2 Signal processing circuit including amplifier, high-pass-filter and root-mean-square circuits.
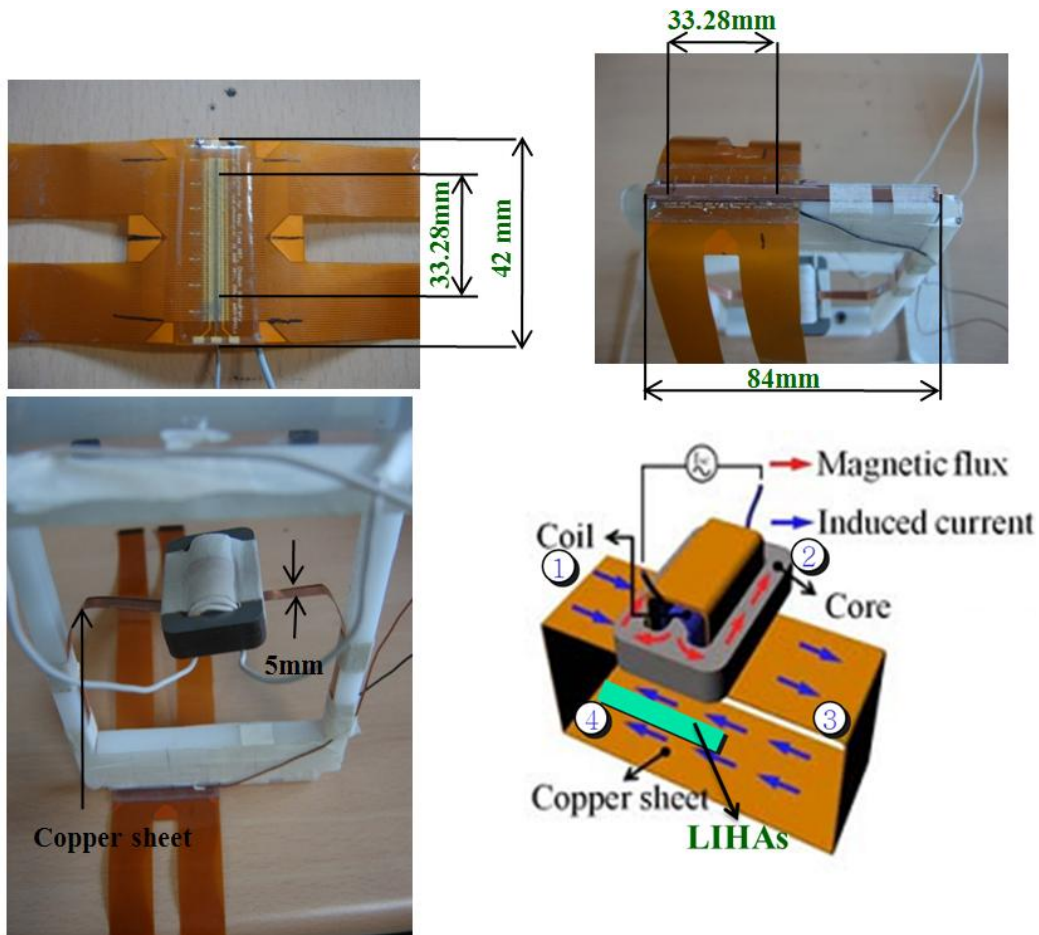
Figure 3-3 LIHaS and a STIC in sensor probe and induced current phenomenon

The LIHaS including 64 Hall sensors with spatial resolution 0.52 mm and the length of the sensing is about 33.28 mm, as shown in the Figure 3-3. It was position upper the surface of a STIC. The LIHaS and STIC are fixed in a rectangular shape to make a sensor probe. The input current for the LIHaS is 0.2A (DC). A double-yoke-type core which includes 15 thin slices made of silicon steel is used in the STIC. The usefulness of the thin slices in the core is to reduce Foucault current then save the magnetic energy and prevent of heating. In addition, the silicon steel material has high conductivity that produces high eddy current intensity into the copper sheet. The width, length, height and thickness of the copper sheet are 5, 84, 100, and 0.2 mm, respectively.

29

The input current for coil is 0.8A and exciter frequency are 1 kHz, 3 kHz, 5 kHz, respectively. The power for signal processing circuit is ±5V (DC). When alternating current is placed to the primary coil (1) then alternating magnetic field occurs in the core (2).This magnetic field generate alternating sheet-type induced current in the copper sheet (3). After that this current turned alternating magnetic field on the copper sheet then sheet-type magnetic field induces current on the specimen. The induced current on the specimen generate magnetic field on the specimen. Because of the existence of cracks on the specimen magnetic field was distorted. Distorted magnetic field effect to LIHaS (4) and transferred to electric signal.

3.2 Test specimen

Four test specimens were prepared with different kinds of materials are titanium, inconel600, copper, and stainless steel (STS304). The components of four material specimens are shown in Table 3-1 and the size, thickness and conductivity of four material specimens are shown in Table 3-2. The conductivity of copper-nickel is the highest and the lowest is inconel600.

There are two kind of crack shape are machined on all specimens which are hole-type crack and circumference-type crack. As shown in the schematics of the specimen in succeeding sections 3.2.1 to 3.2.4, the test specimens consist of several cracks with different depths and diameters. For ease of understanding and to reduce the confusion during the data analysis, the cracks are divided into different groups from A to F. Even though there are longer cracks which are expanded horizontally on the specimen to simulate the circumferential cracks, only smaller circular type defeats are considered for the data analysis. For example let us consider a titanium specimen, there are 5 rows and 5 columns of circular type (cylindrical) cracks (5 X 5 matrixes of cracks), where Φ is the diameter and D is the depth of the cracks. There are 5 cracks in the bottom row of cracks from left to right, here the diameter (Φ) of the cracks are changed while the depth (D) of the crack kept constant. On the other hand, the first column from top to bottom (left side column of cylindrical cracks), the depth (D) of the cracks is changed while diameters of the cracks keep changing (Φ). Since there are total 6 by 5 matrix of cracks in one specimen, each column identified with alphabets A, B, C, D, E and F (from left to right), and rows are identified by the numbers and a name which resemble their depth such as 05, 06, 08, 09 and Through (since D of the cracks in a column from bottom to top are 0.5 mm,

30

0.6 mm, 0.8mm, 0.9 mm and 1.2 mm (through)). For example if we want to identify the crack in the last column bottom row, it can be identified as F05, and in the same way the last column top row crack can be identified as 'FThr'.

Table 3-1 Components of four material specimens

Material	Material Components										
Titanium	%C max	%N max	%O max	%Iron max	%H max	%Other	%Ti				
	0.1	0.03	0.25	0.3	0.015	0.4	Balance				
Copper-nickel	%Cu	%Sn	%Pb	%Zn	%Fe	%Ni	%Sb	%P	%S	%Al	%Mn
	63-67	3.5-4.5	3-5	3-9	1.5	19-21.5	0.25	0.05	0.08	0.005	1
Inconel 600	%C max	%Cr	%Cu max	%Fe	%Mn max	%Ni min	%S	%Si max			
	0.15	14-17	0.5	6-10	1	72	0.015	0.5			
Stainless Steel (STS304)	%C max	%Mn	%Si max	%P	%S max	%Cr	%Ni	%N max			
	0.15	2	0.75	0.045	0.03	18-20	8-10.5	0.1			

Table 3-2 Size, thickness and conductivity of four material specimens

Material	Size [mm]	Thickness [mm]	Conductivity [S/m]
Titanium	430x300	1.2	2.38E+06
Copper-nickel	430x250	1.17	3.48E+06
Inconel600	430x300	1.07	0.97E+06
Stainless Steel (STS304)	430x300	1.15	1.45E+06

31
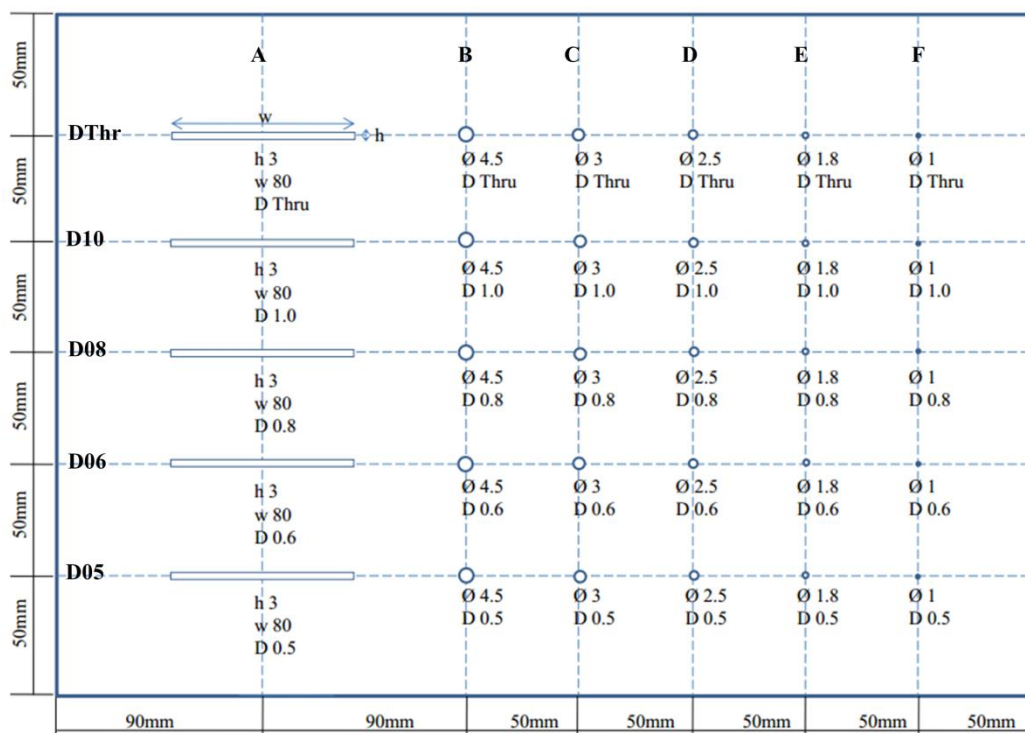
Figure 3-4 Position of cracks on the titanium specimen plate specimen

Table 3-3 Detail name and sizes of cracks on the titanium specimen plate specimen

Name	Depth [mm]	Width [mm]	Volume [mm³]	Name	Depth [mm]	Width [mm]	Volume [mm³]
F05	0.5	1	0.3926991	C05	0.5	3	3.5342917
F06	0.6	1	0.4712389	C06	0.6	3	4.2411501
F08	0.8	1	0.6283185	C08	0.8	3	5.6548668
F10	1	1	0.7853982	C10	1	3	7.0685835
FThr	1.2	1	0.9424778	CThr	1.2	3	8.4823002
E05	0.5	1.8	1.272345	B05	0.5	4.5	7.9521564
E06	0.6	1.8	1.526814	B06	0.6	4.5	9.5425877
E08	0.8	1.8	2.035752	B08	0.8	4.5	12.72345
E10	1	1.8	2.54469	B10	1	4.5	15.904313
EThr	1.2	1.8	3.0536281	BThr	1.2	4.5	19.085175
D05	0.5	2.5	2.4543693				
D06	0.6	2.5	2.9452431				
D08	0.8	2.5	3.9269908				
D10	1	2.5	4.9087385				
DThr	1.2	2.5	5.8904862				
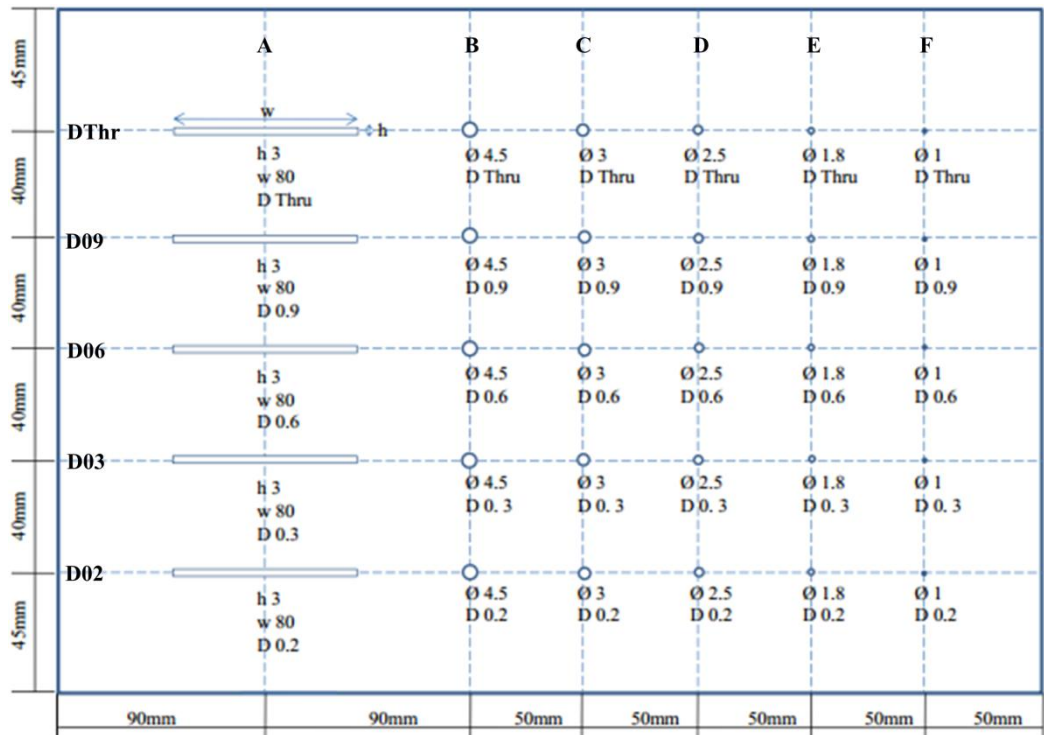
Figure 3-5 Position of cracks on the copper-nickel plate specimen

Table 3-4 Detail name and sizes of cracks on the copper-nickel plate specimen

Name	Depth [mm]	Width [mm]	Volume [mm³]	Name	Depth [mm]	Width [mm]	Volume [mm³]
F02	0.2	1	0.1570796	C02	0.2	3	1.4137167
F03	0.3	1	0.2356194	C03	0.3	3	2.120575
F06	0.6	1	0.4712389	C06	0.6	3	4.2411501
F09	0.9	1	0.7068583	C09	0.9	3	6.3617251
FThr	1.17	1	0.9189159	CThr	1.17	3	8.2702427
E02	0.2	1.8	0.508938	B02	0.2	4.5	3.1808626
E03	0.3	1.8	0.763407	B03	0.3	4.5	4.7712938
E06	0.6	1.8	1.526814	B06	0.6	4.5	9.5425877
E09	0.9	1.8	2.290221	B09	0.9	4.5	14.313882
EThr	1.17	1.8	2.9772874	BThr	1.17	4.5	18.608046
D02	0.2	2.5	0.9817477				
D03	0.3	2.5	1.4726216				
D06	0.6	2.5	2.9452431				
D09	0.9	2.5	4.4178647				
DThr	1.17	2.5	5.7432241				
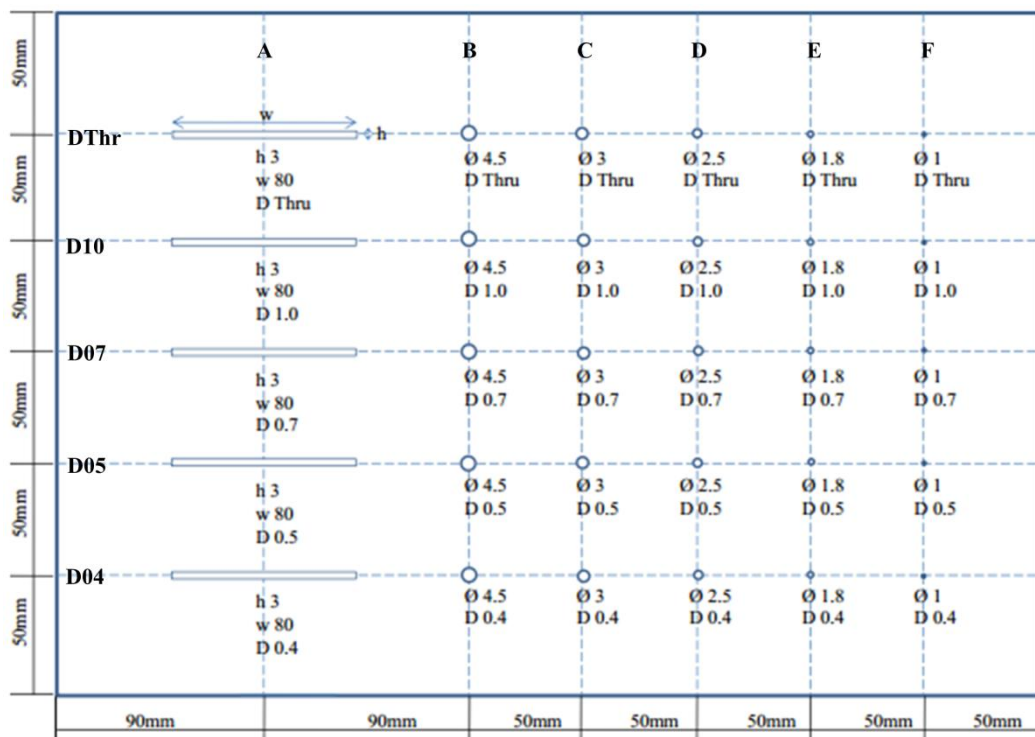
Figure 3-6 Position of cracks on the inconel600 plate specimen

Table 3-5 Detail name and sizes of cracks on a thin thickness Inconel600 specimen

Name	Depth [mm]	Width [mm]	Volume [mm³]	Name	Depth [mm]	Width [mm]	Volume [mm³]
F04	0.4	1	0.3141593	C04	0.4	3	2.8274334
F05	0.5	1	0.3926991	C05	0.5	3	3.5342917
F07	0.7	1	0.5497787	C07	0.7	3	4.9480084
F10	1	1	0.7853982	C10	1	3	7.0685835
FThr	1.07	1	0.840376	CThr	1.07	3	7.5633843
E04	0.4	1.8	1.017876	B04	0.4	4.5	6.3617251
E05	0.5	1.8	1.272345	B05	0.5	4.5	7.9521564
E07	0.7	1.8	1.781283	B07	0.7	4.5	11.133019
E10	1	1.8	2.54469	B10	1	4.5	15.904313
EThr	1.07	1.8	2.7228184	BThr	1.07	4.5	17.017615
D04	0.4	2.5	1.9634954				
D05	0.5	2.5	2.4543693				
D07	0.7	2.5	3.436117				
D10	1	2.5	4.9087385				
DThr	1.07	2.5	5.2523502				

Collection @ chosun
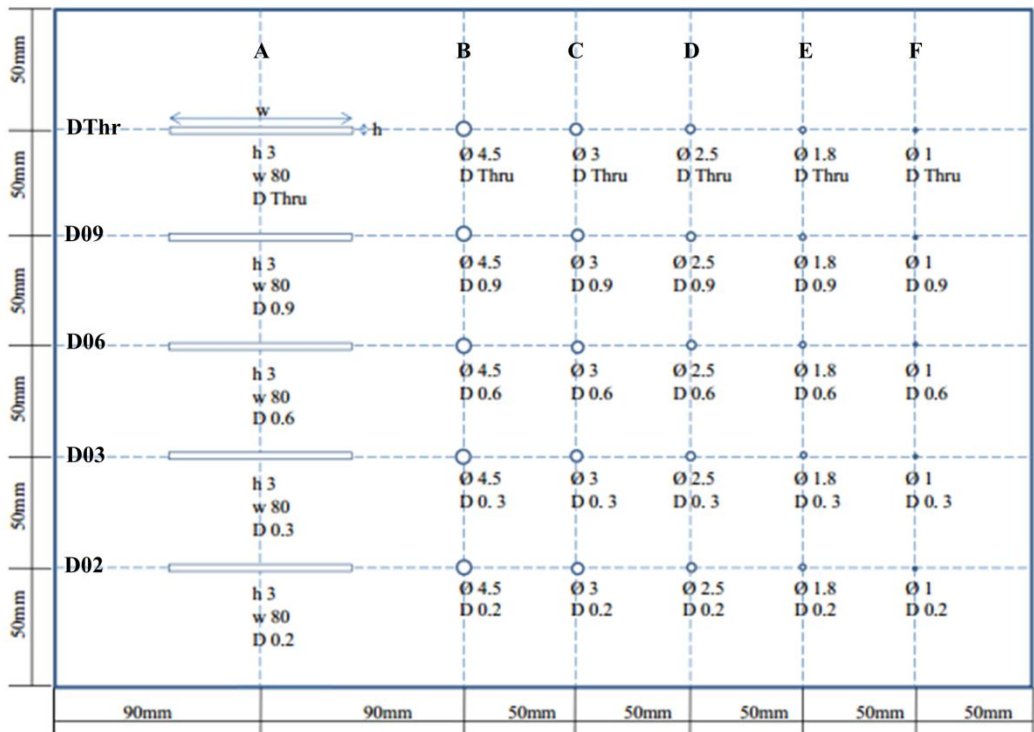
Figure 3-7 Position of cracks on the stainless-steel plate specimen

Table 3-6 Detail name and sizes of cracks on the stainless-steel specimen

Name	Depth [mm]	Width [mm]	Volume [mm³]	Name	Depth [mm]	Width [mm]	Volume [mm³]
F02	0.2	1	0.1570796	C02	0.2	3	1.4137167
F03	0.3	1	0.2356194	C03	0.3	3	2.120575
F06	0.6	1	0.4712389	C06	0.6	3	4.2411501
F09	0.9	1	0.7068583	C09	0.9	3	6.3617251
FThr	1.15	1	0.9032079	CThr	1.15	3	8.128871
E02	0.2	1.8	0.508938	B02	0.2	4.5	3.1808626
E03	0.3	1.8	0.763407	B03	0.3	4.5	4.7712938
E06	0.6	1.8	1.526814	B06	0.6	4.5	9.5425877
E09	0.9	1.8	2.290221	B09	0.9	4.5	14.313882
EThr	1.15	1.8	2.9263936	BThr	1.15	4.5	18.28996
D02	0.2	2.5	0.9817477				
D03	0.3	2.5	1.4726216				
D06	0.6	2.5	2.9452431				
D09	0.9	2.5	4.4178647				
DThr	1.15	2.5	5.6450493				

35

3.3 Scanning results

Experiment has been performed on two sides of the specimen front side and back side, respectively. During the experiment the scanning speed and scanning step was set to 2.4 mm/sec and 0.2 mm, respectively. Front-side scanning means the array has been placed on the side which is having cracks on the specimen, in this case we called as near-side scanning, subsequently flipped the sample to other side for back-side scanning, which means place the array on the surface of the specimen which has no cracks, i.e. all the cracks are on the other side of the specimen, this scanning is called as far-side scanning. The images which are obtained during near-side scanning and far-side scanning are called as near-side images and far-side images respectively. The scanning images of near and far-side cracks of each specimen have been obtained at different excitation frequencies of 1, 3, 5 kHz. The images obtained at 3 frequency conditions on 2 sides of the specimen, so the total of 6 scanning images for each specimen.

3.3.1 Near and far-side images of Titanium specimen

Near-side cracks

Figure 3-8(a) shows the near-side image of titanium specimen which is obtained at 1 kHz of excitation frequency almost all the cracks are successfully detected clearly. Figure 3-8(b) show the detailed sectional views obtained at center of each crack. Line profile of a crack consists of three peaks: two minimum peaks and a maximum peak. The line profile of the cracks resemble a cone shape with height 'h' (height of maximum peak) and base 'w' (distance between two minimum peaks) as shown in Figure 3-8(c). From the Figure 3-8(b), we can recognize that there are two features in the detected signals which clearly show a change related to depth and diameter of the crack, those two features are 'h' and 'w' of the signal. Vertical dotted box in Figure 3-8(b) shows a group of cracks having same diameter but different depths in which the solid lines show a change in 'h' of the signal. The horizontal dotted in Figure 3-8(b) box show the another group of cracks having same depth but different diameters in which solid lines show a change in base 'w' of detected signals related to the diameter of the crack.

36

Effect of crack depth on detected signal

The effect of crack depth on the 'h' of the detected signal can be explained by relating volume of the crack with induced eddy currents [45], let us consider the cracks in column C which are marked in vertical dotted box. Here the peak amplitude 'h' of the signal decreased with decreasing the crack depth. The decrease in depth of a circular crack means decrease in the volume of the crack in a conductive material of fixed volume, conversely the volume of conductive area of the material under the ECT probe increases; this means less volume of crack means that large area of conducting metal under the probe. Thus more induced eddy currents due to large conductive area results more secondary magnetic field from the eddy currents which interacts with the primary magnetic field of the probe, so the resultant magnetic field which is the sum of the primary and opposite secondary magnetic fields will be decreases and hence the ECT response detected by the Hall sensors in the ECT probe will be decreased.

Effect of crack diameter on detected signal

Consider the cracks which are marked in horizontal dotted box in the Figure 3-8(b) to understand the effect of diameter of the crack on 'w' of the detected signal, here the diameter of the crack is changed hence there is a change in 'w' of the signal has been observed. The area covered by the induced currents on the surface of the test material below the ECT probe is called as the foot print of the probe [46]. The size of the foot print depends on two factors, one is the size of the probe and other is lift-off (the gap between the probe and surface of test metal). Foot print size will be reduced by reducing the size of the probe or by increasing the lift-off. In the present study the 'w' of the detected signal is increased with increasing the width of the crack. This can be understood as we are scanning the probe on the specimen with a constant lift-off (the size of the foot print fixed) and at a constant speed, for example when we scan ECT probe on the specimen with different diameter cracks, then the spatial interaction time between the foot print of the probe with the crack depends on the size of the crack. The spatial interaction time between foot print and crack is small for small crack and large for larger diameter crack. As shown in Figure 3-11(a) there are two minimum peaks downwards and distance between these two minimum peaks is indicated as w1 and w2. For example, let us assume we are scanning from left to right on a circular crack, the first minimum peak in the detected signal appears due to the interaction of probe with left side edge of the circle and

signal keep changes as probe moving on the crack and the second minimum peak appears at the right side edge of the circle. The distance between these two peaks depends on the size or diameter of the crack. As shown in Figure 3-11 Comparison of sectional views of cracks having (a) different widths; (b) different depths; (c) same crack at different excitation frequencies (a) width w1 from the smaller diameter crack and w2 is from the larger diameter crack. The experimental results followed the same trend in 'h' and 'w' for all the other test specimens used in this study as shown in following sections in the thesis.

Effect of excitation frequency on detected signal

There is a change in the detected signal depending on the change in excitation frequency as shown in Figure 3-11(c), it can be explained by using the skin effect phenomenon of the induced eddy currents. Comparing the near-side images which are obtained at 1kHz, 3KHz and 5 kHz in Figure 3-8 to 10 respectively, consider the peak height of crack C10 at different frequencies as shown in Figure 3-11(c), the peak height 'h' is changed by changing the frequency. As discussed earlier section 1.3.2, the skin depth depends strongly on the excitation frequency, skin depth is large at lower frequencies and converse is true. The skin effect is the most important factor that affects the detectability of the crack in ECT. The amount of interaction of induced eddy currents and the resultant effect on the detected signal is strongly depends on the excitation frequency, thus selection of excitation frequency is important factor in optimization of ECT system. In the current study we have used three conditions frequency of excitations (1, 3, 5 kHz). Experimental results suggest that 3 kHz of excitation frequency could give the better detectability of the crack as shown in Figure 3-11(c). Previously the researchers utilized the frequency effect on detected signal to identify the location of crack, if the ECT response from a crack is good at high frequency but poor at low frequency then the crack is classified as surface crack or if the ECT response is better at lower frequency than higher frequency then crack can be identified as sub-surface or far-side crack. In the present study LIHaS uses Hall-sensor, since the hall sensor response is good at lower frequencies (few tens of kHz), it is difficult to use frequency as a parameter to Discrimination of near and far-side cracks.
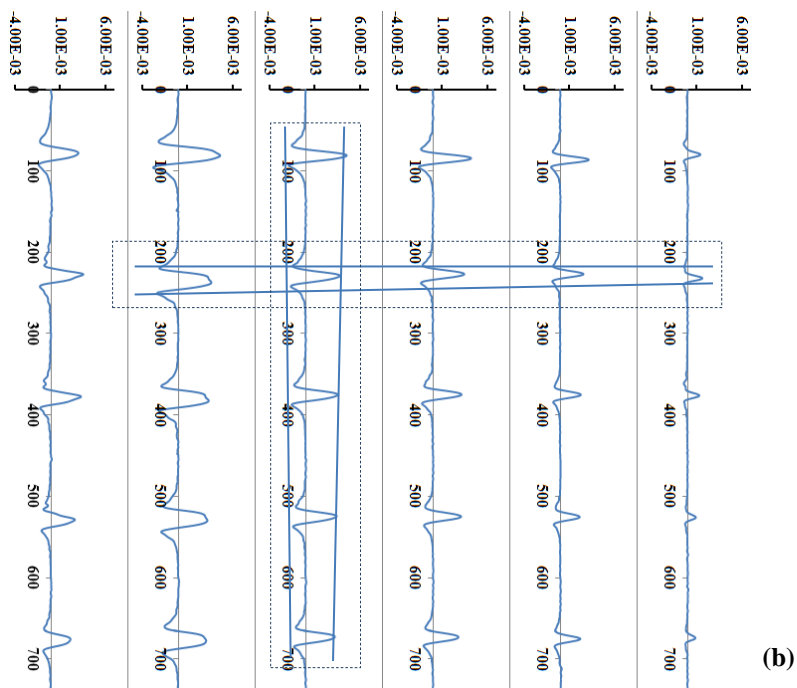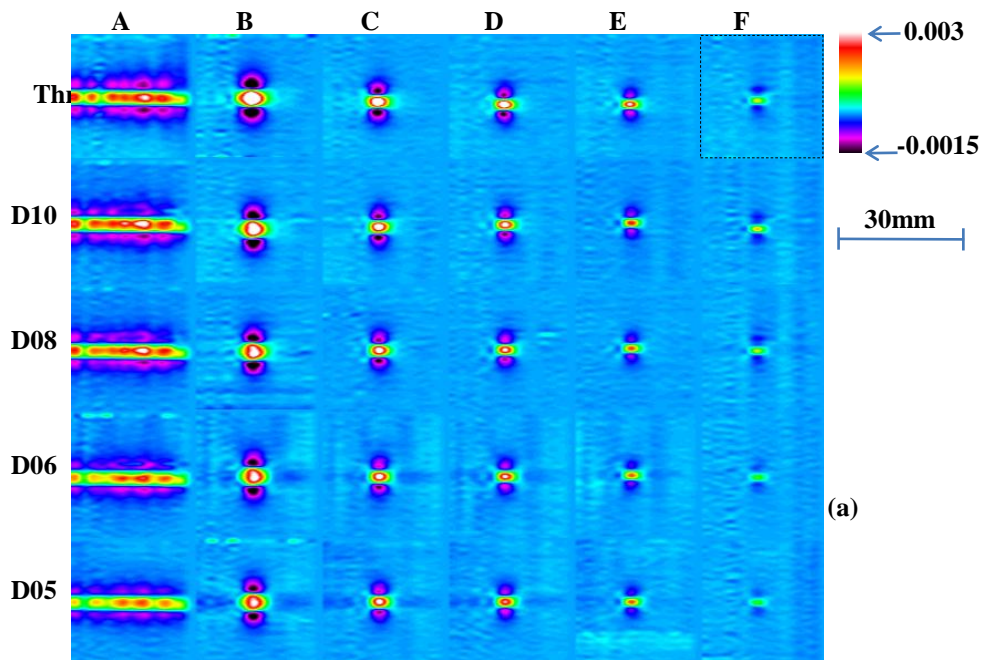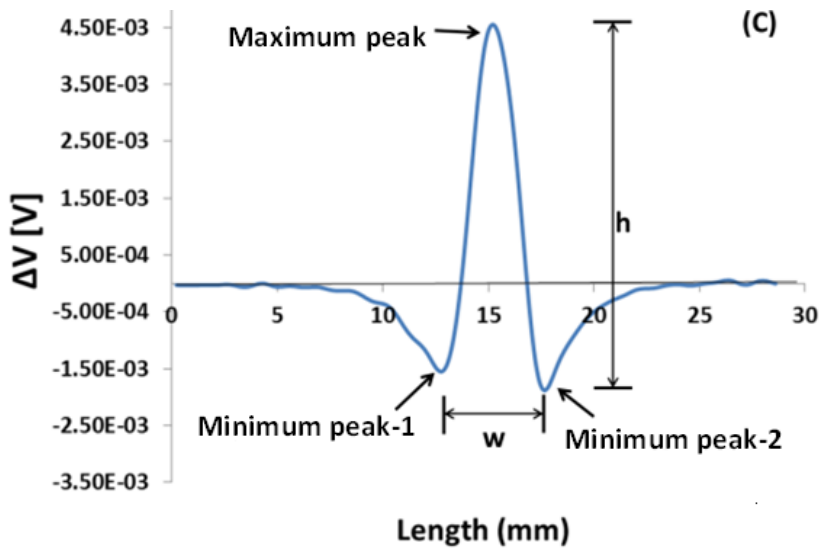
Figure 3-8 The experimental results of Titanium in near-side scanning at 1 kHz
(a) contour figure; (b) section-view (c) section view of one crack
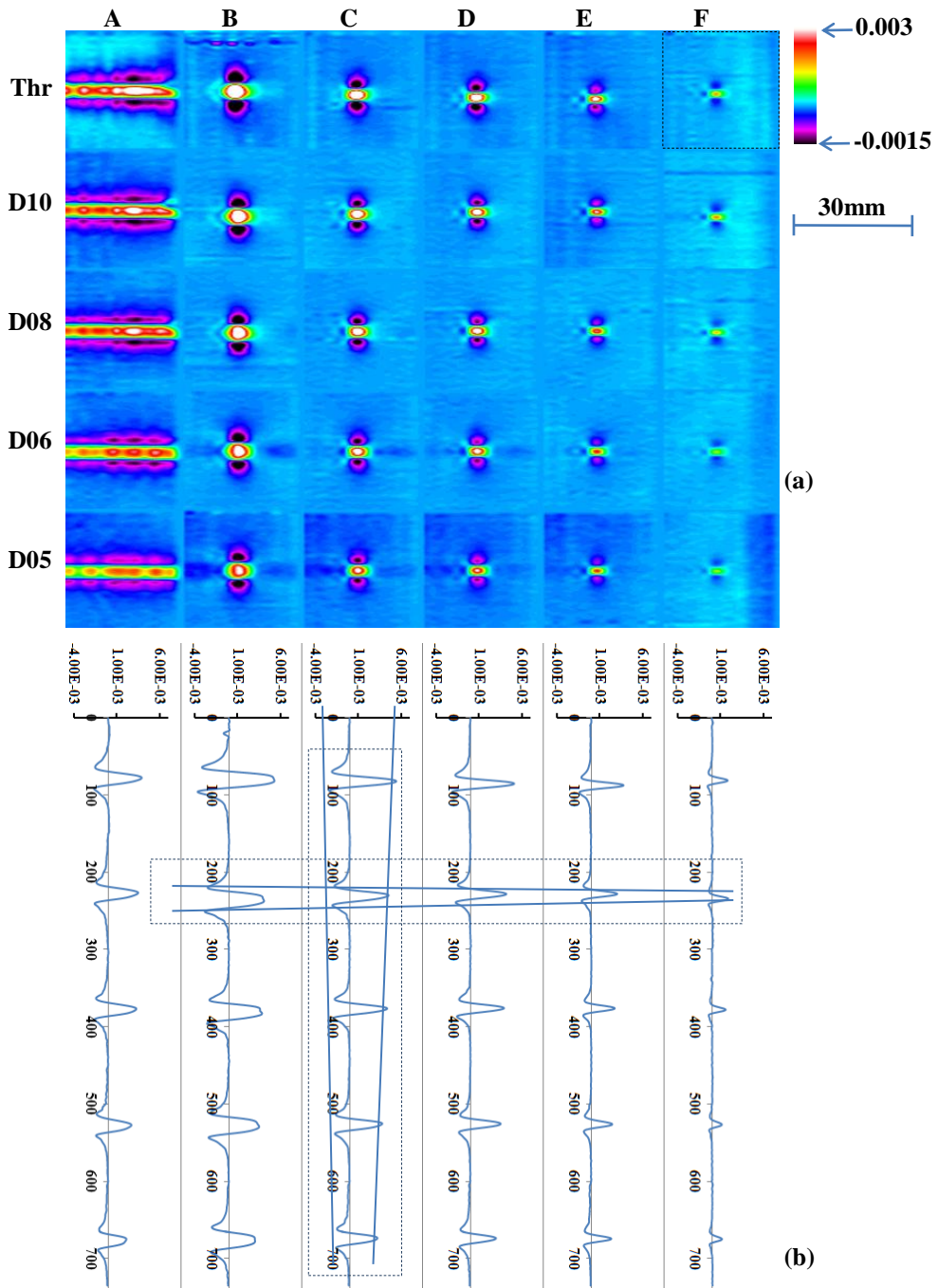
Figure 3-9 The experimental results of Titanium in near side scanning at 3 kHz (a) contour figure; (b) section-view

41
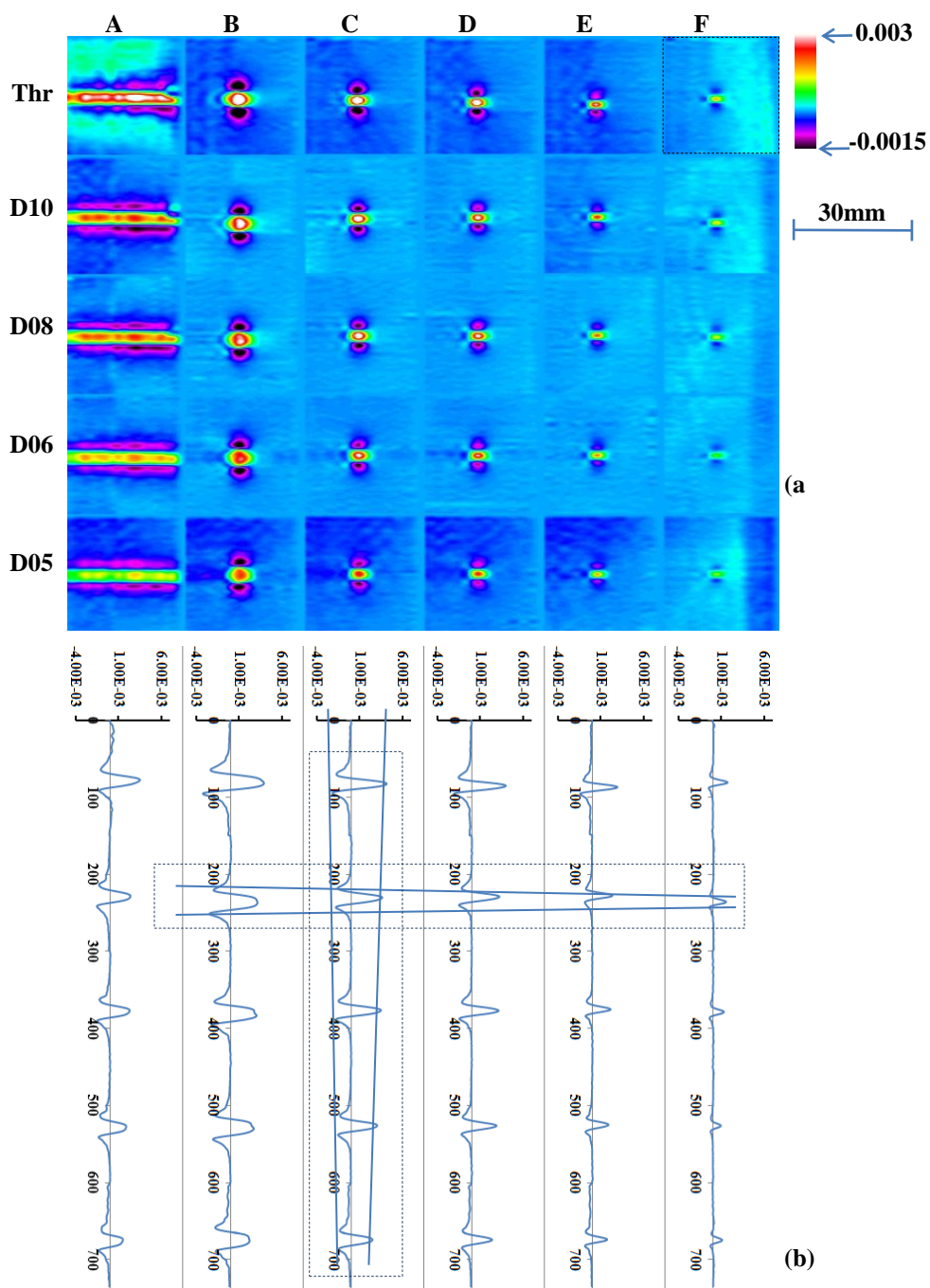
Figure 3-10 The experimental results of Titanium in near-side scanning at 5 kHz

(a) contour figure; (b) section-view

42
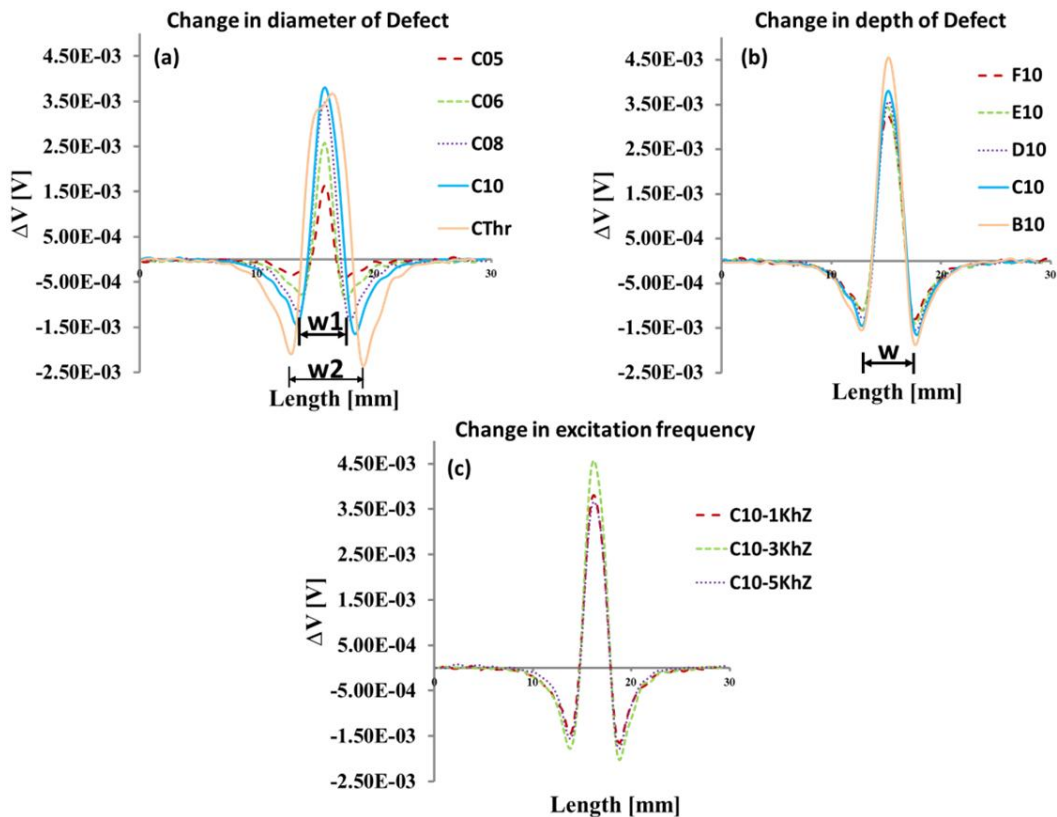
Figure 3-11 Comparison of sectional views of cracks having (a) different widths; (b) different depths; (c) same crack at different excitation frequencies

Far-side cracks

Error! Reference source not found. to Figure 3-14shows the far-side images of Titanium specimen at 1, 3 and 5 kHz respectively. All cracks are detected and most obvious except F05 because of its smallest volume. As the frequency changes, the data also changes. However, the change from 1 kHz to 3 kHz or 1 kHz to 5 kHz greater than the change from 3 kHz to 5 kHz.

Similar near-side scanning, when analysis the section-view of signal at 1 kHz, the cracks have the same diameter, the depth increases then the magnitude of the signal ('h') increases and the crack of the same depth, diameter increases then the distance from the peak to

peak ('w') increase. This result is correct with frequencies 3, 5 kHz. This is shown in the horizontal dotted box and vertical dotted box in Figure 3-13, Figure 3-14
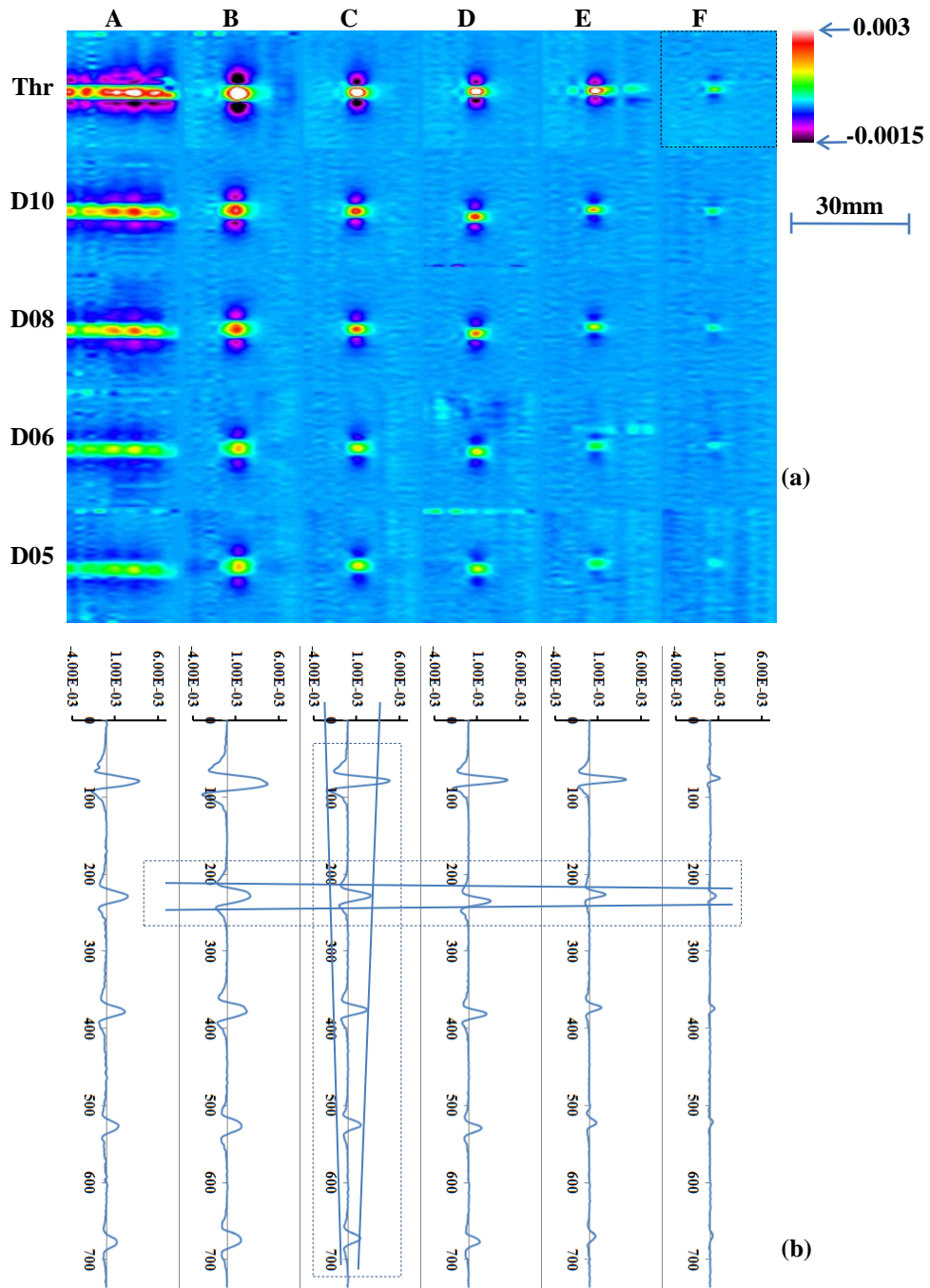
Figure 3-12 The experimental results of Titanium in far-side scanning at 1 kHz (a) contour

figure; (b) section-view

45
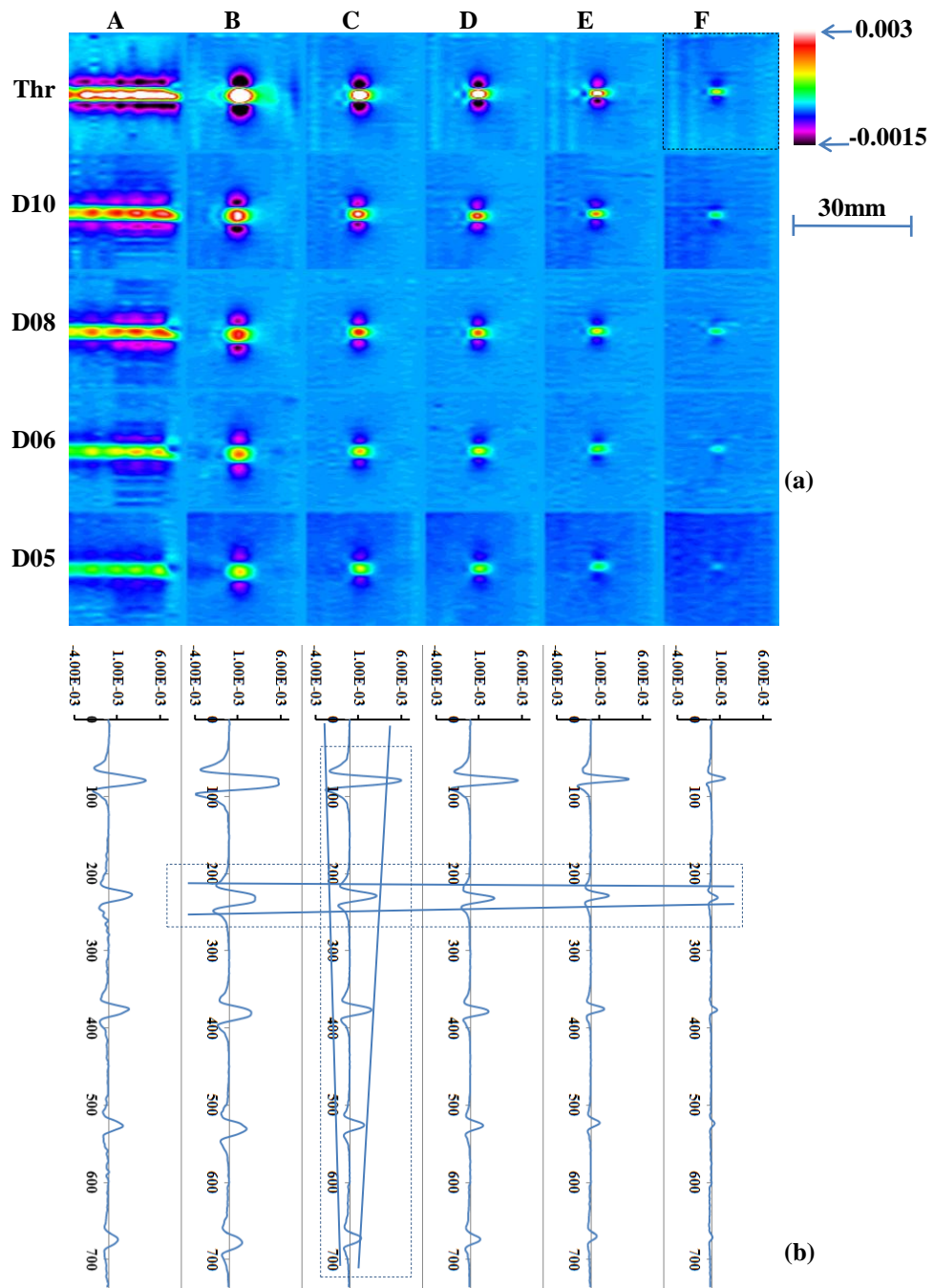
Figure 3-13 The experimental results of Titanium in far-side scanning at 3 kHz

(a) contour figure; (b) section-view

46
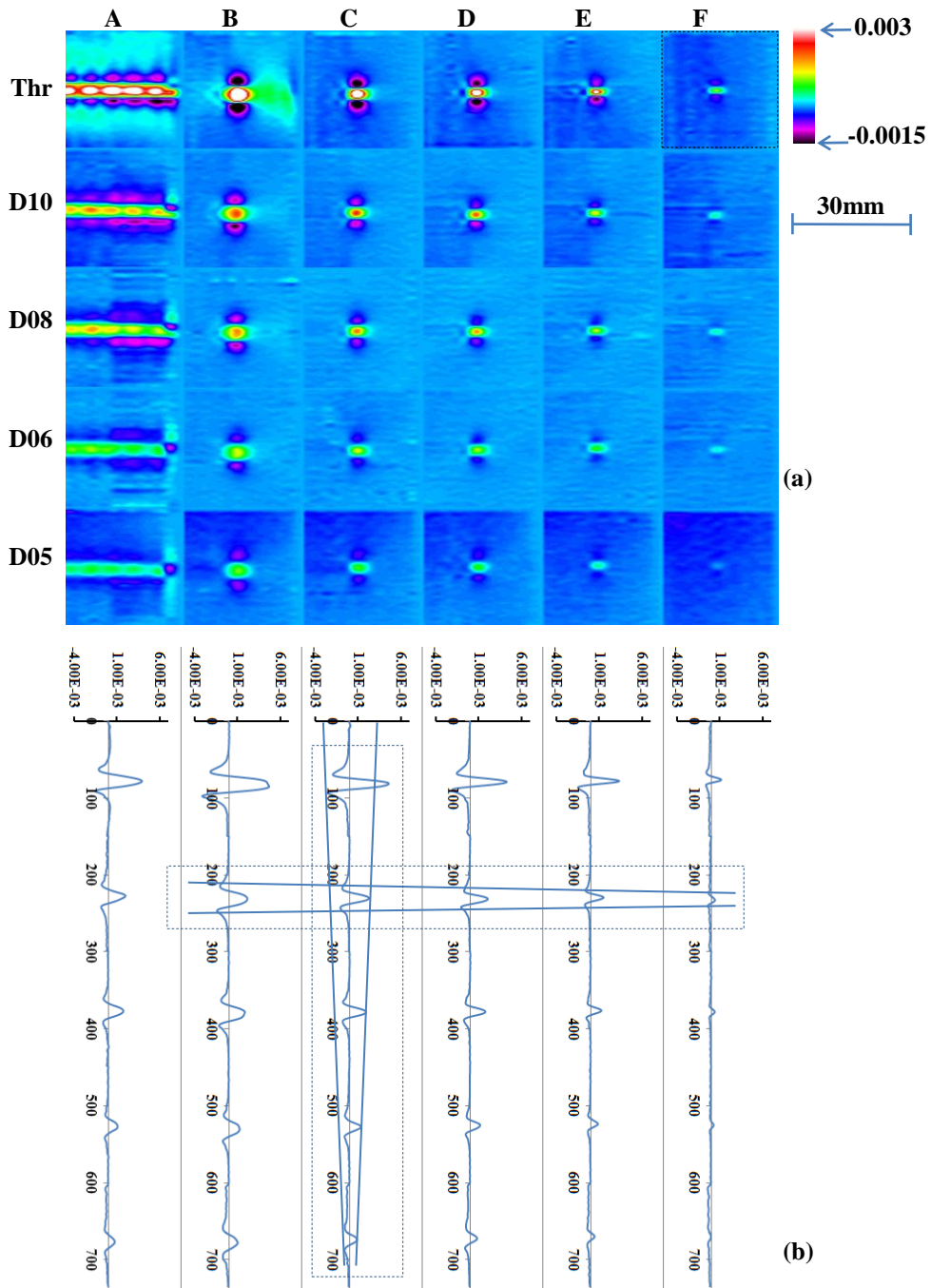
Figure 3-14 The experimental results of Titanium in far-side scanning at 5 kHz (a) contour figure; (b) section-view

47

3.3.2 Near and far-side images of Copper-Nickel specimen

Near-side cracks

Figure 3-15 to 17 shows the experimental results of copper specimen, the images of near-side at 1, 3 and 5 kHz. Several cracks having same diameters are marked in dotted box as shown in Figure 3-15(a) in which the solid lines show the increase trend of signal. As discussed in the earlier section the h and w of the detected signal increased with the increase of the crack depth and diameter, respectively. All the cracks were detected and almost they look clearly except for the smallest crack F02.

Far-side cracks

Figure 3-18 to Figure 3-20 shows the experimental results of copper specimen, the images of near-side and far-side at 1, 3 and 5 kHz. At 1, and 3 kHz, sensor cannot detect F02, E02. At 5 kHz sensor cannot detect F02, F03, and E03. All of them, which cannot detect, which look not clearly because of their small volume.
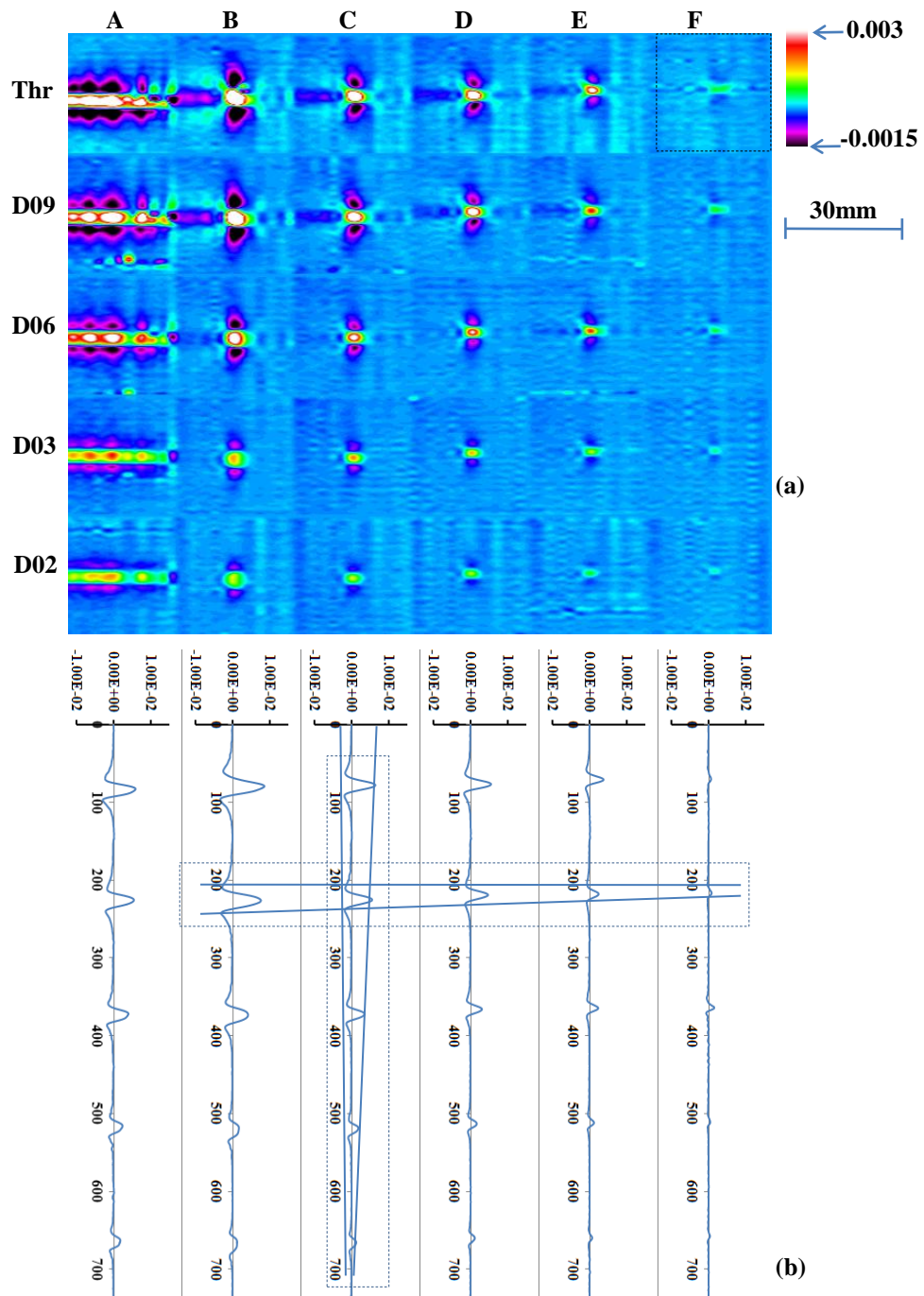
Figure 3-15 The experimental results of copper-nickel in near-side scanning at 1 kHz
(a) contour figure; (b) section-view

49
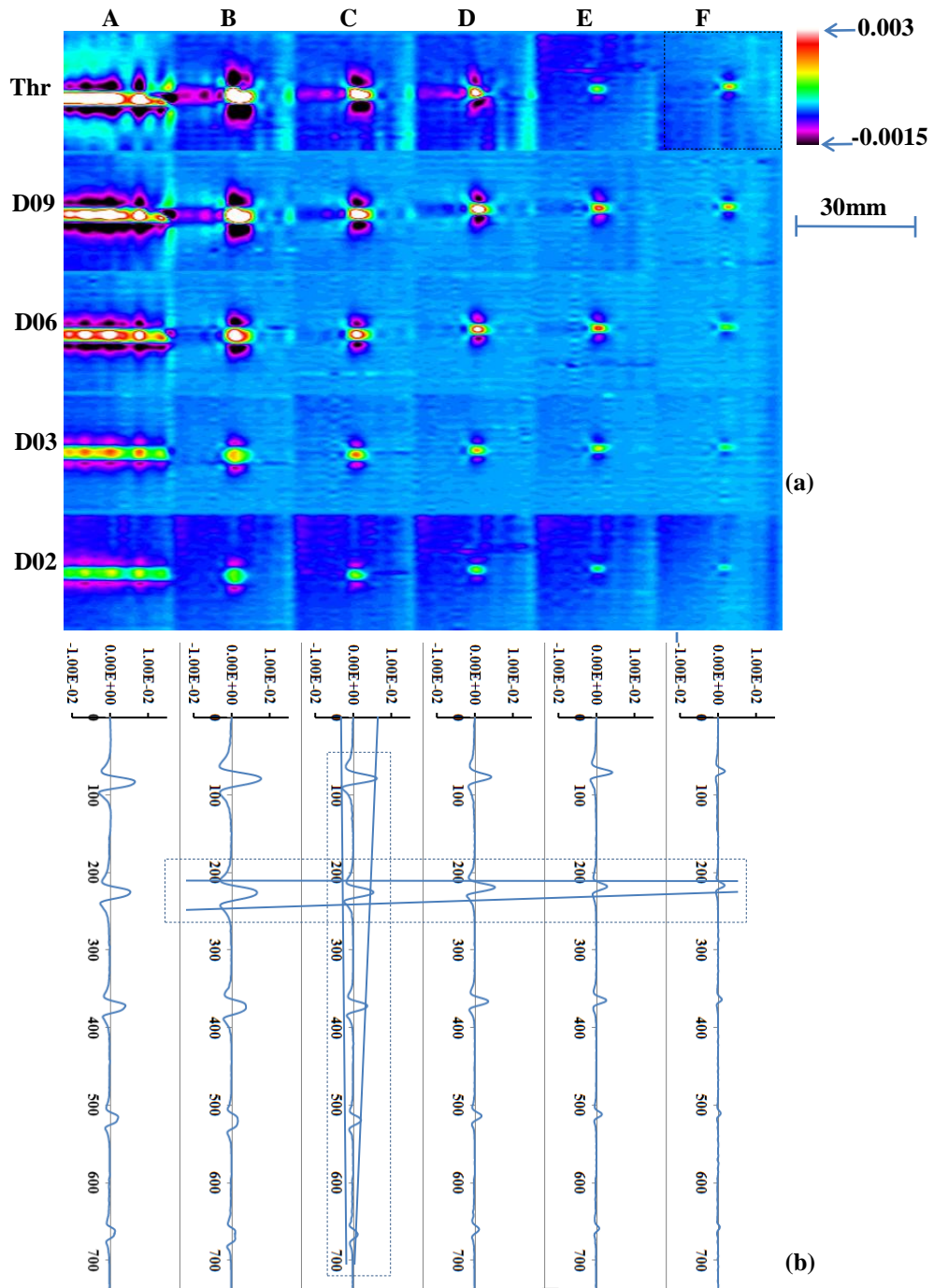
Figure 3-16 The experimental results of copper-nickel in near-side scanning at 3 kHz

(a) contour figure; (b) section-view

50
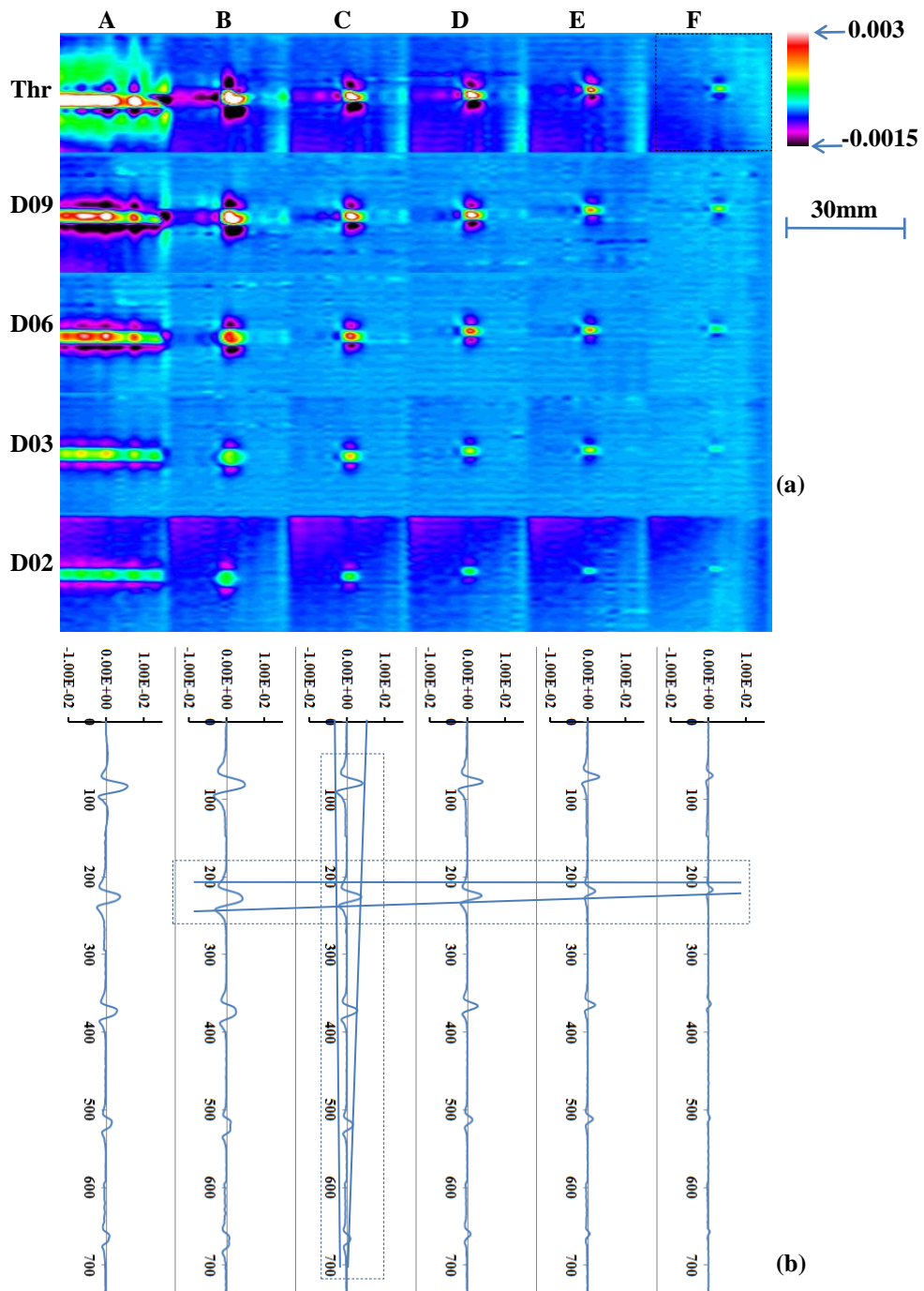
Figure 3-17 The experimental results of copper-nickel in near-side scanning at 5 kHz (a) contour figure; (b) section-view

51
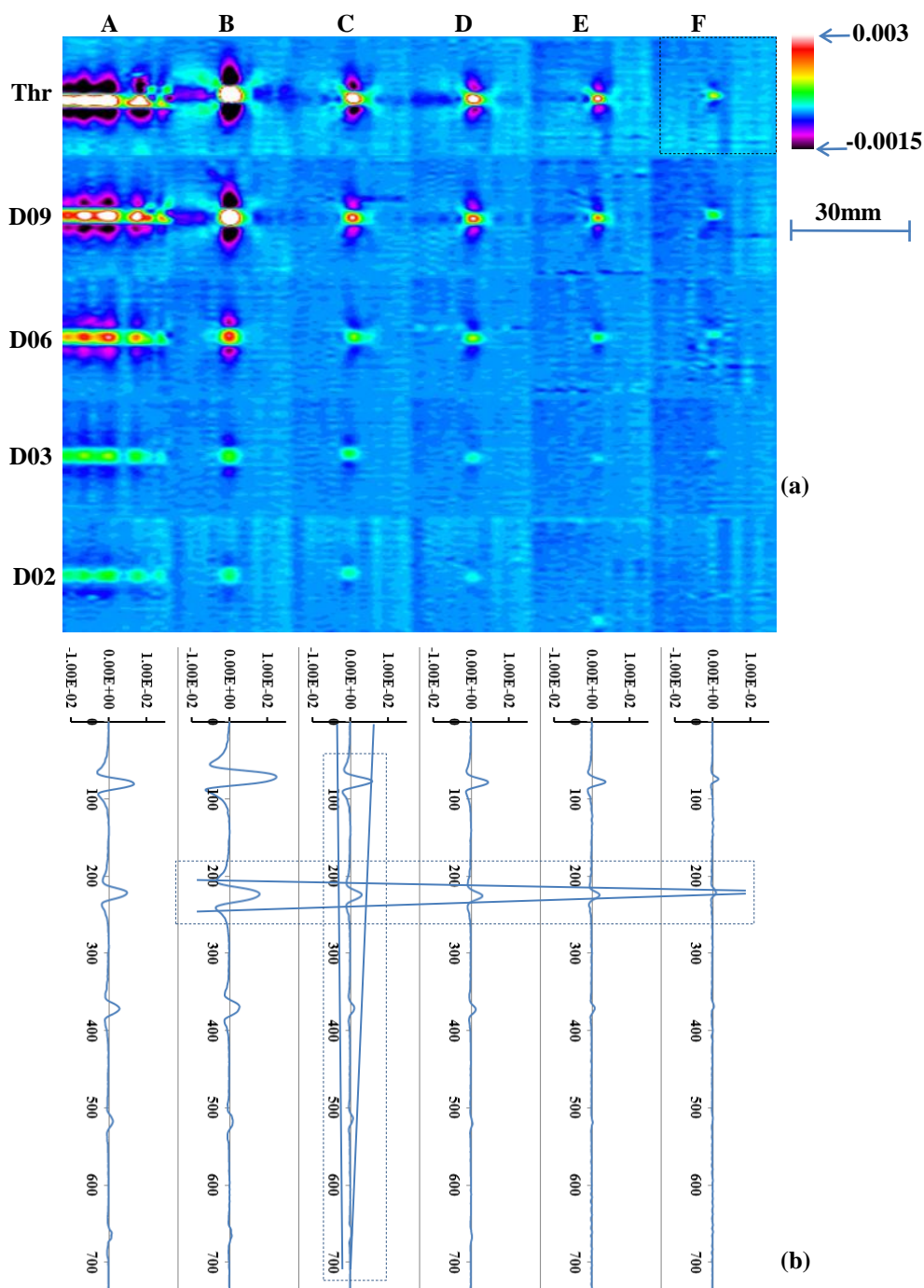
Figure 3-18 The experimental results of copper-nickel in far-side scanning at 1 kHz (a) contour figure; (b) section-view

52
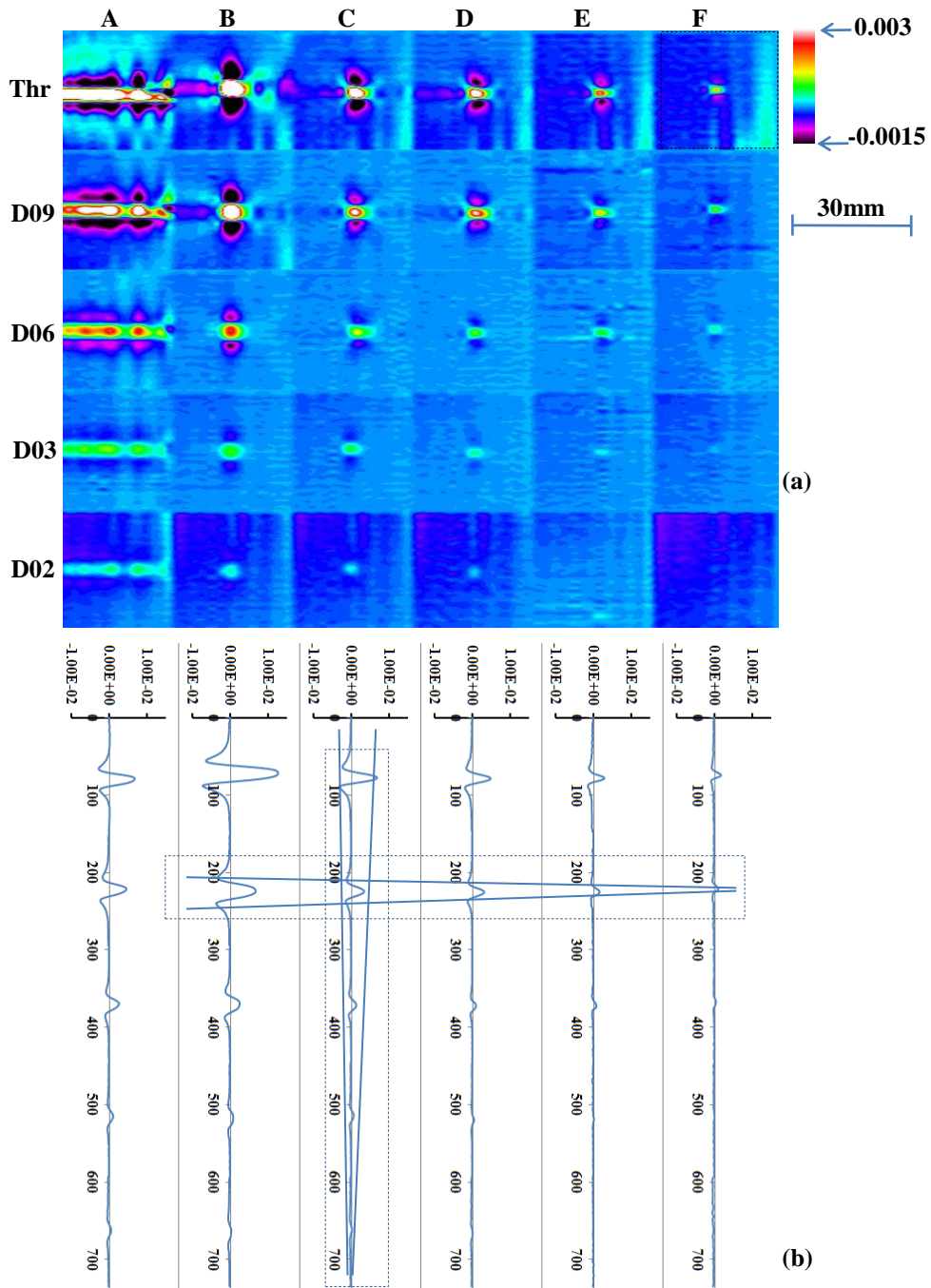
Figure 3-19 The experimental results of copper-nickel in far-side scanning at 3 kHz (a) contour figure; (b) section-view

53
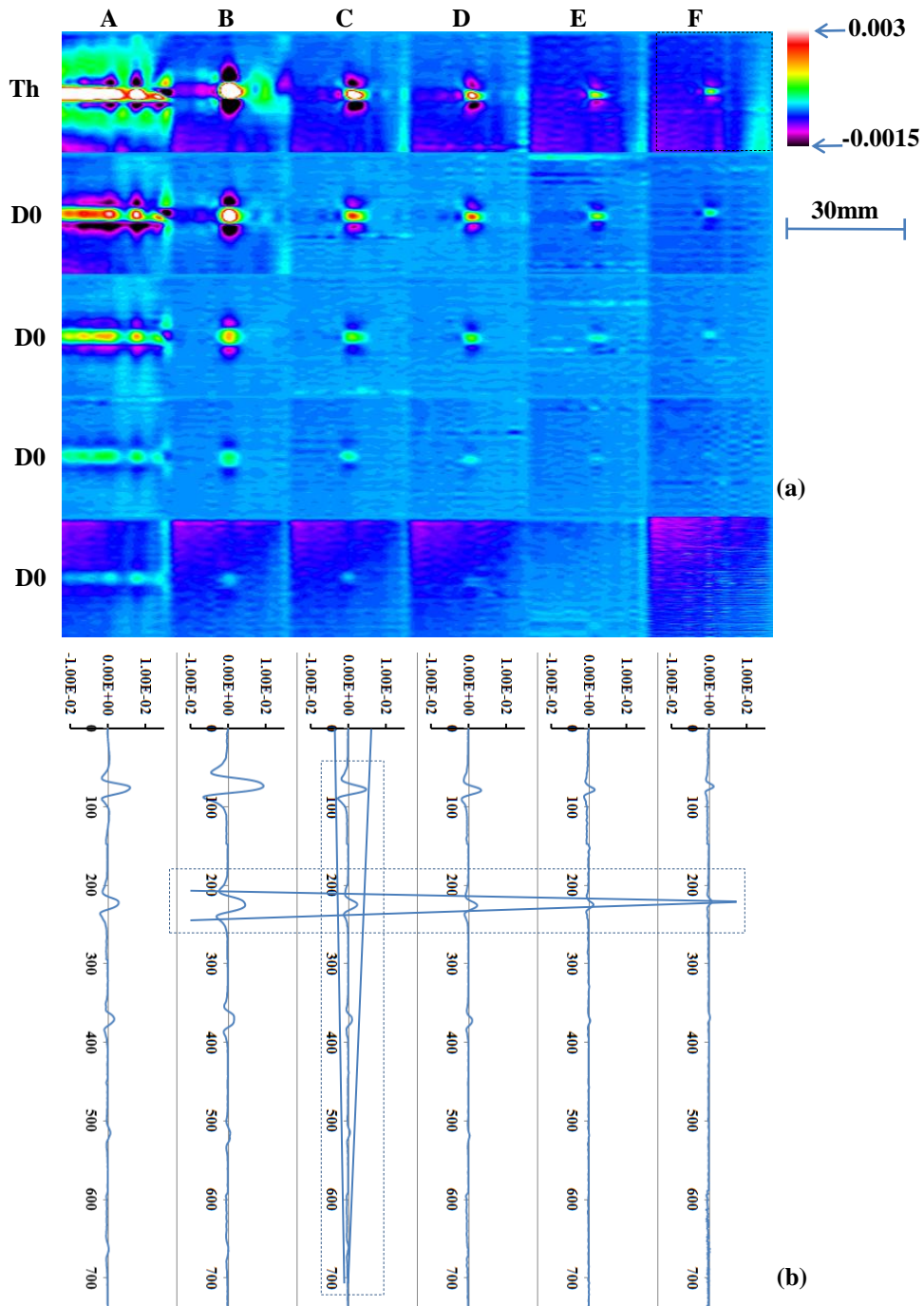
Figure 3-20 The experimental results of copper-nickel in far-side scanning at 5 kHz

(a) contour figure; (b) section-view

54

3.3.3 Near and far-side images of Inconel600 specimen

Near-side and far-side cracks

Error! Reference source not found., 22, and 23 shows the experimental results of nconel 600 alloy in near-side scanning at 1, 3, and 5 kHz, respectively. Almost cracks are detected, except F04 at 1 kHz. Compare contour figure of Inconel600 at three frequencies, we realize that the experimental result of Inconel600 at 3, and 5 kHz are better than the experimental result of Inconel600 at 1 kHz. It means, at 1 kHz, sensor cannot detect a crack F04 but at 3, and 5 kHz, sensor can; and cracks at 3, 5 kHz look clearly then at 1 kHz. The result is similar in far-side scanning. It is shown in Figure 3-24, 25, and 26. However, in the far-side scanning, many cracks were not detected. At 1 kHz, sensor cannot detect cracks F04, F05, E04; at 3, and 5 kHz, cannot detect cracks F04, F05. All cracks which sensor cannot detect because of their small volume. Some other cracks are detected but not clearly. Compare contour figure at near-side and far-side scanning, we recognize that data at near-side scanning is clearer than the data at far-side scanning. This is the effect of skin effect on the material. Similar previous section, the change of amplitude of signal (h) when changing depth and the change of distance from peak-to-peak (w) when changing diameter is a ruler. It mean, cracks are same diameter (vertical dotted box), increase depth then amplitude of signal (h) increase too; and cracks are same depth (horizon dotted box), increase diameter then the distance from peak-to-peak (w) increase too.
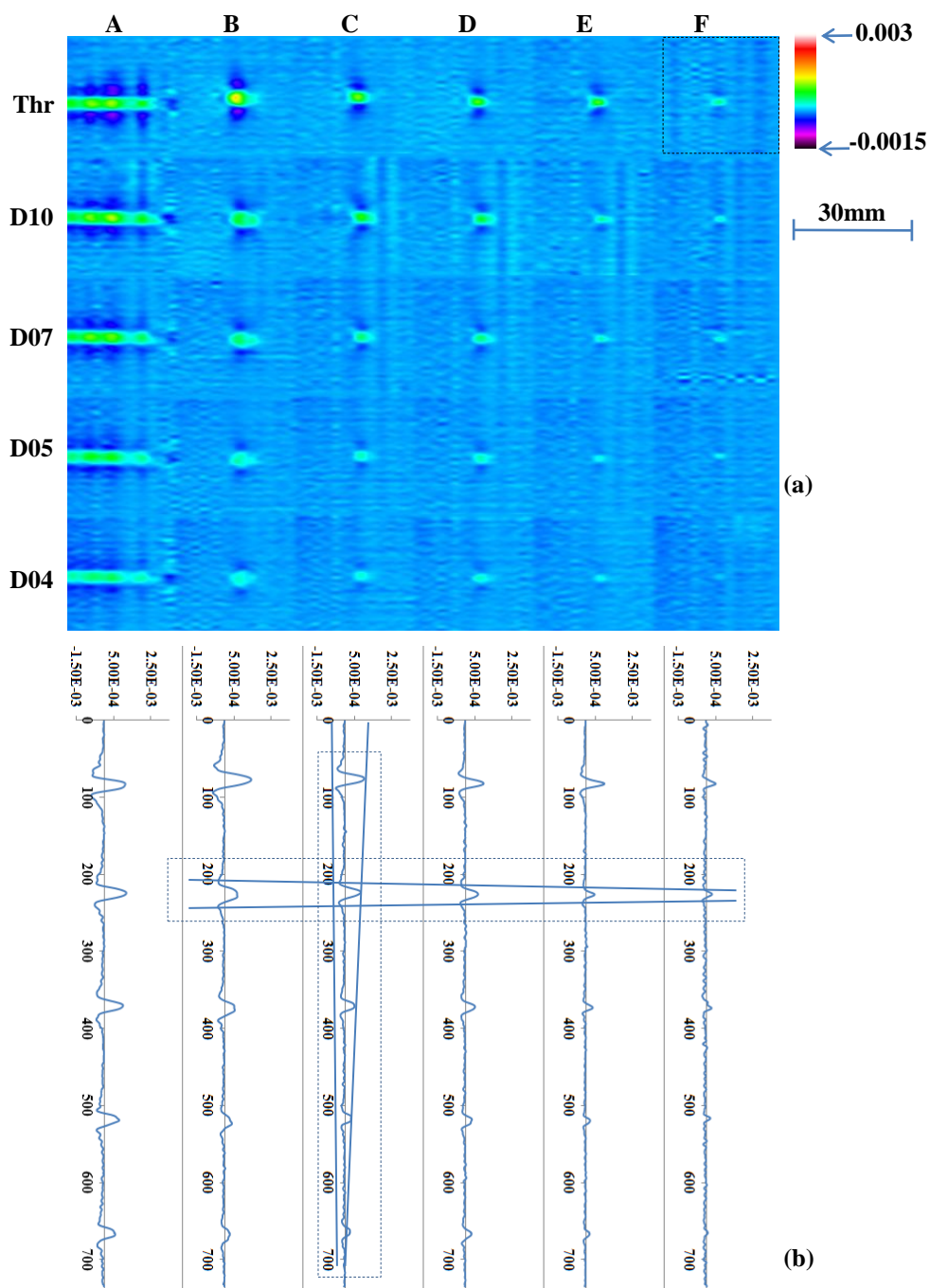
Figure 3-21 The experimental results of Inconel 600 in near-side scanning at 1 kHz (a) contour figure; (b) section-view

56
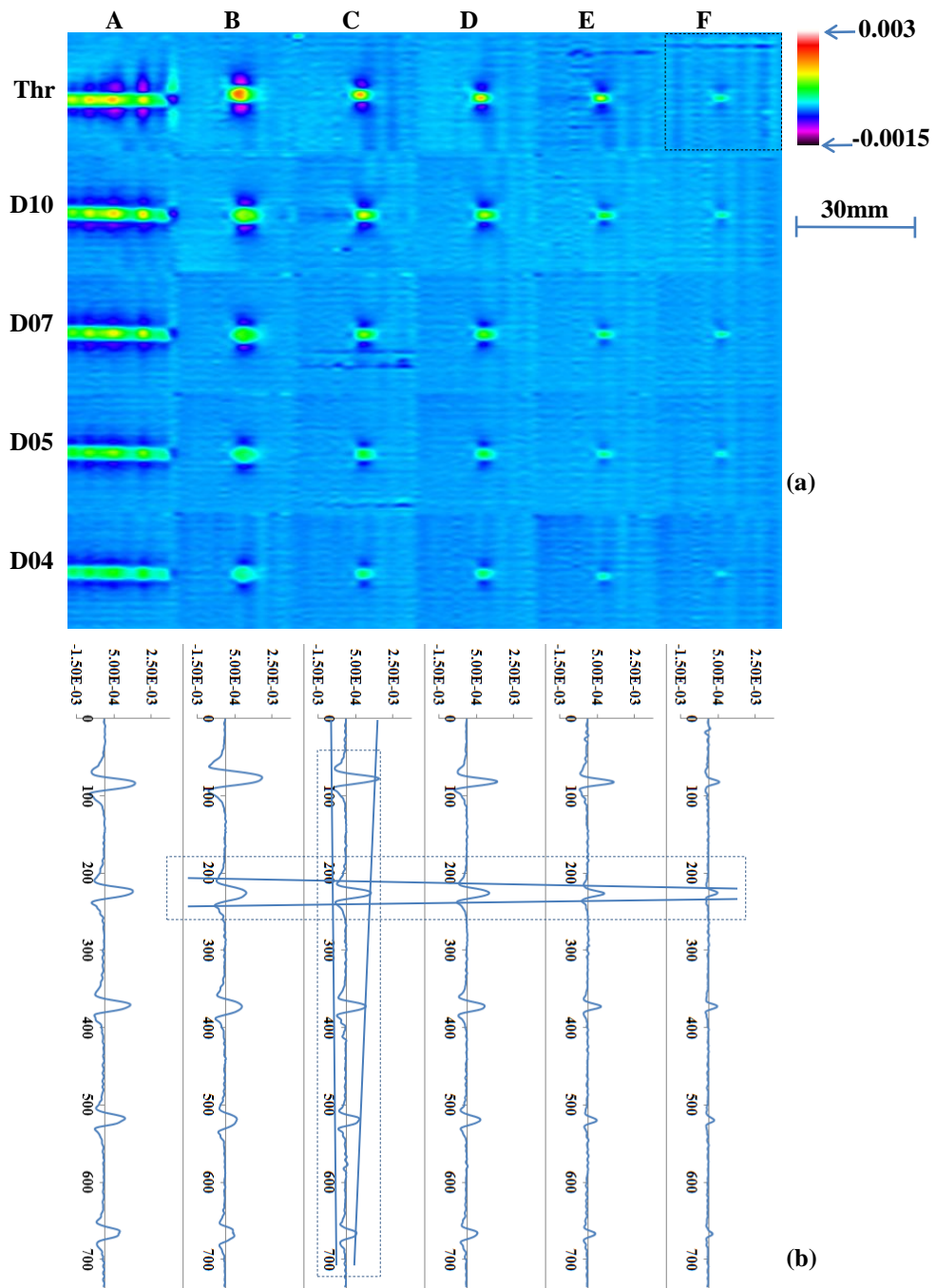
Figure 3-22 The experimental results of Inconel 600 in near-side scanning at 3 kHz (a) contour figure; (b) section-view

57
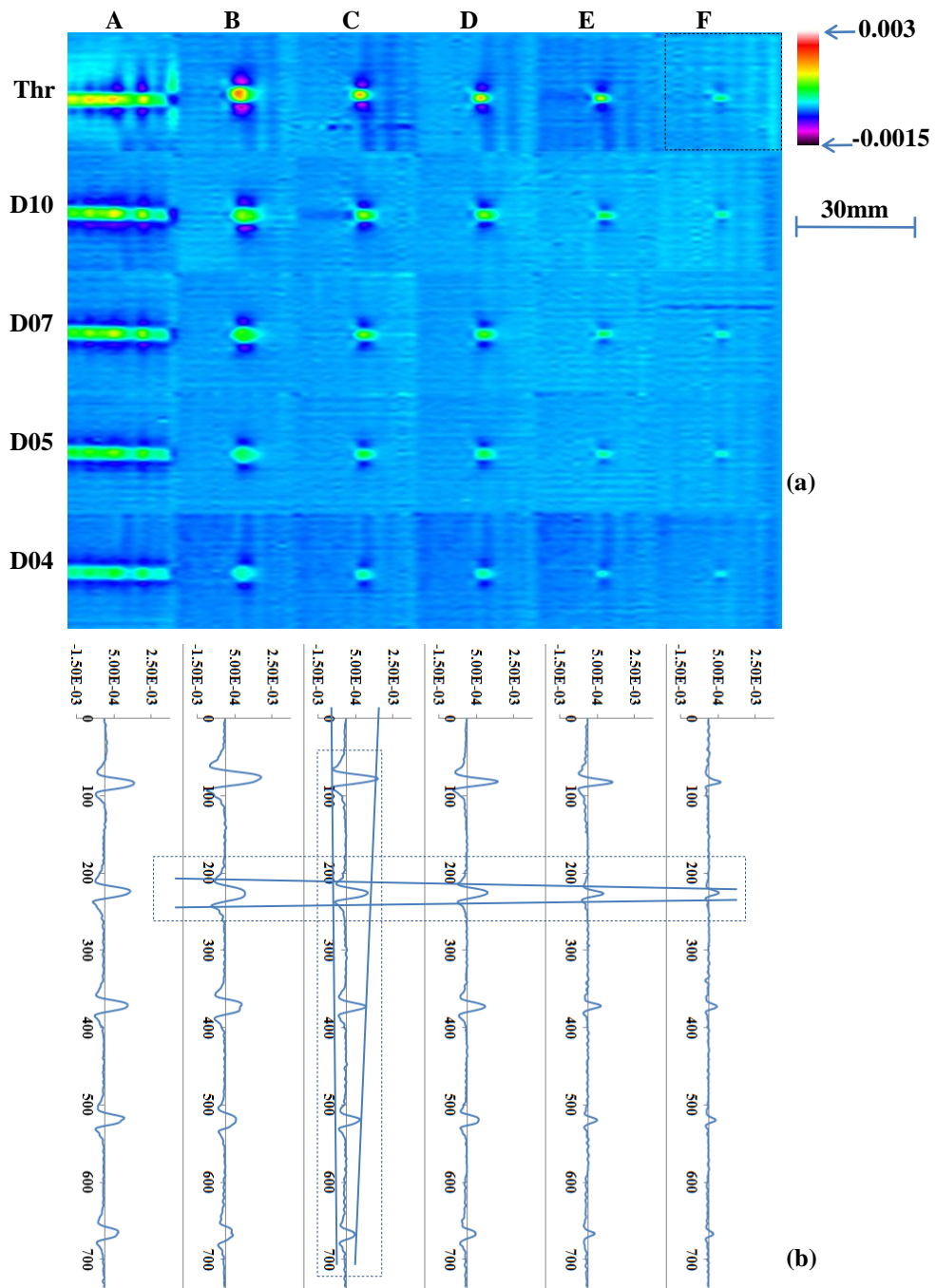
Figure 3-23 The experimental results of Inconel 600 in near-side scanning at 5 kHz (a) contour figure; (b) section-view

58
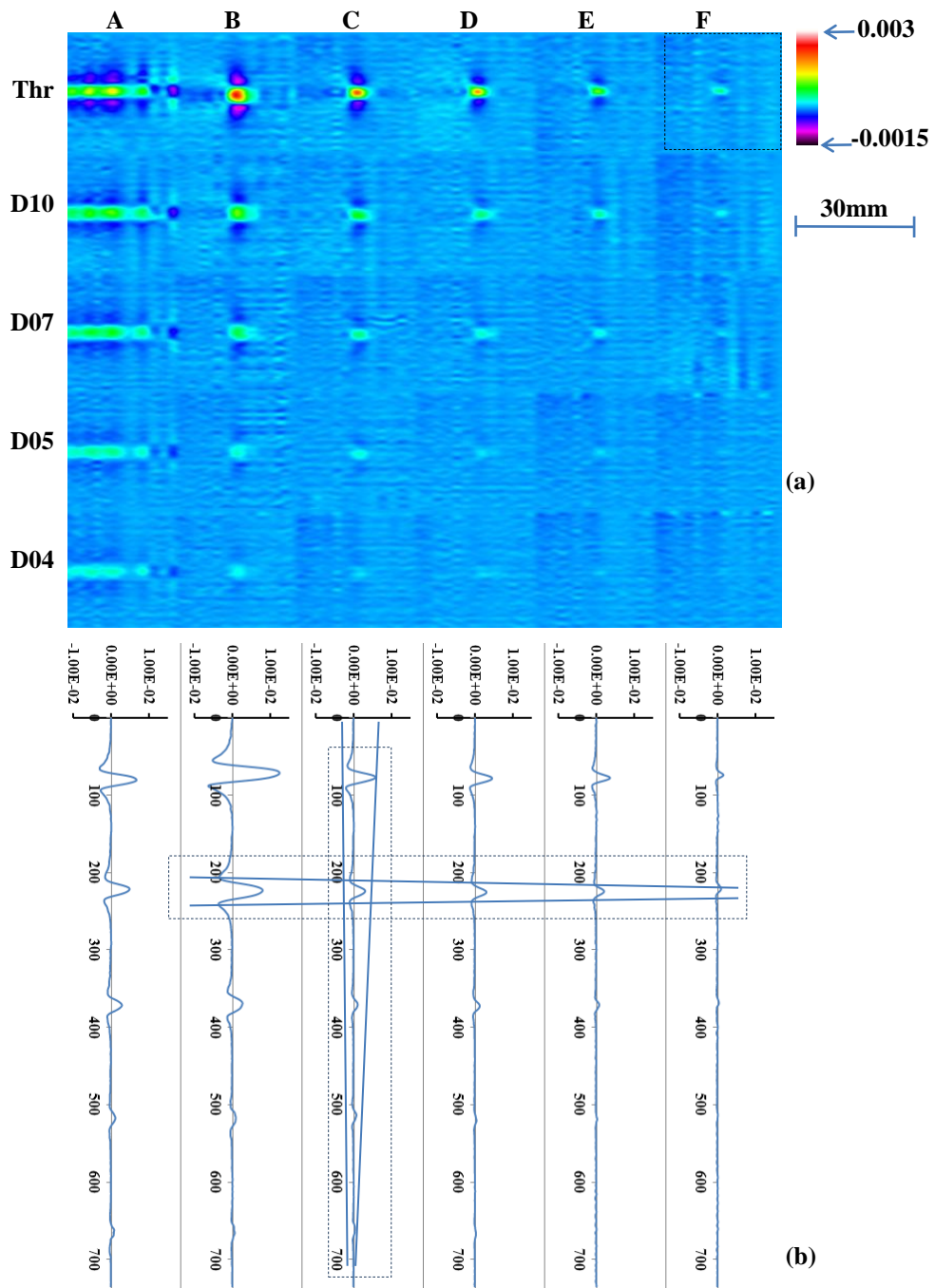
Figure 3-24 The experimental results of Inconel600 in near-side scanning at 1 kHz

(a) contour figure; (b) section-view

59
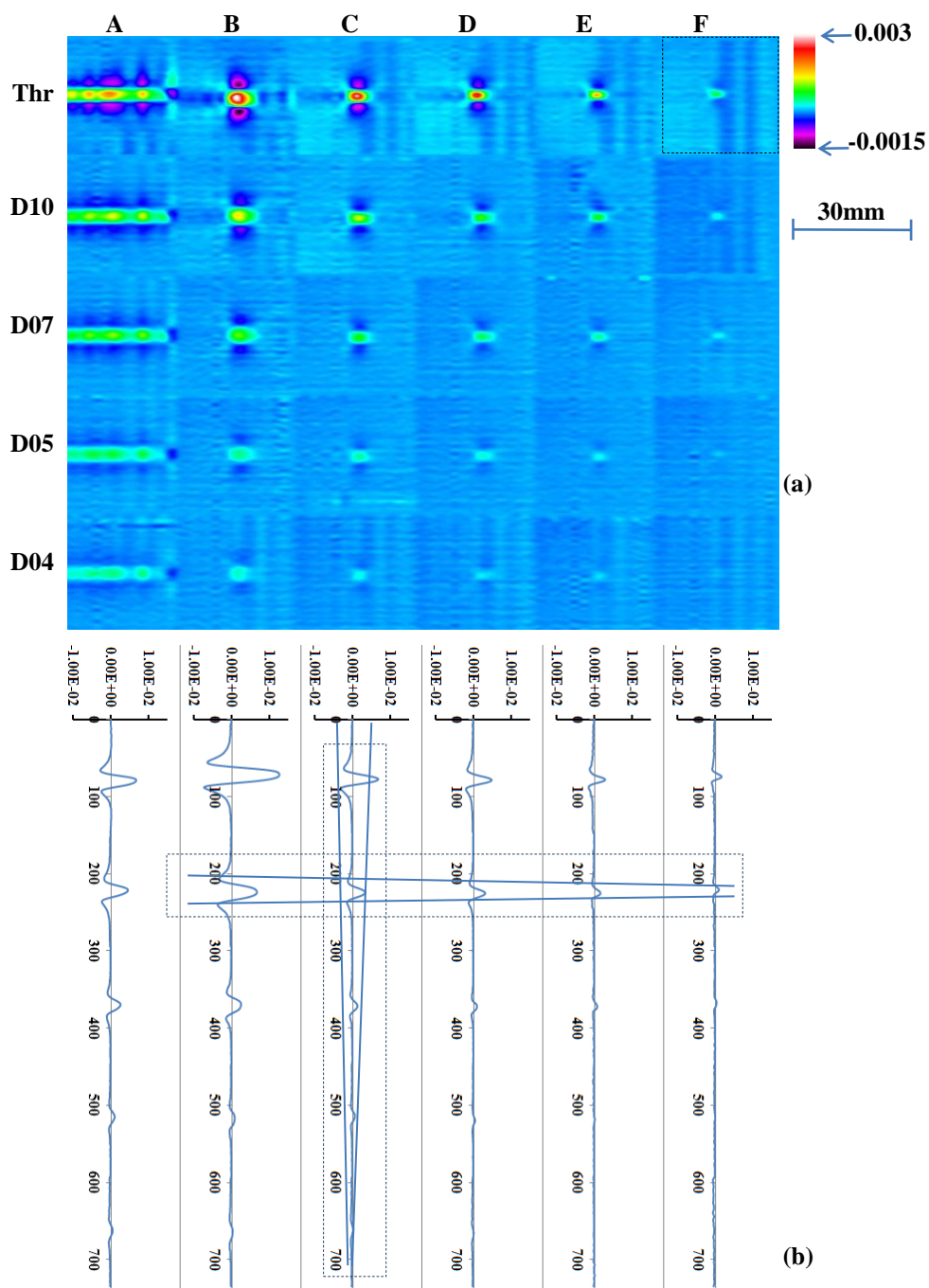
Figure 3-25 The experimental results of Inconel 600 in near-side scanning at 3 kHz

(a) contour figure; (b) section-view

60
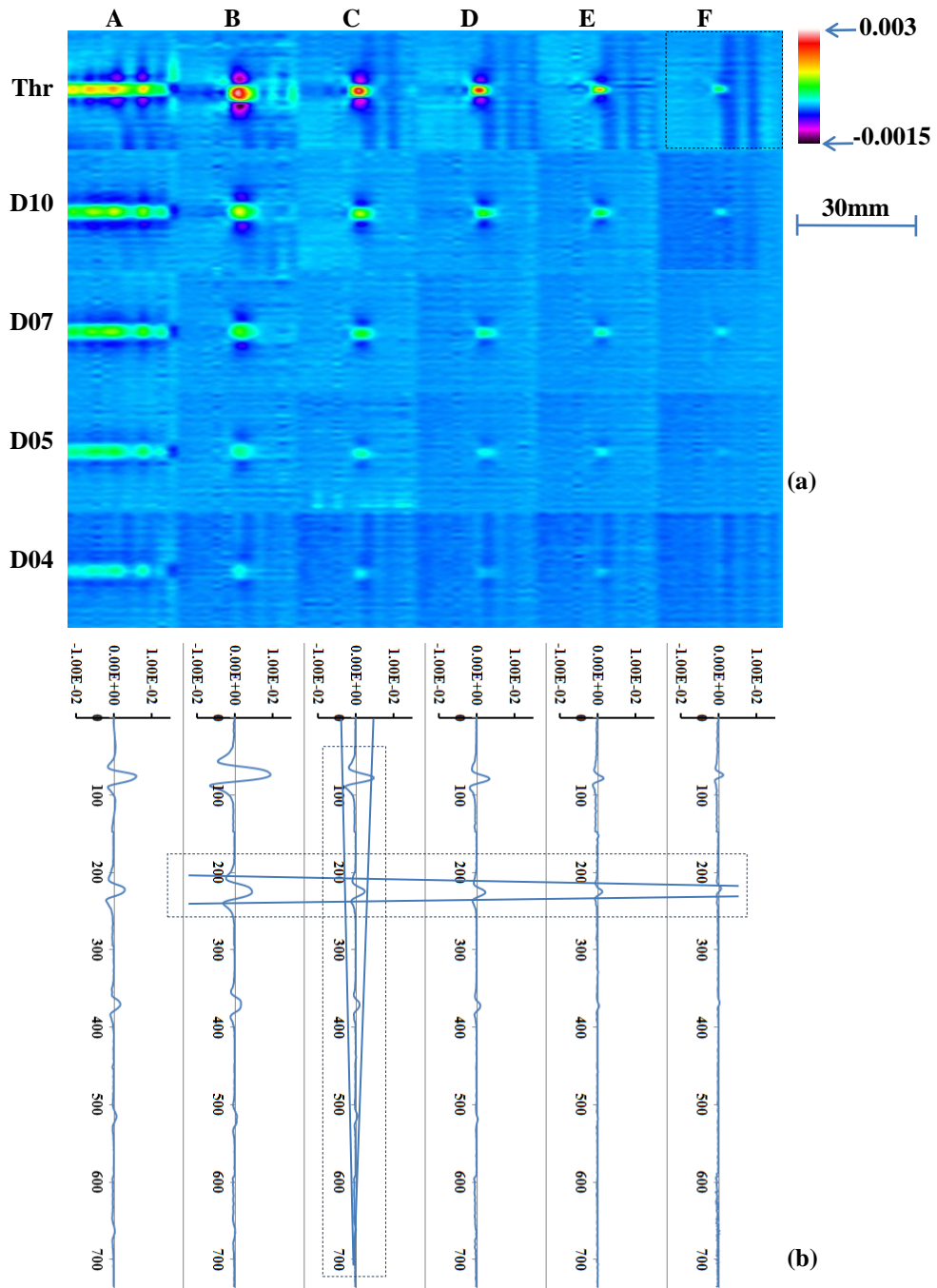
Figure 3-26 The experimental results of Inconel 600 in near-side scanning at 5 kHz

(a) contour figure; (b) section-view

61

3.3.4 Near and far-side images of Stainless-Steel specimen

Near-side cracks

Figure 3-27, Figure 3-28 and Figure 3-29 show the experimental results of near-side cracks on Stainless-Steel alloy (STS304) at 1, 3 and 5 kHz, respectively. All cracks are detected but not clear in the 1 kHz. Crack images are clearer at 3 kHz and the clearest at 5 kHz.

Similarly copper–nickel and Inconel 600 specimen, the analysis section-view of signal at the three frequencies indicates that: cracks having same depth, the distance from peak-to-peak (w) increase with the increase of diameter; cracks have same diameter, the amplitude of signal from peak-to-peak (h) increases with the increase of depth.

Far-side cracks

Figure 3-30, Figure 3-31 and Figure 3-32 show the experimental results of near-side cracks on Stainless-Steel alloy (STS304) at 1, 3 and 5 kHz, respectively. There are several small cracks were not detected or not clear. The cracks F02, F03 could not be detected at all the three frequencies. The cracks E02, E03, D02, and F06 were not clear. The similar behaviors of signal response to the crack depth and diameter were also observed in the results as happened in the near-side cracks.
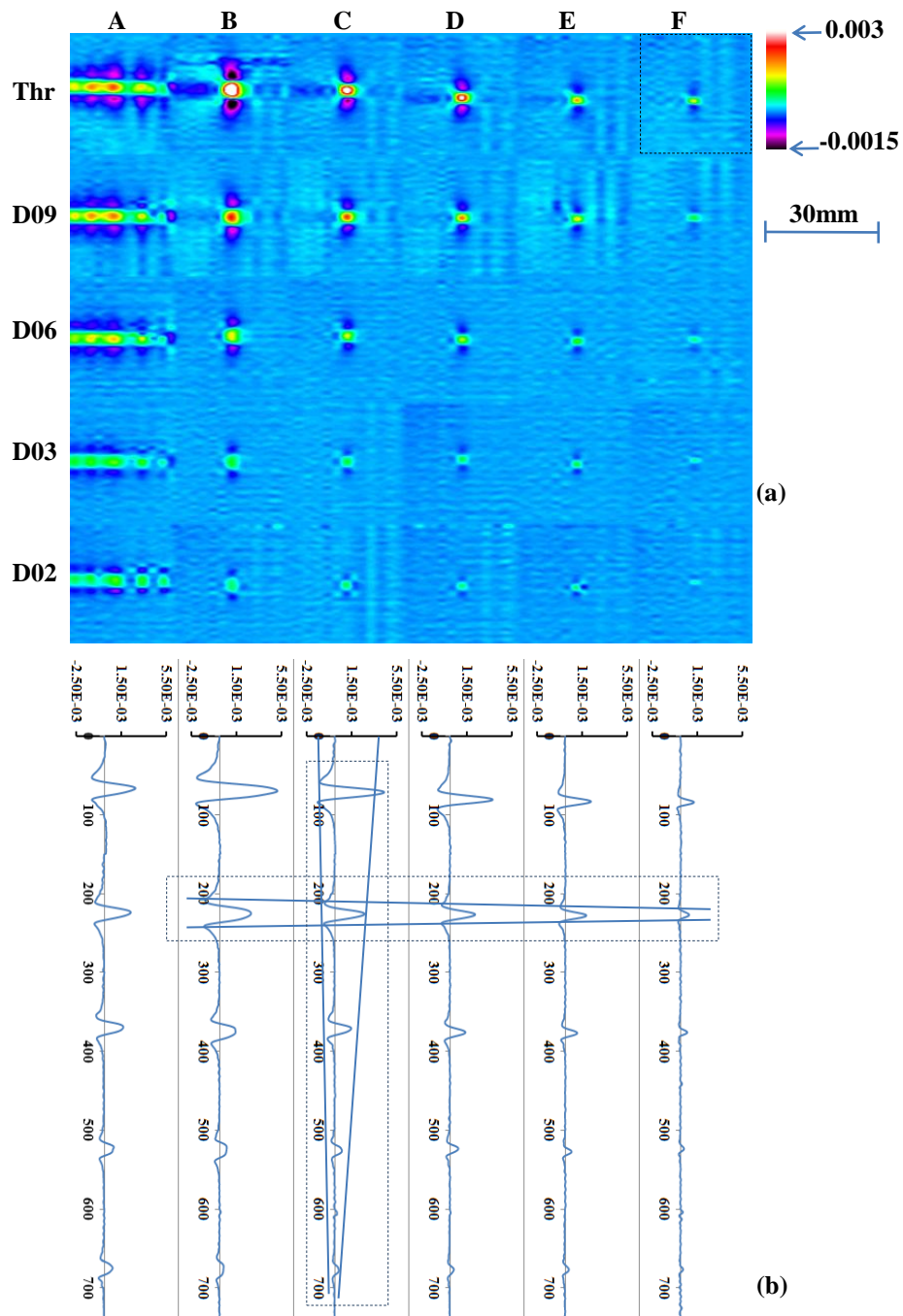
Figure 3-27 The experimental results of Stainless-Steel (STS304) in near-side scanning at 1 kHz (a) contour figure; (b) section-view

63
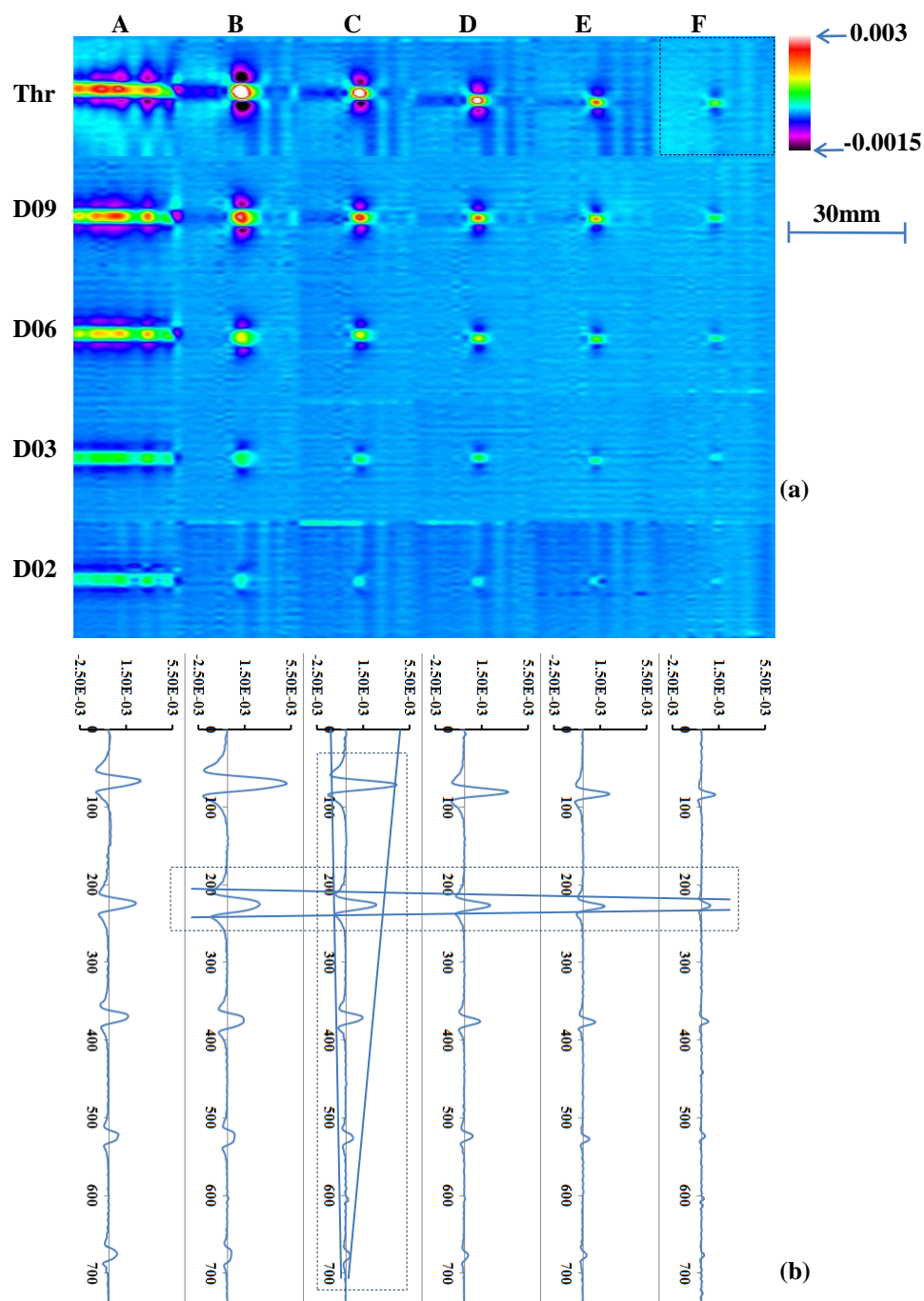
Figure 3-28 The experimental results of Stainless-Steel (STS304) in near-side scanning at 3 kHz (a) contour figure; (b) section-view
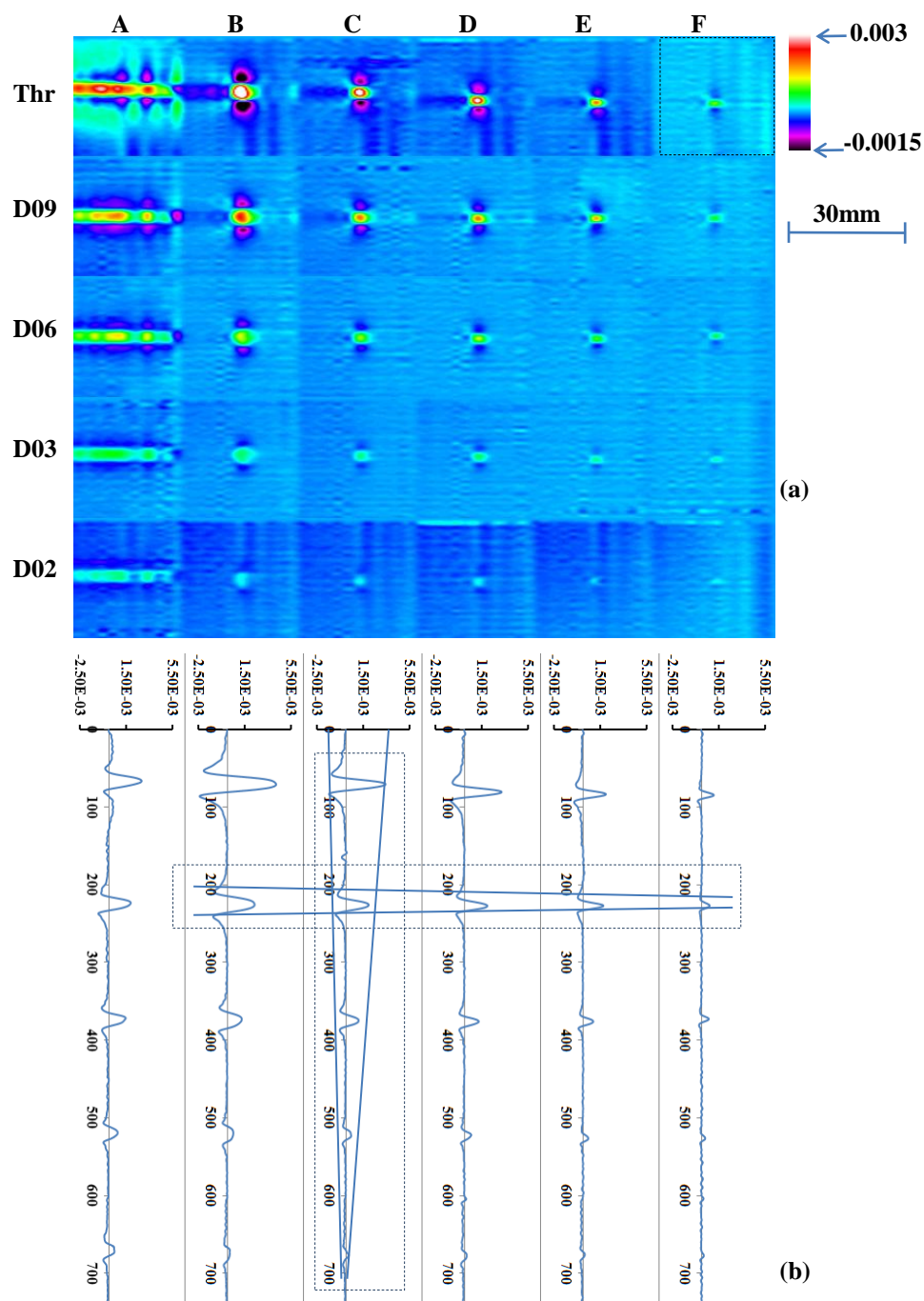
Figure 3-29 The experimental results of Stainless-Steel (STS304) in near-side scanning at 5 kHz (a) contour figure; (b) section-view
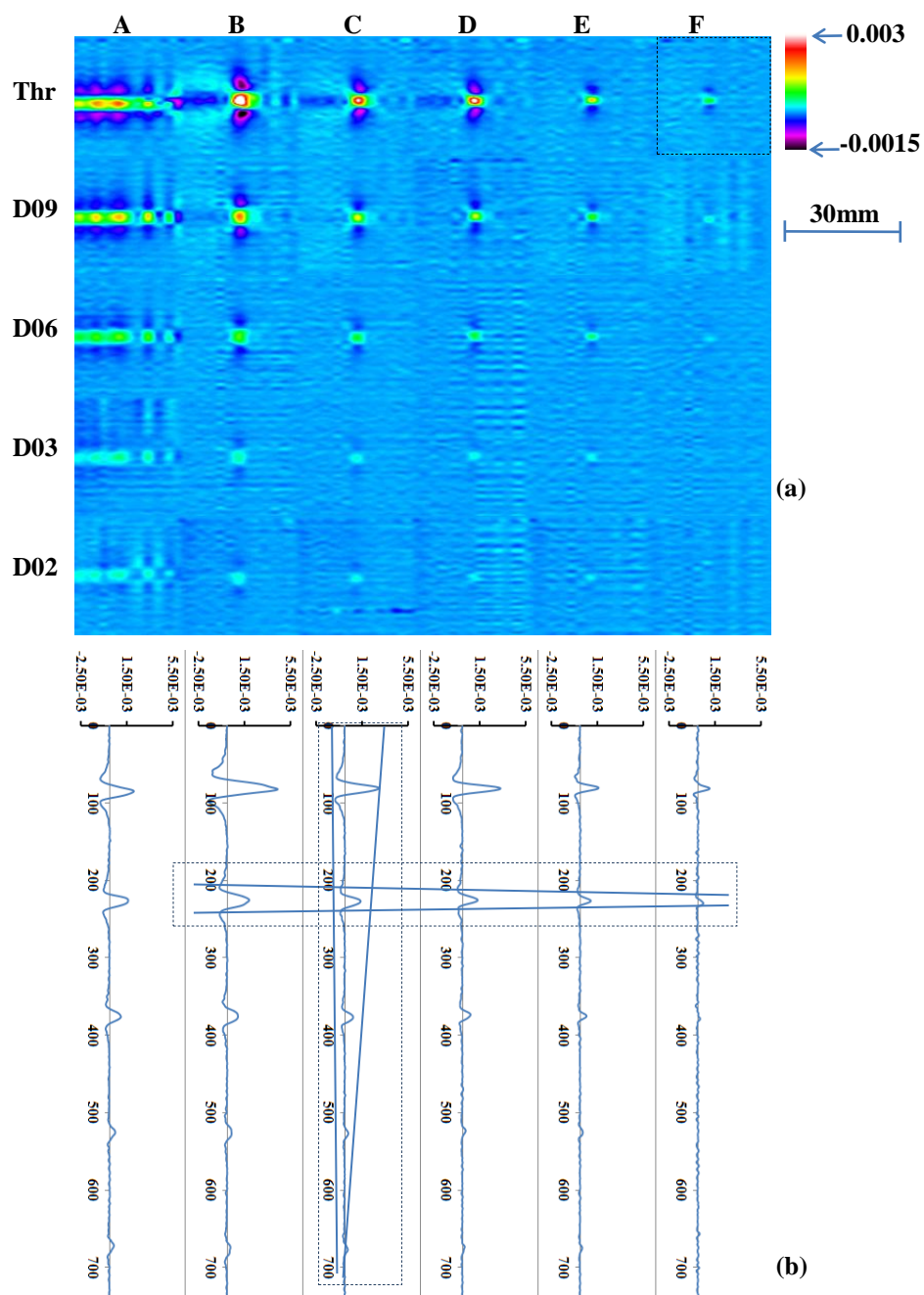
Figure 3-30 The experimental results of Stainless-Steel (STS304) in far-side mode at 1 kHz (a) Contour Figure; (b) section-view
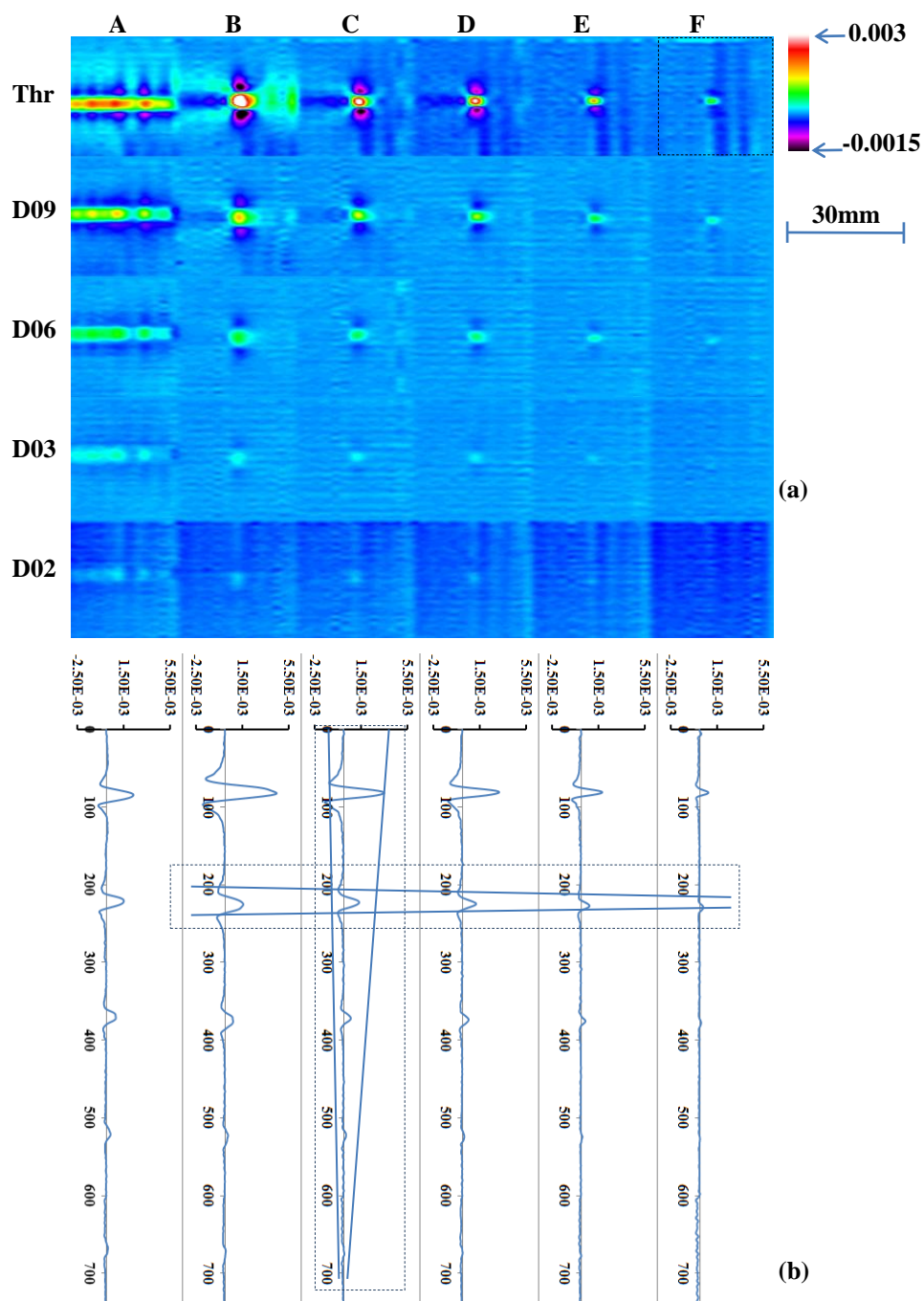
Figure 3-31 The experimental results of Stainless-Steel (STS304) in far-side mode at 3 kHz

(a) Contour Figure; (b) section-view

67
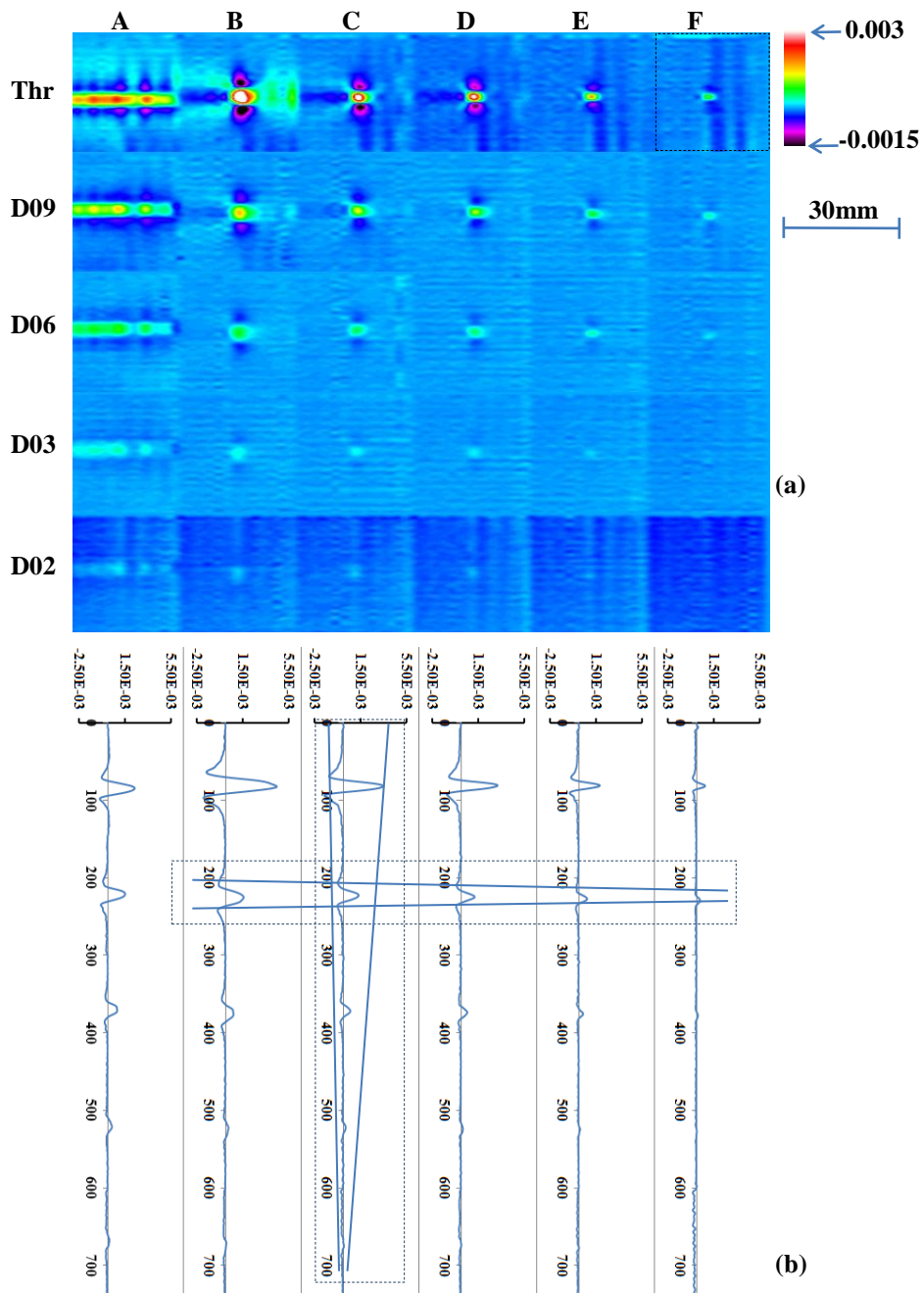
Figure 3-32 The experimental results of Stainless-Steel (STS304) in far-side mode at 5kHz

(a) Contour Figure; (b) section-view

68

3.4 Measurement Signal Analysis

The most important task in improving automation of ECT system is the development of crack classification algorithm. An NDT system should not only examine the existence of cracks, but also quantitatively evaluate the cracks in terms of the position, shape and volume. Although most of data processing and visualization is automated by using commercial software, but the data analysis is performed manually by specialists [47]. Basically there are two types of signals considered in ECT to analyze the obtained data in order to classify the cracks. Amplitude and phase information have utilized by many researchers and designed different types of excitation, detection coil configurations to crack position of crack [48]-[51]. The signal classification algorithm is the core for any automated NDT system, different algorithms such as Fourier descriptor classification scheme, artificial neural networks and fuzzy interference systems were developed since 90's [52]-[55]. Recently Lee et al. [56]-[59] developed simple discrimination algorithms used for the quantitative evaluation of corrosion in small bore piping which uses Hall sensor arrays in a bobbin-type magnetic camera (BMC), which includes a bobbin coil, to inspect the OD and ID cracks.

In our current research, the images are obtained for near sine and far-side cracks in test specimens. Experimental results show that the signal responses of different crack types such as near-side and far-side have different characteristics. Thus we need to use such algorithms which can Discrimination of near and far-side cracks and able to estimate the volume of the crack. In order to Discrimination of the cracks and classify the near-side and far-side cracks we need more detailed understanding of obtained data. For this purpose, in addition to our previous discussion regarding the effect of crack depth, diameter and excitation frequency on the detected signal, we consider another parameter which is the integration of certain area around the image of crack. Here we consider area integration because as we are detecting the volumetric crack in a conductive specimen. Therefore, there are four factors can be used to Discrimination of the near-side and far-side cracks: peak-to-peak value (h), peak-to-peak distance (w), integral of absolute data ($|\Delta V|$ total), and frequency (f). The integral of the crack image is the total of absolute data in the image as defined by equation. (5).

$$\Delta V|_{total} = \sum_{Crack\ area} |\Delta V(i,j)| \qquad (5)$$

Where Σ is the summation and |ΔV(i,j)| is the absolute of the certain area around the crack image including the crack as shown in images in Figure 3-27. *ΔV(i,j)* is differential output voltages of the RMS circuits, it is calculates by using equation (6).

$$\Delta V(i,j) = V_{RMS}(i+1,j) - V_{RMS}(i,j) \qquad (6)$$

Where V_{RMS} is the output voltage from a RMS circuit which is proportional to the Hall-sensor voltage. *i* and *j* are the step size and index of the sensor respectively.
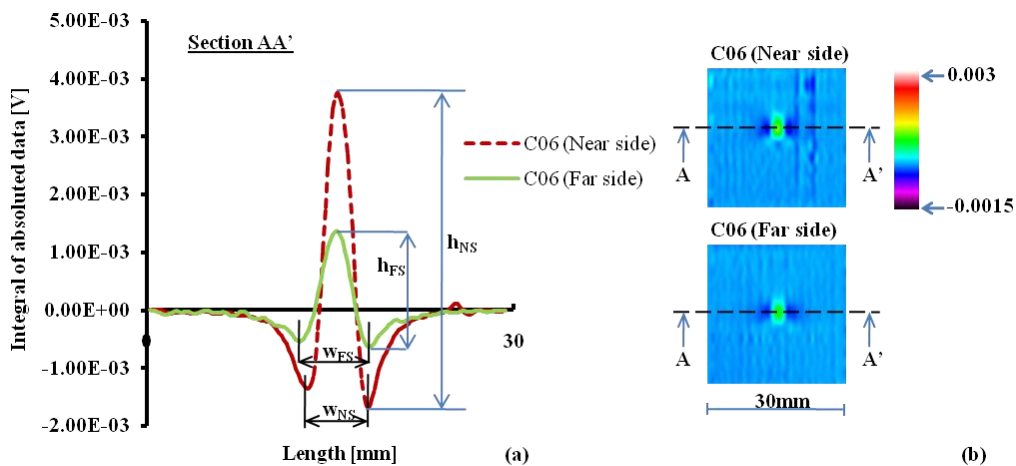
Figure 3-33 Image of near-side and far-side cracks of similar sizes of copper-nickel plate and their cross-sectional view at 3 kHz

Figure 3-33 shows the image and section view of crack C06 (No.18) (Copper-Nickel) at 3 kHz in the near-side and far-side mode. We saw that the peak-to-peak height of the near-side crack (h_{NS}) is higher than that of the far-side crack (h_{FS}); however, the peak-to-peak distance of the near-side crack (w_{NS}) is smaller than that of the far-side crack (w_{FS}). In this research we have developed different numerical algorithms which include the key features 'h' and 'w' of the crack signal. We select 'h' and 'w' for the data analysis because as we discussed earlier the shape of the detected signal look like a cone (Figure 3-34), it is well known that height and base are the key parameters in a cone to calculate the cone characteristics, thus we have interested in these features of the detected signal.

70

$$\text{Volume (V)} = \left(\frac{1}{3}\right)\pi r^2 . h$$
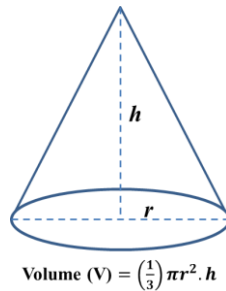
Figure 3-34 Shape of a cone and equation of its volume

3.5 Quantitative evaluation of cracks

The mention previous section 3.4, there are four factors can be used to discrimination of near-side and far-side crack are: peak-to-peak value (h), peak-to-peak distance (w), integrated absolute data ($\Delta V|_{total}$), and frequency (f). This section provides four relationships between the four factors to discriminate far-side and near-side cracks and then estimate the crack volume. The purpose of methods is to present near-side and far-side crack on the one graph (points) so that the near-side and far-side crack group data are separated.

3.5.1 The relationship between Integrated Absolute data and $h*w^2$

Error! Reference source not found.a shows the relationship between integrated bsolute of data with $h * w^2$ at 1 kHz of titanium. As mentioned in the previous section, we divide cracks to five groups B, C, D, E, and F with diameter 4.5, 3, 2.5, 1.8, 1, respectively, for easy to identify the size of the crack. Example the label E05 is known as the diameter of crack is 1.8 mm and the depth of crack is 0.5 mm. On the **Error! Reference source not found.**a, the ed points are data of cracks at near-side scanning and the blue points are data of cracks at far-side scanning. The red line is linear approximation of near-side cracks and blue line is linear approximation of far-side crack. We saw that near-side and far-side cracks seemingly are mixed and linearly distributed, so it is difficult to discrimination near-side and far-side cracks. The distribution is similar for data at 3 and 5 kHz, as shown in **Error! Reference source not ound.** b, c. The result of others specimens is similar and will not presented in this section. Therefore, this method is not useful in discrimination of near/far-side cracks.

71

Titanium

(a)

3 kHz

$y = 3.7675x + 0.0793$

$y = 3.6955x + 0.0909$

- Near side
- Far side
- Linear (Near side)
- Linear (Far side)

(b)

5 kHz

$y = 3.8157x + 0.095$

$y = 3.1352x + 0.1225$

- Near side
- Far side
- Linear (Near side)
- Linear (Far side)

(c)
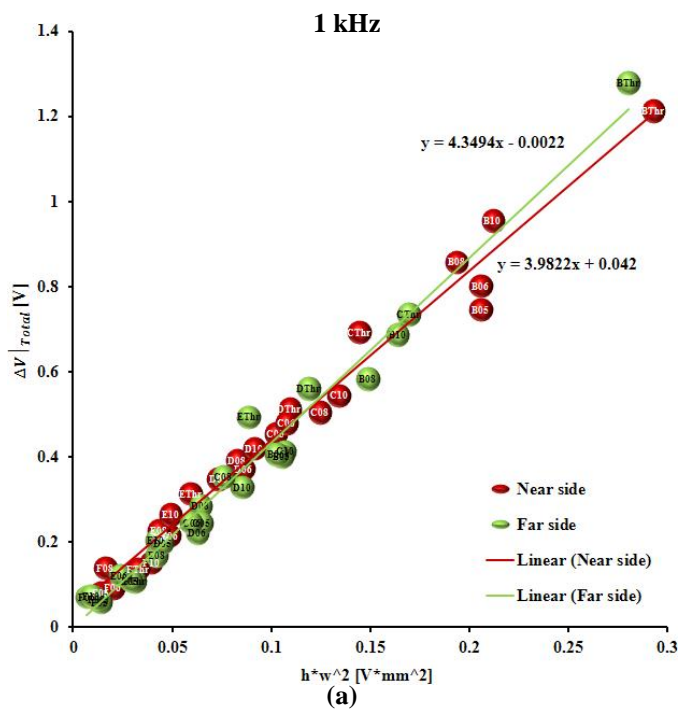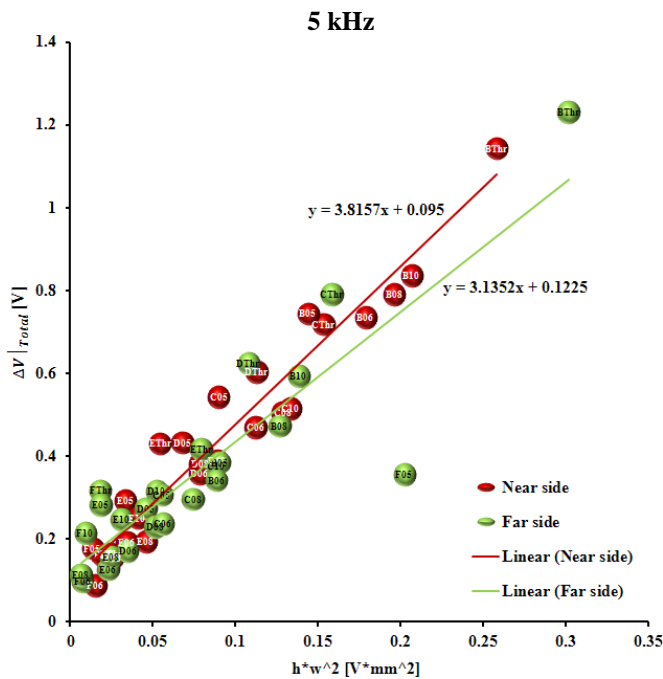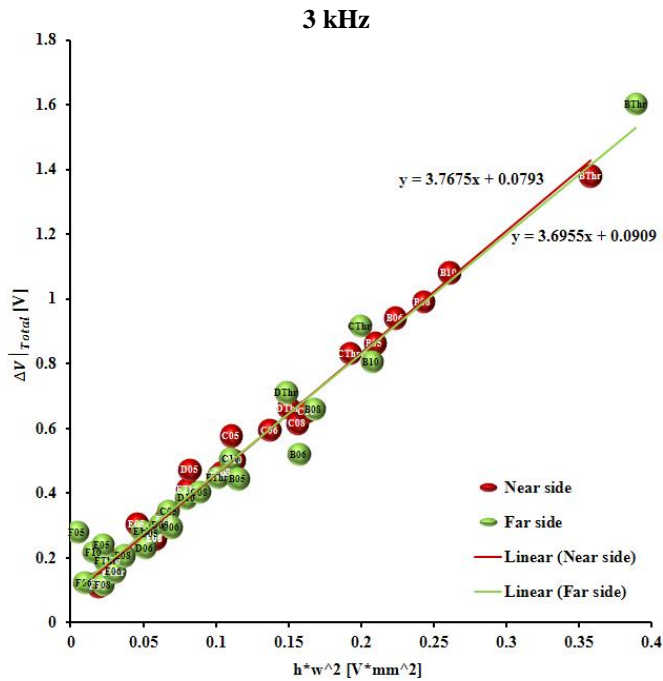
Figure 3-35 Relationship between integrated of absolute data and $h*w^2$ of Titanium at 1 kHz

(a), 3 kHz (b), 5 kHz (c)

73

3.5.2 The relationship between Integrated Absolute data and $\sum(01)/h$

$\sum(01)$ is integrated of absolute data after apply cut-off value and convert to '0', '1' value. The algorithm to convert data to '0', '1' data is presented in Figure 3-36 and Figure 3-37. Firstly, every data of crack image is compared with two cut-off value (High and Low), If the data higher than the High value or smaller than the Low value, it will be converted to '1'. Otherwise, the data will be converted to '0'. The '0', '1' data is then summarized to obtain the integrated of absolute "0", "1" data, $\sum(01)$.
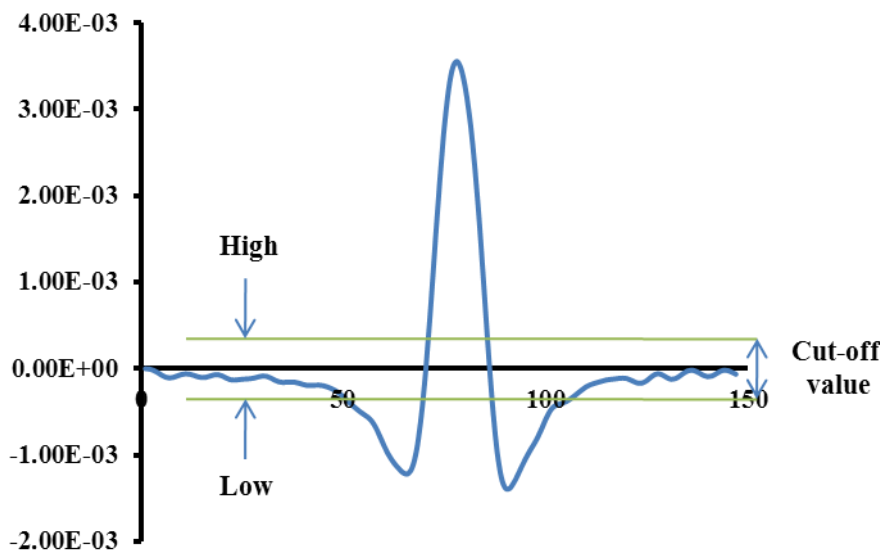
Figure 3-36 The section-view of signal

This section presents four pairs of cut-off value for all the frequencies and specimens. The cut-off values are indicated in Table 3-7.

Table 3-7 Cut-off values in conversion processing to '0',’1' data

Cut-off Number	High Value [V]	Low Value [V]
#1	1.19E-04	-2.17E-04
#2	1.19E-04	-3.25E-04
#3	2.38E-04	-3.25E-04
#4	2.38E-04	-4.33E-04

74
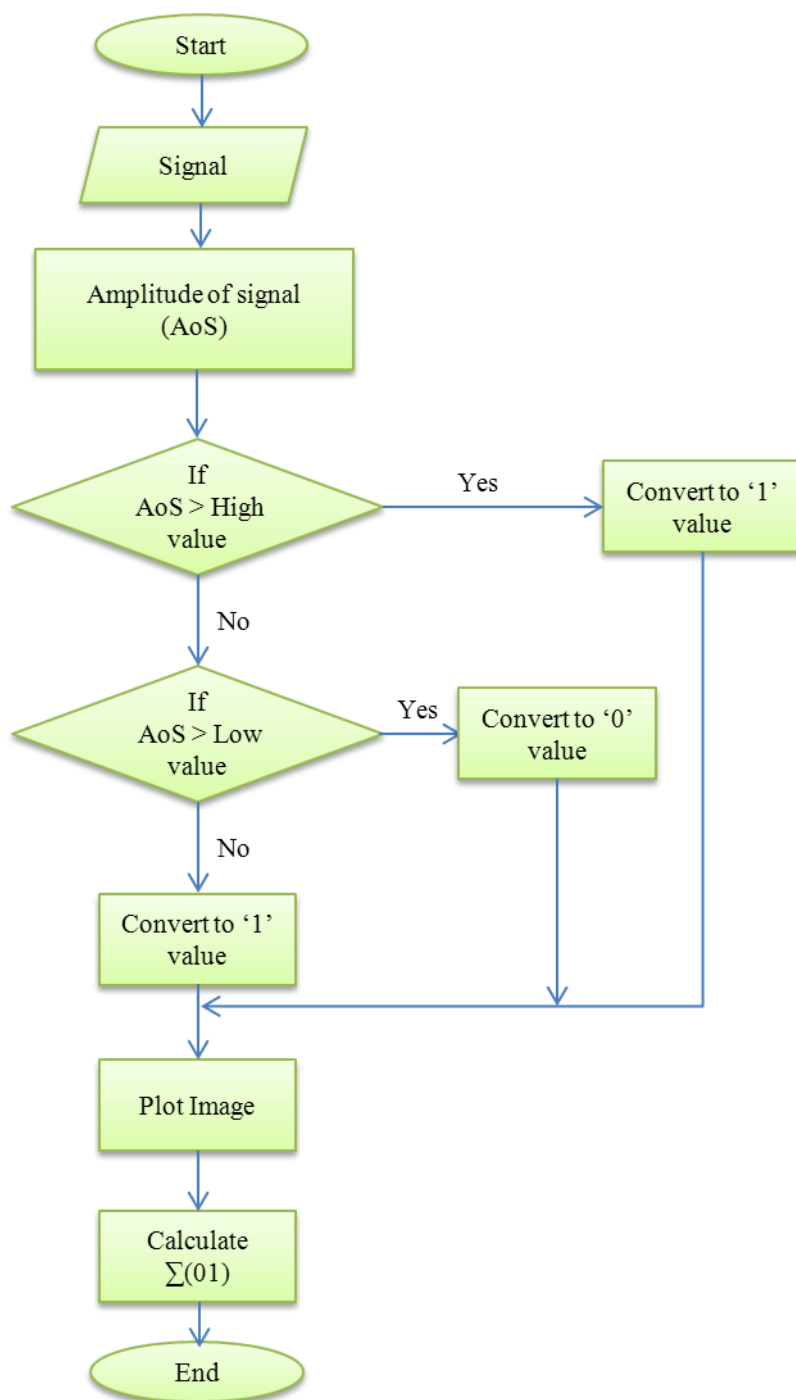
Figure 3-37 The algorithm to calculate $\sum(01)$

Figure 3-38 ~ Figure 3-41 show the relationship between integrated absolute data with '∑(01)/h' for titanium specimen at four cut-offs at 1, 3 and 5 kHz. At 1 kHz, the distribution of the near-side data could be approximated as a linear proportion. However, the far-side data likely distributes randomly. It could separate several far-side cracks in the right-hand side distribution area. But it is still difficult to provide a good discrimination result. At 3 and 5 kHz, the near- and far-side data distributed mixing each other. Thus, we could not discriminate the near/far-side crack using the relationship between integrated absolute data with '∑(01)/h' for titanium specimen. The similar distribution of near- and far-side data was happened in the copper-nickel, inconel600, and stainless-steel specimen. Therefore, this section does not provide the results of the copper-nickel, inconel600, and stainless-steel specimen.

Titanium

Cut-off 1

(a)
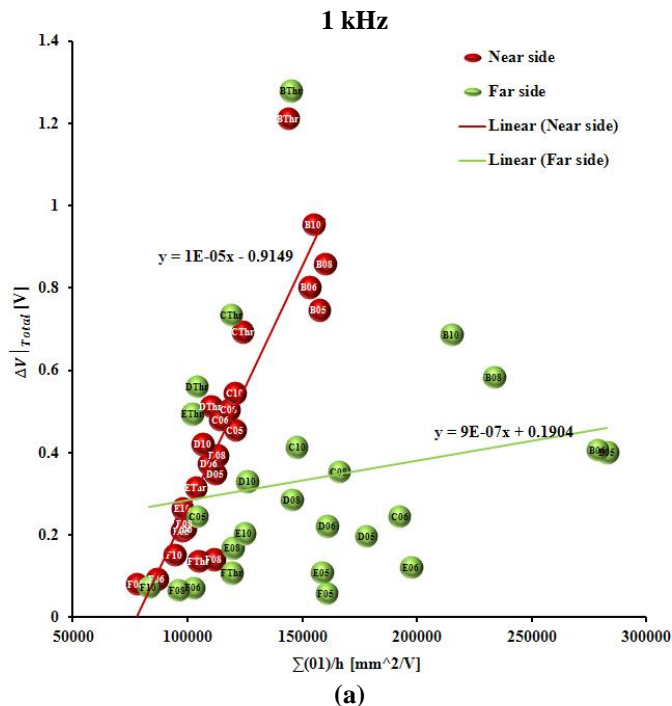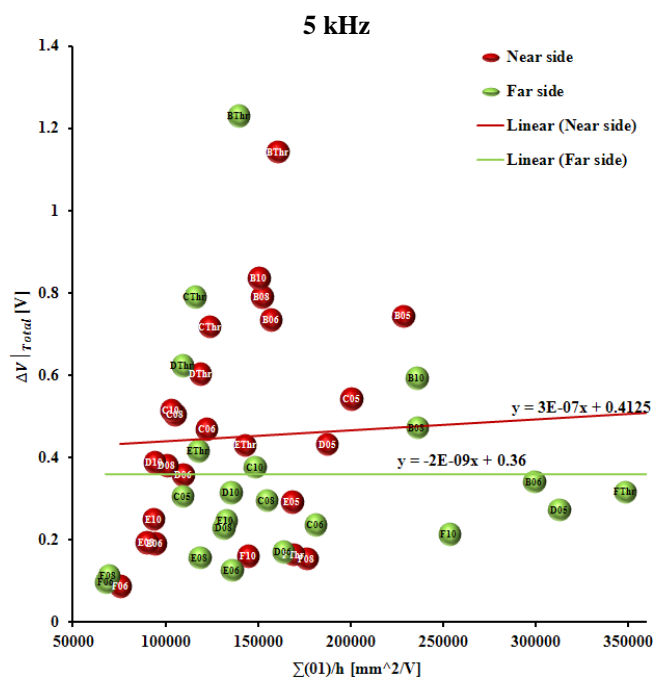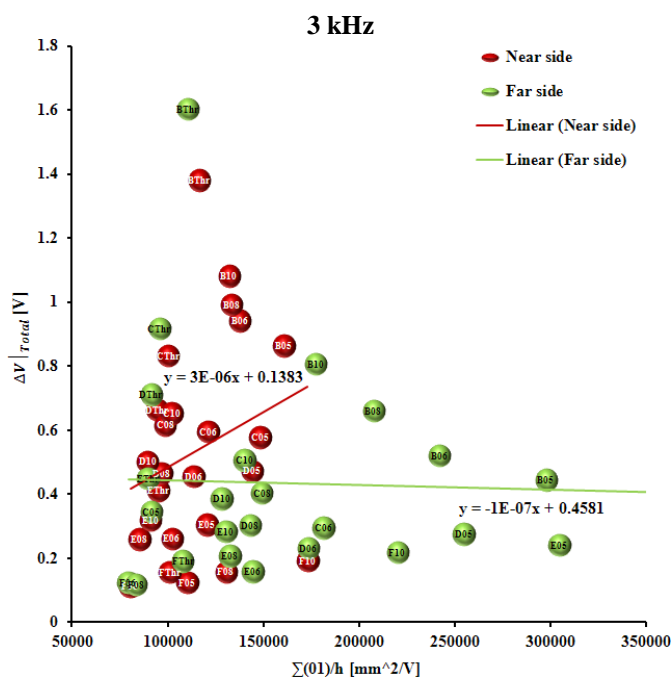
Figure 3-38 The relationship between Integrated absolute data of Titanium at Cut-off 1at 1 kHz (a), 3 kHz (b), 5 kHz (c)

**Cut-off 2**

1 kHz

(a)

3 kHz

(b)

78
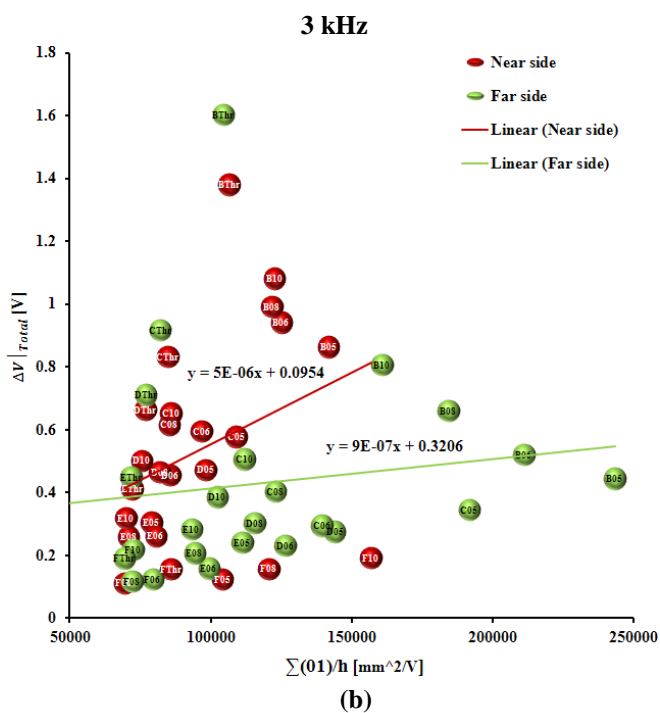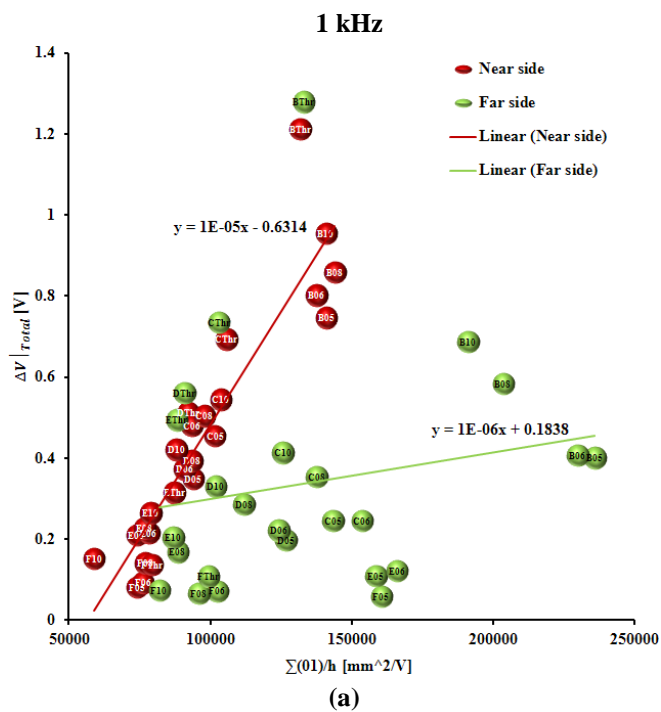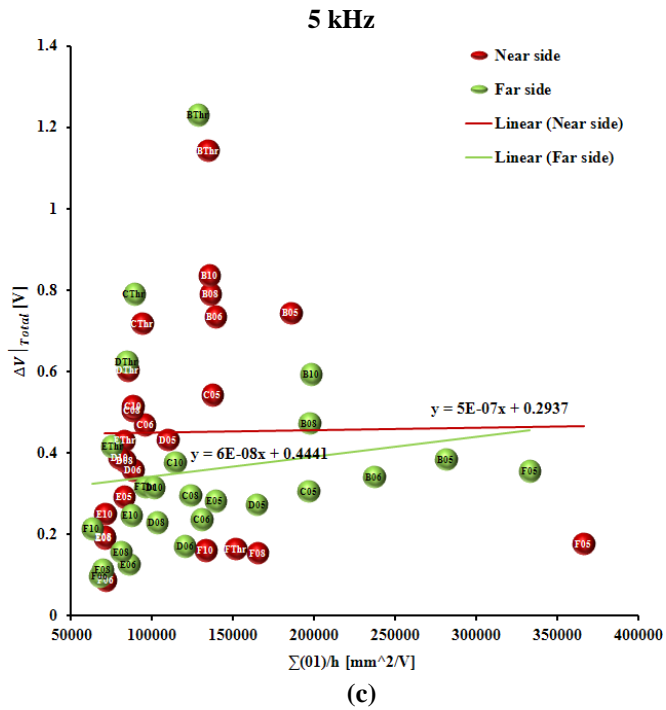
Figure 3-39 The relationship between integrated absolute data for titanium specimen at cut-off 2 at 1 kHz (a), 3 kHz (b), 5 kHz (c)

Cut-off 3

1 kHz

(a)

3 kHz

(b)

5 kHz

$y = 6E\text{-}06x - 0.1068$

$y = 7E\text{-}07x + 0.2798$

(c)
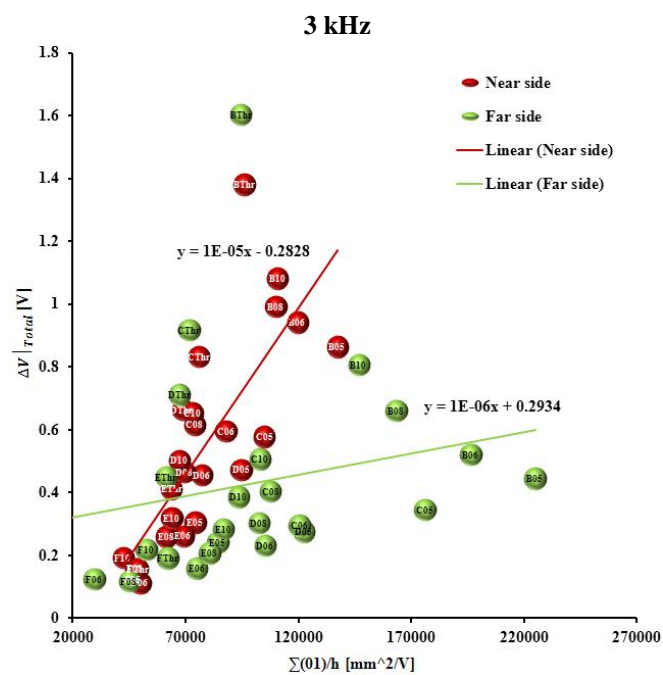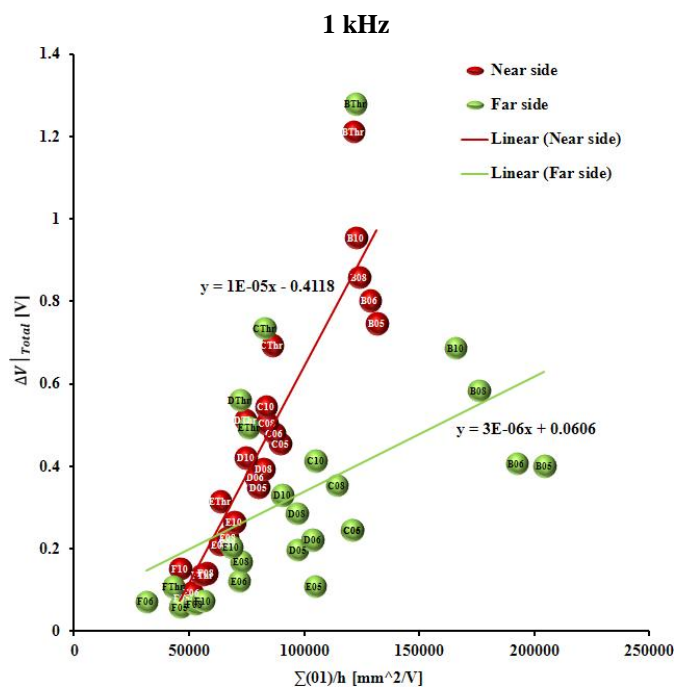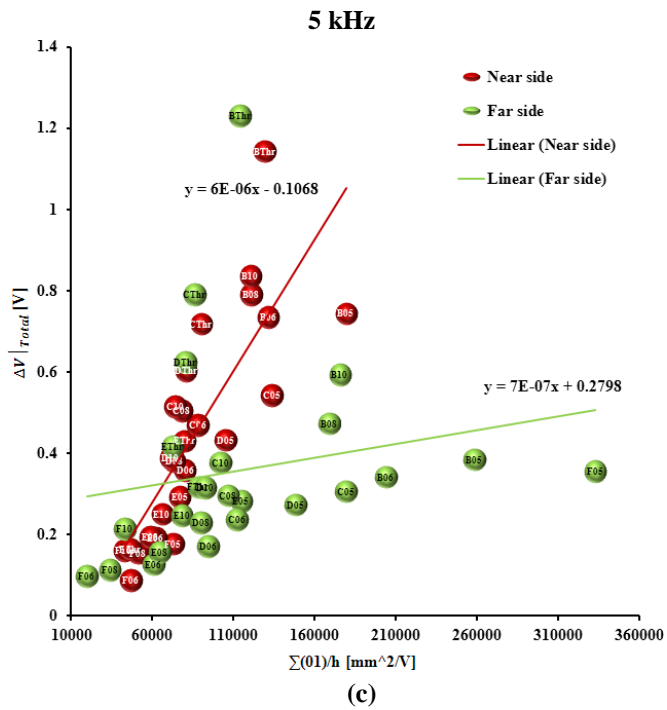
Figure 3-40 The relationship between Integrated absolute data of Titanium at Cut-off 3 at 1 kHz (a), 3 kHz (b), 5 kHz (c)

Cut-off 4

1 kHz

(a)

3 kHz

(b)

82

5 kHz

$y = 8E\text{-}06x - 0.1263$

$y = 2E\text{-}06x + 0.2237$

(c)
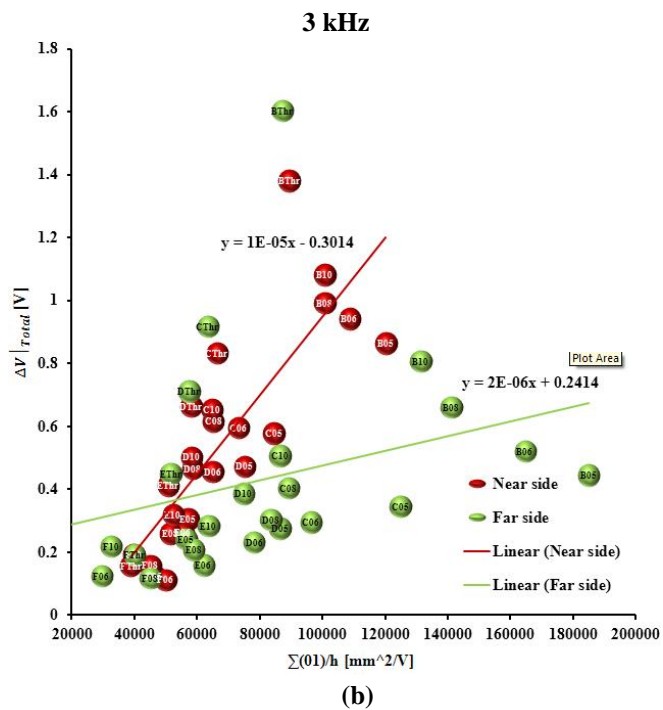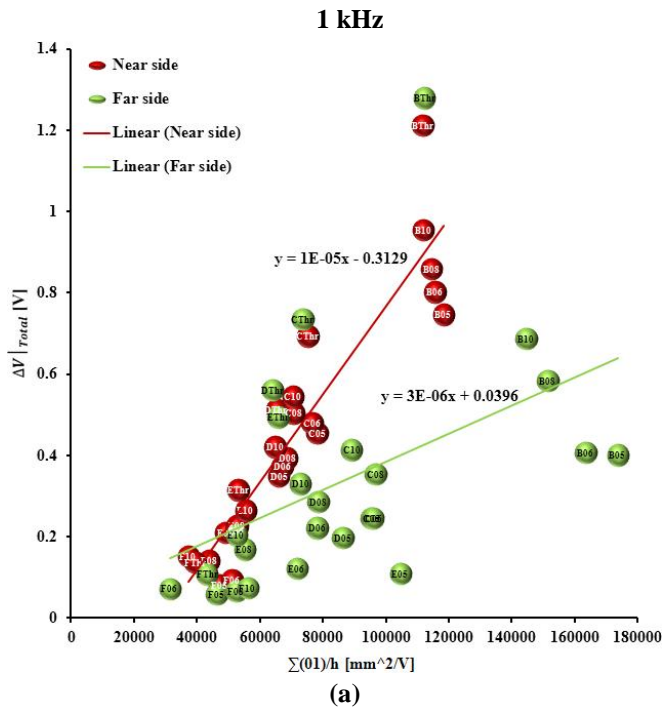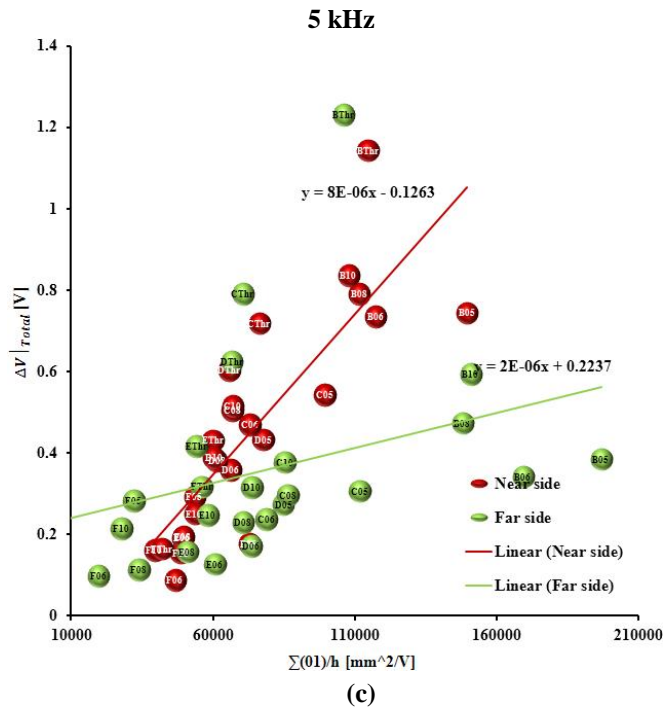
Figure 3-41 The relationship between Integrated absolute data of Titanium at Cut-off 4 at 1 kHz (a), 3 kHz (b), 5 kHz (c)

3.5.3 The Relationship between Integrated Absolute Data and h^2*w

Take into account the sample of near-side and far-side crack in Figure 3-33. We observe that the signal h of the near-side crack increases about 150% than the signal h of the far-side crack. But, the signal w of the far-side crack increases only about 12% than the signal w of the near-side crack. Thus, the ratio change of signal h is much higher than the ratio change of signal w. So, if we build relationship between the integrated of absolute data with the h^2*w, we expect a good separation of the distribution of far-side and near-side crack.

<u>Titanium</u>

Discrimination of near-side and far-side crack

Figure 3-42 shows the relationship between the integrated of absolute of crack image with the h^2*w at three frequencies – 1, 3 and 5 kHz. It shows a good separation between the near-side and far-side crack in the three researching frequencies. The distribution of far-side cracks is higher than the distribution of the near-side cracks, because the ratio of signal h between near-side and far-side crack is much higher than the ratio of signal w between far-side and near-side crack. The better separate distribution of near-side and far-side crack is observed in the 1 and 3 kHz of frequencies than the 5 kHz.

(a)

(b)

85

5 kHz

$y = 3800.1x + 0.1317$

$y = 4752.1x + 0.1772$

- ● Near side
- ● Far side
- — Linear (Near side)
- — Linear (Far side)

$\Delta V|_{Total}$ [V]

h^2*w [V^2*mm]

(c)
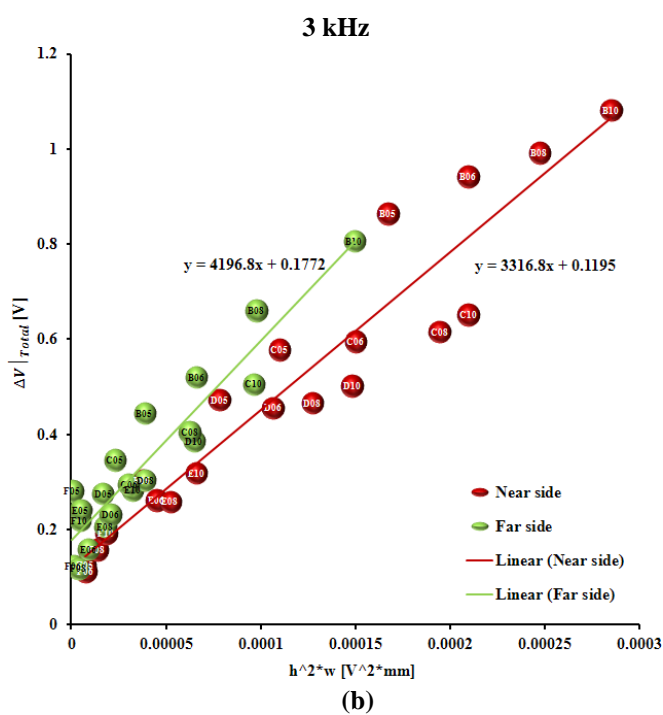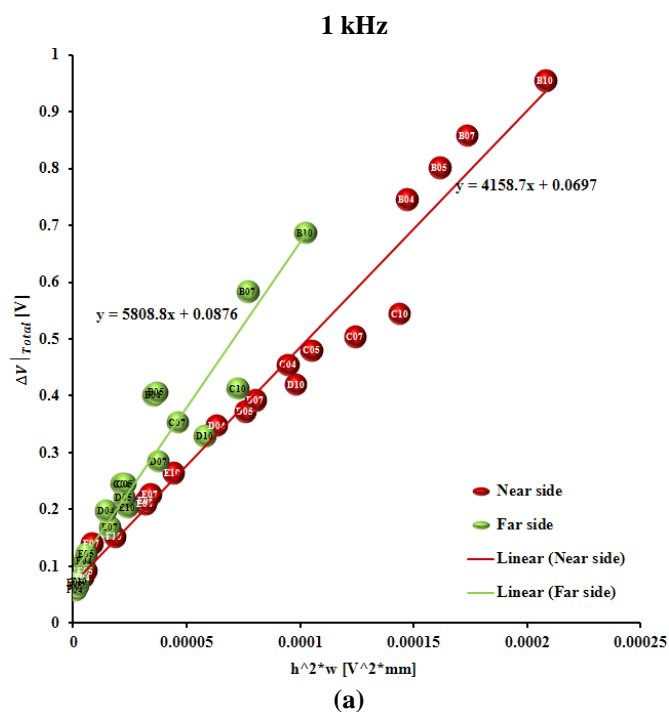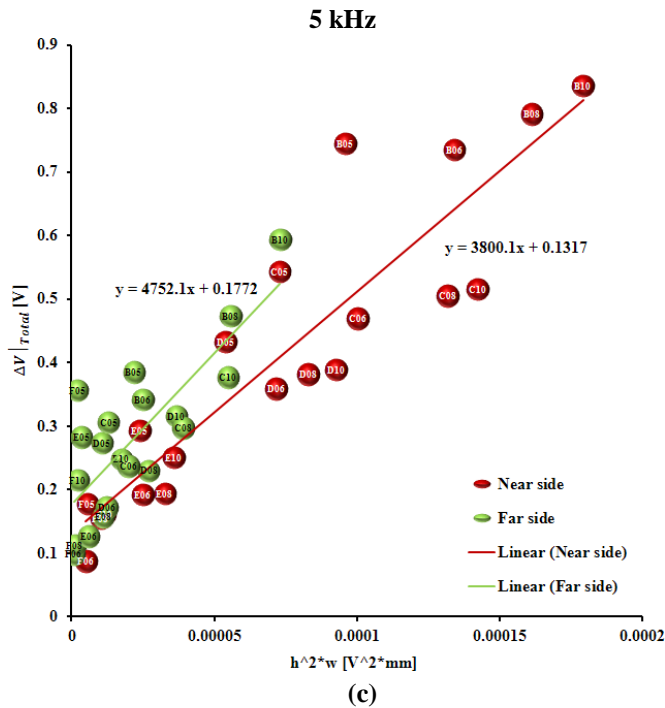
Figure 3-42 Relationship between integrated of absolute of crack image with h^2*w at 1, 3 and 5 kHz

Probability of Near-side (PNS) and Far-side (PFS) Crack

It is necessary to quantitative evaluate the discrimination probability of near-side (PNS) and far-side (PFS) crack using the relationship between the integrated of absolute of crack image with the h2*w. The relationship could be estimated as a linear relationship as shown in the Figure 3-42. The linear equations for each group of near-side and far-side cracks at each frequency are expressed in Eqs. (7-12).

1 kHz	Near side	$y = 4158 \cdot x + 0.069$	(7)
	Far side	$y = 5808 \cdot x + 0.087$	(8)
3 kHz	Near side	$y = 3316 \cdot x + 0.119$	(9)
	Far side	$y = 4196 \cdot x + 0.177$	(10)
5 kHz	Near side	$y = 3800 \cdot x + 0.131$	(11)
	Far side	$y = 4752 \cdot x + 0.177$	(12)

Where: y is integrated of absolute data, x is $h^2 * w$.

The PNS and PFS are calculated by the rate change of integrated of absolute data in the experiment $(\Delta V|_{total}^{exp})$ and linear approximation $(\Delta V|_{total}^{est})$, which is expressed by Eq. (13).

$$PNS, PFS = 1 - \frac{\left| \Delta V|_{total}^{exp} - \Delta V|_{total}^{est} \right|}{\Delta V|_{total}^{exp}} \qquad (13)$$

Figure 3-43 shows the discrimination probability result of the near-side and far-side crack at 1, 3 and 5 kHz. At each frequency, two graphs were plotted for near-side scan and far-side scan of experiment data. The near-side scan means entire the cracks are near-side (ID). Inversely, the far-side scan means entire the cracks are far-side (OD). At 1 kHz, entire the cracks were correctly discriminated in the near-side scan except cracks F08 which has high smallest diameter. However, in the far-side scan, the 6/25 cracks were wrong discriminated. The through-type cracks were considered as the near-side cracks. Four cracks having smallest diameter of 1 mm were wrong discriminated because of weak signal. Two cracks D10 and C10 also were wrong discriminated because they have deep depth. A deep crack is close a near-side crack leading difficulty of discrimination. The same phenomenon was happened in the 3 and 5 kHz. However, the number of wrong discrimination increases. At 3 kHz, the wrong discriminations are 4 and 6 for near-side scan and far-side scan, respectively. At 5 kHz, the wrong discriminations are 7 and 8 for near-side scan and far-side scan, respectively. Thus, the low frequency 1 kHz provides the best discrimination probability of the near-side and far-side cracks.

1 kHz

(a)

3 kHz

(b)

5 kHz

Near side

Far side

(c)
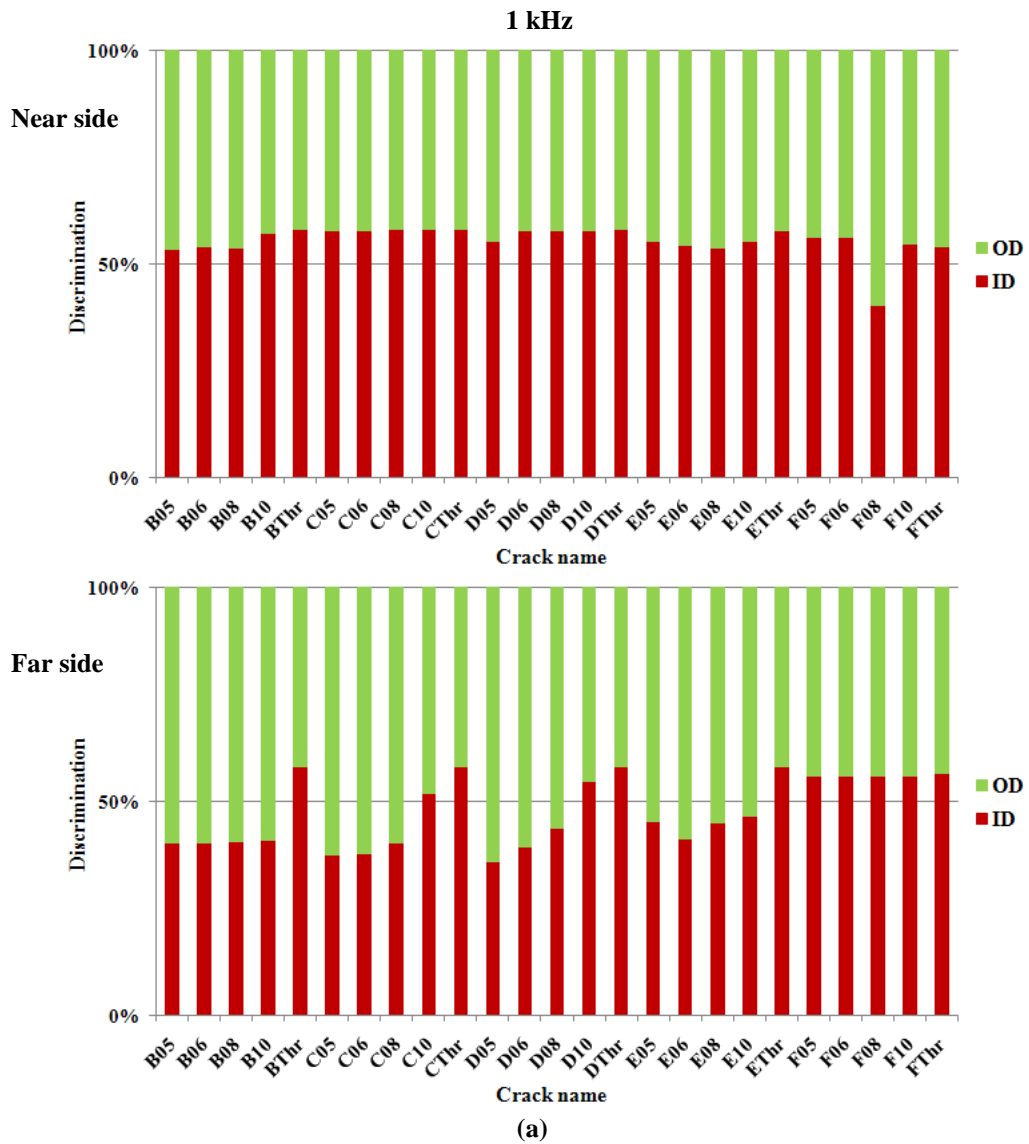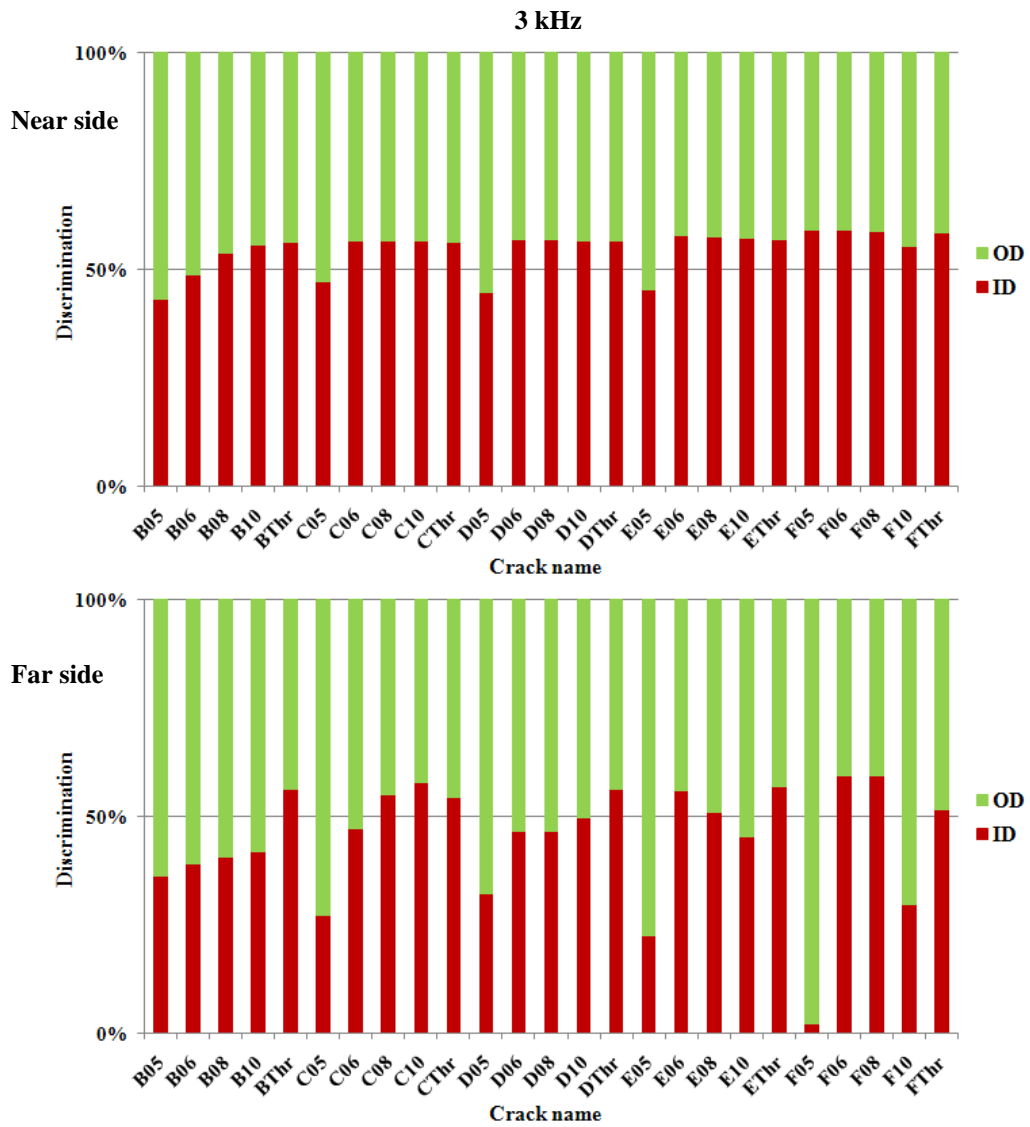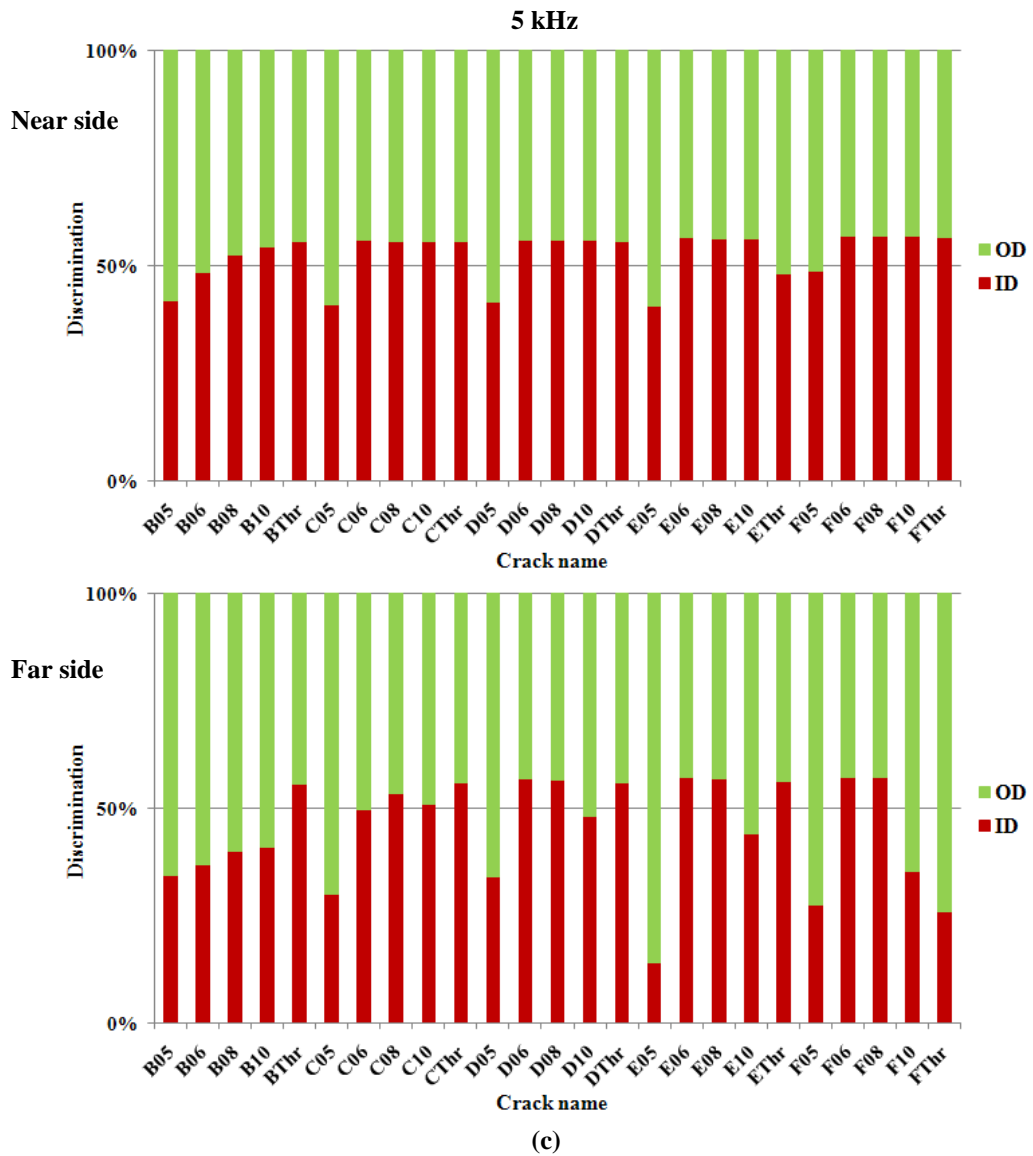
Figure 3-43 Discrimination results of near-side and far-side cracks at 1, 3 and 5 kHz

90

Estimation of Crack Volume

Once the near-side and far-side cracks are discriminated, the quantitative evaluation of crack size is necessary. Establish the relationship between crack volume with the integrated of absolute data for 1, 3 and 5 kHz, as shown in Figure 3-44. We observe that the distribution of near-side and far-side data is separated in each group. The relationship could be approximately fitted by quadric function for each type of crack at each frequency. The quadric functions are expressed in the Eqs. (14-19). Thus, if crack type is identified and the integrated of absolute data is obtained from crack image, the crack volume can be estimated by the equivalent equation.

1 kHz	Near side	$\text{Vol} = 12.31 \cdot \Delta V|_{\text{total}}^{\text{ID}}{}^2 + 3.528 \cdot \Delta V|_{\text{total}}^{\text{ID}} + 0.173$	(14)
	Far side	$\text{Vol} = 16.43 \cdot \Delta V|_{\text{total}}^{\text{OD}}{}^2 + 12.96 \cdot \Delta V|_{\text{total}}^{\text{OD}} + 0.477$	(15)
3 kHz	Near side	$\text{Vol} = 11.65 \cdot \Delta V|_{\text{total}}^{\text{ID}}{}^2 + 0.321 \cdot \Delta V|_{\text{total}}^{\text{ID}} + 0.515$	(16)
	Far side	$\text{Vol} = 12.28 \cdot \Delta V|_{\text{total}}^{\text{OD}}{}^2 + 12.52 \cdot \Delta V|_{\text{total}}^{\text{OD}} + 1.535$	(17)
5 kHz	Near side	$\text{Vol} = 21.37 \cdot \Delta V|_{\text{total}}^{\text{ID}}{}^2 - 2.777 \cdot \Delta V|_{\text{total}}^{\text{ID}} + 0.983$	(18)
	Far side	$\text{Vol} = 51.58 \cdot \Delta V|_{\text{total}}^{\text{OD}}{}^2 - 3.826 \cdot \Delta V|_{\text{total}}^{\text{OD}} + 0.804$	(19)

1 kHz

$y = 16.434x^2 + 12.96x - 0.4772$

$y = 12.312x^2 + 3.5284x + 0.1733$

- Near side
- Far side
- Poly. (Near side)
- Poly. (Far side)

(a)

3 kHz

$y = 12.281x^2 + 12.526x - 1.5352$

$y = 11.652x^2 + 0.3217x + 0.5157$

- Near side
- Far side
- Poly. (Near side)
- Poly. (Far side)

(b)

92

$$y = 51.589x^2 - 3.8266x + 0.8043$$

$$y = 21.375x^2 - 2.7775x + 0.9837$$
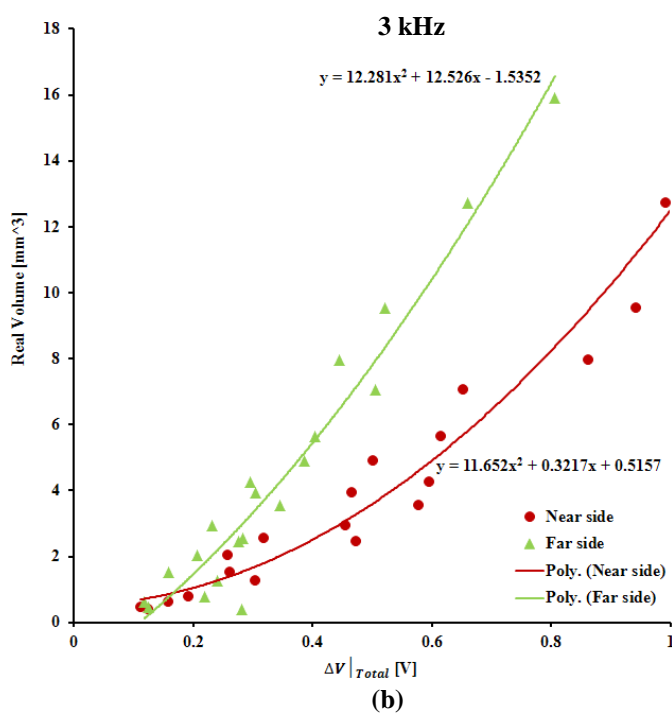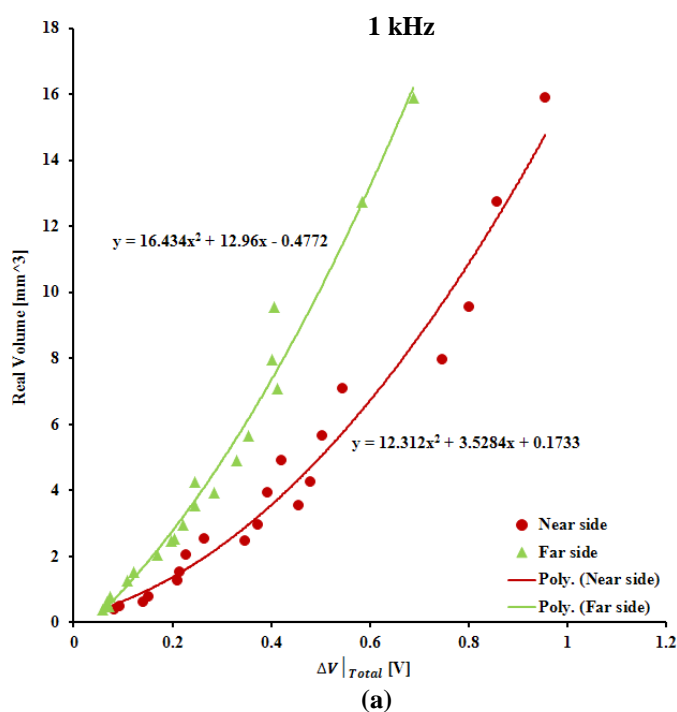
Figure 3-44 Relationship between integrated of absolute of crack image with crack volume at 1, 3 and 5 kHz.

Figure 3-45 shows the estimation of crack volume in near-side and far-side scan results at 1, 3 and 5 kHz. The estimation is done following the discrimination results in Figure 3-43. The standard deviations of estimated crack volume at 1 kHz are 1.1260 mm^3 and 1.7117 mm^3 for near-side and far-side scan, at 3 kHz are 5.028 mm^3 and 6.8618 mm^3 for near-side and far-side scan, at 5 kHz are 5.4739 mm^3 and 3.3656 mm^3 for near-side and far-side scan. The results at 1 kHz provide the best estimation compared with 3 and 5 kHz.

94
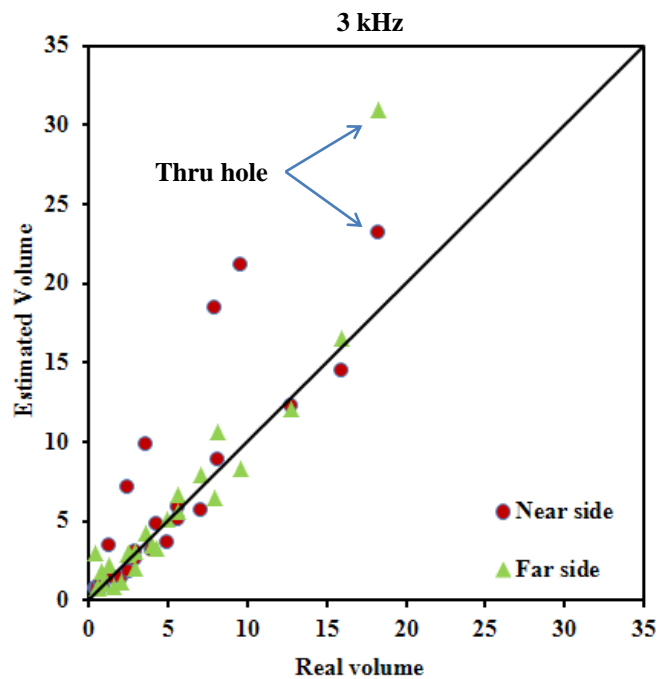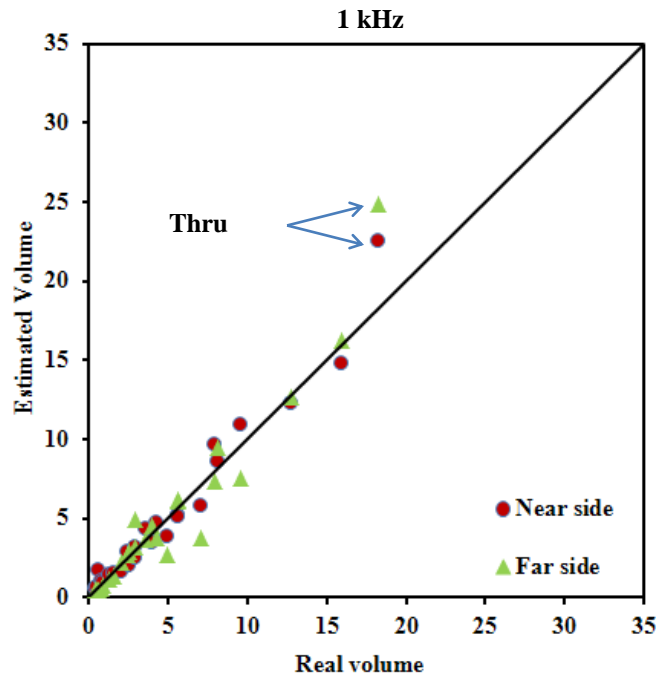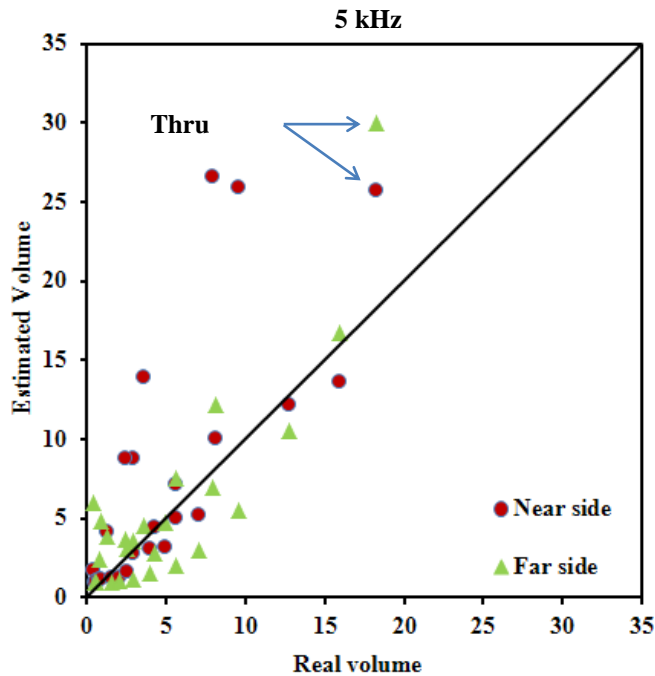
Figure 3-45 Estimation of crack volume in near-side and far-side scan results at 1, 3 and 5 kHz

Copper-Nickel

Discrimination of near-side and far-side crack

The same procedure analysis data of titanium specimen is applied for the copper-nickel specimen. The relationship between the integrated of absolute crack image with h^2*w at 1, 3 and 5 kHz is shown in Figure **3-46**. The linear fitting function for near-side and far-side cracks at each frequency is expressed in Eqs. (14)-(19).

1 kHz	Near side	$y = 1624 \cdot x + 0.159$	(14)
	Far side	$y = 1895 \cdot x + 0.183$	(15)
3 kHz	Near side	$y = 1945 \cdot x + 0.232$	(16)
	Far side	$y = 2596 \cdot x + 0.218$	(17)
5 kHz	Near side	$y = 2423 \cdot x + 0.199$	(18)
	Far side	$y = 3135 \cdot x + 0.194$	(19)

1 kHz

y = 1895.2x + 0.1833

y = 1621.8x + 0.1594

(a)

3 kHz

y = 2596.8x + 0.2187

y = 1945.5x + 0.2321

(b)

96

5 kHz

$y = 3153.1x + 0.1941$

$y = 2423.4x + 0.1998$

- ● Near side
- ● Far side
- — Linear (Near side)
- — Linear (Far side)

(c)
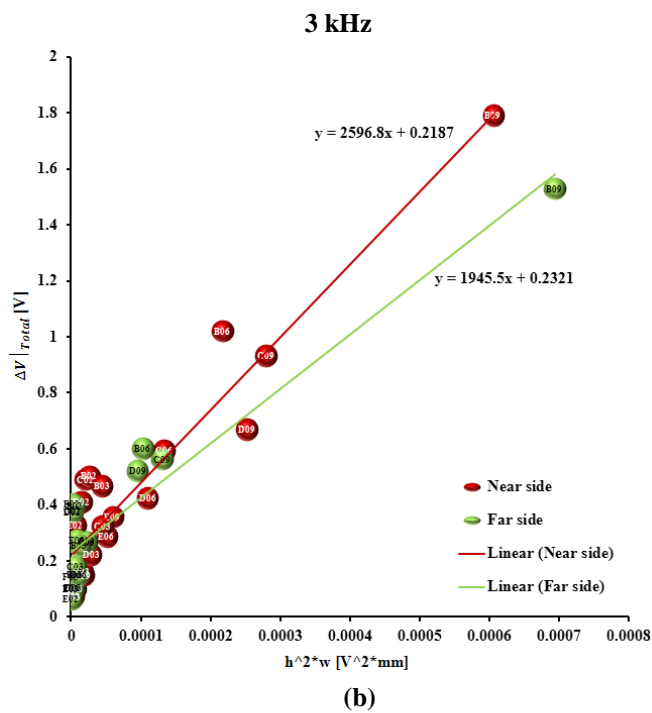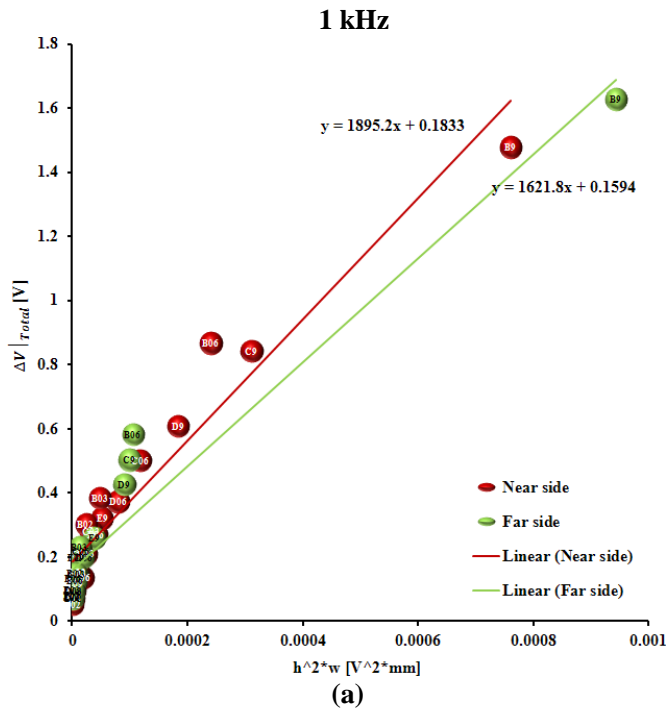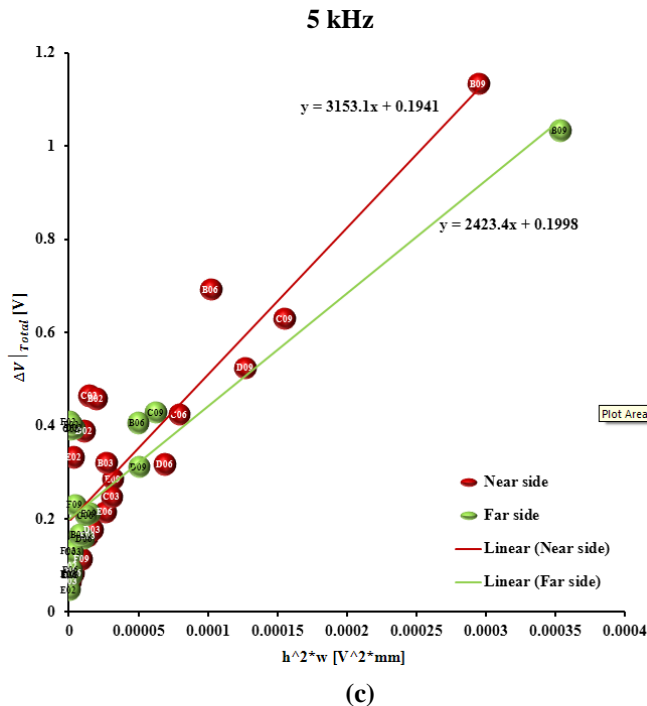
Figure 3-46 Relationship between integrated of absolute of crack image with h^2*w at 1, 3 and 5 kHz for Copper-Nickel specimen

Discrimination Results

Figure 3-47 shows the discrimination probability result using Eq. (13) of the near-side and far-side crack at 1, 3 and 5 kHz for copper-nickel specimen. At each frequency, two graphs were plotted for near-side scan and far-side scan of experiment data. The results of near-side scan data at 1 kHz, the cracks in column F were not correctly discriminated because they have high smallest diameter (1 mm). The cracks D02, D03, E02 and E03 also were not correctly discriminated, which have smallest depth. The cracks B06 and B09 have big diameter and deep depth. However they were not correctly discriminated because they have deep depths which are easy to be mixed with the far-side crack type. In the results of far-side scan data at 1 kHz, the cracks B03, B06, C06, C09, D06, D09, E06, E09, F09 and FThr were not correctly discriminated because they have deep depth and easy mixing with the near-side crack type.

At the 3 kHz and 5 kHz, the number of wrong discrimination increases. At 3 kHz, the wrong discriminations are 10/25 and 12/25 for near-side scan and far-side scan, respectively. At 5 kHz, the wrong discriminations are 7/25 and 8/25 for near-side scan and far-side scan, respectively. Thus, the low frequency 1 kHz provides the best discrimination probability of the near-side and far-side cracks as it happened in the titanium specimen.

(a)

3 kHz

(b)

99
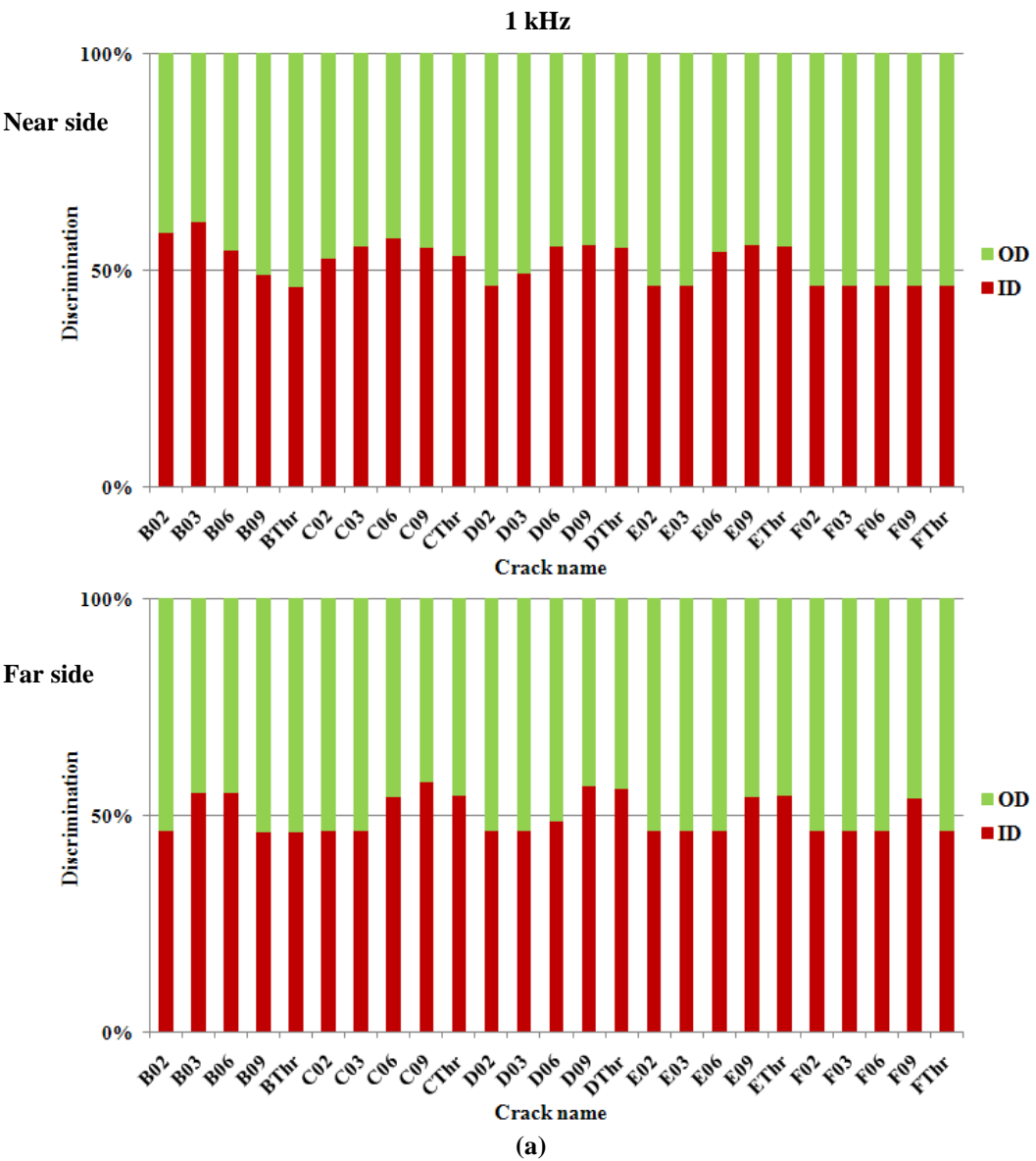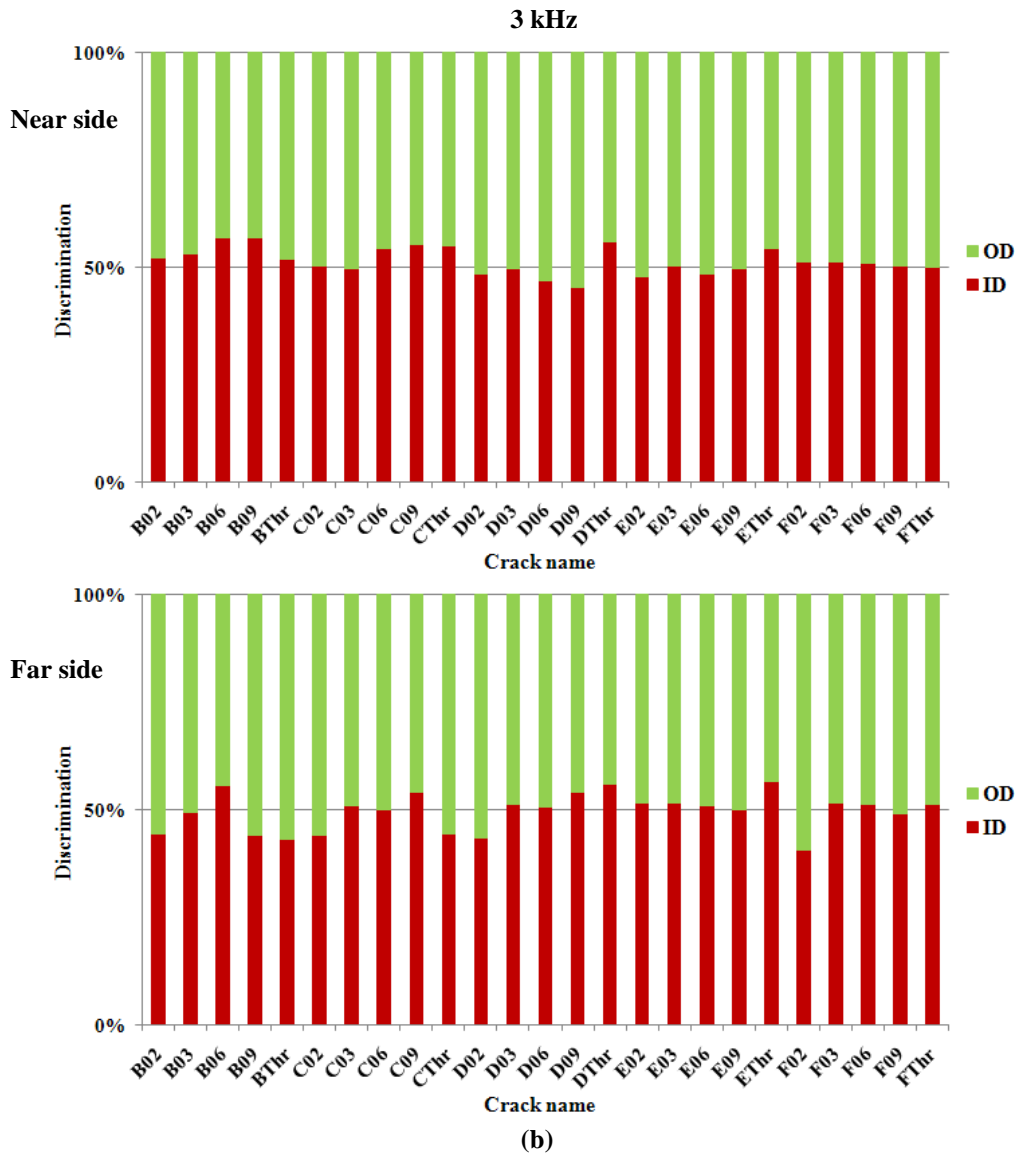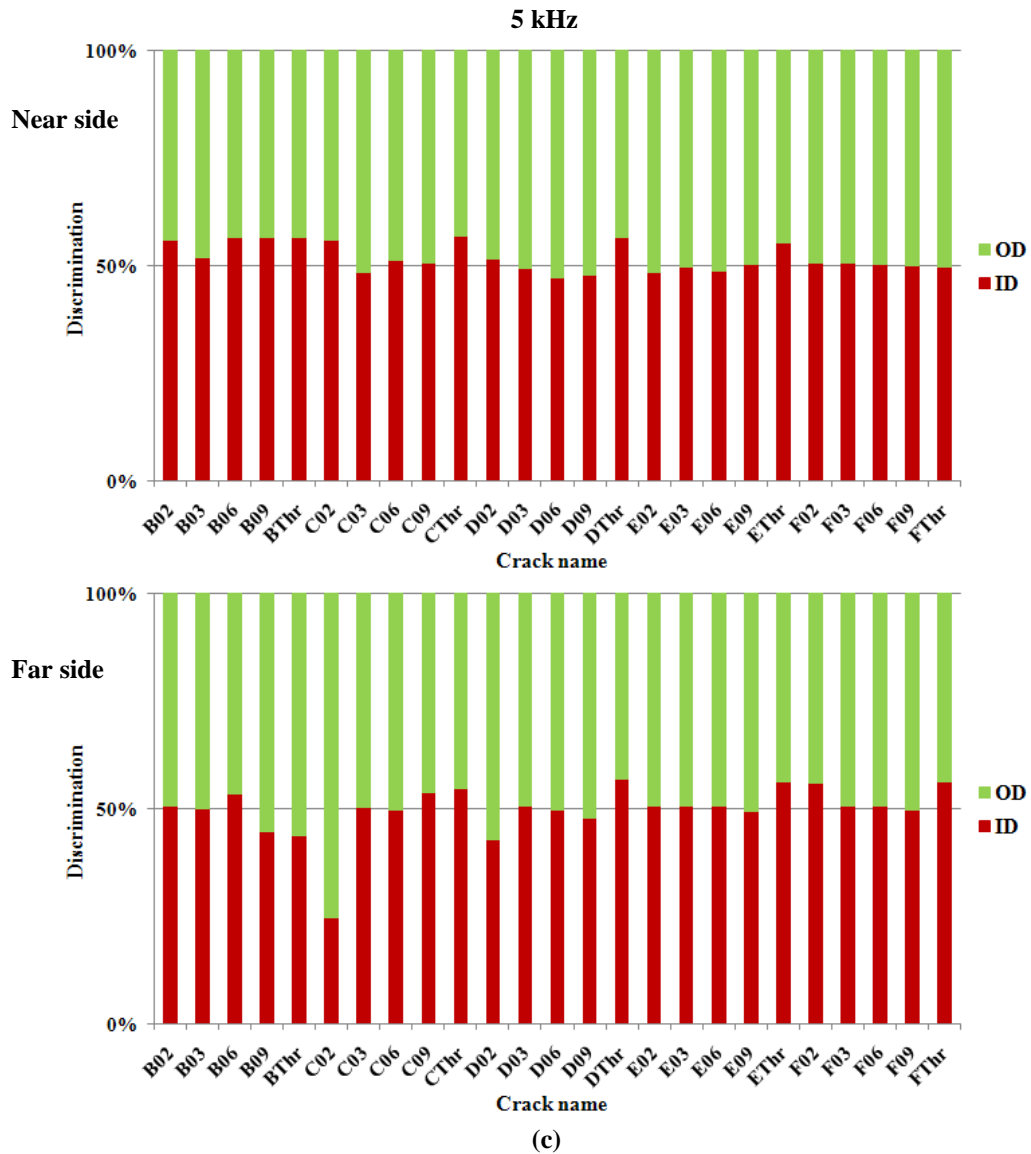
5 kHz

Figure 3-47 Discrimination results of near-side and far-side cracks at 1, 3 and 5 kHz for
Copper-Nickel specimen

Estimation of Crack Volume

Once the near-side and far-side cracks are discriminated, the quantitative evaluation of
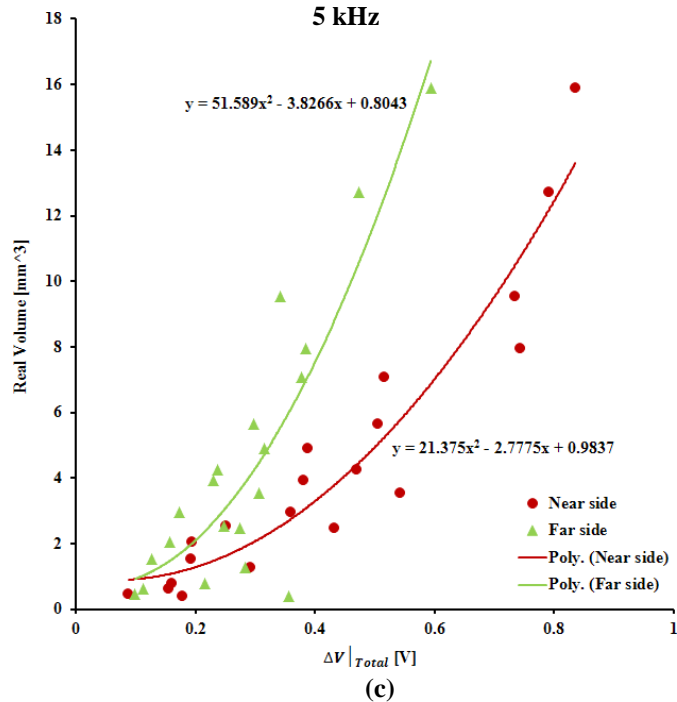crack size is necessary. Establish the relationship between crack volume with the integrated of
absolute data for 1, 3 and 5 kHz, as shown in Figure 3-48. We observe that the distribution of

100

near-side and far-side data is separated in each group. We approximate the fitting curve by quadric function for each type of crack at each frequency. The quadric functions are expressed in the Eqs. (20-25). Thus, if crack type is identified and the integrated of absolute data is obtained from crack image, the crack volume can be estimated by the equivalent equation.

1 kHz	Near side	$\text{Vol} = -5.245 \cdot \Delta V\|_{\text{total}}^{\text{ID}}{}^2 + 17.77 \cdot \Delta V\|_{\text{total}}^{\text{ID}} - 0.675$	(20)
	Far side	$\text{Vol} = 0.470 \cdot \Delta V\|_{\text{total}}^{\text{OD}}{}^2 + 9.302 \cdot \Delta V\|_{\text{total}}^{\text{OD}} - 0.452$	(21)
3 kHz	Near side	$\text{Vol} = 0.546 \cdot \Delta V\|_{\text{total}}^{\text{ID}}{}^2 + 7.555 \cdot \Delta V\|_{\text{total}}^{\text{ID}} - 0.637$	(22)
	Far side	$\text{Vol} = 0.155 \cdot \Delta V\|_{\text{total}}^{\text{OD}}{}^2 + 9.362 \cdot \Delta V\|_{\text{total}}^{\text{OD}} - 0.110$	(23)
5 kHz	Near side	$\text{Vol} = 8.483 \cdot \Delta V\|_{\text{total}}^{\text{ID}}{}^2 + 3.970 \cdot \Delta V\|_{\text{total}}^{\text{ID}} + 1.026$	(24)
	Far side	$\text{Vol} = 6.586 \cdot \Delta V\|_{\text{total}}^{\text{OD}}{}^2 + 5.736 \cdot \Delta V\|_{\text{total}}^{\text{OD}} - 0.176$	(25)

1 kHz

$y = 0.4706x^2 + 9.3029x - 0.4523$

$y = -5.2459x^2 + 17.779x - 0.6753$

- Near side
- Far side
- Poly. (Near side)
- Poly. (Far side)

(a)

101

3 kHz

$y = 0.1552x^2 + 9.3622x - 0.1108$

$y = 0.5466x^2 + 7.5555x - 0.6372$

(b)

5 kHz

$y = 6.5869x^2 + 5.7368x - 0.1764$

$y = 8.483x^2 + 3.9702x + 1.0264$
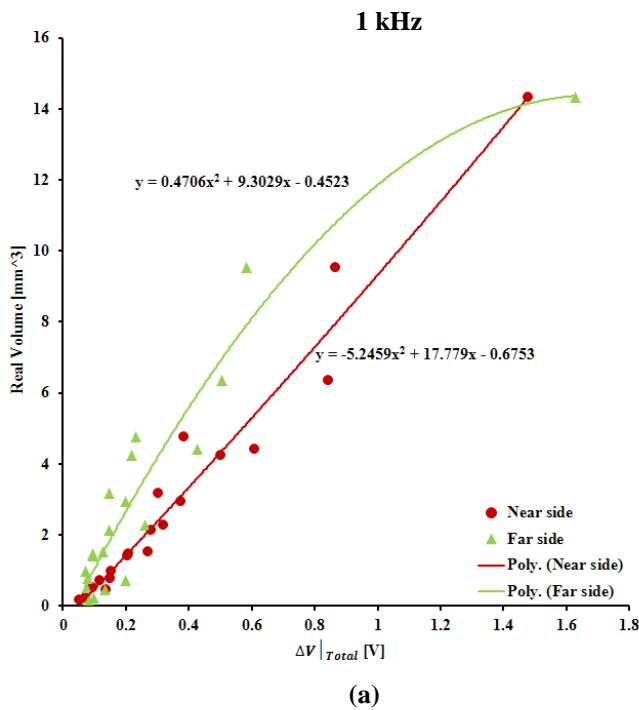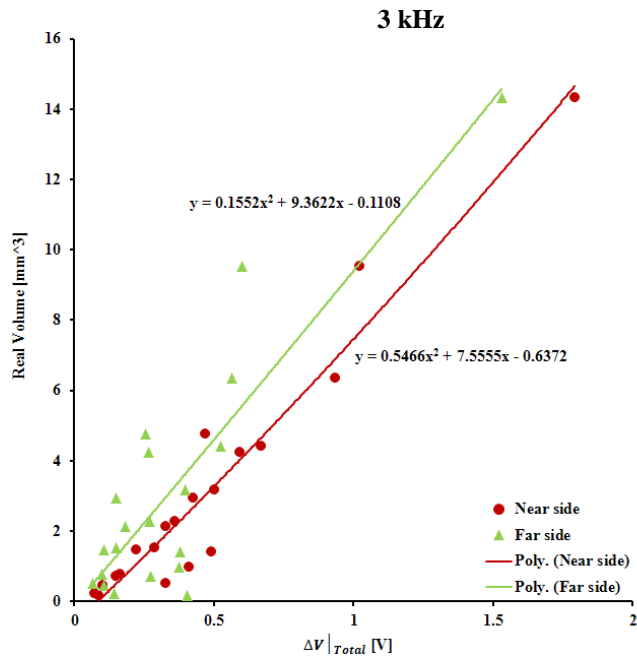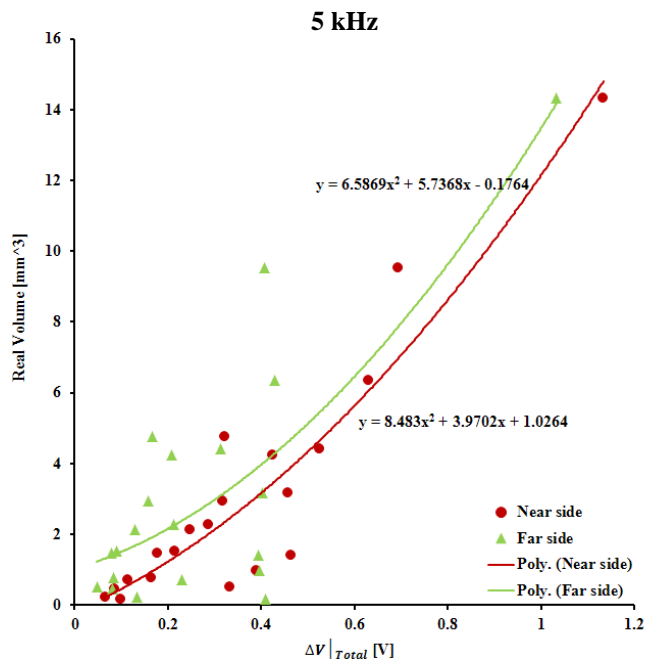
(c)

Figure 3-48 Relationship between integrated of absolute of crack image with crack volume at 1, 3 and 5 kHz for Copper-Nickel specimen

102

Figure 3-49 shows the estimation of crack volume in near-side and far-side scan results at 1, 3 and 5 kHz. The estimation is done following the discrimination results in Figure 3-47. The estimation is better for the small cracks than the big cracks. The standard deviations of estimated crack volume at 1 kHz are 2.1046 mm^3 and 2.6826 mm^3 for near-side and far-side scan, at 3 kHz are 2.0528 mm^3 and 3.4371 mm^3 for near-side and far-side scan, at 5 kHz are 2.6536 mm^3 and 6.4554 mm^3 for near-side and far-side scan. The results at 1 kHz provide the best estimation compared with 3 and 5 kHz as it happened in the titanium specimen.
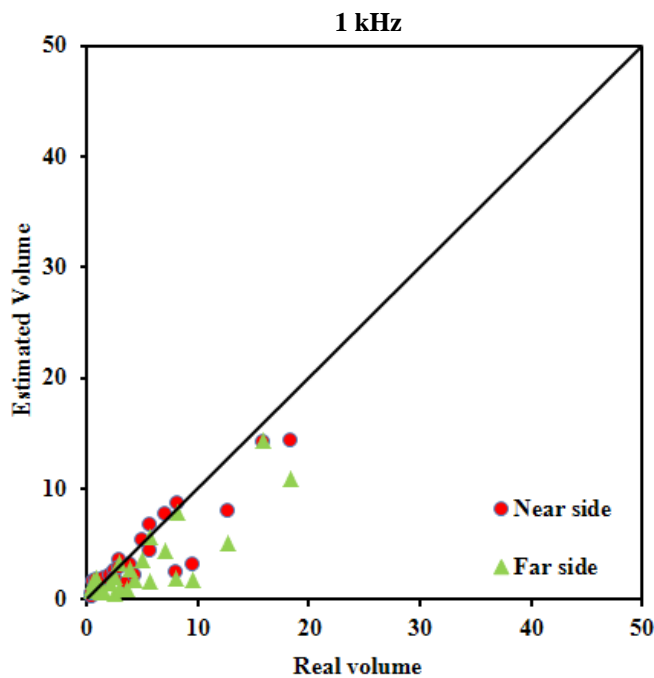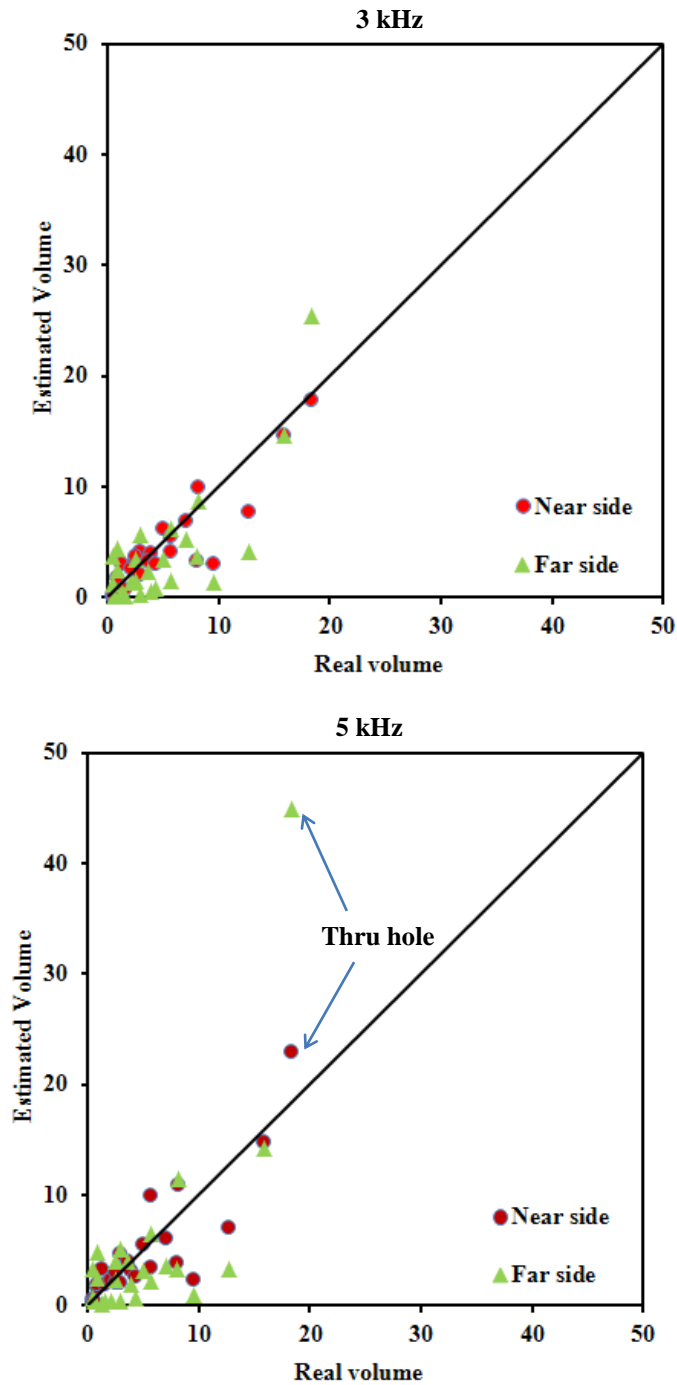
Figure 3-49 Estimation of crack volume in near-side and far-side scan results at 1, 3 and 5 kHz for Copper-Nickel specimen

Inconel600

Discrimination of near-side and far side

The relationship between the integrated of absolute crack image with h^2*w at 1, 3 and 5 kHz is shown in

Figure 3-50. We observed that the distribution of the near-side and far-side cracks were mixed and difficult to be discriminated. However, we still calculate the discrimination probability as done for Titanium and Copper-Nickel specimen. The linear fitting function for near-side and far-side cracks at each frequency is expressed in Eqs. (26-31).

1 kHz	Near side	$y = 14269 \cdot x + 0.051$	(26)
	Far side	$y = 17511 \cdot x + 0.048$	(27)
3 kHz	Near side	$y = 12218 \cdot x + 0.060$	(28)
	Far side	$y = 14149 \cdot x + 0.048$	(29)
5 kHz	Near side	$y = 9883 \cdot x + 0.083$	(30)
	Far side	$y = 12286 \cdot x + 0.064$	(31)

(a)

3 kHz

$y = 14149x + 0.0486$

$y = 12218x + 0.0606$

(b)

5 kHz

$y = 12286x + 0.0642$

$y = 9883x + 0.0835$

(c)
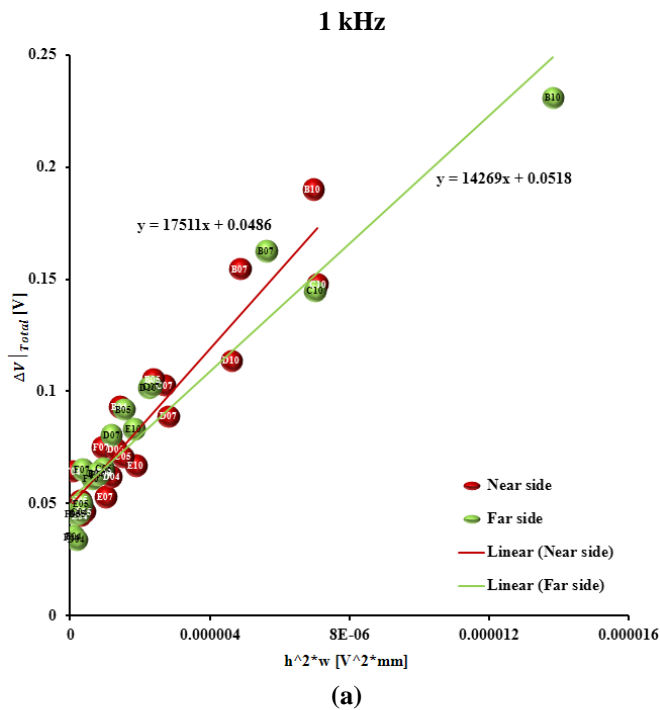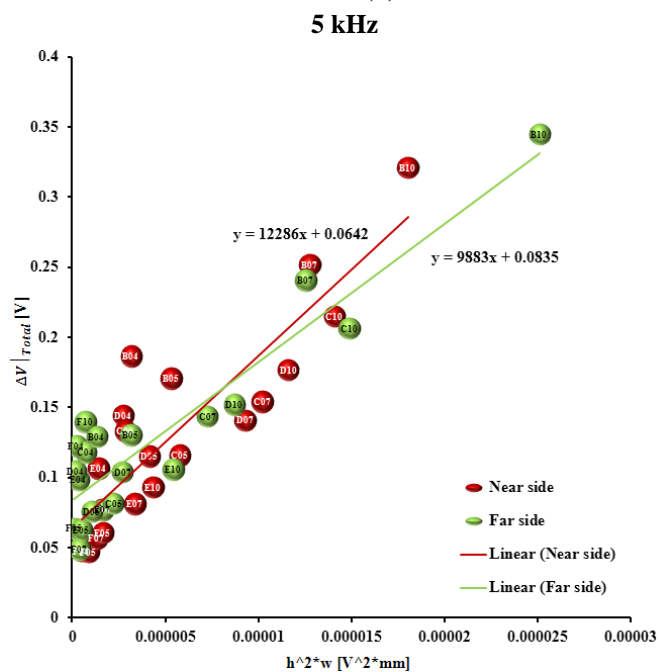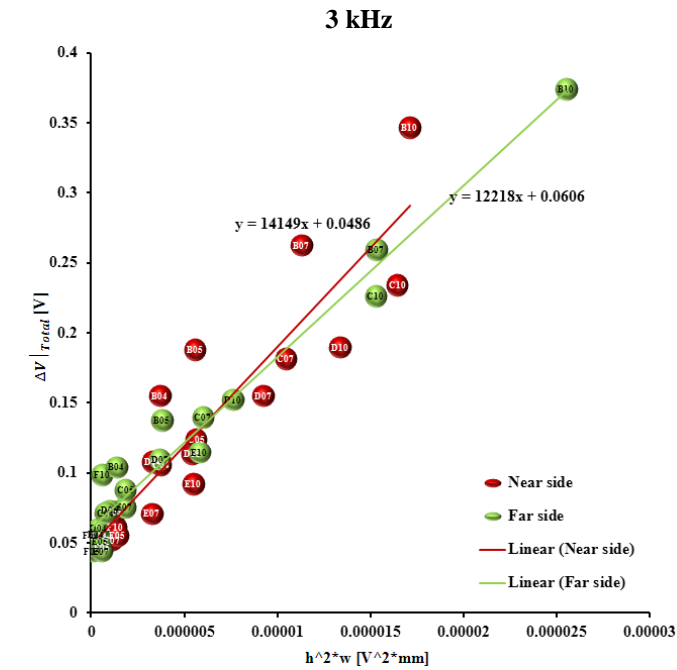
Figure 3-50 Relationship between integrated of absolute of crack image with h^2*w at 1, 3 and 5 kHz for Inconel specimen

106

Discrimination Results

Figure 3-51shows the discrimination probability result using Eq. (13) of the near-side and far-side crack at 1, 3 and 5 kHz for Inconel specimen. All the discrimination results were not good. At 1 kHz, only 10/25 cracks in near-side and 9/25 cracks in far-side scan were correctly discriminated. At 3 kHz, 13/25 cracks in near-side and 14/25 cracks in far-side scan were correctly discriminated. At 5 kHz, 12/25 cracks in near-side and 13/25 cracks in far-side scan were correctly discriminated.

1 kHz

(a)

3 kHz

Near side

Far side

(b)
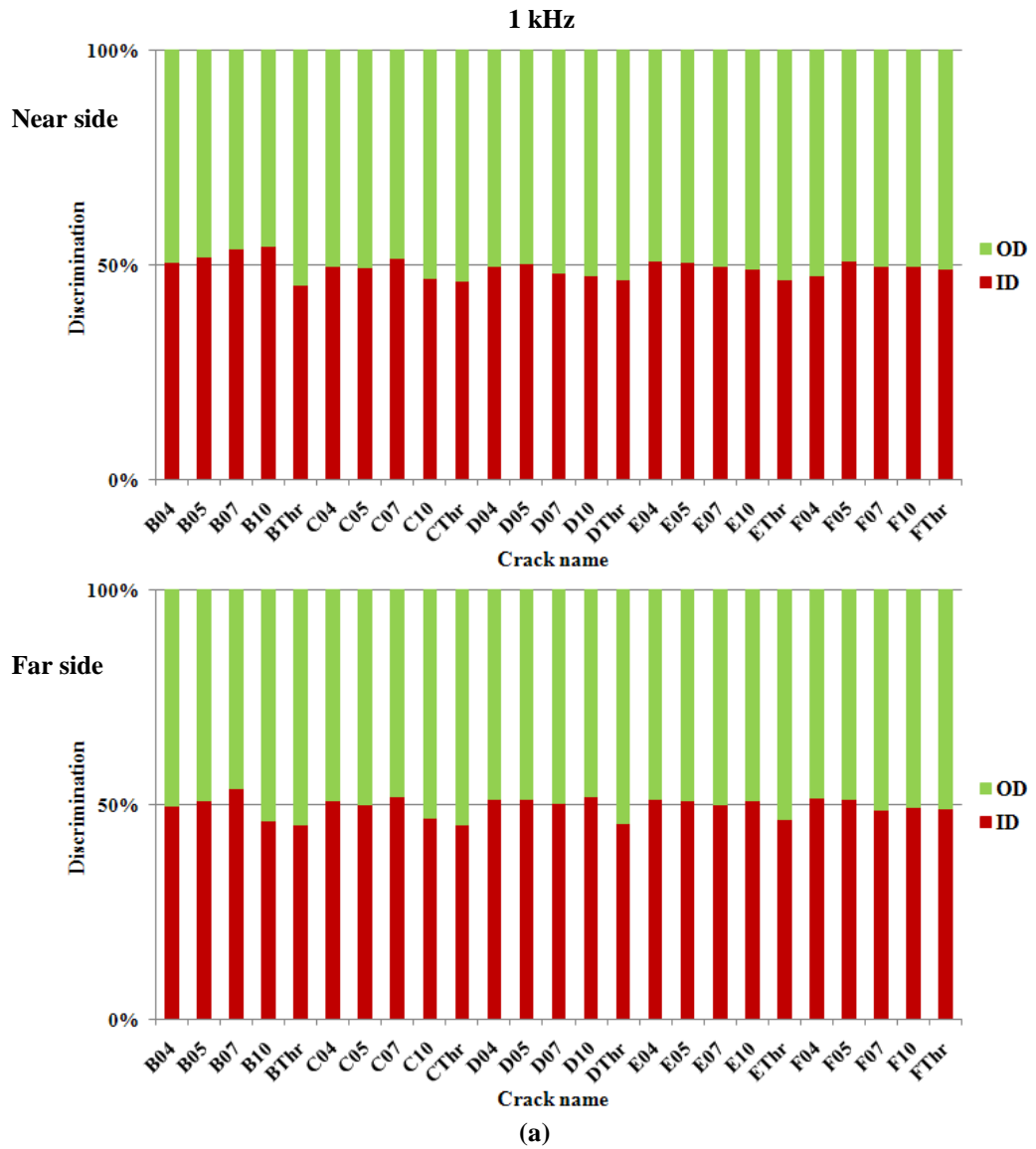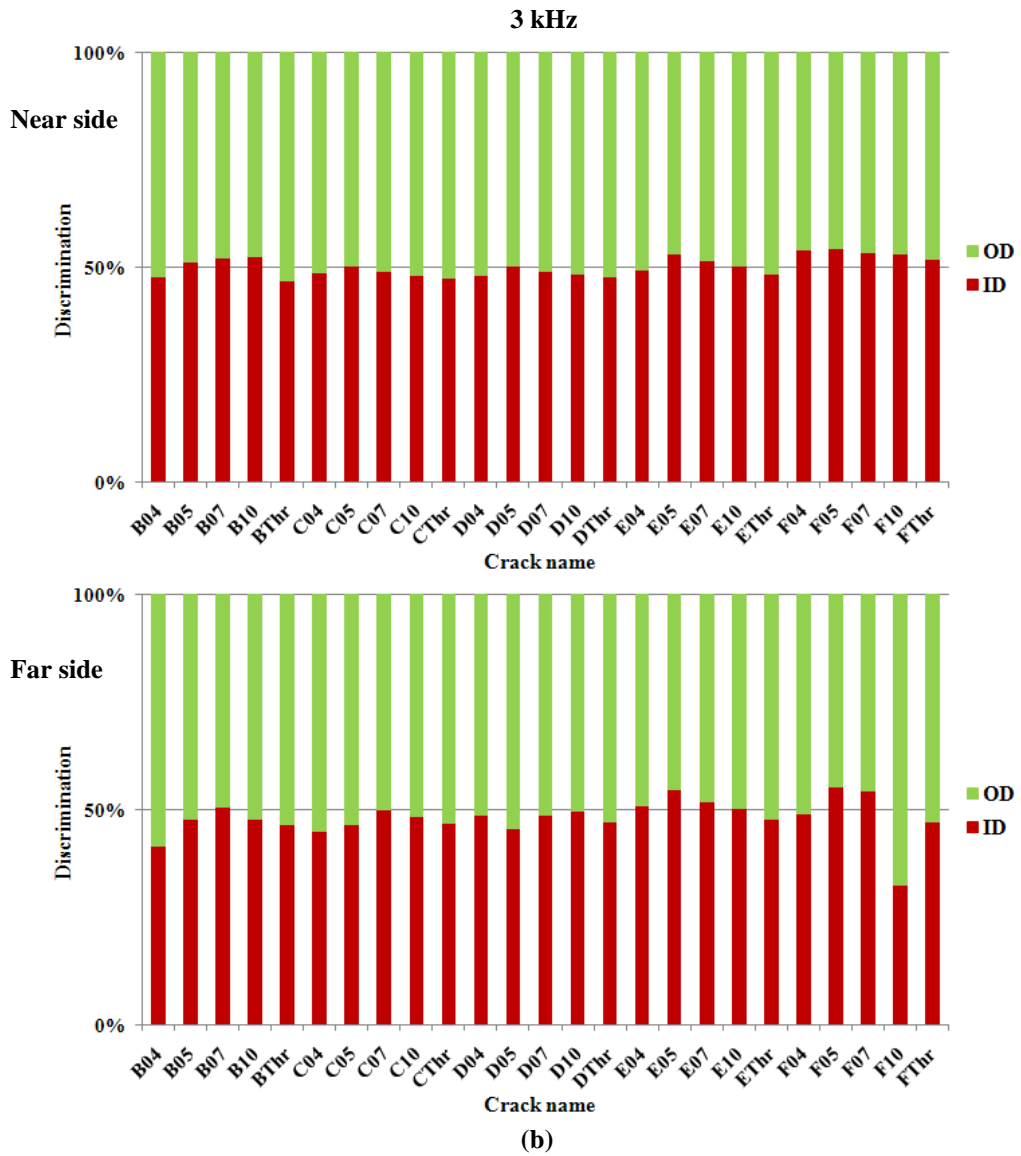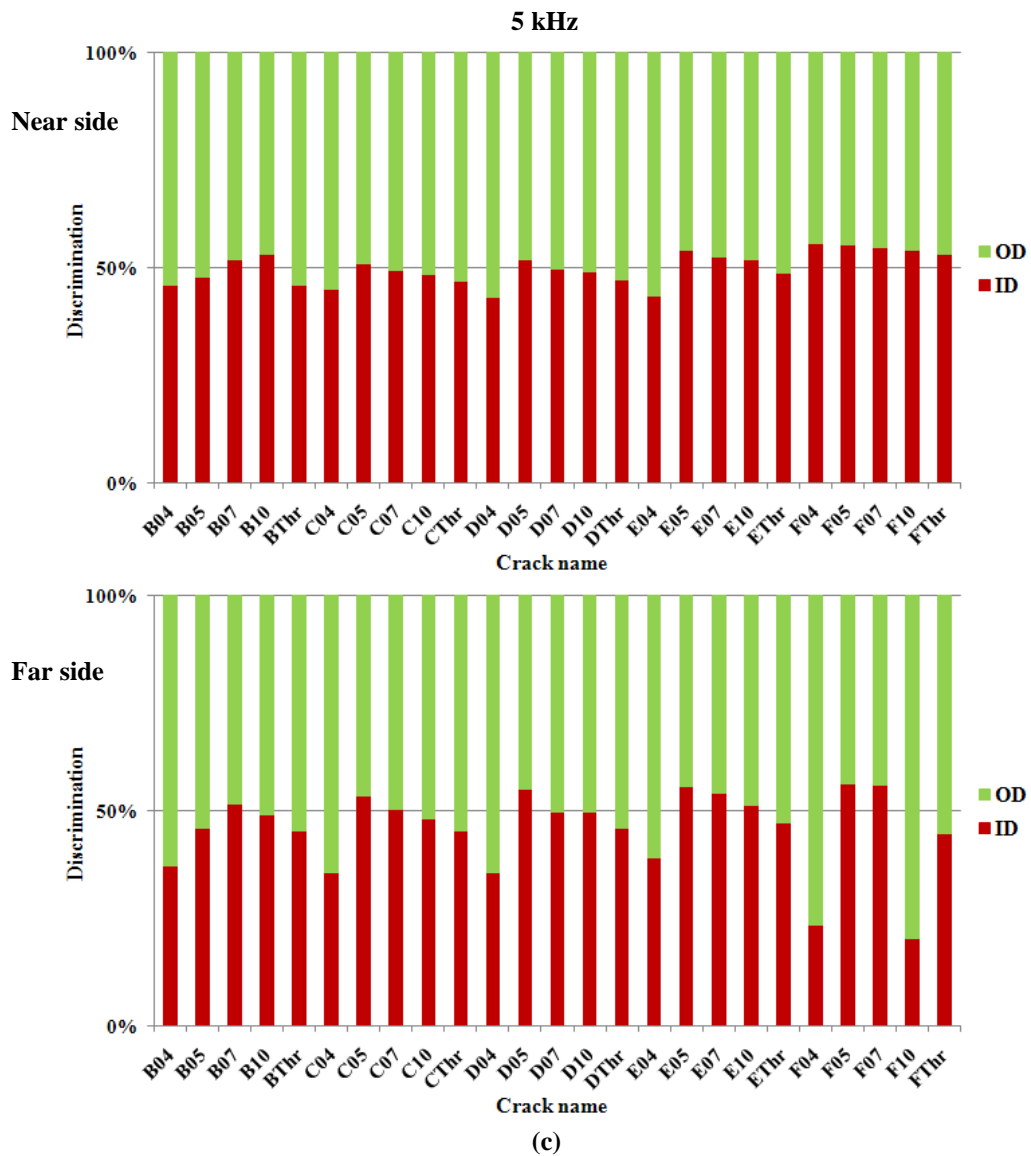
Figure 3-51 Discrimination results of near-side and far-side cracks at 1, 3 and 5 kHz for Inconel specimen

Estimation of Crack Volume

Once the near-side and far-side cracks are discriminated, the quantitative evaluation of crack size is necessary. Establish the relationship between crack volume with the integrated of absolute data for 1, 3 and 5 kHz, as shown in Figure 3-52. We observe that the distribution of

110

near-side and far-side data is mixed. However, we still approximate the fitting curve by quadric function for each type of crack at each frequency. The quadric functions are expressed in the Eqs. (32-37). Thus, if crack type is identified and the integrated of absolute data is obtained from crack image, the crack volume can be estimated by the equivalent equation.

1 kHz	Near side	$Vol = 97.28 \cdot \Delta V|_{total}^{ID}{}^{2} + 50.71 \cdot \Delta V|_{total}^{ID} - 0.882$	(32)
	Far side	$Vol = 311.4 \cdot \Delta V|_{total}^{OD}{}^{2} + 26.68 \cdot \Delta V|_{total}^{OD} - 1.060$	(33)
3 kHz	Near side	$Vol = -0.161 \cdot \Delta V|_{total}^{ID}{}^{2} + 45.27 \cdot \Delta V|_{total}^{ID} - 1.229$	(34)
	Far side	$Vol = 75.42 \cdot \Delta V|_{total}^{OD}{}^{2} + 21.42 \cdot \Delta V|_{total}^{OD} - 0.617$	(35)
5 kHz	Near side	$Vol = 54.00 \cdot \Delta V|_{total}^{ID}{}^{2} + 31.73 \cdot \Delta V|_{total}^{ID} - 1.115$	(36)
	Far side	$Vol = 119.6 \cdot \Delta V|_{total}^{OD}{}^{2} + 13.47 \cdot \Delta V|_{total}^{OD} - 0.517$	(37)

(a)

111

3 kHz

$y = 75.429x^2 + 21.42x - 0.6178$

$y = -0.1612x^2 + 45.279x - 1.2298$

- Near side
- Far side
- Poly. (Near side)
- Poly. (Far side)

$\Delta V\big|_{Total}$ [V]

Real Volume [mm^3]

(b)

5 kHz

$y = 119.6x^2 + 13.475x - 0.5179$

$y = 54.009x^2 + 31.738x - 1.1159$

- Near side
- Far side
- Poly. (Near side)
- Poly. (Far side)

$\Delta V\big|_{Total}$ [V]

Real Volume [mm^3]
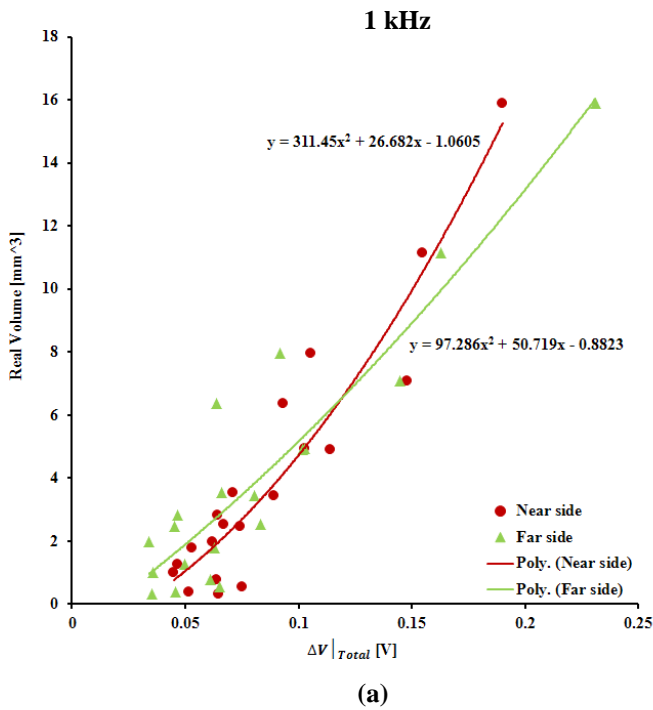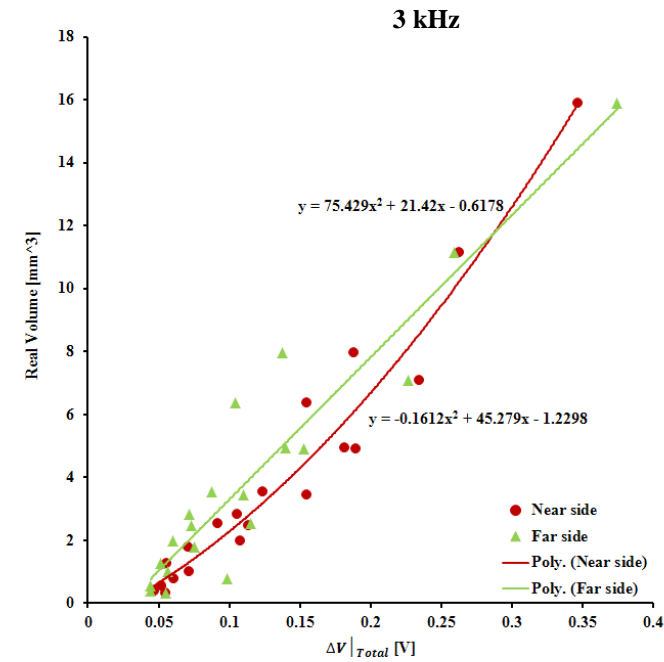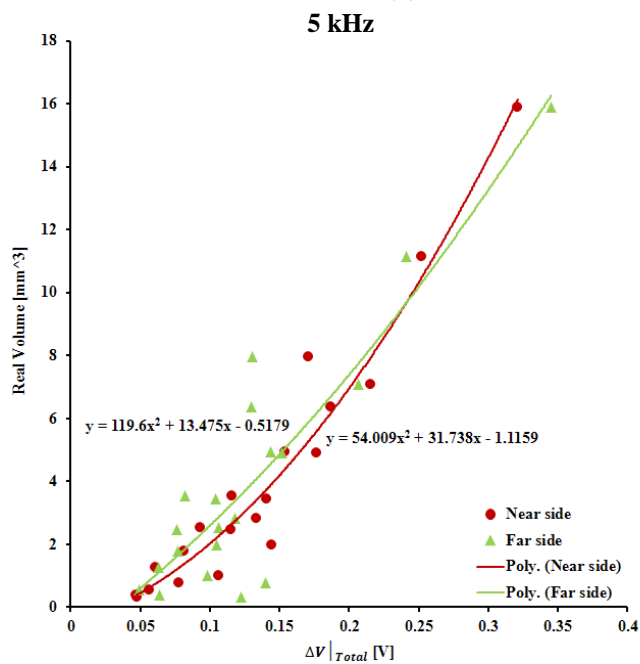
(c)

Figure 3-52 Relationship between integrated of absolute of crack image with crack volume at 1, 3 and 5 kHz for Inconel specimen

Figure 3-53 shows the estimation of crack volume in near-side and far-side scan results at 1, 3 and 5 kHz for Inconel specimen. The estimation is done following the discrimination results in Figure **3-51**. The estimation is better for the small cracks than the big cracks. The standard deviations of estimated crack volume at 1 kHz are 2.2543 mm^3 and 7.5460 mm^3 for near-side and far-side scan, at 3 kHz are 1.8167 mm^3 and 4.4433 mm^3 for near-side and far-side scan, at 5 kHz are 2.4036 mm^3 and 7.mm^3 for near-side and far-side scan. The results estimation of crack volume for Inconel specimen is better than that in the Copper-Nickel specimen. Because, the integrated of absolute data increase with the increase of the crack volume and the data of near-side and far-side was mixed. Thus, the discrimination results are not good but it is still good in evaluation of crack volume.
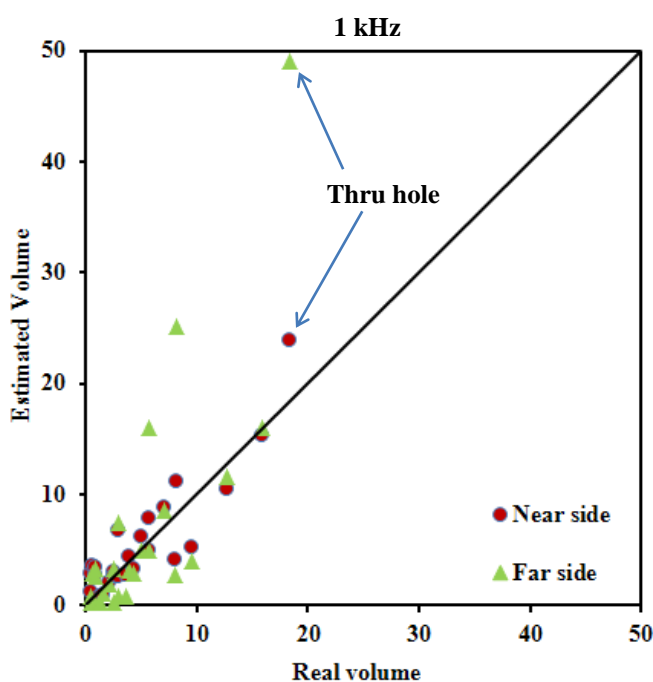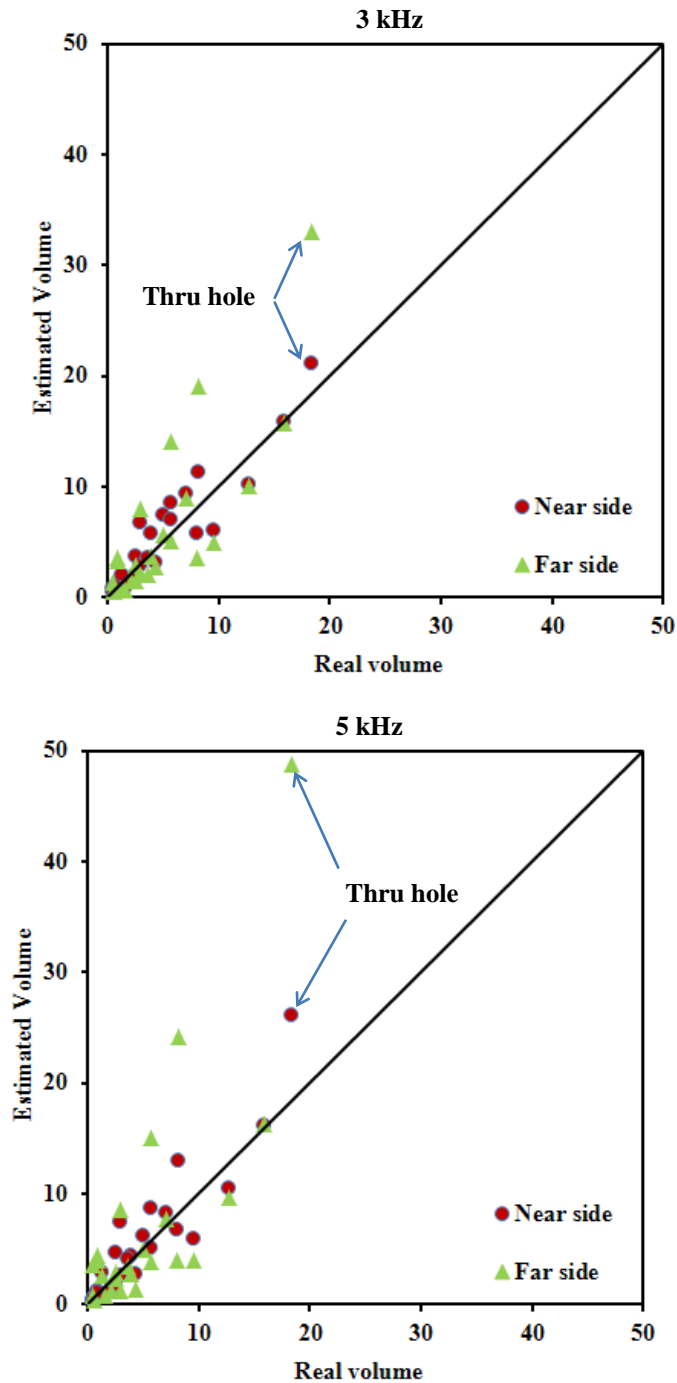
Figure 3-53 Estimation of crack volume in near-side and far-side scan results at 1, 3 and 5 kHz for Inconel specimen

114

Stainless-Steel

Discrimination of near-side and far-side crack

The relationship between the integrated of absolute crack image with $h^2 * w$ at 1, 3 and 5 kHz is shown in Figure 3-54. We observed that the distribution of the near-side and far-side cracks were not clearly and difficult to be discriminated. However, we still calculate the discrimination probability as done for Titanium, Copper-Nickel, and Inconel specimen. The linear fitting function for near-side and far-side cracks at each frequency is expressed in Eqs. (38-43).

1 kHz	Near side	$y = 5677 \cdot x + 0.065$	(38)
	Far side	$y = 7008 \cdot x + 0.059$	(39)
3 kHz	Near side	$y = 5277 \cdot x + 0.085$	(40)
	Far side	$y = 7238 \cdot x + 0.077$	(41)
5 kHz	Near side	$y = 5715 \cdot x + 0.102$	(42)
	Far side	$y = 7781 \cdot x + 0.106$	(43)

(a)

3 kHz

$y = 7238x + 0.0776$

$y = 5277x + 0.0854$

(b)

5 kHz

$y = 5715.7x + 0.102$

$y = 7781.1x + 0.1063$

(c)
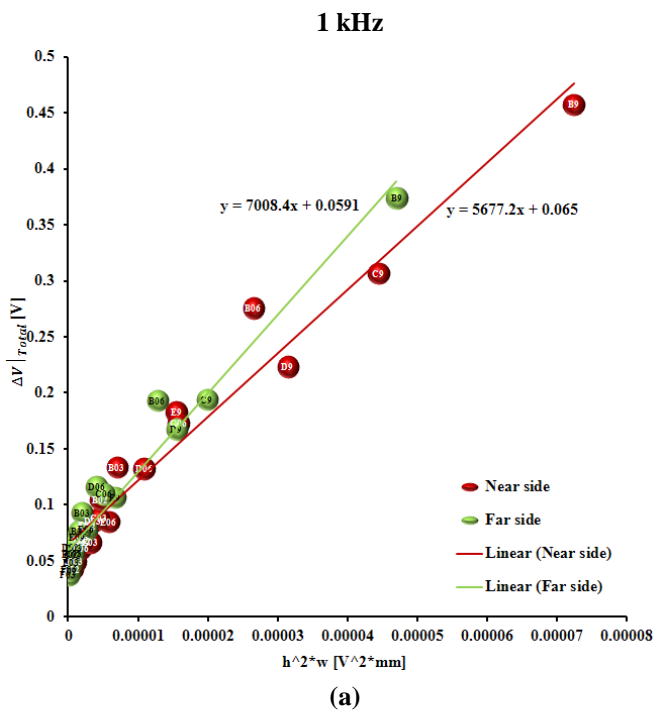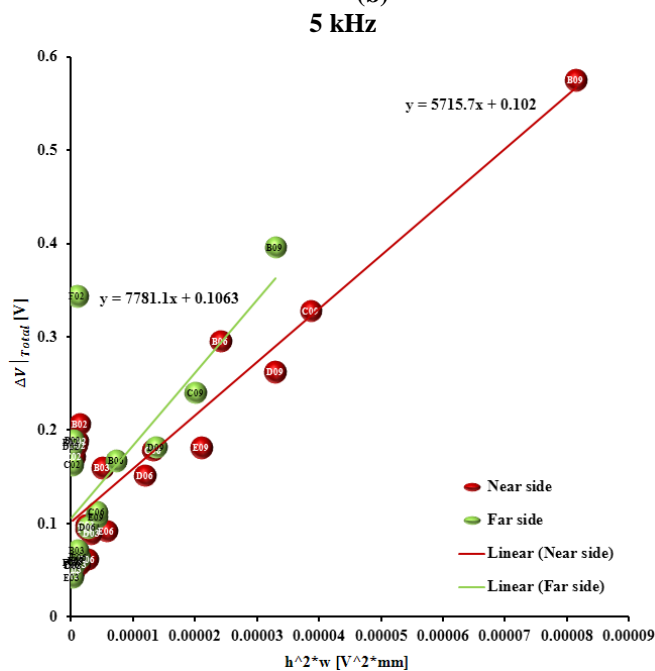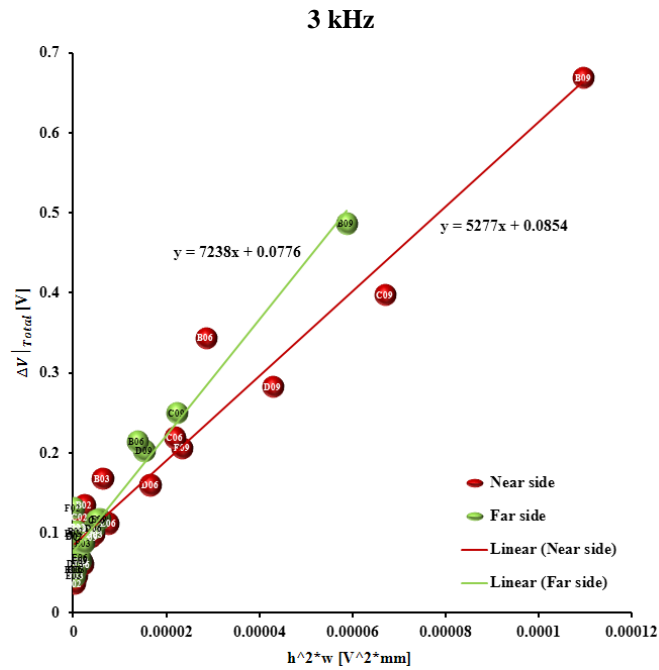
Figure 3-54 Relationship between integrated of absolute of crack image with h^2*w at 1, 3 and 5 kHz for Stainless-Steel specimen

116

Discrimination Results

Figure 3-55 shows the discrimination probability result using Eq. (13) of the near-side and far-side crack at 1, 3 and 5 kHz for stainless steel specimen. All the discrimination results were not good. At 1 kHz, only 12/25 cracks in near-side and 16/25 cracks in far-side scan were correctly discriminated. At 3 kHz, 16/25 cracks in near-side and 14/25 cracks in far-side scan were correctly discriminated. At 5 kHz, 19/25 cracks in near-side and 10/25 cracks in far-side scan were correctly discriminated.

1 kHz

Near side

Far side

(a)

118

3 kHz

Near side

Far side

(b)

119
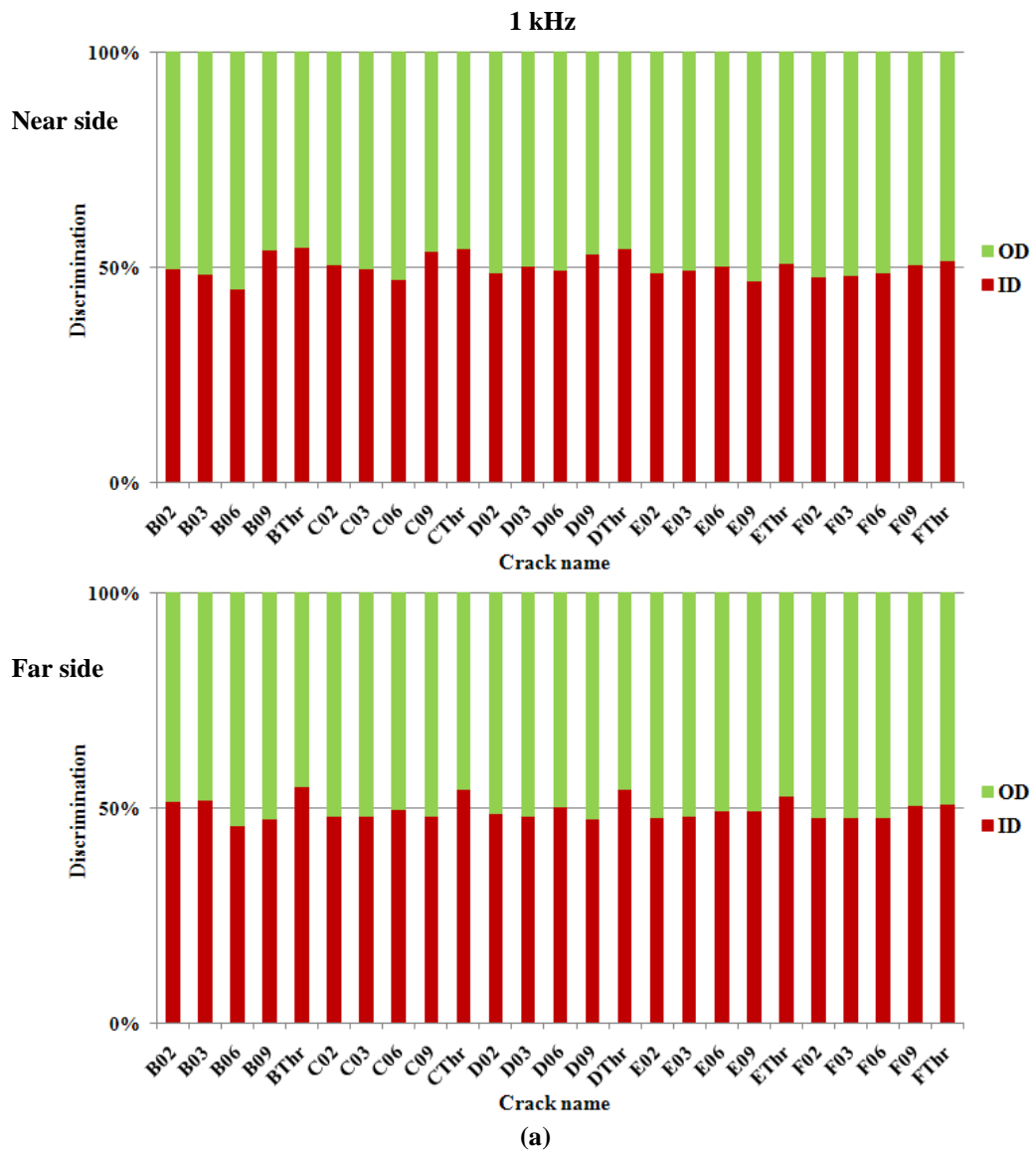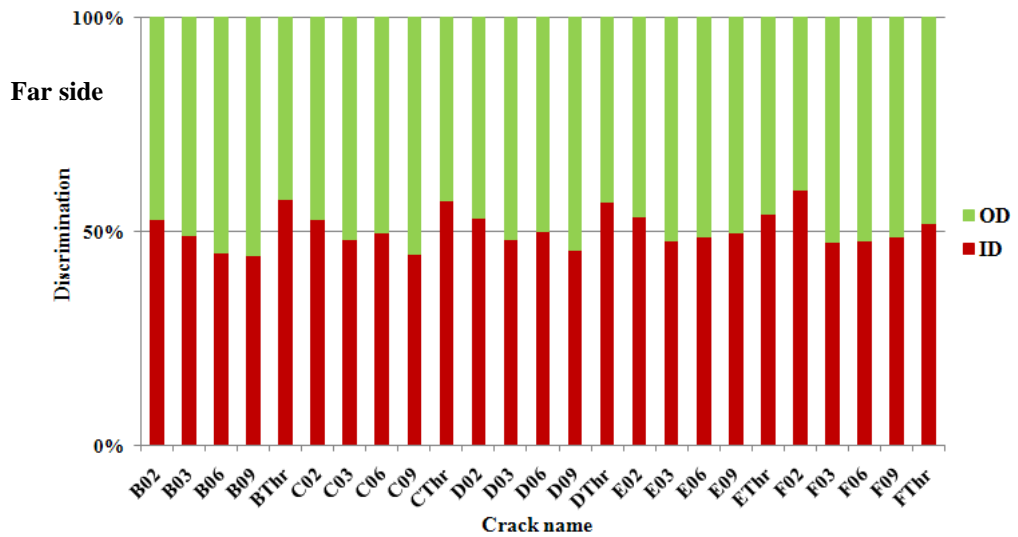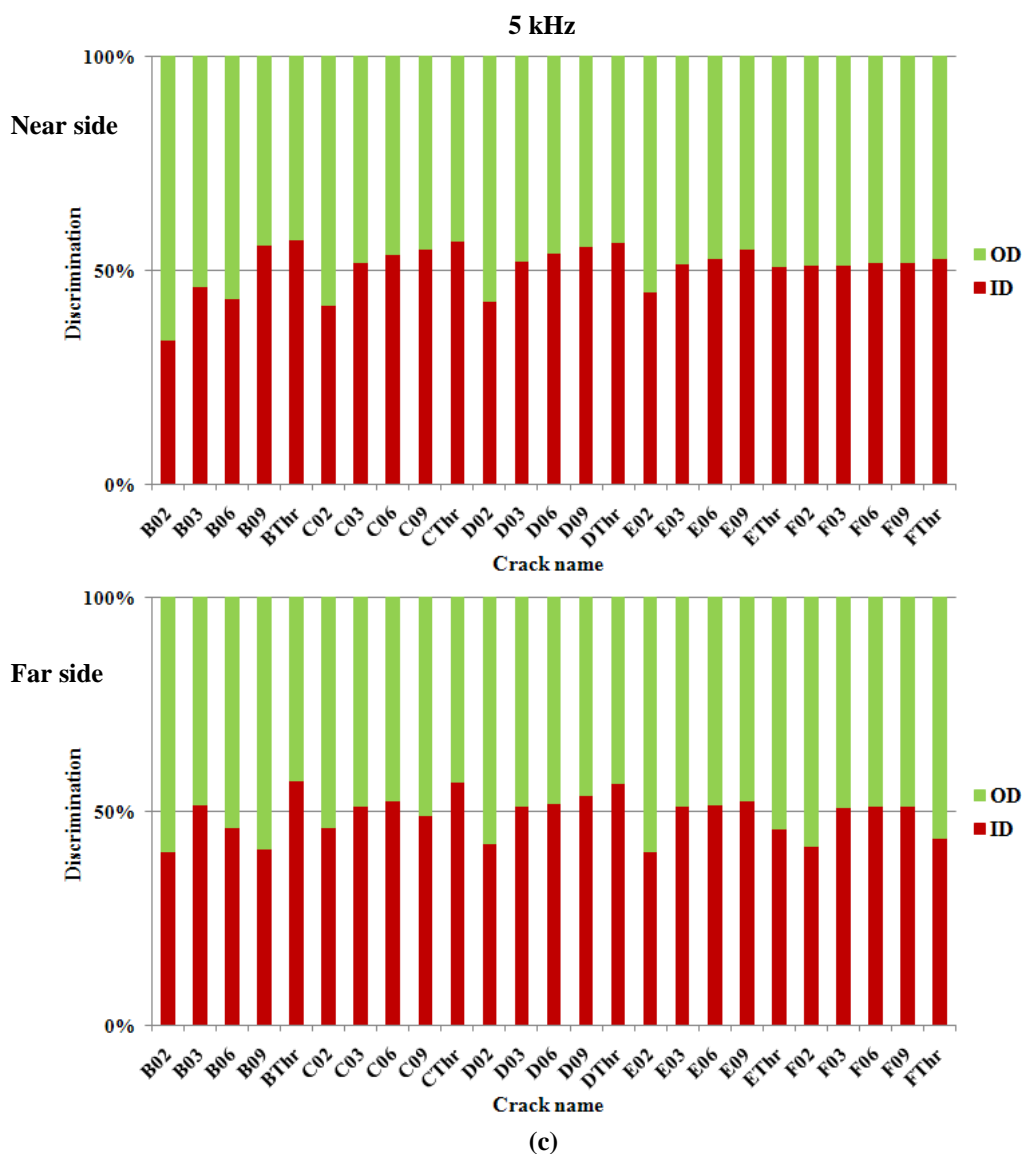
Figure 3-55 Discrimination results of near-side and far-side cracks at 1, 3 and 5 kHz for Stainless-Steel specimen

Establish the relationship between crack volume with the integrated of absolute data for 1, 3 and 5 kHz, as shown in Figure 3-56. We observe that the distribution of near-side and far-side data is not clearly. However, we still approximate the fitting curve by quadric function for each type of crack at each frequency. The quadric functions are expressed in the Eqs. (44-

49). Thus, if crack type is identified and the integrated of absolute data is obtained from crack image, the crack volume can be estimated by the equivalent equation.

1 kHz	Near side	$Vol = 19.81 \cdot \Delta V|_{total}^{ID}{}^2 + 23.01 \cdot \Delta V|_{total}^{ID} - 0.652$	(44)
	Far side	$Vol = -13.44 \cdot \Delta V|_{total}^{OD}{}^2 + 47.47 \cdot \Delta V|_{total}^{OD} - 1.497$	(45)
3 kHz	Near side	$Vol = 0.211 \cdot \Delta V|_{total}^{ID}{}^2 + 22.35 \cdot \Delta V|_{total}^{ID} - 0.839$	(46)
	Far side	$Vol = -1.928 \cdot \Delta V|_{total}^{OD}{}^2 + 32.43 \cdot \Delta V|_{total}^{OD} - 0.905$	(47)
5 kHz	Near side	$Vol = 15.96 \cdot \Delta V|_{total}^{ID}{}^2 + 17.23 \cdot \Delta V|_{total}^{ID} - 0.587$	(48)
	Far side	$Vol = 46.60 \cdot \Delta V|_{total}^{OD}{}^2 + 0.612 \cdot \Delta V|_{total}^{OD} + 1.610$	(49)

1 kHz

$y = -13.443x^2 + 47.47x - 1.4978$

$y = 19.813x^2 + 23.011x - 0.6527$

- ● Near side
- ▲ Far side
- — Poly. (Near side)
- — Poly. (Far side)

Real Volume [mm^3]

$\Delta V|_{Total}$ [V]

(a)

121

3 kHz

$y = -1.9286x^2 + 32.431x - 0.9051$

$y = 0.2117x^2 + 22.351x - 0.8397$

- ● Near side
- ▲ Far side
- — Poly. (Near side)
- — Poly. (Far side)

Real Volume [mm^3]

$\Delta V \big|_{Total}$ [V]

(b)

5 kHz

$y = 15.961x^2 + 17.238x - 0.5875$

$y = 48.608x^2 + 0.6128x + 1.6104$

- ● Near side
- ▲ Far side
- — Poly. (Near side)
- — Poly. (Far side)

Real Volume [mm^3]

$\Delta V \big|_{Total}$ [V]

(c)

Figure 3-56 Relationship between integrated of absolute of crack image with crack volume at 1, 3 and 5 kHz for Inconel specimen

Figure 3-57 shows the estimation of crack volume in near-side and far-side scan results at 1, 3 and 5 kHz for stainless-steel specimen. The estimation is done following the discrimination results in Figure 3-55. The estimation is better for the small cracks than the big cracks. The standard deviations of estimated crack volume at 1 kHz are 5.2564 mm^3 and 4.2694 mm^3 for near-side and far-side scan, at 3 kHz are 3.0899 mm^3 and 3.5263 mm^3 for near-side and far-side scan, at 5 kHz are 4.7579 mm^3 and 5.4742 mm^3 for near-side and far-side scan. The results estimation of crack volume for Stainless-Steel is better than that in the Copper-Nickel, and Inconel specimen. Because, the integrated of absolute data increase with the increase of the crack volume and the data of near-side and far-side was mixed. Thus, the discrimination results are not good but it is still good in evaluation of crack volume.
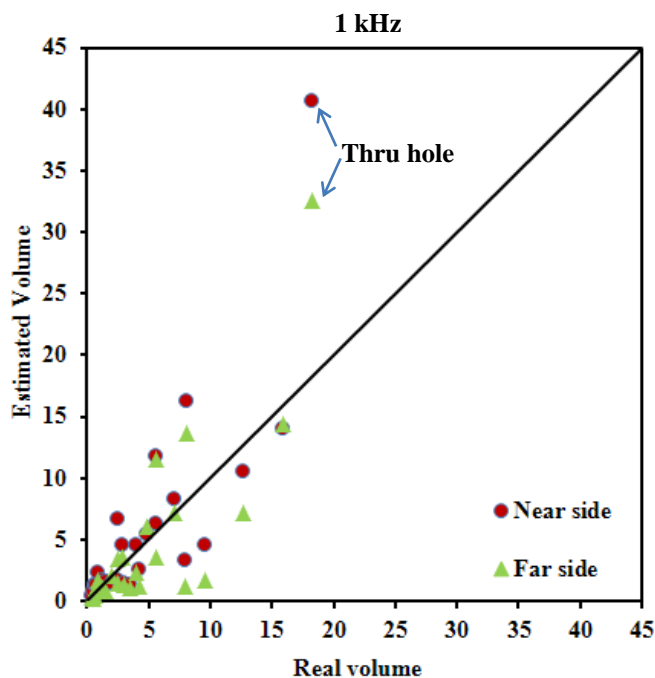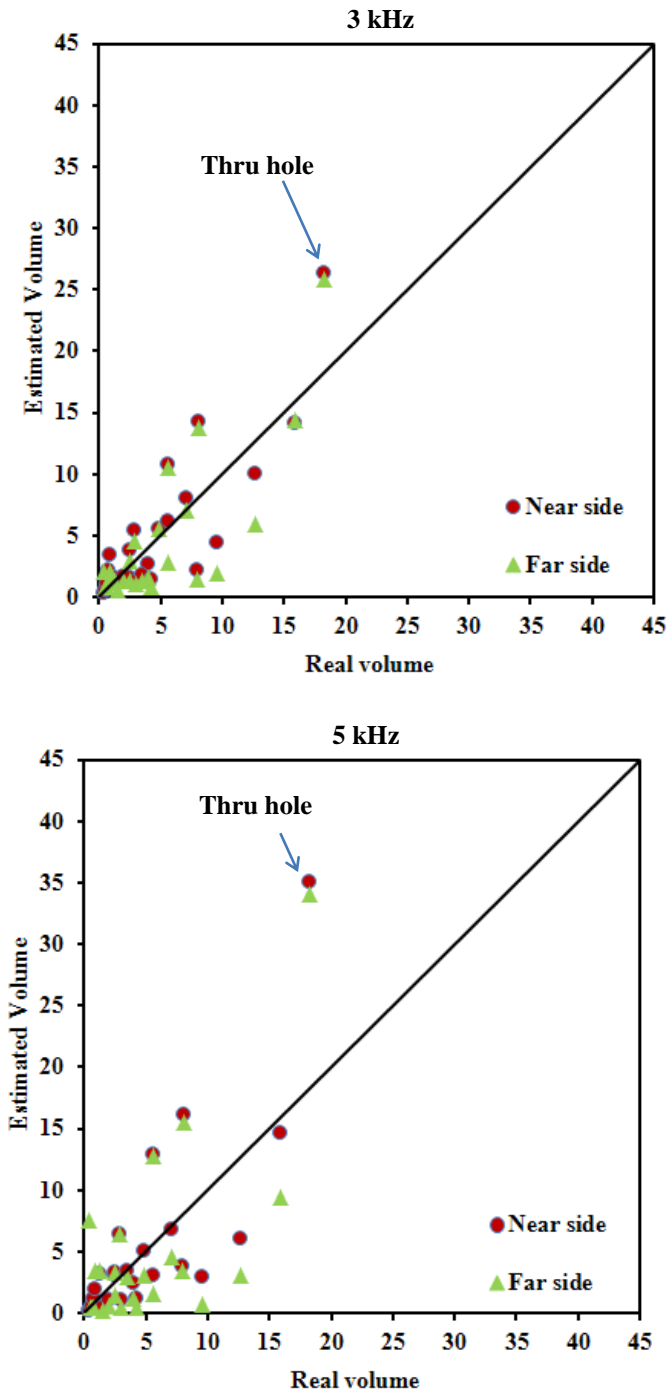
Figure 3-57 Estimation of crack volume in near-side and far-side scan results at 1, 3 and 5 kHz for Inconel specimen

124

3.5.4 The relationship between Integrated Absolute Data and $\sum(01)/h^2$

Titanium

Discrimination of near-side and far-side crack

Figure 3-58 shows the relationship between the integrated of absolute data with the $\sum(01)/h^2$ at 1, 3 and 5 kHz with the cut-off 1. It shows a good separation between the data of near-side and far-side crack for the three frequencies. The near-side crack data concentrate on the left-hand side of the graph which closes to the Y-axis. The far-side crack data distribute more widely in the right-hand side. The two group data mix at the deep depth of the crack. For instance, the data of through crack in the far-side scanning mixes in the group of near-side crack data, because the through cracks are actually can be considered as near-side crack. In the both near- and far-side data, the data of larger diameter crack distributes in the higher position in the Y-axis which is higher value of integrated absolute data. The near-side data distributes the most concentrate at 1 kHz and the worst concentrate at 5 kHz.

The distribution of data in cut-off 2, 3, and 4 has similar behaviors as data in the cut-off 1. However, the distribution becomes wider as increase of cut-off value. The widest distribution of data is at cut-off 4.

Cut-off 1   **1 kHz**

(a)

Cut-off 1   **3 kHz**

(b)

126
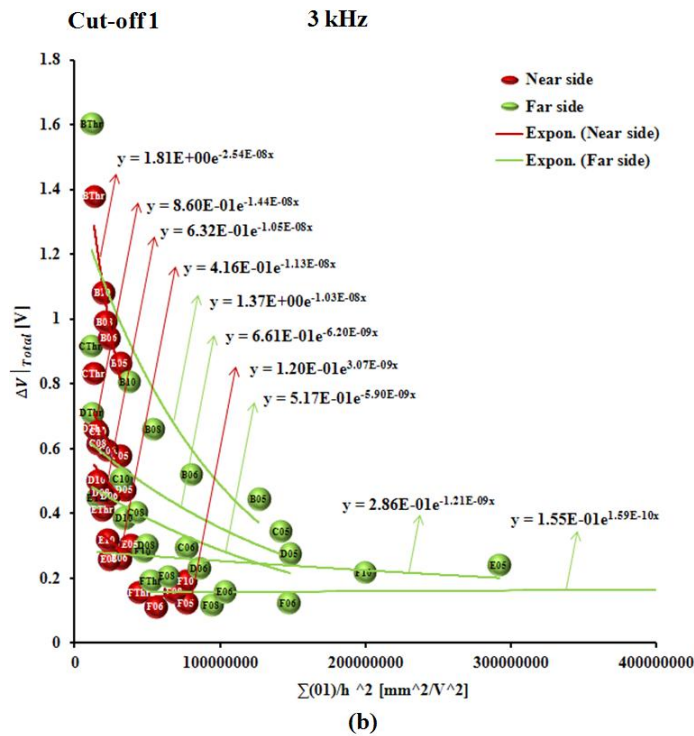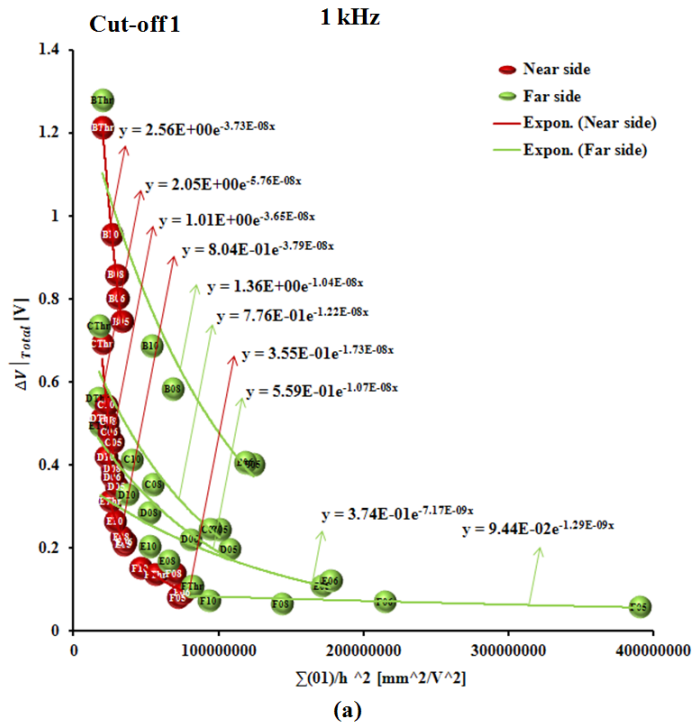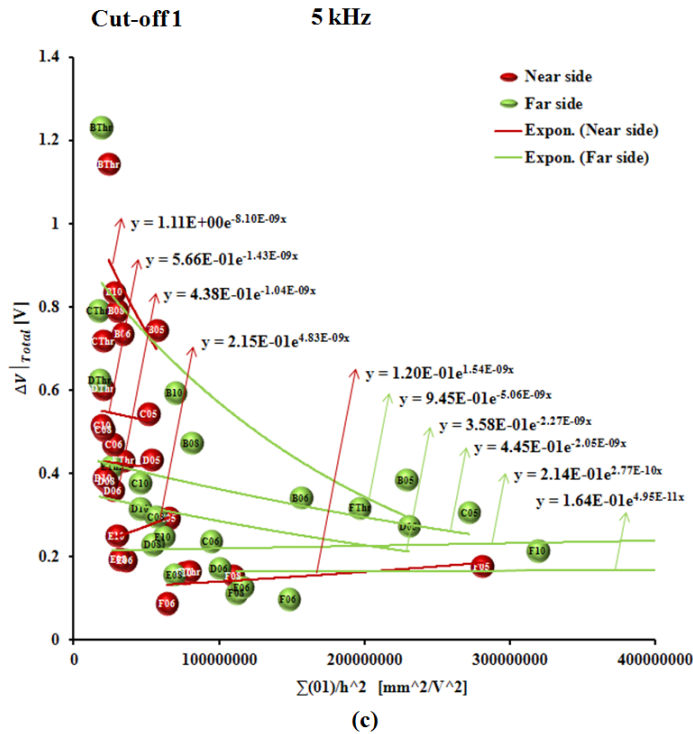
Figure 3-58 Relationship between integrated of absolute of crack image with h^2*w at (a) 1 kHz, (b) 3 kHz, and (c) 5 kHz for cut-off 1.

(a)

(b)
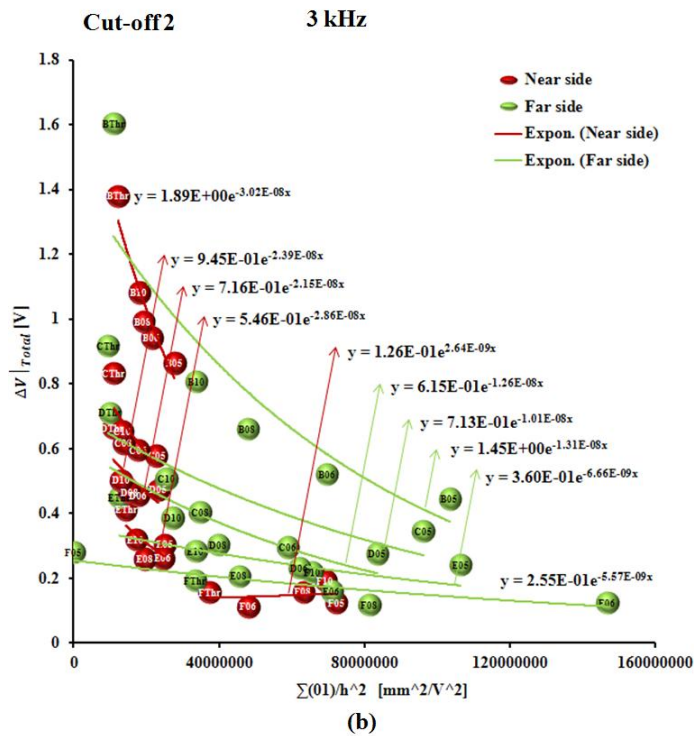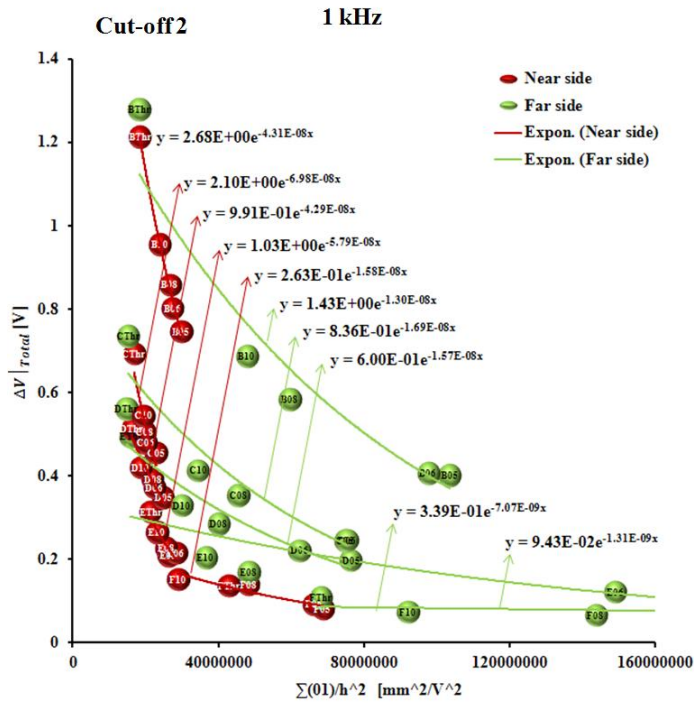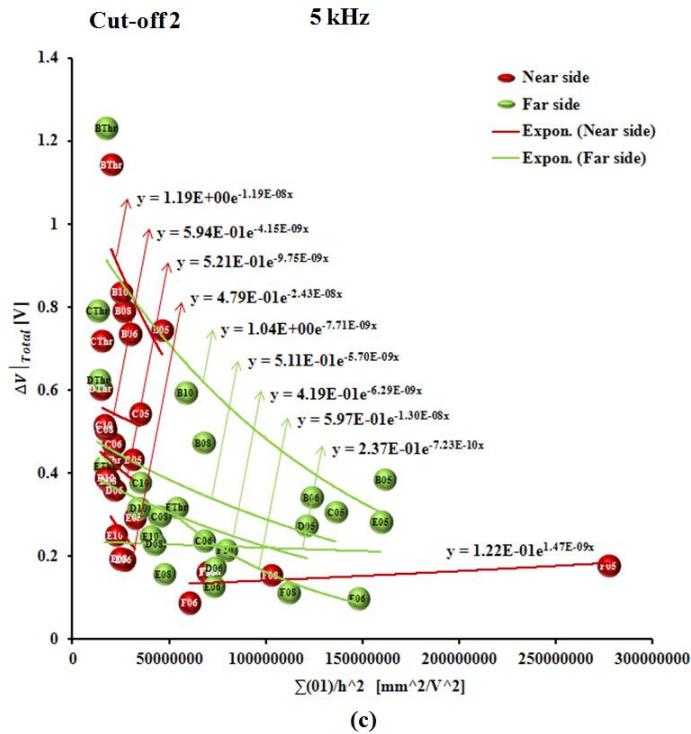
Figure 3-59 Relationship between integrated of absolute of crack image with h^2*w at (a) 1 kHz, (b) 3 kHz, and (c) 5 kHz for cut-off 2.

(a)

(b)

130
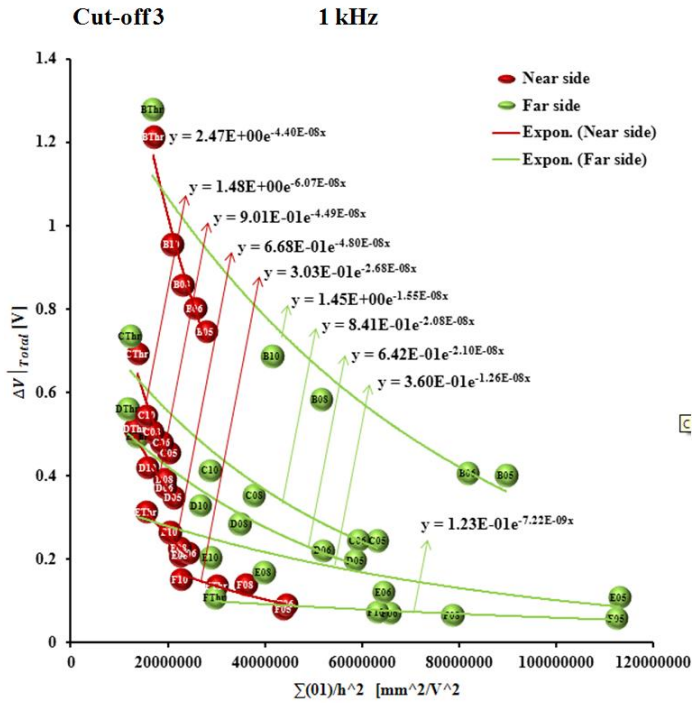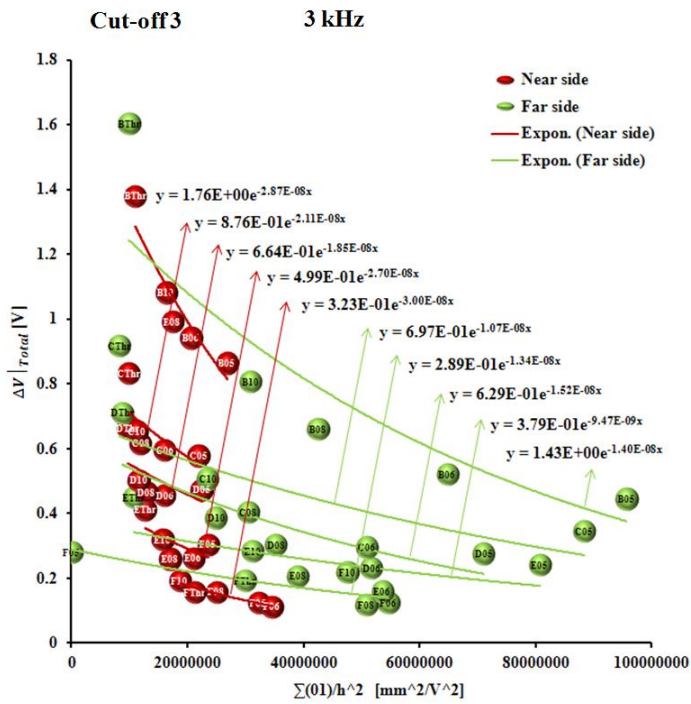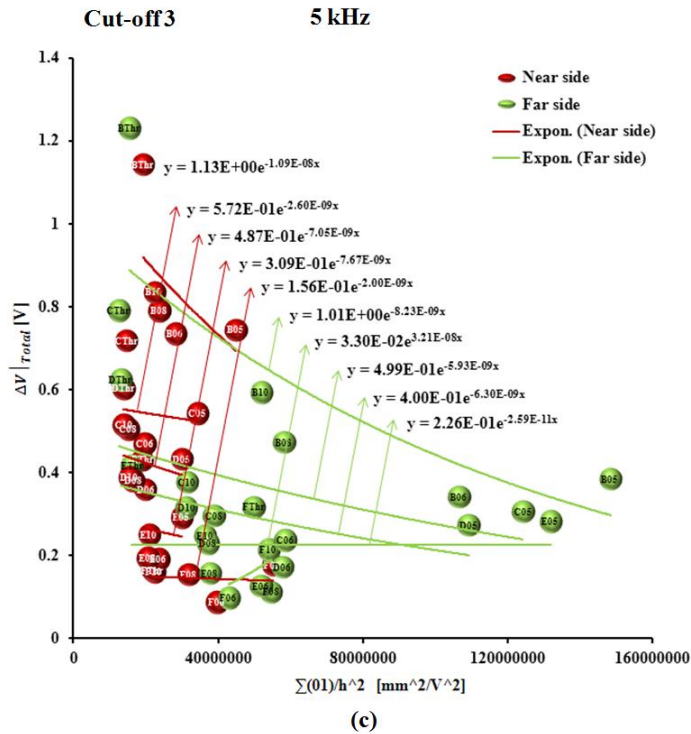
Figure 3-60 Relationship between integrated of absolute of crack image with h^2*w at (a) 1 kHz, (b) 3 kHz, and (c) 5 kHz for cut-off 3.

$y = 2.61\text{E+00}e^{-5.10\text{E-08}x}$

$y = 1.35\text{E+00}e^{-6.36\text{E-08}x}$

$y = 1.02\text{E+00}e^{-6.10\text{E-08}x}$

$y = 7.70\text{E-01}e^{-6.91\text{E-08}x}$

$y = 2.30\text{E-01}e^{-2.17\text{E-08}x}$

$y = 1.49\text{E+00}e^{-1.86\text{E-08}x}$

$y = 9.01\text{E-01}e^{-2.76\text{E-08}x}$

$y = 6.18\text{E-01}e^{-2.42\text{E-08}x}$

$y = 3.24\text{E-01}e^{-1.14\text{E-08}x}$

$y = 1.23\text{E-01}e^{-7.22\text{E-09}x}$

- Near side
- Far side
- Expon. (Near side)
- Expon. (Far side)

$\Delta V\big|_{Total}$ [V]

$\sum(01)/h^2$ [mm^2/V^2]

(a)

Cut-off 4   **3 kHz**

$y = 1.85\text{E+00}e^{-3.46\text{E-08}x}$

$y = 9.30\text{E-01}e^{-2.99\text{E-08}x}$

$y = 6.99\text{E-01}e^{-2.65\text{E-08}x}$

$y = 5.65\text{E-01}e^{-4.22\text{E-08}x}$

$y = 2.66\text{E-01}e^{-2.39\text{E-08}x}$

$y = 2.86\text{E-01}e^{-1.55\text{E-08}x}$

$y = 4.21\text{E-01}e^{-1.61\text{E-08}x}$

$y = 6.86\text{E-01}e^{-2.31\text{E-08}x}$

$y = 7.58\text{E-01}e^{-1.65\text{E-08}x}$

$y = 1.49\text{E+00}e^{-1.75\text{E-08}x}$

- Near side
- Far side
- Expon. (Near side)
- Expon. (Far side)

$\Delta V\big|_{Total}$ [V]

$\sum(01)/h^2$ [mm^2/V^2]

(b)

Figure 3-61 Relationship between integrated of absolute of crack image with h^2*w at (a) 1 kHz, (b) 3 kHz, and (c) 5 kHz for cut-off 4.

Probability of Near-side (PNS) and Far-side (PFS) Crack

It is necessary to quantitative evaluate the discrimination probability of near-side (PNS) and far-side (PFS) crack using the relationship between the integrated of absolute of crack image with the $\sum(01)/h^2$. The relationship could be estimated as an exponential relationship. Totally, 10 equations was obtained, in which there are 5 equations for 5 same diameter groups in near- side cracks and similarly 5 equations for the far-side cracks. The exponential equations for each group of near-side and far-side cracks at each cut-offs value are expressed in Eqs. (50-89).

The PNS and PFS are calculated by the rate change of integrated of absolute data in the experiment $(\Delta V|_{total}^{exp})$ and linear approximation $(\Delta V|_{total}^{est})$, which is expressed by Eq. (13).

133

Cut-off 1

1 kHz	Near side	B	$y = 1.0612E + 00e^{-1.1197E-08x}$	(50)
		C	$y = 8.1066E - 01e^{-1.8271E-08x}$	(51)
		D	$y = 7.9930E - 01e^{-2.4085E-08x}$	(52)
		E	$y = 1.2672E - 01e^{-2.0268E-09x}$	(53)
		F	$y = 1.9290E - 01e^{-2.1085E-08x}$	(54)
1 kHz	Far side	B	$y = 6.9686E - 01e^{-5.3248E-09x}$	(55)
		C	$y = 3.7711E - 01e^{-5.3505E-09x}$	(56)
		D	$y = 2.3810E - 01e^{-2.7308E-09x}$	(57)
		E	$y = 1.3728E - 01e^{-2.7273E-09x}$	(58)
		F	$y = 9.2438E - 01e^{-2.6147E-09x}$	(59)

Cut-off 2

1 kHz	Near side	B	$y = 2.6821E + 00e^{-4.3120E-08x}$	(60)
		C	$y = 2.1037E + 00e^{-6.9821E-08x}$	(61)
		D	$y = 9.9087E - 01e^{-4.2885E-08x}$	(62)
		E	$y = 1.0329E + 00e^{-5.7867E-08x}$	(63)
		F	$y = 2.6277E - 01e^{-1.5836E-08x}$	(64)
1 kHz	Far side	B	$y = 1.4252E + 00e^{-1.3009E-08x}$	(65)
		C	$y = 8.3558E - 01e^{-1.6890E-08x}$	(66)
		D	$y = 5.9966E - 01e^{-1.5723E-08x}$	(67)
		E	$y = 3.3868E - 01e^{-7.0723E-09x}$	(68)
		F	$y = 9.4288E - 01e^{-1.3092E-09x}$	(69)

Cut-off 3

		B	$y = 2.4682E + 00e^{-4.4049E-08x}$	(70)
		C	$y = 1.4843E + 00e^{-1.0654E-08x}$	(71)
1 kHz	Near side	D	$y = 9.0090E - 01e^{-4.4869E-08x}$	(72)
		E	$y = 6.6781E - 01e^{-4.8000E-08x}$	(73)
		F	$y = 3.0255E - 01e^{-2.2.6797E-08x}$	(74)
		B	$y = 1.4532E + 00e^{-1.5463E-08x}$	(75)
		C	$y = 8.4139E - 01e^{-2.0776E-08x}$	(76)
1 kHz	Far side	D	$y = 6.4201E - 01e^{-2.1003E-08x}$	(77)
		E	$y = 3.5964E - 01e^{-1.2628E-08x}$	(78)
		F	$y = 1.2308E - 01e^{-7.2211E-09x}$	(79)

Cut-off 4

		B	$y = 2.60730E + 00e^{-5.1047E-08x}$	(80)
		C	$y = 1.3459E + 00e^{-6.3581E-08x}$	(81)
1 kHz	Near side	D	$y = 1.0173E + 00e^{-6.1001E-08x}$	(82)
		E	$y = 7.7027E - 01e^{-6.9053E-08x}$	(83)
		F	$y = 2.2973E - 01e^{-2.1675E-08x}$	(84)
		B	$y = 1.4940E + 00e^{-1.8574E-08x}$	(85)
		C	$y = 9.0099E - 01e^{-2.7556E-08x}$	(86)
1 kHz	Far side	D	$y = 6.1780E - 01e^{-2.4234E-08x}$	(87)
		E	$y = 3.2421E - 01e^{-1.1426E-08x}$	(88)
		F	$y = 1.2308E - 01e^{-7.2211E-09x}$	(89)

Where y is integrated absolute data $\Delta V|_{total}$, and x is $\sum(01)/h^2$

Figure 3-62~Figure 3-65 show the discrimination probability result of the near-side and far-side crack at 1 kHz at cut-off 1~ 4, respectively. At each cut-off value, two graphs of results were plotted equivalent to the near-side scan and far-side scan data in the experiment. A

135

crack in near-side scan is near-side crack; inversely, a crack in far-side scan is far-side crack. In the graph, the probability of near- and far-side crack were plotted in radar plots with 5 peaks respect to 5 groups of diameter B, C, D, E, and F. There are 5 data points for near-side crack and 5 data points for far-side crack in each radar plot. The data point which has highest value indicates the crack belongs to the equivalent group of diameter and near/far-side crack. Thus, the algorithm could estimate the diameter of crack and its near/far-side location.

At cut-off 1, entire the cracks were correctly discriminated in the near-side scanning except cracks F05, F08, F10, and D10. The correct discrimination is 22/25 cracks. In the far-side scanning, 21/25 cracks were correct discriminated. The through-type cracks were considered as the near-side cracks. Cracks having the smallest diameter of 1 mm were wrong discriminated because of weak signal. Several deep cracks were wrong discriminated because they are close a near-side crack leading difficulty of discrimination.

At cut-off 2, in the near-side scan 13/25 cracks were correct discriminated. In the far-side scan, 23/25 cracks were correct discriminated. At cut-off 3, in the near-side scan 9/25 cracks were correct discriminated. In the far-side scan, 24/25 cracks were correct discriminated. At cut-off value 4, in the near-side scan 5/25 cracks were correct discriminated. In the far-side scan, 24/25 cracks were correct discriminated.
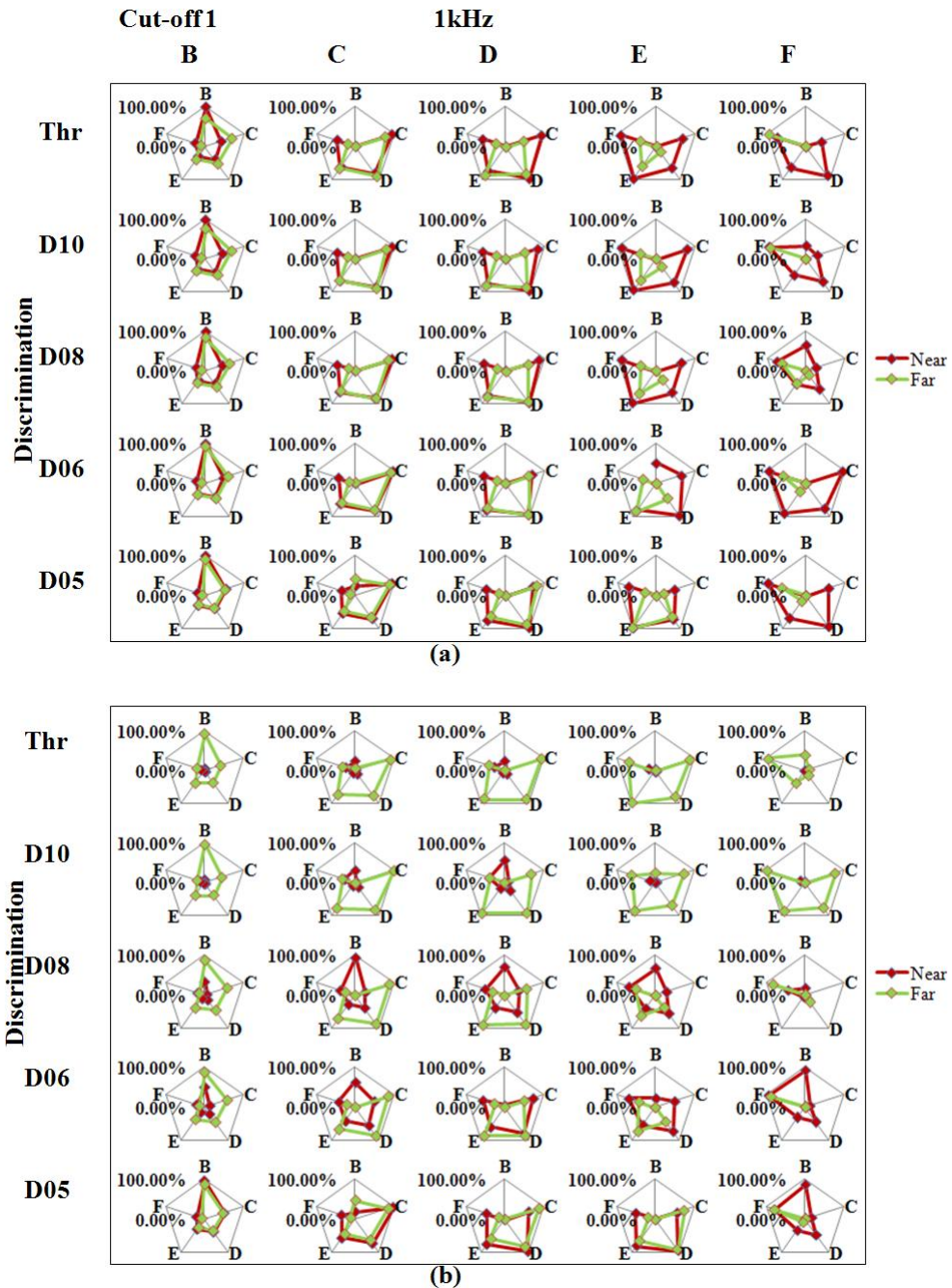
Figure 3-62 Discrimination result of near- side and far-side cracks at 1 kHz with cut-off 1 (a) Near-side scan; (b) Far-side scan

137
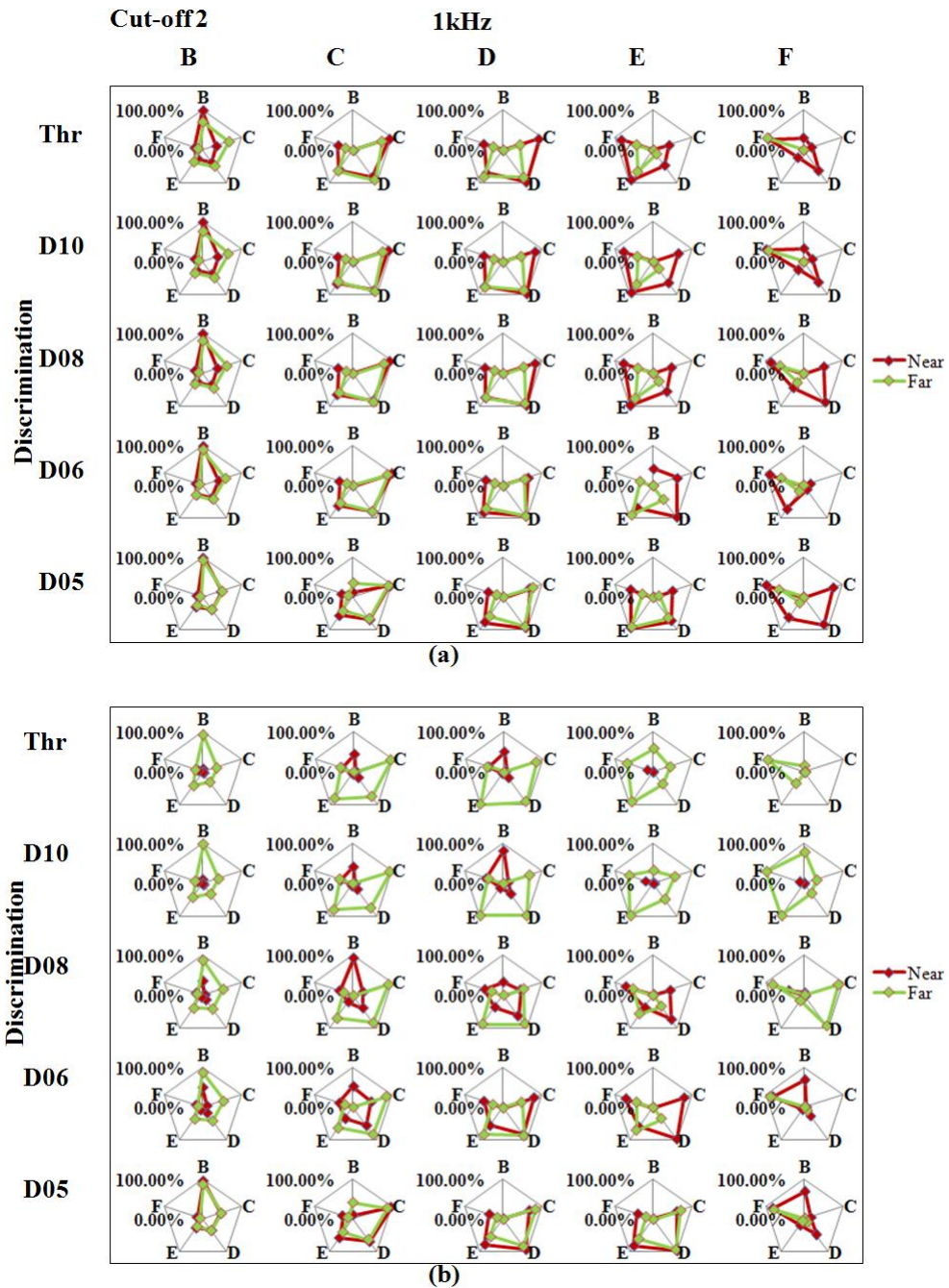
Figure 3-63 Discrimination results of near-side and far-side cracks at 1 kHz with cut-off 2 (a)

Near-side scan; (b) Far-side scan
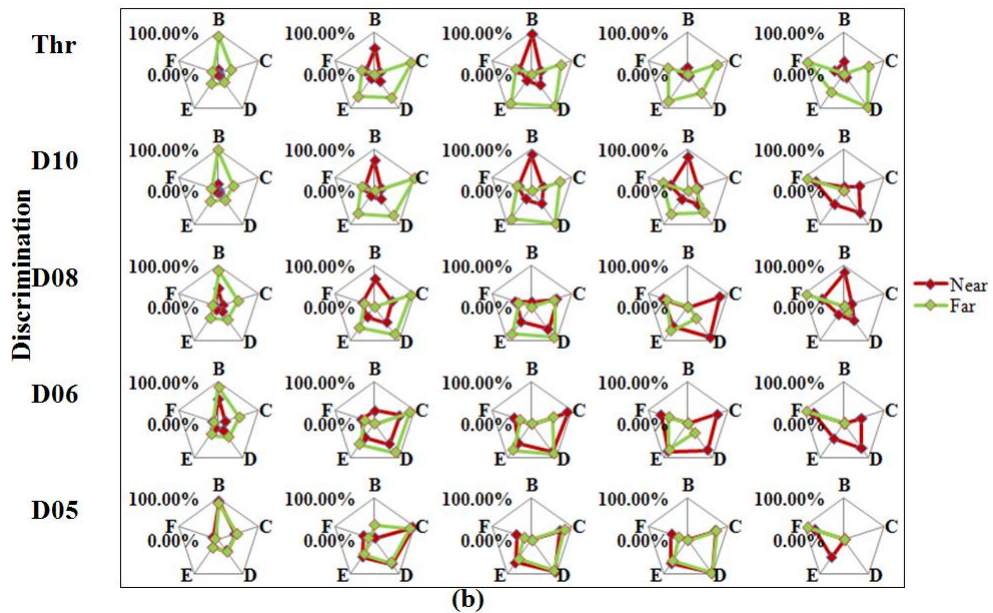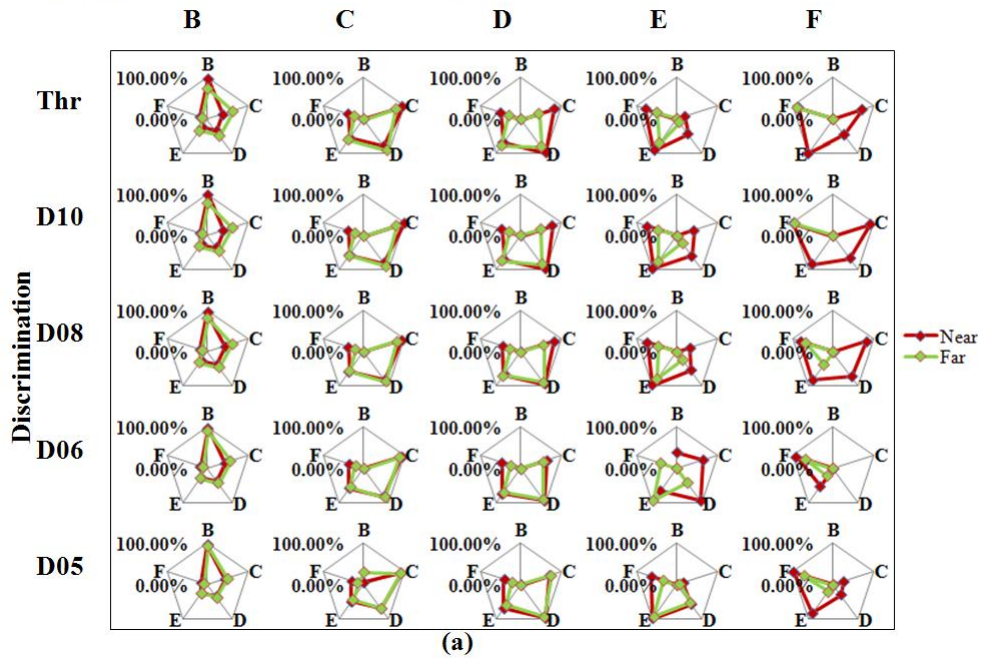
Figure 3-64 Discrimination results of near-side and far-side cracks at 1 kHz with cut-off 3 (a) Near-side scan; (b) Far-side scan

139
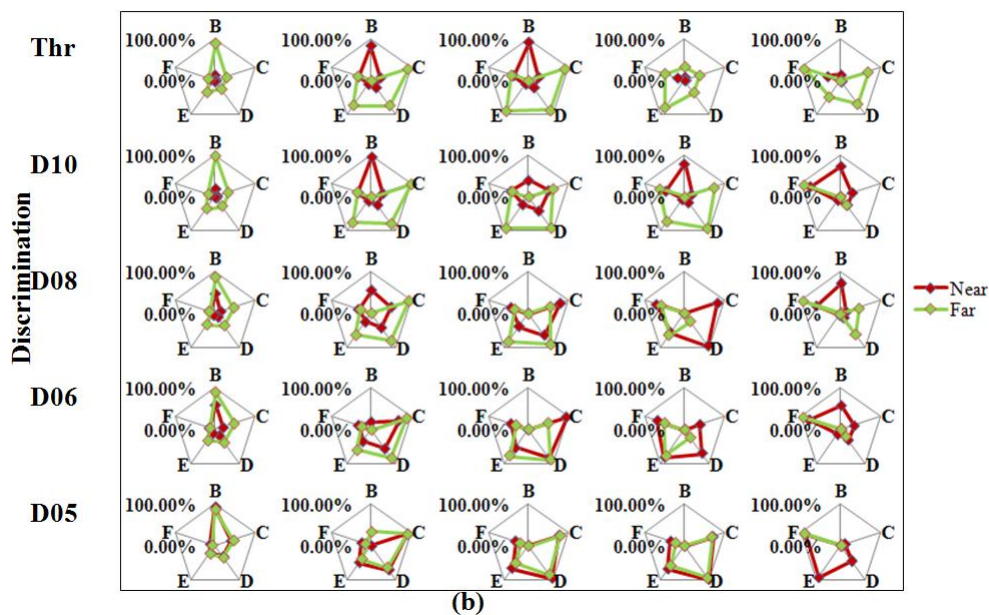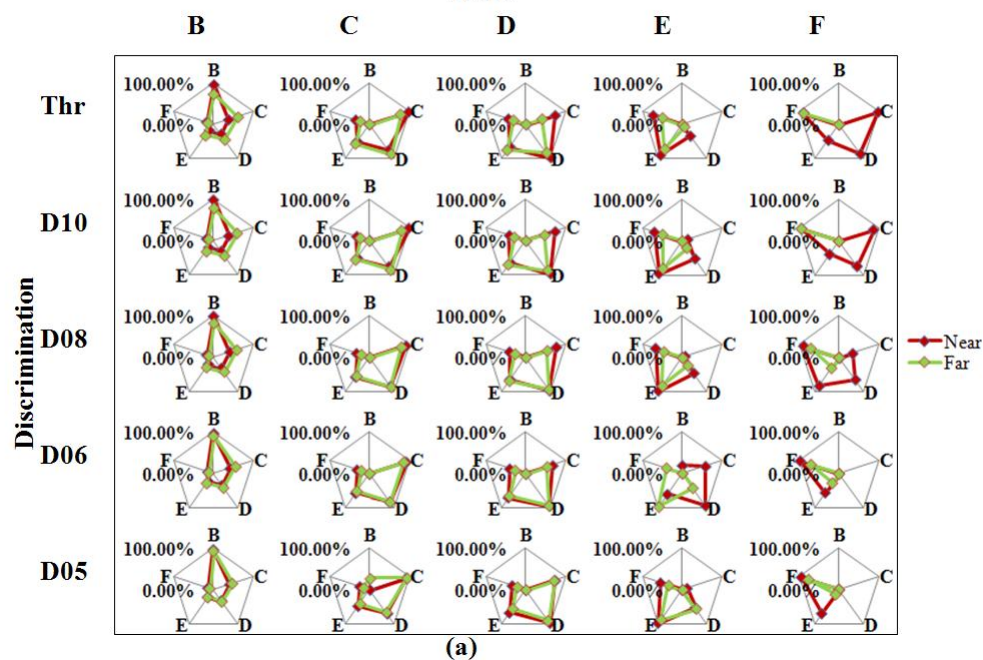
Figure 3-65 Discrimination results of near-side and far-side cracks at 1 kHz with cut-off (a) Near-side scan; (b) Far-side scan

Estimation of Crack Volume

Once the near-side and far-side cracks were discriminated and the diameter of crack was estimated, the quantitative evaluation of crack volume could be obtained. Establish the relationship between crack volume with the integrated of absolute data for 1 kHz, as shown in Figure 3-66. The relationship is actually same with the relationship in the method 3, but 10 groups of diameter is separated in this method. Each near- and far-side crack provides 5 groups which could be approximated as linearity. The general form of the linearly approximation is described in Eq. (90). The coefficients $A_{ID/OD}$ and $B_{ID/OD}$ are called "volume coefficients".
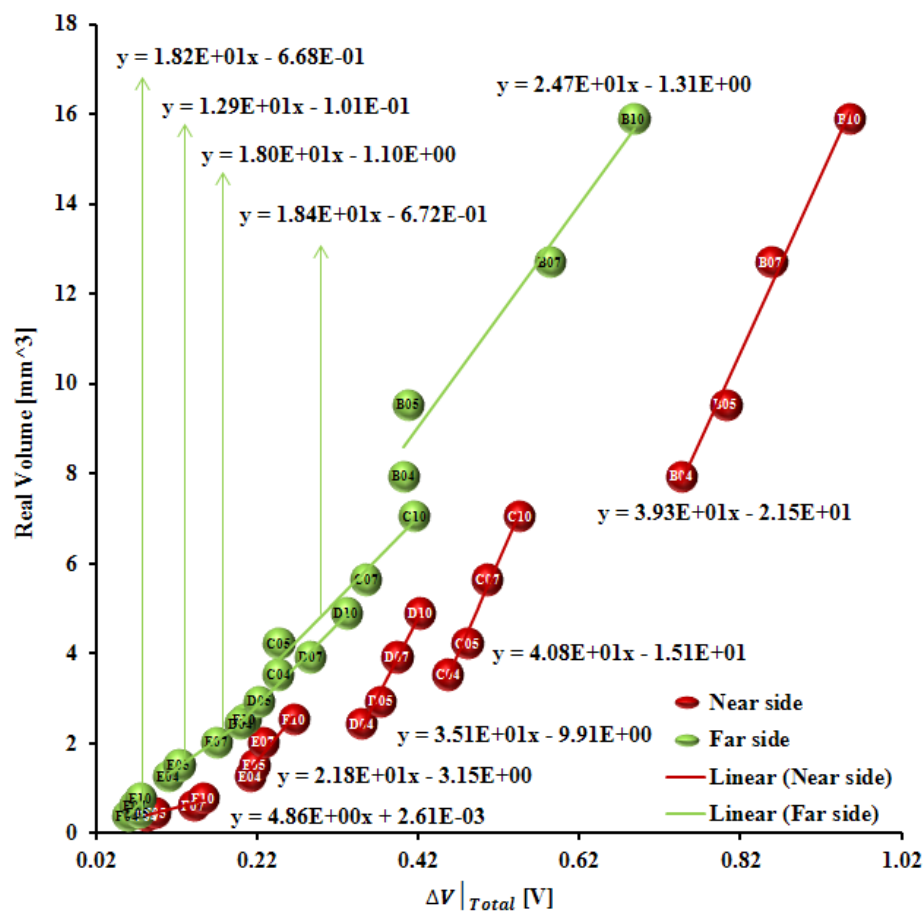
Figure 3-66 Relationship between integrated of absolute of crack image with crack volume at 1 kHz

$$\text{Vol} = A_{ID/OD} \cdot \Delta V|_{\text{total}}^{ID/OD} + B_{ID/OD} \tag{90}$$

The relationship between volume coefficients with crack diameter could be fitted by two orders: order 1- linearly approximation, order 2-quadric approximation. The relationships are shown in Figure 3-67 and Figure 3-68. The general form of the approximation for volume coefficients are described in Eqs. (91)-(95).

Order1	$A_{ID/OD} = a_{ID/OD} \cdot \emptyset + b_{ID/OD}$	(91)
	$B_{ID/OD} = a_{ID/OD} \cdot \emptyset + b_{ID/OD}$	(92)
Order2	$A_{ID/OD} = a_{ID/OD} \cdot \emptyset^2 + b_{ID/OD} \cdot \emptyset + c_{ID/OD}$	(93)
	$B_{ID/OD} = a_{ID/OD} \cdot \emptyset^2 + b_{ID/OD} \cdot \emptyset + c_{ID/OD}$	(94)

Figure 3-69 shows the estimation results of crack volume in near-side and far-side scan results at 1 kHz with cut-off 1~4 and linear approximation of volume coefficients (order1). The approximation is good for small crack, but worst for big crack. This is because that the result is obtained after approximation of crack diameter leading to accumulative errors of approximations. The estimation is better in the cut-offs 3 and 4 than that in the cut-offs 1 and 2, and the cut-offs 3 and 4 were not affected much by accumulative error. The reason could be that the cut-offs 1 and 2 has small cut-off values leading to including noise of background in the calculation of integrated of '0','1' data ($\sum(01)$). The standard deviations of estimated crack volume at 1 kHz at cut-off 1 are 21.416 mm^3 and 17.828 mm^3 for near-side and far-side scan, at cut-off 2 are 19.070 mm^3 and 17.147 mm^3 for near-side and far-side scan, at cut-off 3 are 6.683mm^3 and 8.270mm^3 for near-side and far-side scan, at cut-off 4 are 6.527 mm^3 and 8.267 mm^3 for near-side and far-side scan, respectively.

Figure 3-70 shows the estimation results of crack volume in near-side and far-side scan results at 1 kHz with cut-off 1~4 and quadric approximation of volume coefficients (order 2). It shows a better estimation results than using order 1, because the data was better fitted in the quadric approximation than in the linear approximation. The estimation is better in the cut-offs 3 and 4 than that in the cut-offs 1 and 2 as same reasons presented in the order 1 results. The standard deviations of estimated crack volume at 1 kHz at cut-off 1 are 6.372 mm^3 and 6.844 mm^3 for near-side and far-side scan, at cut-off 2 are 6.909 mm^3 and 6.661 mm^3 for near-side

and far-side scan, at cut-off 3 are 5.859 mm^3 and 3.106 mm^3 for near-side and far-side scan, at cut-off 4 are 4.730 mm^3 and 3.250 mm^3 for near-side and far-side scan, respectively.
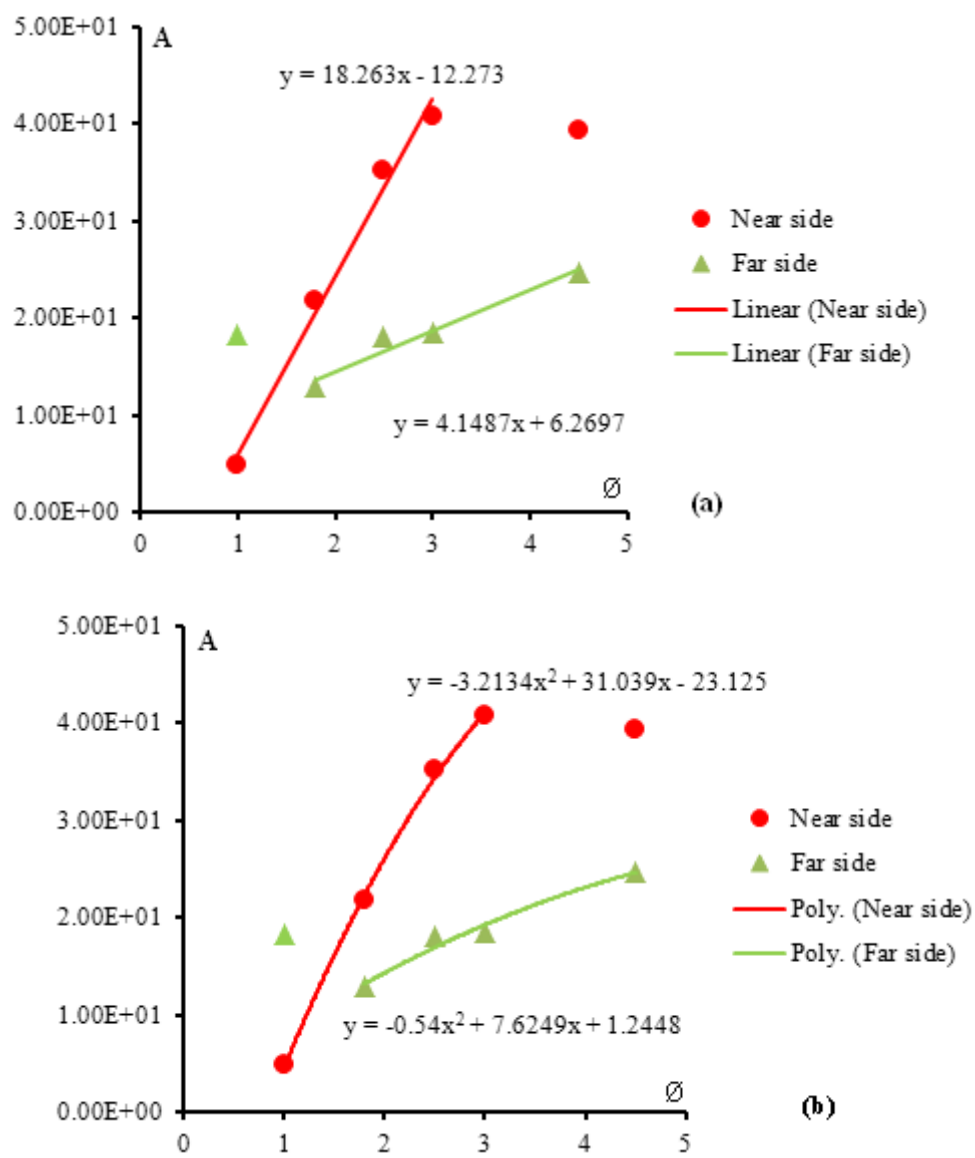
Figure 3-67 Relationship between volume coefficients $A_{ID/OD}$ and $B_{ID/OD}$ with and diameter by (a) order 1 and (b) order 2.

Figure 3-68 Relationship between volume coefficients $A_{ID/OD}$ and $B_{ID/OD}$ with and diameter by (a) order 1 and (b) order 2.

Order 1 1kHz
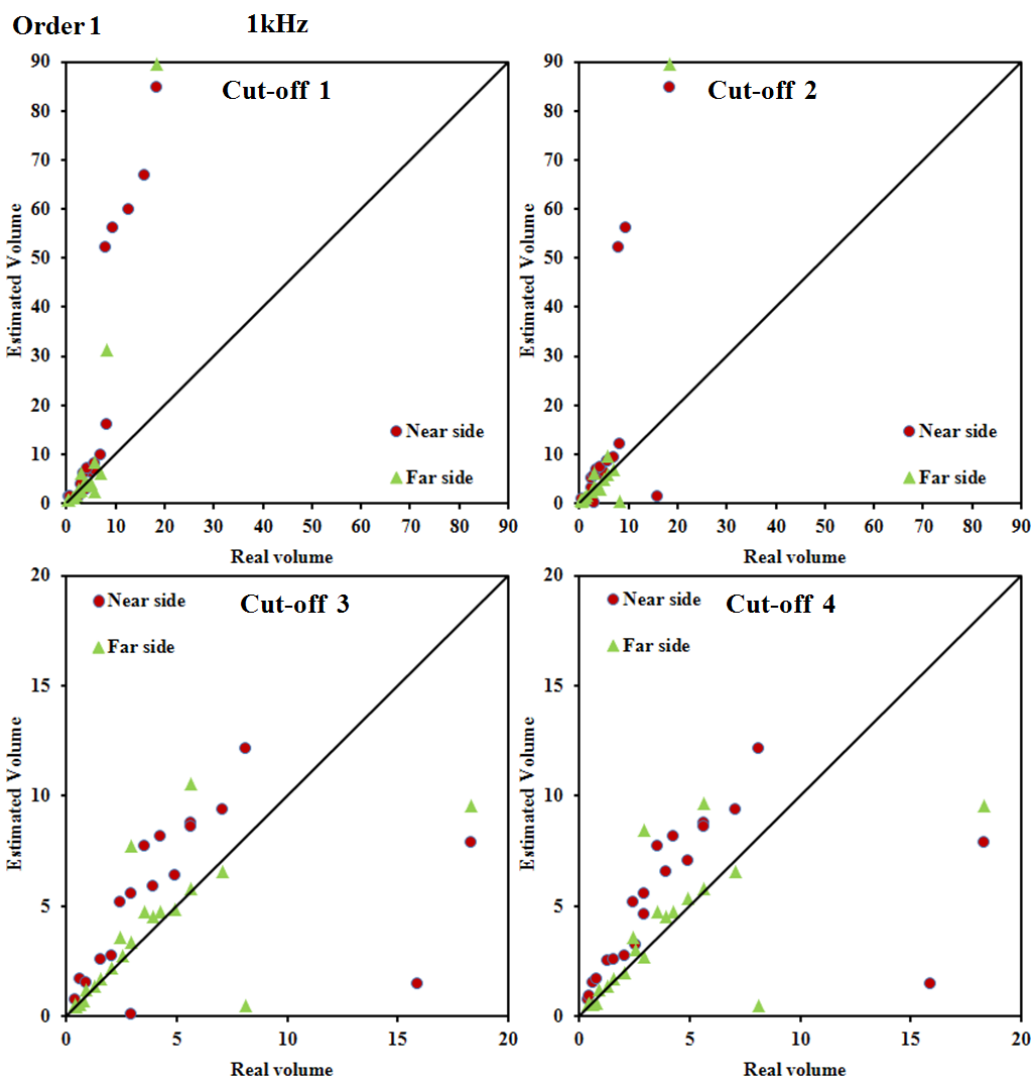
Figure 3-69 Estimation of crack volume in near-side and far-side scan results at 1 kHz with cut-offs 1~4 and linear approximation of volume coefficients (order 1).
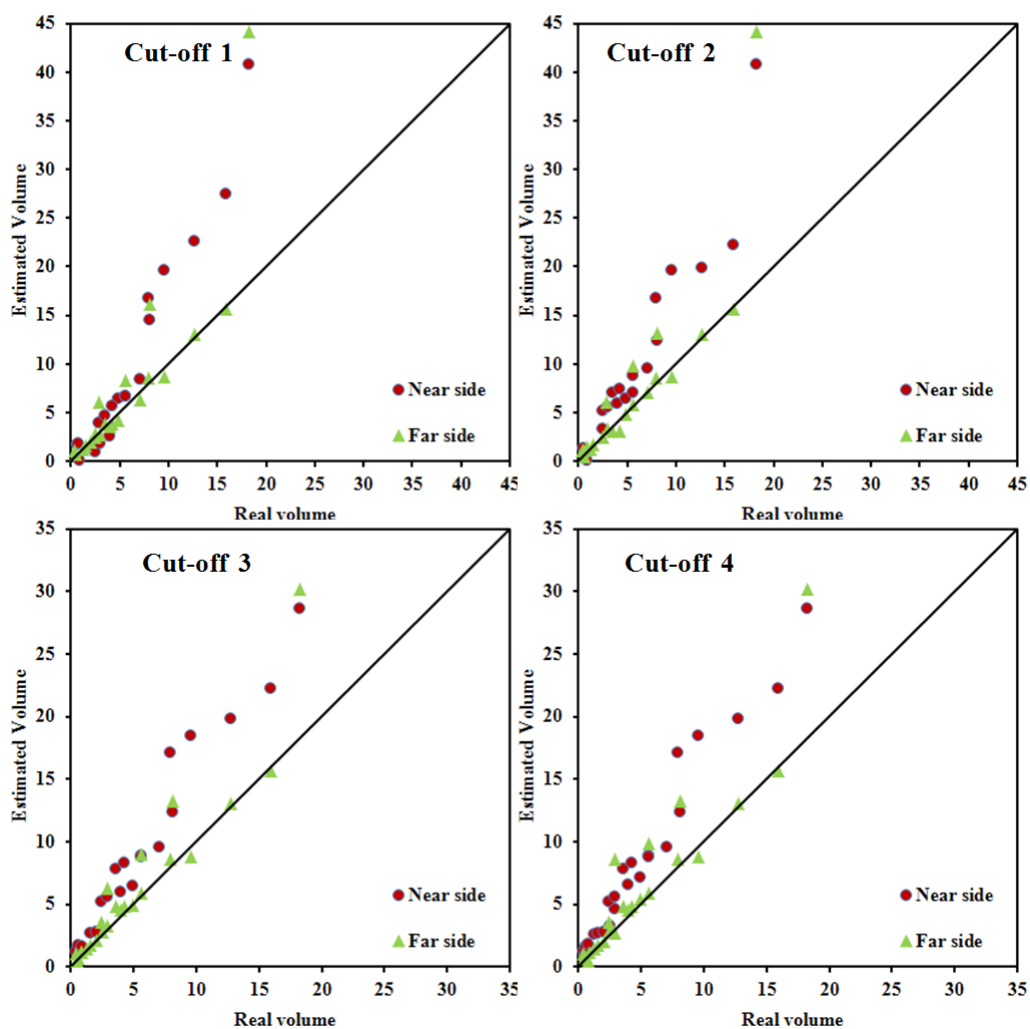
Figure 3-70 Estimation of crack volume in near-side and far-side scan results at 1 kHz with cut-offs 1~4 and quadric approximation of volume coefficients (order 2).

Probability of Discrimination Near/Far-side Crack and Estimation of Crack Volume at 3 and 5 kHz

The same steps as processed for data at 1 kHz were applied for data at 3 and 5 kHz. The same cut-offs 1, 2, 3 and 4 was used in conversion of crack data to '0','1'data.

Table 3-8 Number cracks were corrected discrimination at 3 and 5 kHz.

Frequency	Scan side	Cut-off 1	Cut-off 1	Cut-off 1	Cut-off 1
3 kHz	Near-side	16	15	13	18
	Far-side	17	19	17	18
5 kHz	Near-side	14	9	11	12
	Far-side	17	16	11	17

Figure 3-71~Figure 3-72 show the estimation results of crack volume in near-side and far-side scan results at 3 kHz with cut-off 1~4 using linear (order 1) quadric approximation of volume coefficients (order 2). And Figure 3-73~Figure 3-74 shows the estimation results of crack volume in near-side and far-side scan results at 5 kHz with cut-off 1~4 using linear (order 1) quadric approximation of volume coefficients (order 2). The error of estimation of large crack volume was not appeared in the 3 and 5 kHz as in the 1 kHz. In the both frequencies, the cut-off 4 provides the best estimation result compared with other cut-offs. The quadric approximation of volume coefficients method provides better estimation results than the linear approximation as same at 1 kHz.

Table 3-9 Standard deviation of estimation of crack volume at 3 and 5 kHz in order 1, [mm^3]

Frequency	Scan side	Cut-off 1	Cut-off 1	Cut-off 1	Cut-off 1
3 kHz	Near-side	19.215	20.065	19.451	19.571
	Far-side	18.785	18.316	18.713	18.810
5 kHz	Near-side	6.245	6.344	6.05	6.346
	Far-side	5.902	6.362	6.290	5.456

Table 3-10 Standard deviation of estimation of crack volume at 3 and 5 kHz in order 2, [mm^3]

Frequency	Scan side	Cut-off 1	Cut-off 1	Cut-off 1	Cut-off 1
3 kHz	Near-side	19.215	20.065	19.451	19.571
	Far-side	18.785	18.316	18.713	18.810
5 kHz	Near-side	6.245	6.344	6.05	6.346
	Far-side	5.902	6.362	6.290	5.456

Order 1　　　　　　　　　3kHz
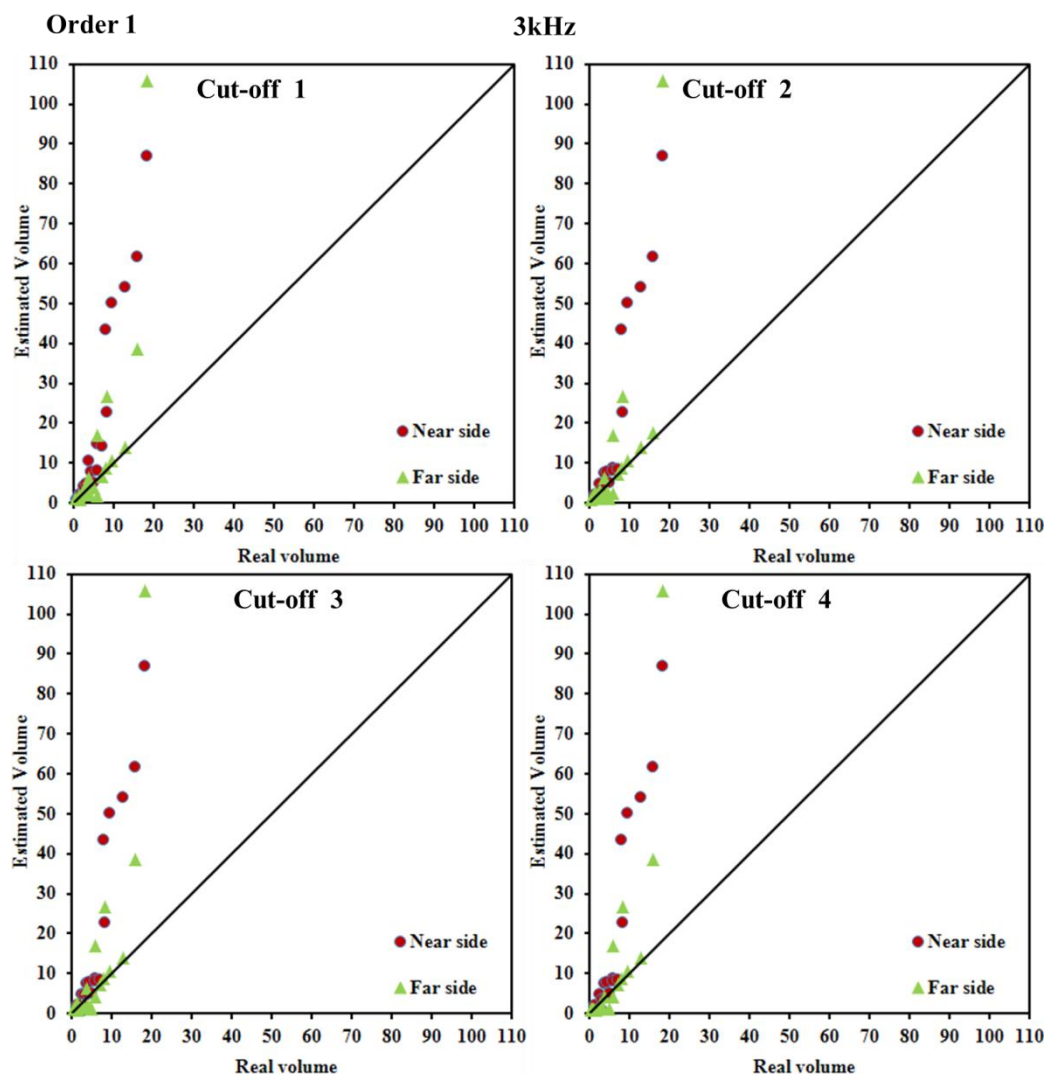
Figure 3-71 Estimation of crack volume in near-side and far-side scan results at 3 kHz with cut-offs 1~4 and linear approximation of volume coefficients (order 1).

149
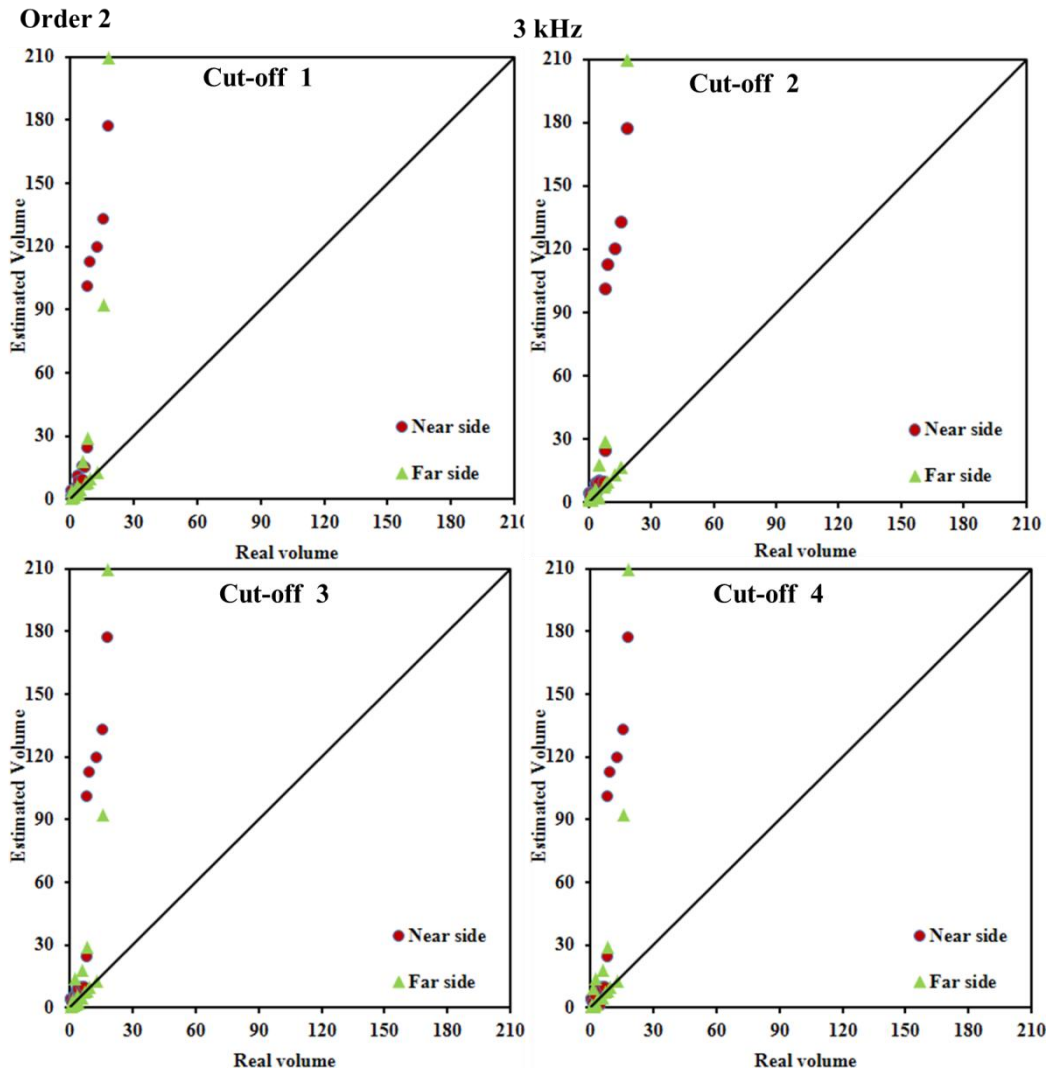
Figure 3-72 Estimation of crack volume in near-side and far-side scan results at 3 kHz with cut-offs 1~4 and quadric approximation of volume coefficients (order 2).
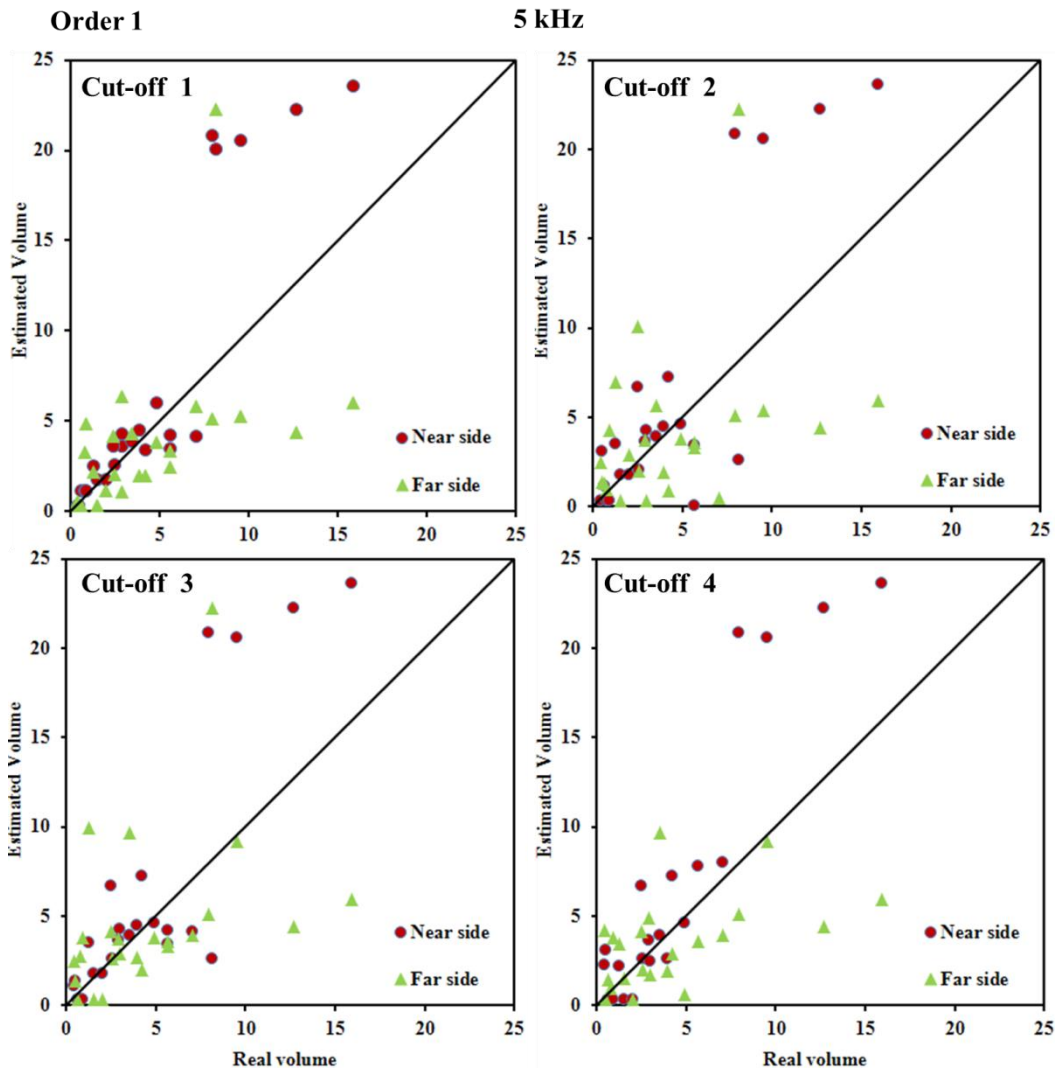
Figure 3-73 Estimation of crack volume in near-side and far-side scan results at 5 kHz with cut-offs 1~4 and linear approximation of volume coefficients (order 1).
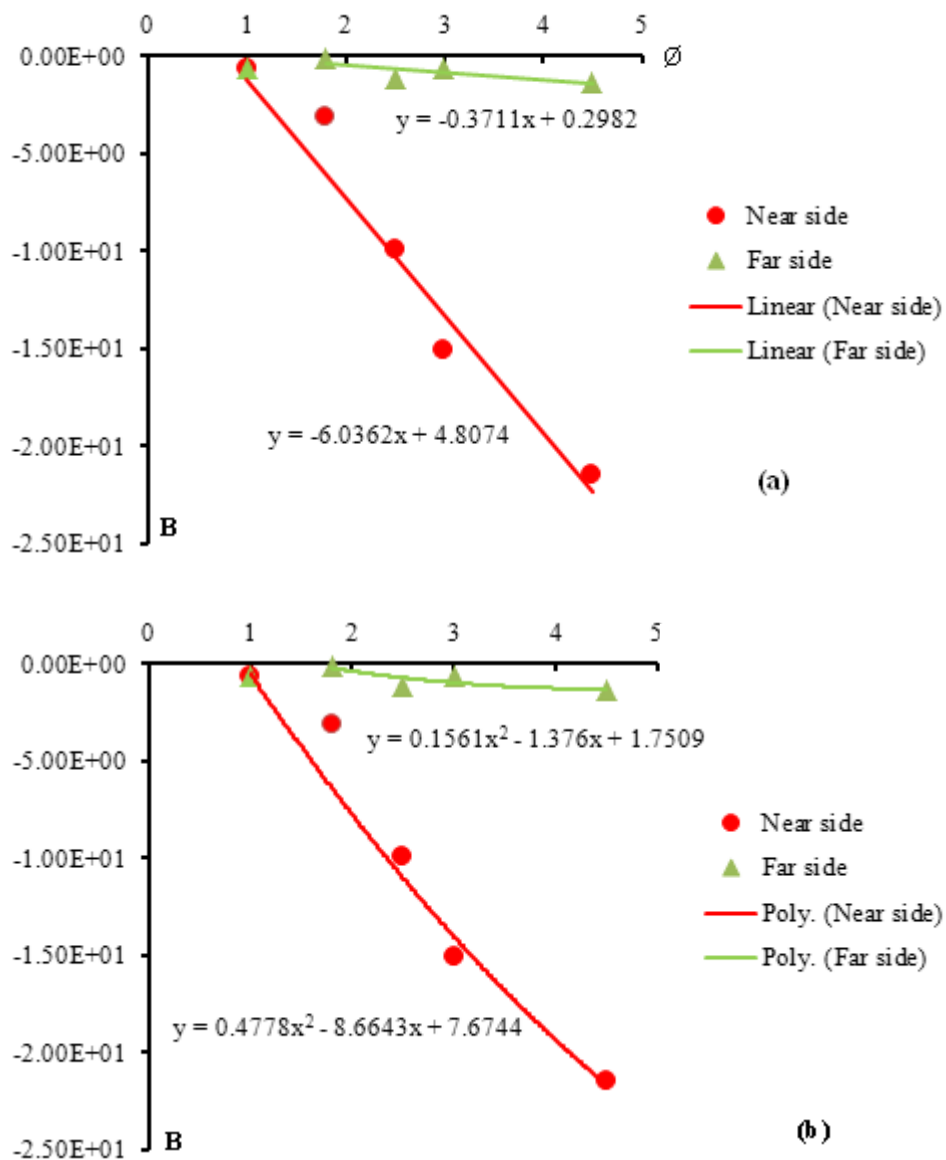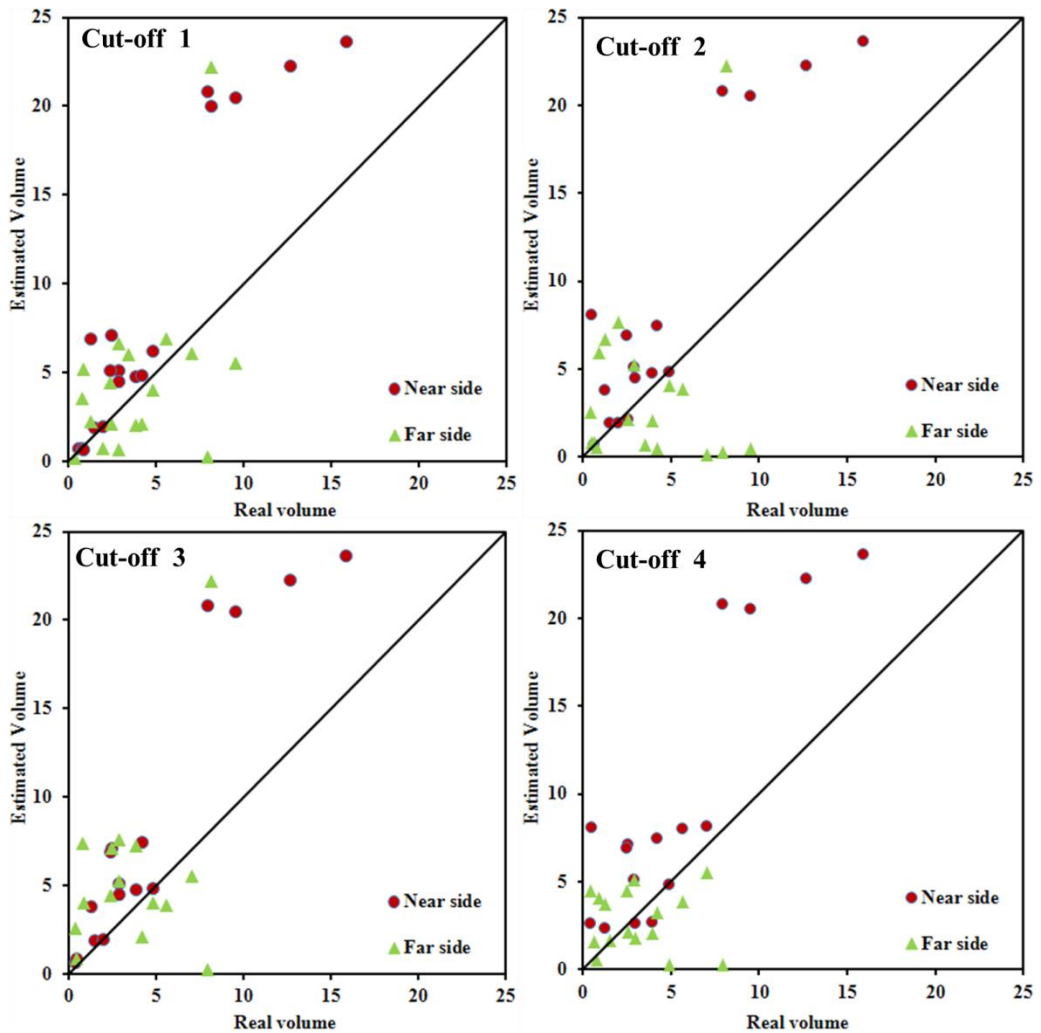
Figure 3-74 Estimation of crack volume in near-side and far-side scan results at 5 kHz with cut-offs 1~4 and quadric approximation of volume coefficients (order 2).

Copper-nickel, Inconel 600, Stainless Steel (STS304) Specimen

The same process of analysis data with titanium specimen were applied copper-nickel, Inconel 600, STS304 specimen. The same cut-offs 1, 2, 3 and 4 was used in conversion of crack data to '0','1'data for the entire material specimen. The number of correction discrimination of near/far-side crack is indicated in **Table 3-11** Number cracks were corrected discrimination at 3 and 5 kHz for different materials.. In titanium specimen, the best discrimination of near/far-side crack is at 1 kHz. There are 22/25 near-side cracks were correct discriminated using cut-off 1 and 24/25 far-side cracks were correct discrimination using cut-off 3 and 4. However, the best discrimination of near/far-side crack on copper-nickel specimen is at 3 kHz. There are 22/25 and 21/25 correct discrimination were obtained for near- and far-side crack using cut-off 1, respectively. The best discrimination of near/far-side crack on Inconel specimen is at 5 kHz. There are 19/25 and 18/25 correct discrimination were obtained for near- and far-side crack using cut-off 1, respectively. The best discrimination of near/far-side crack on stainless steel specimen is at 5 kHz. There are 18/25 and 18/25 correct discrimination were obtained for near- and far-side crack using cut-off 1, respectively. Among the 4 specimens, the discrimination of near/far-side crack on titanium specimen is the best.

Table 3-12 presents estimation results of crack volume for the three material specimens using linear approximation of volume coefficients. The best estimation of volume of near/far-side crack on titanium specimen is at 5 kHz. The best standard deviation using cut-off 4 for near- and far-side crack are 6.346 and 5.456 mm3, respectively. The best estimation of volume of near/far-side crack on copper-nickel specimen is at 3 kHz. The best standard deviation using cut-off 4 for near- and far-side crack are 2.022 and 3.128 mm3, respectively. The best estimation of volume of near/far-side crack on Inconel specimen is at 3 kHz. The best standard deviation using cut-off 1 for near- and far-side crack is 1.596 and 3.037 mm3, respectively. The best estimation of volume of near/far-side crack on stainless steel specimen is at 5 kHz. The best standard deviation using cut-off 4 for near- and far-side crack are 3.990 and 4.954 mm3, respectively. Among the 4 specimens, the estimation of crack volume on Inconel specimen is the best.

Table 3-13 presents estimation results of crack volume for the three material specimens using quadric approximation of volume coefficients. The best estimation of volume

of near/far-side crack on titanium specimen is at 1 kHz. The best standard deviation using cut-off 4 for near- and far-side crack are 4.730 and 3.250mm3, respectively. The best estimation of volume of near/far-side crack on copper-nickel specimen is at 3 kHz. The best standard deviation using cut-off 4 for near- and far-side crack are 1.878 and 3.010 mm3, respectively. The best estimation of volume of near/far-side crack on Inconel specimen is at 3 kHz. The best standard deviation using cut-off 1 for near- and far-side crack is 1.564 and 2.679 mm3, respectively. The best estimation of volume of near/far-side crack on stainless steel specimen is at 5 kHz. The best standard deviation using cut-off 4 for near- and far-side crack are 3.779 and 4.687 mm3, respectively. Among the 4 specimens, the estimation of crack volume on Inconel specimen is the best. And, the quadric approximation of volume coefficients is better than the linear approximation of volume coefficients.

Table 3-11 Number cracks were corrected discrimination at 3 and 5 kHz for different materials.

Material	Frequency	Scan side	Cut-off 1	Cut-off 2	Cut-off 3	Cut-off 4
Titanium	1 kHz	Near-side	22	13	9	5
		Far-side	21	23	24	24
	3 kHz	Near-side	16	15	13	18
		Far-side	17	19	17	18
	5 kHz	Near-side	14	9	11	12
		Far-side	17	16	11	17
Copper-nickel	1 kHz	Near-side	15	16	14	9
		Far-side	20	17	17	15
	3 kHz	Near-side	22	19	14	14
		Far-side	21	14	15	10
	5 kHz	Near-side	18	18	13	15
		Far-side	15	19	15	9
Inconel 600	1 kHz	Near-side	14	18	16	17
		Far-side	16	15	16	17
	3 kHz	Near-side	24	13	9	11
		Far-side	13	20	19	21
	5 kHz	Near-side	19	18	12	13
		Far-side	18	16	21	21
Stainless Steel STS304	1 kHz	Near-side	17	15	8	9
		Far-side	16	17	23	22
	3 kHz	Near-side	17	16	10	11
		Far-side	17	20	16	14
	5 kHz	Near-side	18	14	17	18
		Far-side	18	15	10	7

Table 3-12 Standard deviation of estimation of crack volume using linear approximation of volume coefficients (order 1) at 3 and 5 kHz for different materials, [mm^3]

Material	Frequency	Scan side	Cut-off 1	Cut-off 2	Cut-off 3	Cut-off 4
Titanium	1 kHz	Near-side	21.416	19.070	6.683	6.527
		Far-side	17.828	17.147	8.270	8.267
	3 kHz	Near-side	19.215	20.065	19.451	19.571
		Far-side	18.785	18.316	18.713	18.810
	5 kHz	Near-side	6.245	6.344	6.05	6.346
		Far-side	5.902	6.362	6.290	5.456
Copper-nickel	1 kHz	Near-side	3.428	3.394	3.245	3.017
		Far-side	6.032	6.109	6.313	6.302
	3 kHz	Near-side	1.881	2.269	3.866	2.022
		Far-side	3.529	3.485	3.120	3.128
	5 kHz	Near-side	3.537	3.256	3.161	3.001
		Far-side	3.915	3.780	3.599	3.319
Inconel 600	1 kHz	Near-side	3.374	1.933	5.102	5.175
		Far-side	5.611	5.450	6.129	6.463
	3 kHz	Near-side	1.596	2.100	2.475	2.271
		Far-side	3.037	4.713	3.732	5.405
	5 kHz	Near-side	2.234	2.322	3.663	3.883
		Far-side	5.081	4.896	6.113	4.161
Stainless Steel STS304	1 kHz	Near-side	3.229	3.95	4.118	4.097
		Far-side	3.528	3.462	3.620	3.695
	3 kHz	Near-side	8.157	6.014	8.688	8.805
		Far-side	8.221	5.282	6.656	8.599
	5 kHz	Near-side	4.231	4.579	5.769	3.990
		Far-side	4.700	4.953	6.345	4.954

Table 3-13 Standard deviation of estimation of crack volume quadric approximation of volume coefficients (order 1) at 3 and 5 kHz for different materials, [mm^3]

Material	Frequency	Scan side	Cut-off 1	Cut-off 2	Cut-off 3	Cut-off 4
Titanium	1 kHz	Near-side	6.372	6.909	5.859	4.730
		Far-side	6.844	6.661	3.106	3.250
	3 kHz	Near-side	47.564	48.556	47.519	48.048
		Far-side	41.293	39.026	41.102	40.929
	5 kHz	Near-side	10.825	10.761	10.693	10.694
		Far-side	13.745	15.723	19.259	17.144
Copper-nickel	1 kHz	Near-side	2.067	1.879	2.112	2.497
		Far-side	3.178	6.546	3.200	3.221
	3 kHz	Near-side	1.946	2.423	3.478	1.878
		Far-side	3.172	3.447	3.112	3.010
	5 kHz	Near-side	3.772	3.330	3.444	3.103
		Far-side	4.070	3.782	3.963	3.298
Inconel 600	1 kHz	Near-side	9.784	7.781	6.383	6.797
		Far-side	10.836	10.723	7.607	6.772
	3 kHz	Near-side	1.564	2.249	2.500	2.621
		Far-side	2.679	5.573	3.491	5.639
	5 kHz	Near-side	2.236	2.371	3.681	4.175
		Far-side	4.907	4.447	5.965	4.481
Stainless Steel STS304	1 kHz	Near-side	3.489	4.646	5.332	5.443
		Far-side	4.117	4.057	4.614	4.939
	3 kHz	Near-side	10.227	13.705	12.362	12.371
		Far-side	13.373	14.925	12.020	13.279
	5 kHz	Near-side	3.948	4.277	5.422	3.779
		Far-side	4.710	4.987	6.055	4.687

Chapter 4 CONCLUSION

The thesis presents a magnetic camera for inspection of near-side and far-side cracks in metal specimens, specifically targeted for the thin thickness plates in nuclear and aerospace industries. The magnetic camera includes a sheet-type induced current as a magnetic source, a linearly integrated Hall sensor array, and signal processing circuits. The signal processing circuit includes amplifiers, high-pass-filter, root-mean-square circuits, analogue-to-digital converter and interface. The number of amplifiers, high-pass-filter and root-mean-square circuits are same with the number of Hall sensor element. In the current system, they are 64 components. The linearly integrated Hall sensor array has high spatial resolution of 0.52 mm and total length of 33.28 mm. The sensor measures the entire of specimen by using XY stage motor with high resolution of scanning step, 0.2 mm. The high spatial resolution and small scan step help to detect small crack size, obtain high quality of crack image and accurate in quantitative evaluation of crack size. Thus, the smallest crack diameter of 1 mm could be inspected.

Four plate specimens of titanium, copper-nickel, Inconel 600 and stainless steel (STS304) were used under experiment which could be consider as a transformation of a thin-small-bore pipe such as steam generators. Hole-type cracks and slit-type cracks were manufactured in the specimens, which are considered as transformation of inner/outer diameter and circumferential corrosions in a small-bore pipe. The cracks were measured in the both near-side and far-side as corrosions in the inner diameter and outer diameter of a pipe. The measurements were performed in different frequencies of 1, 3, and 5 kHz to research the effect of frequency to the inspection capability of the magnetic camera. The hole-type cracks having diameter from 1.0~4.5 mm and depth from 0.2~1.2 mm in the four specimens were measured in the both near-side and far-side. We know that eddy current density exponentially decreases with its depth from surface of specimen in the skin effect. The depth that eddy currents penetrate into a material is affected by the excitation frequency and the electrical conductivity of the specimen. When the excitation frequency or conductivity of material increase then the depth of penetration decrease, it means that the eddy current will be focused near the surface of specimen; thus, the sensor is easy to detect cracks in the near side can. In contrast, when frequency or conductivity of material decrease, the depth of penetration increase; thus, the

sensor is easier to detect cracks in the far side can than at high frequency or with high conductivity. In the titanium specimen, all the cracks were clearly inspected in near-side scan but crack depth of 0.2~0.6 and diameter of 1 mm in the far-side scan were not clear, and at the 3 kHz the images were the most clear. In the copper-nickel specimen, all the cracks in near-side scan were detected except crack diameter of 1 mm and depth of 0.2 mm for the both sides of scan, and the results at 3 and 5 kHz are better than that at 1 kHz. In the Inconel specimen, all the cracks in near-side scan were detected except crack diameter of 1 mm and depth of 0.4 mm, and crack diameter of 1 mm and depth of 0.5 mm at far-side scan. The results at 3 and 5 kHz are better than that at 1 kHz. In the stainless steel specimen, almost the cracks in near-side scan look clearly except crack diameter of 1 and 1.8 and depth 0.5 and 5.6 mm. At far-side cracks diameter of 1 mm and depth of 0.4 and 0.5 mm were not detected. The results at 3 and 5 kHz are the better than at 1 kHz. The slit-type cracks having same length of 80 mm, depth from 0.2~1.2 mm which are considered as circumferential corrosion in a pipe, were all clearly inspected although the eddy current flux is parallel to the length of the cracks. It was observed that the area of crack image increases as the crease of the crack diameter, and the strength of signal increases as the increase of the crack depth.

Four methods were discussed in the quantitative evaluation of crack size. Among the four proposed methods, the methods 3 and 4 provide a good quantitative evaluation of crack size. In the method 3, the discrimination of near-side and far-side cracks were done by the separated group of data in the graph of the integrated of absolute crack image with h^2*w. In there, h is the peak-peak height and w is the peak-peak distance. Once the near/far-side crack is discriminated, the crack volume were estimated by using the integrated of absolute crack image. The discrimination result and estimation of crack volume result were the best at 1 kHz for titanium and copper-nickel specimen but the best at 3 kHz for Inconel and stainless steel specimen. And the results of titanium and copper-nickel are better than the Inconel and stainless steel. These are because the titanium and copper-nickel has similar high conductivity, but the Inconel and stainless steel has similar low conductivity. For instance, at 1 kHz of the titanium specimen, 24/25 and 19/25 correct discriminated for near-side and far-side scan, respectively. The standard deviations of estimation of crack volume for near-side and far-side scan were 1.1260 mm^3 and 1.7117 mm^3, respectively. At 3 kHz of the Inconel specimen, 13/25 and 14/25 correct discriminated for near-side and far-side scan, respectively. The standard

Collection @ chosun

deviations of estimation of crack volume for near-side and far-side scan were 1.8167 mm^3 and 4.4433 mm^3, respectively.

In the method 4, the discrimination and estimation of crack diameter were performed using the relationship between the integrated of absolute crack image and ratio of total digital crack image with h^2. Each group data of crack having same diameter and same position (near-side and far-side) was classified and totally 10 equations were established. Then calculation of the probability of a crack belongs to each group is performed. The maximum probability is used to determine the crack diameter group and its side (near- or far-side). Finally, the crack volume were estimated by using the integrated of absolute crack image. The linear approximation and quadric approximation methods of volume coefficients were used in estimation of crack volume. The quadric approximation method provides better estimation results than the linear approximation method. Among the 4 specimens, the discrimination of near/far-side crack on titanium specimen is the best. There are 22/25 near-side cracks and 24/25 far-side cracks were correct discrimination at 1 kHz. By using the two approximation methods, the estimation of crack volume on Inconel specimen is the best. Using linear approximation method, the best standard deviation for near- and far-side crack on Inconel specimen is 1.596 and 3.037 mm^3, respectively. Using quadric approximation method, the best standard deviation for near- and far-side crack on Inconel specimen is 1.564 and 2.679 mm^3, respectively. However, there were only 5 value of diameter in the sample specimen were estimated. But, if we could increase more number of crack diameter in the sample specimens, the estimation would be more accurate.

REFERENCES

[1]   Zuuk Inspection. History of Non-Destructive Testing, 2011

[2]   Louis Cartz, Nondestructive Testing, ASM International, 1995, ISBN: 087170 5176

[3]   JOHN P.SMITH, Effective and Efficient Non-Destructive Testing of Large and Complex Shaped Aircraft Structures, Thesis, University of Central Lancashire.

[4]   http://www.ndt-ed.org/EducationResources/CommunityCollege/MagParticle/Introduction/basicprinciples.htm

[5]   Sato, Development of a 3-d ultrasonic inspection device for steel pipe

[6]   S Dixon, C. Edwards, and S. B. Palmer, A laser-EMAT system for ultrasonic weld inspection, Ultrasonics, Vol. 37, No 4, pp. 273-281, 1999.

[7]   R. H. Bossi, F. A. Iddings, G. C. Wheeler, Radiographic testing, Nondestructive testing hand book , Vol. 4, ASNDT,Columbus, OH, 2002.

[8]   Jack Blitz, Nondestructive testing using electromagnetic instrumentation, J. PIiys. E: Sci. Instrum., Vol. 16. 1983.

[9]   http://www.cyberphysics.co.uk/topics/nuclear/nuclear_power_plant.html

[10]   http://www.window.state.tx.us/specialrpt/energy/nonrenewable/nuke.php

[11]   Obrutsky L, Renaud R, Lakhan R. "Steam generator inspections: faster, cheaper and better, are we there yet ?" , IV ConferenciaPanamericana de END, 2007 1-17.

[12]   Duck-Gun Park, Kwon-Sang Ryu and Derac Son, Detection of Magnetic Phase in the Steam Generator Tubes of NPP, Steam Generator Systems: Operational Reliability and Efficiency, Dr. ValentinUchanin (Ed.). 2011, Chapter.9, 165-183.

[13]   (http://www.ndt-
       ed.org/AboutNDT/SelectedApplications/AircraftInspection/Aircraft%20Inspection.ht
       m)

[14]   (http://www.ndt.net/article/ecndt98/aero/031/031.htm)

[15]   http://en.wikipedia.org/wiki/Michael_Faraday

[16]   http://www.ndt-
       ed.org/EducationResources/CommunityCollege/EddyCurrents/Introduction/historyofE
       T.htm

[17]   http://www.ndt-
       ed.org/EducationResources/CommunityCollege/EddyCurrents/Physics/
       depthcurrentdensity.htm

[18]   Javier García-Martín, Jaime Gómez-Gil and Ernesto Vázquez-Sánchez, Non-
       Destructive Techniques Based on Eddy Current Testing, Sensors 2011, 11, 2525-2565

[19]   J Hansen, The eddy current inspection method, Part 1. History and electrical theory,
       Insight Vol 46 No 5 May 2004, pp.249.

[20]   Yamada, S.; Chomsuwan, K.; Iwahara, M. Application of giant magnetoresistive
       sensor for nondestructive evaluation. In Proceedings of the IEEE Sensors, Daegu,
       South Korea, October 2006; pp. 927-930.

[21]   Obrutsky L, Renaud R, Lakhan R. Steam generator inspections: faster, cheaper and
       better, are we there yet? IV Conferencia Panamericana de END 2007, pp. 1–17.

[22]   Drunen G.V, Cecco V.S. Recognizing limitations in eddy current testing. NDT & E Int
       1984;17(1):7–9.

[23]   Sadek HM. NDE technologies for the examination of heat exchangers and boiler tubes
       – principles, advantages and limitations. Insight 2006;48(3):181–3.

[24]   Uchanin V, Najda V. The Development of Eddy Current Technique for WWER Steam
       Generators Inspection. InTech 2011, pp. 145–64.

162

[25]   Kurokawa M, Miyauchi R, Enami K, Matsumoto M. New eddy current probe for NDE of steam generator tubes. Electromagnetic nondestructive evaluation (III). IOS Press; 1999. p. 57 – 64.

[26]   Lafontaine G, Hardy F, Renaud J. X-Probe® ECT array: A high-Speed Replacement for Rotating Probes. 3nd International Conference on NDE in Relation to Structural Integrity for Nuclear and Pressurized Components, Nov 14-16, 2001, Seville Spain.

[27]   http://www.ndt-ed.org/EducationResources/CommunityCollege/EddyCurrents/ Applications/thicknessmeasurements.htm

[28]   Lee, J. Hwang, J. Jun and S. Choi, "Nondestructive Testing and Crack Evaluation of Ferromagnetic Material by Using the Linearly Integrated Hall Sensor Array," Journal of Mechanical Science and Technology, vol. 22(12), pp. 2310- 2317, 2008.

[29]   Hwang, J. Lee, J. Jun, R. Wang, S. Choi, and S. Hong, "Scan type magnetic camera images with a high spatial resolution for NDT obtained by using a linearly integrated hall sensor array," Proceedings of IEEE International Workshop on Imaging Systems and Techniques, Poland, pp. 1-6, 2007

[30]   Magnetic Images of Surface Crack on Heated Specimen using an Area-Type Magnetic Camera with High Spatial Resolution I2MTC 2009 - International Instrumentation and Measurement Technology Conference Singapore, 5-7 May 2009

[31]   Inspection of the Internal Cracks on a Pipe Using a Cylinder-Type Magnetic Camera Jung Min Kim, Jin Yi Lee; Key Engineering Materials (Volumes 417 - 418) P 165-168 10.4028/www.scientific.net/KEM.417-418.165 Edited by M.H Aliabadi, S. Abela, S. Baragetti, M. Guagliano and Han-Seung Lee

[32]   2-D vector field visualization of corrosion in a small-bore piping system using bobbin-type integratedHall and GMR sensors arrays Le, Minhhuy ; Kim, Jungmin ; Sik Do, Hwa ; Lee, Jinyi ; Sensors Applications Symposium (SAS), 2014 IEEE ;Digital Object Identifier: 0.1109/SAS.2014.6798913 Publication Year: 2014 , Page(s): 38 – 41

163

[33] Lee, J. Y. and Hwang, J. S. (2006b) A Study of the Quantitative Nondestructive Evaluation Using the Cross Type Magnetic Source, Key Engineering Materials, 321, pp. 1447-1450

[34] Lee, J. Y., Hwang, J. S., Jun, J. W. and Choi, S. H. (2008a) Nondestructive Testing and Crack Evaluation of Ferromagnetic Material by Using the Linearly Integrated Hall Sensor Array, Journal of Mechanical Science and Technology, Vol. 22, pp. 2310-2317

[35] Lee, J. Y., Kim, J. W., Jun, J. W. and Hwang, J. S. (2008d) A Study of the Cylindrical Type Magnetic Camera, Proceedings of Fall conference of the Korea Society for Nondestructive Testing, pp. 247-252

[36] Lee, J. Y., Seo, D. W. and Shoji, T. (2004b) Theoretical Consideration of Nondestructive Testing by Use of Vertical Magnetization and Magneto-Optical Sensor, KSME International, Vol. 18, No. 4, pp. 640-648

[37] p39 Lee, J. Y. and Jun, J. W. (2008b) NDT of the Crack on the Austenite Stainless Steel Using the Improved Sheet Type Induced Current and the Linearly Integrated Hall Sensor Array, Abstracts of 13th ENDE, p. 48

[38] Jun, J. W., Lee, J. Y. and Park, D. K. (2007a) NDT of a Nickel Coated Inconel Specimen Journal of the KSNT Vol. 30 No. 3 223 Using by the Complex Induced Current – Magnetic Flux Leakage Method and Linearly Integrated Hall Sensor Array, Journal of the Korean Society for Nondestructive Testing, Vol. 27, No. 5, pp. 375-382

[39] Lee, J. Y. and Jun, J. W. (2008a) NDT of Non-Metallic Material Using Penetration of Magnetic Fluid, Proceedings of Fall conference of the Korean Society for Nondestructive Testing, pp. 198-202

[40] J. Jun, J. Lee, D. Park, "NDT of a nickel inconel specimen using by the complex induced current-magnetic flux leakage method and linearly integrated Hall sensor array," J Korean SocNondestr Test, vol. 27(5), pp. 375-382, 2007.

[41] J. Jun, M. Choi, J. Lee, "Nondestructive evaluation of austenitic stainless steel using CIC-MFL and LIHaS," IEEE Trans. Mag. Vol. 47(10), pp.3959-62, 2011.

[42] J. Jun, Y. Park, J. Lee, "Real time visualization of alternating magnetic fields using 2-dimensional integrated hall sensor array," Journal of Electrical Engineering-ElektrotechnickyCasopis, vol.61(7), pp.32-35, 2010.

[43] J. Kim, M. Le, J. Lee, Y.H. Hwang, "Non-destructive Testing and Evaluation of Far-side Corrosion around Rivet in Jet-Engine Intake of Aging Supersonic Aircraft," Journal of Nondestructive Evaluation, Accepted, 2013.

[44] J. Kim, M. Le, J. Lee, "Non-destructive evaluation of far-Side corrosion around the multi-layered rivet by using the solid-State Hall sensor array," Prooceeding of Sensors Applications Symposium (SAS), 2014 IEEE, 18-20 Feb. 2014Queenstown, New Zealand. pp. 42 – 46.

[45] Harold R V JANSEN, Eddy Current Testing: Profiled eddy current probes for complex shape inspection, 18th World Conference on Nondestructive Testing, 16-20April 2012, Durban, South Africa.

[46] M.A. Robers, R. Scottini, Pulsed Eddy Current In Corrosion Detection, NDT.net - October 2002, Vol. 7 No.10.

[47] 47 R. N. De mesquita, D. K. S. Ting, E. L. L. Cabral, B. R. Upadhaya, Classification of steam generator tube cracks for real time application using eddy current data and self-organizing maps, Real time systems, Vol. 27, pp. 49-70, 2004.

[48] Huang, H., Sakurai, N., Takagi, T., Uchimoto, T.: Design of an eddy-current array probe for crack sizing in steam generator tubes. NDT E Int. 36(7), 515–522 (2003)

[49] 36 Uchanin, V., Najda, V.: The development of eddy current technique for WWER steam generators inspection. In: InTech 2011, pp. 145–164 (2011).

[50] 37 Joubert, P.Y., Bihan, Y.L., Placko, D.: Localization of cracks in steam generator tubes using a multi-coil eddy current probe dedicated to high speed inspection. NDT E Int. 35(1), 53–59 (2002)

[51]   38 Yusa, N., Chen, Z., Miya, K.: Quantitative profile evaluation of natural cracks in a steam generator tube from eddy current signals. Int. J. Appl. Electromagn. Mech. 12, 139–150 (2000)

[52]   39 L.Udpa, S.S. Udpa, Eddy current crack characterization using neural networks, Materials Evaluation, Vol. 48, pp. 342-347, 1990.

[53]   40 B. P. C. Rao, B. Raj, T. Jayakumar, using artificial networks to quantify discontinuities in eddy current testing, Materials Evaluation, Vol. 60, pp. 84-88, 2000.

[54]   41 S. S. Udpa and W. Lord, Fourier descriptor classification scheme for differential probe signals, Materials Evaluation, 42, pp. 1136-1141, 1984.

[55]   42 B. R. Upadhyaya, B. R. Yan, R. C. Bercan, Hybrid digital signal processing and neural networks for automated diagnostics using NDE method, annual of nuclear engineering dept. of the university of Tennessee for the US nuclear regulatory commission office of nuclear regulatory research, USA, 1993.

[56]   43 Minhhuy Le, Hoanghai Vu, Jungmin Kim, Chandra SekharAngani, Jinyi Lee, Qantitative Evaluation of Corrosion in a Thin Small-Bore Piping System Using Bobbin-Type Magnetic Camera, J NondestructEval, 2013.

[57]   44 Lee, J., Jun, J., Kim, J., Choi, H., Le, M.: Bobbin-type solid-state hall sensor array with high spatial resolution for cracks inspection in small-bore piping systems. IEEE Trans. On Magn. 48(11), 3704-3707 (2012)

[58]   45 Jun, J., Lee, J., Kim, J., Le,M., Lee, S.: Eddy current imager based on bobbin-type Hall sensor array for nondestructive evaluation in small-bore piping system. In: Proceedings of the 39th Annual Review of Progress in Quantitative Nondestructive Evaluation, Denver, Colorado, USA, 12–20 July (2012).

[59]   46 Le, M., Lee, J., Jun, J., Kim, J.: Estimation of sizes of cracks on pipes in nuclear power plants using dipole moment and finite element methods. NDT E Int. 58, 56–63 (2013).

ACKNOWLEDGEMENT

I would like to express my gratitude to my advisor, Prof. Jinyi Lee at Department of Control, Instrumentation and Robot Engineering for his supports. That he willingly shared the knowledge with me during the research and writing of my thesis. His advices are always very helpful in both doing research and living in Korea.

I would also like to thanks to Prof. Han-Soo Choi, Prof. Chang-Hyun Cho, Prof. N. Ko, Keun-Chang Kwak, Soon-Suck Jang and all professors at Department of Control, Instrumentation and Robot Engineering for teaching me the knowledge.

I like to thanks to my lab-mates of Research Center for Real Time-NDT Chosun University for 3 years of my studying and living in Korea: Dr. Jungmin Kim, Dr. Minhhuy Le, Dr. Chandra, Mr. Hoyoun Choi, Mr. Myungki Choi.

I am extremely thankful to my parents, all my family and friends for their love, support, and encouragement in every moment of my life. From my heart, I always wish and pray for them.

Vu Hoang Hai

저작물 이용 허락서

학 과	제어계측공학과	학 번	20117743	과 정	석사
성 명	한글 부황하이 한문 영문 VU HOANG HAI				
주 소	광주 동구 지산1동 504-8번지 2층				
연락처	e-mail : HAITNUT@GMAIL.COM				
논문제목	한글:유도형면전류와선형홀센서배열을이용한박판금속의비파괴평가 영문: **Nondestructive Evaluation of Thin Thickness Metal Plate by using the Sheet-Type Induced Current and Linearly Integrated Hall Sensor Arrays**				

본인이 저작한 위의 저작물에 대하여 다음과 같은 조건 아래 조선대학교가 저작물을 이용할 수 있도록 허락하고 동의합니다.

- 다 음 -

1. 저작물의 DB 구축 및 인터넷을 포함한 정보통신망에의 공개를 위한 저작물의 복제, 기억장치에의 저장, 전송 등을 허락함
2. 위의 목적을 위하여 필요한 범위 내에서의 편집과 형식상의 변경을 허락함(다만, 저작물의 내용변경은 금지함)
3. 배포·전송된 저작물의 영리적 목적을 위한 복제, 저장, 전송 등은 금지함
4. 저작물에 대한 이용기간은 5년으로 하고, 기간종료 3개월 이내에 별도의 의사 표시가 없을 경우에는 저작물의 이용기간을 계속 연장함
5. 해당 저작물의 저작권을 타인에게 양도하거나 출판을 허락을 하였을 경우에는 1개월 이내에 대학에 이를 통보함
6. 조선대학교는 저작물 이용의 허락 이후 해당 저작물로 인하여 발생하는 타인에 의한 권리 침해에 대하여 일체의 법적 책임을 지지 않음
7. 소속 대학의 협정기관에 저작물의 제공 및 인터넷 등 정보통신망을 이용한 저작물의 전송·출력을 허락함

동의여부 : 동의(○) 반대( )

2014년 8월 25일 Vu Hoang Hai

조선대학교 총장 귀하